Research Group

Scanning Probe Methods

Triannual Report 2014 - 2016

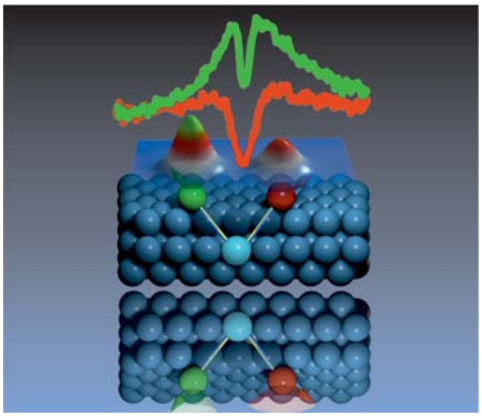
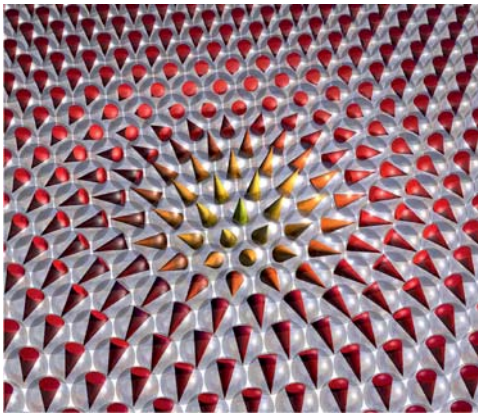

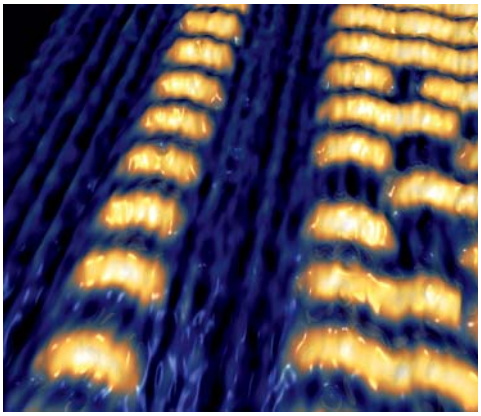

University of Hamburg

Gate to the World of Science

Triannual Report 2014 – 2016

Research Group “Scanning Probe Methods”

University of Hamburg
Department of Physics

Interdisciplinary Nanoscience Center
Hamburg (INCH)

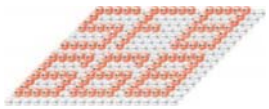

Sonderforschungsbereich 668
(DFG Collaborative Research Center)

ERC Advanced Grant Group
"ASTONISH"

Contact:
Prof. Dr. Roland Wiesendanger
Tel. (++49) 40-42838-5244 (direct)
(++49) 40-42838-3203/-7045 (secretary)
FAX (++49) 40-42838-6188
e-mail wiesendanger@physnet.uni-hamburg.de
WWW www.nanoscience.de

Contents

Chapter 1

Preface

This is the eighth triannual report of the research group „Scanning Probe Methods“ at the Physics Department of the University of Hamburg. Based on the strategic development of nanoscience-related infrastructure at the University of Hamburg over a time period of almost 25 years, several research centers and international networks of scientific excellence could be established in recent years and are recognized worldwide:

Since 2006 we have established a Collaborative Research Center, DFG-Sonderforschungsbereich (SFB 668), entitled „Magnetism from single atoms to nanostructures“ (chairman: Prof. Dr. Roland Wiesendanger). The SFB 668 is focused on fundamental studies of magnetic properties of nanostructures in contact with a substrate, including spin structures in thermal equilibrium as well as transport and dynamic properties. It involves research groups from the Institute of Applied Physics, from the I. Institute of Theoretical Physics, from the Institute of Experimental Physics, from the Institute of Inorganic and Applied Chemistry (all from Hamburg University), and from the Institute of Experimental Physics of the University of Kiel. In total more than 100 researchers are working within the SFB 668. In 2013 the SFB 668 was evaluated with great success and received funding for the third period (2014 – 2017).

Since 2013, Dr. Jens Wiebe successfully leads a project in the framework of the DFG Priority Program on “Topological Insulators” with the goal of combining advanced scanning tunneling spectroscopy techniques, angle-resolved photoemission, and XMCD measurements in order to correlate structural, electronic, and magnetic properties of this novel class of materials. This project was recently evaluated with great success and received funding for an additional three years period.

Since 2014, Dr. Stefan Krause leads another project in the framework of a DFG Priority Program, namely on “Spin Caloritronics” with the goal of combining advanced scanning tunneling spectroscopy techniques with concepts of spin caloritronics down to the atomic scale for well-defined model systems.

Dr. Anika Schlenhoff and Dr. Torben Hänke successfully applied for DFG grants involving the funding of their own positions which allowed them to start innovative research projects as independent researchers. Moreover, Dr. Alexandra Palacio-Morales was successful with her application for an Alexander von Humboldt postdoctoral fellowship for two years and can now focus on exciting research on non-

collinear spin states down to the atomic level.

In Europe we have become partners within numerous research networks funded by the European Community in recent years. Since September 2015 our research group is involved in an EU-FET-Open research project named "MAGicSky" devoted to the development of novel types of spintronic devices based on nano-scale magnetic skyrmions. These tiny knots in the magnetization of ultrathin magnetic films and multilayer structures exhibit an exceptional stability against external perturbations on one hand, while they can be manipulated easily by spin currents as well as local electric and magnetic fields. Our first demonstration of local electric-field induced writing and deleting of single skyrmions in ultrathin iron films as a basis for a future ultra-dense magnetic hard-disk technology, as recently reported in the journal "Nature Nanotechnology" was one of the highlights within the first project year. It was complemented by the demonstration of stable magnetic skyrmions at room temperature by our partners from CNRS (Paris) and PSI (Villigen). The recent evaluation of this project after the first year was excellent.

Furthermore, a second ERC Advanced Grant of the European Research Council (ERC) was awarded to Roland Wiesendanger in 2013 for "Atomic-scale studies of the nature of and conditions for inducing superconductivity at high-temperatures". This funding program allows individual researchers to build up a significant activity in an innovative field of science based on previous outstanding research achievements. While the first ERC Advanced Grant project entitled "Fundamental studies and innovative approaches of research on magnetism" has ended in 2013, the second ERC Advanced Grant for the time period of 2014 - 2018 has allowed starting innovative research activities on interface-induced superconductivity in various kinds of novel hybrid systems.

Based on our previous scientific achievements in the field of molecular spintronics, we recently received a grant from the US Office of Naval Research (ONR) for a project focusing on the development of planar molecular spintronic devices. Starting from a fundamental understanding of molecular adsorption, molecular reactions as well as spin-dependent intra- and inter-molecular interactions on surfaces, we will aim at novel types of molecular-scale data storage and logic devices capable of energy-efficient room-temperature operation.

Several prizes and awards were given to members of our group in the past three years. Roland Wiesendanger was awarded with the "Hamburger Wissenschaftspreis 2015" by the Hamburg Academy of Sciences, accompanied with the highest donation among all prizes of German academies. This allowed the support of an exceptionally talented young international fellow, Dr. Pin-Jui Hsu, who contributed significantly to our worldwide recognized research activities on nano-scale magnetic skyrmions in ultrathin films. Another great recognition of the research achievements of Roland Wiesendanger came with the first awarding of the Heinrich Rohrer Grand Medal and Prize in 2014 by the Surface Science Society of Japan. The award ceremony took place during an international conference in Matsue, Japan. In 2016, Roland Wiesendanger received the Julius Springer Prize for Applied Physics, together with

Prof. Xiang Zhang from Berkeley. Another great event was the awarding of the title Doctor honoris causa for Roland Wiesendanger by the Technical University of Poznan, Poland, in 2015. Furthermore, Roland Wiesendanger has been elected as International Fellow of the Surface Science Society of Japan (SSSJ) in 2015 and as Member of the European Academy of Sciences (EURASC) in 2016. Finally, Roland Wiesendanger has been honored as cfaed Distinguished Lecturer by the TU Dresden, Germany.

In addition, several recognitions for our young researchers could be celebrated in the past three years: Dr. Alexander Khajetoorians received the Nicholas Kurti European Science Prize 2014 and shortly after an offer for a Full Professor position at the Radboud University in Nijmegen, Netherlands. Dr. Yingshuang Fu was awarded by the National Thousand Talent Program, China, in 2014 which also allowed him setting up a new research group. Dr. Maciej Bazarnik was honored by the "First degree individual scientific award" of the President of Poznan University of Technology in 2015, while Dr. Sujit Manna received the "INSPIRE Faculty Award" of the Government of India in 2016. Finally, our PhD student Lorenz Schmidt received the "Best Student Poster Award" at the JEMS meeting in 2016.

In the present triannual report 2014-2016 the scientific achievements of the research group "Scanning Probe Methods" are summarized covering the following topics: magnetic nanostructures, superconductivity, topological insulators, molecular systems, and instrumental developments. The research activities of our group in the time period 2014-2016 resulted in 73 scientific publications (among them 11 in Science and Nature Journals, 10 in "Physical Review Letters") and 288 presentations at conferences, colloquia or seminars (including 97 plenary and invited talks at international meetings).

This research report provides a good opportunity to thank all funding agencies including the EU, the ERC, the DFG, the ONR (USA), the Alexander von Humboldt Foundation, the DAAD, the Hamburgische Stiftung für Wissenschaften, Entwicklung und Kultur Helmut und Hannelore Greve, as well as several industrial companies for their financial support of our research activities. In particular we would like to thank the University of Hamburg for the continued support of our research activities in nanoscience and nanotechnology. I would also like to take the opportunity to thank all the past and present members of the research group „Scanning Probe Methods" for their strong devotion to scientific excellence. Finally, we gratefully acknowledge the great support by our central mechanical and electronic workshops, as well as by our secretaries and administration staff.

Hamburg, December 2016

Prof. Dr. Roland Wiesendanger

(Chairman of the DFG Collaborative Research Center SFB 668 and Scientific Coordinator of the Interdisciplinary Nanoscience Center Hamburg)

Chapter 2

Staff Members

Head

Prof. Dr. Roland Wiesendanger

Secretary

Andrea Beese
Ute Brenger
Sigrid Schmidtke

Public Relations Office

Dipl.-Chem. Heiko Fuchs

Technical Support

PTA Norbert Dix
Dipl.-Ing. Michael Langer
Dipl.-Ing. Jörg Völkel

Senior Scientists

Dr. Maciej Bazarnik
Dr. Kirsten von Bergmann
Dr. Jens Brede (until December 2014)
Dr. Régis Decker (until April 2014)
Dr. Thomas Eelbo
Dr. Josef Grenz
Dr. Torben Hänke (until August 2016)
Dr. Pin-Jui Hsu
Dr. Anand Kamlapure
Dr. Alexander Khajetoorians (until August 2014)
Dr. Howon Kim
Dr. Stefan Krause
Dr. André Kubetzka
Dr. Sujit Manna (until October 2016)

Dr. Safia Ouazi (until April 2014)
Dr. Alexandra Palacio-Morales
Dr. Anika Schlenhoff
Dr. Alexander Schwarz
Dr. Udai Raj Singh
Dr. Andreas Sonntag (until December 2015)
Dr. Elena Vedmedenko
Dr. Jens Wiebe
Dr. Robert Wieser (until June 2014)
Dr. Vladimir Zdravkov (until December 2015)
Dr. Hai Zhong

Ph. D. Students

Henning von Allwörden (until July 2014)
David Altwein
Lasse Cornils
Andreas Eich (until June 2014)
Micha Elsebach
Aurore Finco
Johannes Friedlein
Cody Friesen
Julian Hagemeister
Christian Hannecken (until March 2015)
Jonas Harm
Jan Hermenau
Arne Köhler
Mario Krizanac
Philipp Lindner
Peter Löptien (until May 2014)
Marco Perini
Niklas Romming
Kai Ruschmeier (until March 2014)
Jonas Sassmannshausen
Lorenz Schmidt
Jörg Schwöbel
Emil Sierda
Manuel Steinbrecher
Jonas Warmuth

Master Students

Martin Bendschneider
Gotthold Fläschner (until May 2014)
Gideon Henkelmann
Davide Iaia (until August 2014)
Maximilian Meyer (until November 2015)

Hermann Osterhage
David Schwickert (until October 2016)
Ansgar Siemens
Khai Ton That
Lennart Tunze
Tobias Wagner (until April 2016)
Yangye Zhang (until February 2016)

Chapter 3

Research Activities 2014-2016

Overview

R. Wiesendanger

Our research activities are concentrated on fundamental studies of emergent quantum phases and topological states of matter, making use of advanced scanning probe methods. Further emphasis is put on the detailed investigation of the fundamental relationship between nanostructure and nanophysical properties. Scanning probe methods (SPM) are ideally suited for such investigations because they provide atomic-scale spatial resolution combined with spectroscopical capabilities at low energy scales (down to micro-eV). By choosing an appropriate type of interaction between probe tip and sample, almost any kind of nanophysical property can be studied by scanning probe methods. In particular, spin-dependent phenomena can be investigated by spin-resolving SPM methods, such as Spin-Polarized Scanning Tunneling Microscopy (SP-STM) and Spectroscopy (SP-STS), or Magnetic Exchange Force Microscopy (MExFM). Recently, SPM methods have been combined with pump-probe techniques, thereby additionally yielding high temporal resolution of dynamic processes down to the single-atom limit. We apply these advanced SPM methods to various classes of materials, including metals, semiconductors, insulators, superconductors, magnetic materials, as well as organic thin films and molecular materials.

To be able to make significant contributions to this rapidly developing field, a major part of our activities is devoted to new developments or further improvements on SPM instrumentation, including the development of new positioning devices with nanometer-scale accuracy, the development of new types of sensors, or the development of dedicated SPM instruments which can operate under extreme conditions (e.g. UHV, low temperatures and high magnetic fields). Special emphasis is also put on the development of new experimental methods based on the local probe geometry, which usually requires adjustments of the hardware and software for SPM data acquisition.

In the following, a brief summary of the highlights of our research activities in the time period of 2014 - 2016 is provided. For further information, please do not hesitate to contact us. We will be glad to provide reprints of publications on specific topics.

3.1 Interactions of magnetic atoms on metallic surfaces

J. Wiebe and R. Wiesendanger

Using the tip of the STM as a tool, one can fabricate artificial arrays of magnetic atoms adsorbed on surfaces of initially non-magnetic metals. Using different facets of single crystals, these arrays can have almost any topology from hexagonal to rectangular. For mutual distances of several lattice constants between the constituent magnetic atoms, the substrate conduction-electron mediated Ruderman-Kittel-Kasuya-Yosida (RKKY) interaction is usually the dominant magnetic interaction. Since the RKKY interaction strength is strongly distance dependent, and since its sign additionally oscillates between ferromagnetic and antiferromagnetic coupling, the interatomic interactions in such artificial arrays can be tailored at wish. Therefore, artificial adatom arrays offer an ideal playground for the fundamental investigation of model systems for magnetic quantum phases of matter.

Within this triannual research period, we successfully extended our investigation of artificial adatom arrays in three directions. First, we realized model systems for the basic constituents of so called Hund's metals, i.e. metals in which electron correlations are driven by Hund's rule coupling, and which are recently thought to explain the exotic magnetic and electronic behaviour of strongly correlated electron systems of multi-orbital metallic materials. Second, we directly revealed the non-collinear Dzyaloshinskii–Moriya (DM) contribution to the RKKY interaction, which can be used to construct adatom arrays with a tailored magnetic chirality. Third, we extended the adatom species to rare earth materials, which turned out to resist a detection of their magnetic moment by STM based techniques.

3.1.1 Investigation of the magnetism of model systems for Hund's impurities

A. A. Khajetoorians, M. Valentyuk, M. Steinbrecher, T. Schlenk, A. Shick, J. Kolorenc, A. I. Lichtenstein, T. O. Wehling, R. Wiesendanger, and J. Wiebe

The recently proposed concept of a Hund's metal can be used to explain many exotic phases of matter, including unconventional superconductivity in iron pnictides and chalcogenides, as well as non-Fermi liquid behaviour in ruthenates. Tuning the abundance of parameters that determine these materials was so far experimentally challenging. We showed that the basic constituent of a Hund's metal, a Hund's impurity, can be realized using a single iron atom adsorbed on a platinum surface (Fig.3.1(a)), a system that comprises a magnetic moment in the presence of strong charge fluctuations [1]. The magnetic properties can be controlled by using the tip of a scanning tunnelling microscope to change the binding site and degree of hydrogenation of the 3d transition-metal atom (Fig.3.1(b)-(e)). We were able to experimentally explore a regime of four almost degenerate energy scales (Fig.3.1(f), Zeeman energy, temperature, Kondo temperature and magnetic anisotropy) and probe the magnetic excitations with the microscope tip. The regime of the Hund's

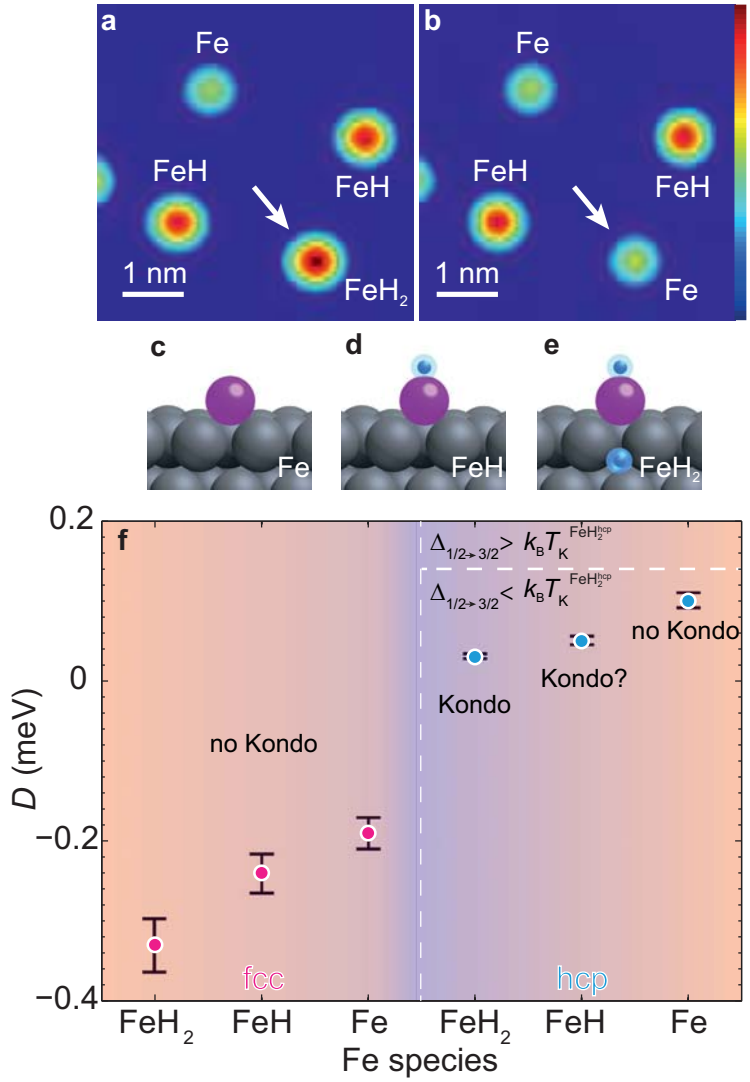

Figure 3.1: Investigation of the magnetism of model systems for Hund's impurities [1]. (a,b) STM images of Fe and Fe–hydrogen complexes adsorbed on a Pt(111) surface. The arrow indicates FeH_2 before (a) and after (b) controlled dehydrogenation with a voltage pulse. (c)-(e) Side views of DFT-calculated positions of Fe (pink spheres), hydrogen (blue spheres) and Pt atoms of the substrate (grey spheres) for the three different types of complexes. (f) Experimental values of the magnetic anisotropy parameter D analysed within an effective spin model for each of the six Fe species. Significant or negligible Kondo screening as revealed by the experimental line shapes of inelastic tunneling spectroscopy of each impurity are indicated. The dashed horizontal line indicates the D value at which the splitting between the magnetic ground and first excited states becomes larger than the Kondo energy scale.

impurity was tuned from an emergent magnetic moment to a multi-orbital Kondo state, and the system can be used to test predictions of advanced many-body theories for non-Fermi liquids in quantum magnets or unconventional superconductors.

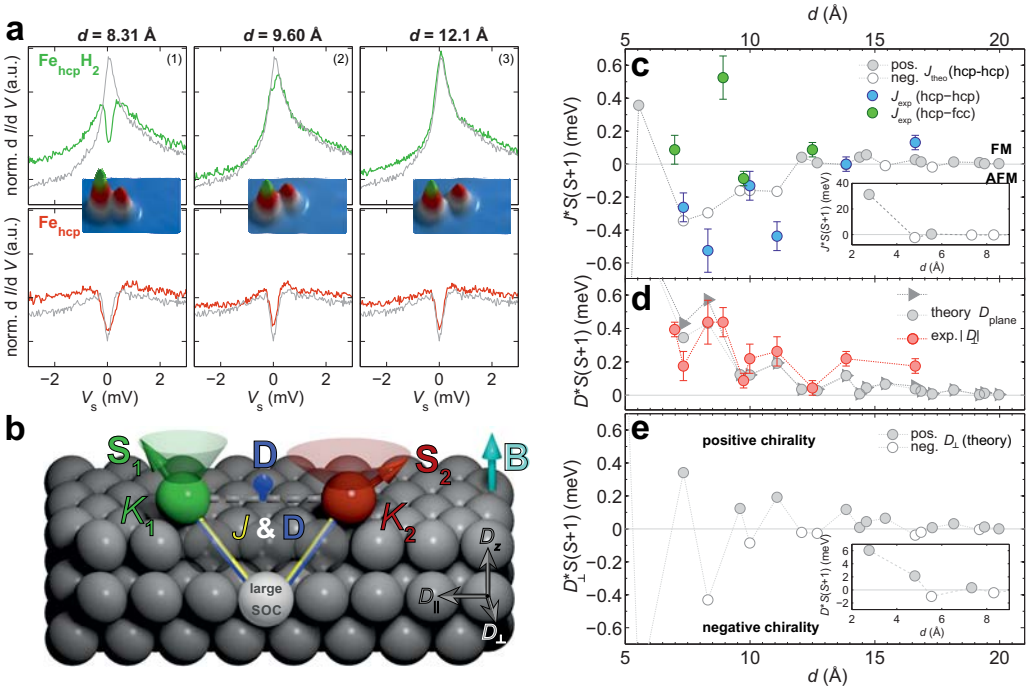

Figure 3.2: Experimentally determined Heisenberg and DM components of the interaction between Fe impurities on Pt(111) [2]. (a) Inelastic scanning tunneling spectroscopy of $Fe_{hcp}H_2$ (green) and Fe_{hcp} (red) within selected pairs of different distance as shown in the topographs in insets. In comparison, the spectra measured on the corresponding isolated atoms are shown in grey. The exchange interaction within the pair forces a splitting of the Kondo resonance of $Fe_{hcp}H_2$ and a modification of the magnetic excitation of Fe_{hcp} as compared with the isolated atoms. (b) Cartoon diagram of the Heisenberg (J) and DM contributions to indirect conduction electron-mediated exchange interactions between two magnetic atoms with spins S_1 and S_2, and magnetic anisotropies K_1 and K_2. The interaction is mediated by scattering of conduction electrons at a substrate atom (grey) with strong spin-orbit coupling (SOC). The arrows show the orientation of the experimental magnetic field B and components of the DM vector. (c)-(e) Experimentally determined values of J and the DM interaction (coloured circles) compared with the $ab-initio$ calculations of J and the different components of the DM vector (grey and white circles and triangles). Insets illustrate theoretical data at small separations.

3.1.2 Tailoring chiral magnetic interactions

A.A. Khajetoorians, M. Steinbrecher, M. Ternes, M. Bouhassoune, M. dos Santos Dias, S. Lounis, J. Wiebe, and R. Wiesendanger

Chiral magnets are a promising route towards dense magnetic storage technology due to their inherent nano-scale dimensions and energy efficient properties. Engineering chiral magnets requires atomic-level control of the magnetic exchange interactions, including the DM interaction, which defines a rotational sense for the magnetization of two coupled magnetic moments. By inelastic tunneling spectroscopy (Fig.3.2(a)) we showed that the indirect conduction electron-mediated DM interaction between two individual magnetic atoms on a metallic surface (Fig.3.2(b)) can be manipulated by changing the interatomic distance with the tip of the STM [2].

We quantify this interaction by comparing our measurements to a quantum magnetic model and DFT calculations yielding a map of the chiral ground states of pairs of atoms depending on the interatomic separation (Fig.3.2(c),(d). The map enables tailoring the chirality of the magnetization in dilute atomic-scale magnets (Fig.3.2(e)).

3.1.3 Rare earth adatoms

M. Steinbrecher, A. Sonntag, M. dos Santos Dias, M. Bouhassoune, S. Lounis, J. Wiebe, R. Wiesendanger, and A.A. Khajetoorians

Whether rare-earth materials can be used as single-atom magnetic memory was an ongoing debate in recent literature. We showed, by inelastic and spin-resolved scanning tunnelling based methods [3], that we observe a strong excitation (Fig.3.3(a),(b)) and magnetic signal (Fig.3.3(d),(e)) from Fe atoms adsorbed on Pt(111), but see no signatures of magnetic excitation (Fig.3.3(c)) or spin-based telegraph noise (Fig.3.3(f)) for Ho atoms. Moreover, we observe that the indirect exchange field produced by a single Ho atom is negligible, as sensed by nearby Fe atoms (Fig.3.3(a)-(c)). We demonstrate, using DFT methods, that this stems from

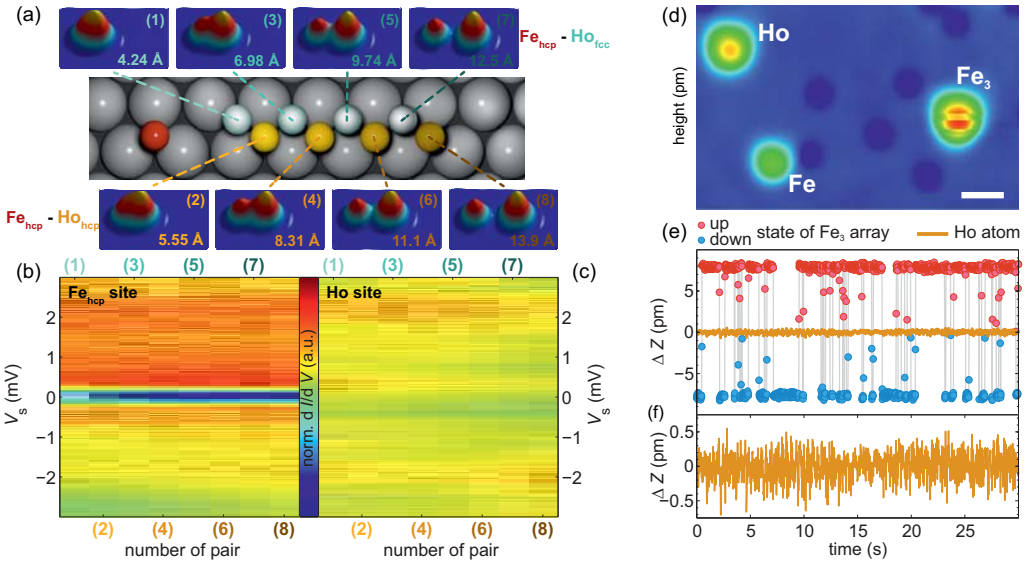

Figure 3.3: Comparison of inelastic tunneling spectroscopy and spin-resolved STM measured on Fe and Ho atoms adsorbed on Pt(111) [3]. (a) STM images of different Fe_{hcp}–Ho atom pairs with indicated distances and related ball-models in between. (b) Spectra measured on the Fe_{hcp} atom and (c) on the Ho atom for each pair with the differential conductance signal represented by the given colour scale. (d) STM image of an Fe_3-cluster, an Fe and a Ho atom recorded with a spin-polarized tip (white scale bar has a width of 1 nm). The height of the Fe_3-cluster changes randomly while recording the image due to switching of its magnetization. (e) Time trace of the magnetic telegraph noise of the Fe_3-cluster (colours red and blue represent the two magnetization states up and down) and of a Ho atom recorded with the same magnetic tip (orange line). The magnetic tip is sensitive to the out-of-plane magnetization component. (c) Time trace of the Ho atom from (e) shown in a more narrow height range.

a relatively weak coupling of the Ho 4f electrons with both tunnelling electrons and substrate itinerant electrons, making magnetic coupling and detection very difficult when compared to 3d elements.

References

[1] A. A. Khajetoorians, M. Valentyuk, M. Steinbrecher, T. Schlenk, A. Shick, J. Kolorenc, A. I. Lichtenstein, T. O. Wehling, R. Wiesendanger, and J. Wiebe, Tuning emergent magnetism in a Hund's impurity, Nature Nanotechnology **10**, 958 (2015).

[2] A.A. Khajetoorians, M. Steinbrecher, M. Ternes, M. Bouhassoune, M. dos Santos Dias, S. Lounis, J. Wiebe, and R. Wiesendanger, Tailoring the chiral magnetic interaction between two individual atoms, Nature Communications **7:10620**, doi: 10.1038/ncomms10620 (2016).

[3] M. Steinbrecher, A. Sonntag, M. dos Santos Dias, M. Bouhassoune, S. Lounis, J. Wiebe, R. Wiesendanger, and A. A. Khajetoorians, Absence of a spin-signature from a single Ho adatom as probed by spin-sensitive tunneling, Nature Communications **7:10454**, doi: 10.1038/ncomms10454 (2016).

3.2 Non-collinear magnetism: spin spirals and magnetic skyrmions

K. von Bergmann and R. Wiesendanger

Recent interest in non-collinear magnetic states has been triggered by the insight into interfacial Dzyaloshinskii-Moriya interactions (DMI) that can be decisive for the magnetic state, and the proposal to use magnetic skyrmions in racetrack-type devices, see [1, 2] and references therein. In the following we highlight our results obtained in a three year timeframe with (spin-polarized) scanning tunneling microscopy, (SP-)STM. This includes non-collinear states in one and two dimensions, and their coupling to open boundaries or to other magnetic states. Furthermore, various conceptually different magnetic field behaviors of different magnetic states are presented. The precise measurement of the size and shape of magnetic skyrmions yielded the decisive material parameters for their creation and a novel all-electrical mechanism for skyrmion detection was identified due to the spatial resolution capabilities of STM. The lateral manipulation of skyrmions exploiting their pinning to adsorbed magnetic clusters is demonstrated and a controlled switching between the skyrmion and the ferromagnetic state is ascribed to an electric field based mechanism.

3.2.1 Fe and Co chains on Ir(001): magnetism in one dimension

M. Menzel, J. E. Bickel, A. Kubetzka, K. von Bergmann, and R. Wiesendanger

The magnetic ground state of biatomic Fe chains on reconstructed Ir(001) is a spin spiral, where adjacent magnetic moments enclose an angle of about 120°, see sketch in Fig. 3.4(a). Whereas this magnetic state fluctuates due to thermal excitations at $T = 8$ it can be stabilized by direct exchange coupling to a ferromagnetic Co chain, see Fig. 3.4(b) left and central chain, respectively. Combined SP-STM and DFT studies have demonstrated that the magnetocrystalline anisotropy axis of one structural type of these biatomic ferromagnetic Co chains is canted by about 30° with respect to the surface normal, compare sketch in Fig. 3.4(c) [3]. This unusual behavior originates from the asymmetric adsorption sites of the two strands of the Co chain in combination with the spin-orbit coupling of the Ir substrate, as revealed by a detailed analysis of the DFT calculations [3].

The effective magnetocrystalline anisotropy of Fe chains on the other hand was found to depend on the exact length of the chain [4], as demonstrated for three examples in Fig. 3.4(d): micromagnetic simulations using the magnetic interaction parameters as determined by DFT show that 30-atom long chains possess an effective out-of-plane anisotropy, in contrast to the effective in-plane anisotropy of 31-atom long chains; chains with 32 atom pairs along their axis have a negligible magnetocrystalline anisotropy. Also in spin-resolved STM measurements a variation in the behavior is observed for different chain lengths [4]: whereas in the absence of an external magnetic field no magnetic signal is detected due to rapid thermal fluc-

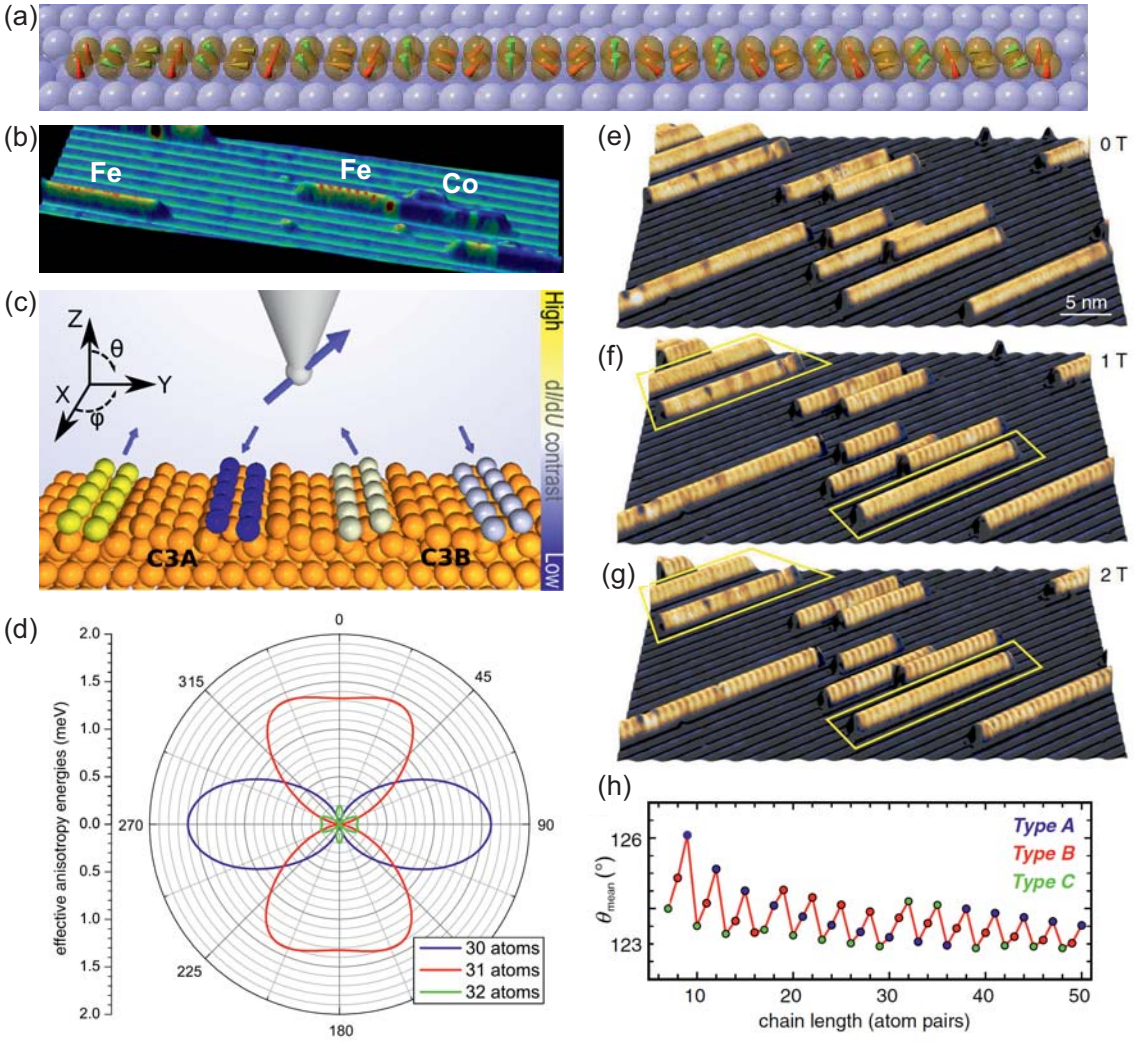

Figure 3.4: Magnetism in biatomic Fe and Co chains on reconstructed Ir(001). (a) Sketch of the spin spiral state of Fe chains. (b) The magnetic state of Fe chains fluctuates at a temperature of about 8 K (left) but can be stabilized by an adjacent ferromagnetic Co chain (center). (c) Sketch of the four degenerate magnetization directions of ferromagnetic biatomic Co chains with canted magnetocrystalline anisotropy. (d) Effective anisotropy energies shown for three exemplary biatomic Fe chains as obtained from micromagnetic simulations. (e),(f),(g) Sample area with biatomic Fe chains of different lengths at three different values of the external magnetic field as indicated. (h) Mean angle between adjacent atom pairs as a function of chain length, the three chain types categorized by their effective anisotropy are indicated.

tuations of the spin spiral state, see Fig. 3.4(e), with increasing magnetic field more and more chains exhibit the typical magnetic period on the order of three atomic distances (Fig. 3.4(f) and (g) at 1 T and 2 T, respectively). The simulations predict an oscillatory behavior of the mean angle between neighboring magnetic moments as a function of chain length, Fig. 3.4(h), resulting from a compromise between the chain type, i.e. characterized by the effective magnetocrystalline anisotropy, and a preferential nearest neighbor moment angle.

3.2.2 Fe monolayer on Re(0001): spin states and spin friction

S. Ouazi, A. Palacio-Morales, T. Pohlmann, A. Kubetzka, K. von Bergmann, and R. Wiesendanger

When Fe is deposited onto a Re(0001) single crystal surface it grows pseudomorphically at a coverage below half a monolayer but starts to incorporate dislocation lines along $\langle 1\bar{1}2\rangle$ for larger coverage [5], see topography and simultaneously acquired map of differential conductance in Fig. 3.5(a) and (b). The dislocation lines occur both as regular dense networks as well as single lines, and indicate a transition from hcp over bridge to fcc sites and again via bridge to hcp sites, see STM image in (c) and atomic structure model in (d).

The SP-STM image of Fig. 3.5(e) reveals that the magnetic ground state of the pseudomorphic Fe monolayer on Re(0001) is the Néel state [6], which is characterized by 120° between adjacent magnetic moments due to geometric frustration of antiferromagnetic exchange interactions. Both the real space image and its one-dimensional fast Fourier transformation to the right are in very good agreement with the respective simulations below. Figure 3.5(f) and (g) show atom manipulation images, i.e. constant-current images with a single magnetic atom in the tunnel junction that is moved over the surface during imaging. In addition to the structural atomic period, the magnetic period is visible due to spin friction; however, the intensity of the magnetic signal is very sensitive to the tip-sample distance during the manipulation process and was found to be maximum for a gap resistance of 29 kΩ, see real space image and fast Fourier transform to the right in Fig. 3.5(f) [6].

The magnetic state within the dislocation lines was found to be different: a spin spiral state with a propagation direction along the dislocation line is observed, see periodic superstructure in Fig. 3.5(h) [7]. From a comparison of measurements with out-of-plane and in-plane magnetic tips and the relative magnetic signal strengths it can be deduced that the spins within the spin spiral are canted by about ±25° with respect to the propagation direction. The transition between the spin spiral state and the Néel state was found to be on the order of a few atomic distances, see Fig. 3.5(j) for the experimental and (k) for simulated SP-STM measurements of this interface. Accompanying Monte-Carlo simulations, see Fig. 3.5(l), have revealed a strict lateral correlation between the two states [7].

3.2.3 Fe monolayer on Ir(111): nanoskyrmion lattices

A. Kubetzka, M. Menzel, D. Iaia, K. von Bergmann, and R. Wiesendanger

The Fe monolayer on Ir(111) exhibits a two-dimensional magnetic state, namely a skyrmion lattice. The fcc stacking grows either as stripes at the step edges or as free-standing triangular islands pointing in a specific direction, see Fig. 3.6(a). Due to the roughly square symmetry of the magnetic state on the hexagonal atom arrangement three rotational magnetic domains are possible, denoted by A, B, and C. A correlation between the rotational domain and close-packed Fe step edges is observed where the diagonal of a magnetic unit cell couples to such a Fe-to-vacuum interface. In triangular islands this leads to the coexistence of the three possible

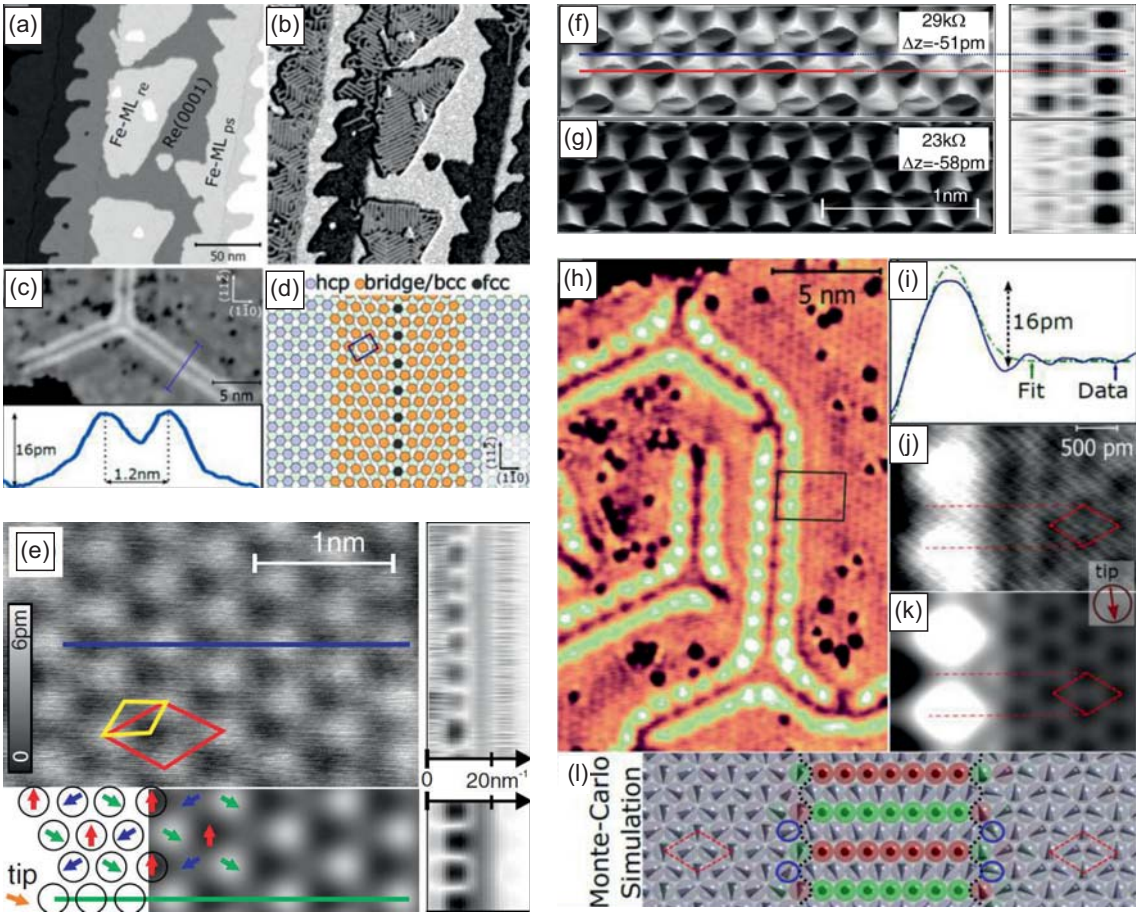

Figure 3.5: Non-collinear states in the Fe monolayer on Re(0001). (a) Topography and (b) simultaneously acquired map of differential conductance showing pseudomorphic and reconstructed Fe monolayer areas. (c) Three rotational symmetric dislocation lines and a height profile below. (d) Atomic structure model of a single dislocation line in the otherwise hcp stacked Fe monolayer. (e) SP-STM image of the Néel state in the pseudomorphic Fe monolayer, and one-dimensional fast Fourier transformation to the right; below is a spin model and a SP-STM simulation of the Néel state with a tip magnetization as indicated. (f),(g) Manipulation images of the Néel state at different gap resistances; due to spin friction the magnetic period becomes visible in both the real space as well as in the one-dimensional fast Fourier transformation to the right. (h) Overview image showing both the Néel state in the pseudomorphic areas as well as the spin spiral state along the dislocation lines. (i),(j),(k) Height profile, SP-STM image, and simulation of the rather sharp transition from the spin spiral to the Néel state. (l) Monte-Carlo simulation showing the preferred relative position between the Néel state and the spin spiral.

rotational magnetic domains and frustration at positions where they merge, see magnified view of the lower central triangular Fe monolayer island in Fig. 3.6(a) [8].

When the nanoskyrmion lattice is in the vicinity of a ferromagnet, such as a NiFe bilayer island, see Fig. 3.6(b)-(e) [9], the coupling of the diagonal of the magnetic unit cell to a close-packed row can be destroyed in favor of a coupling of the edge of the magnetic unit cell to the ferromagnet [9]; for Monte-Carlo simulations of these coupling phenomena see Chapt. 3.3.1.5.

The other stacking of the Fe monolayer on Ir(111), i.e. the hcp monolayer, also

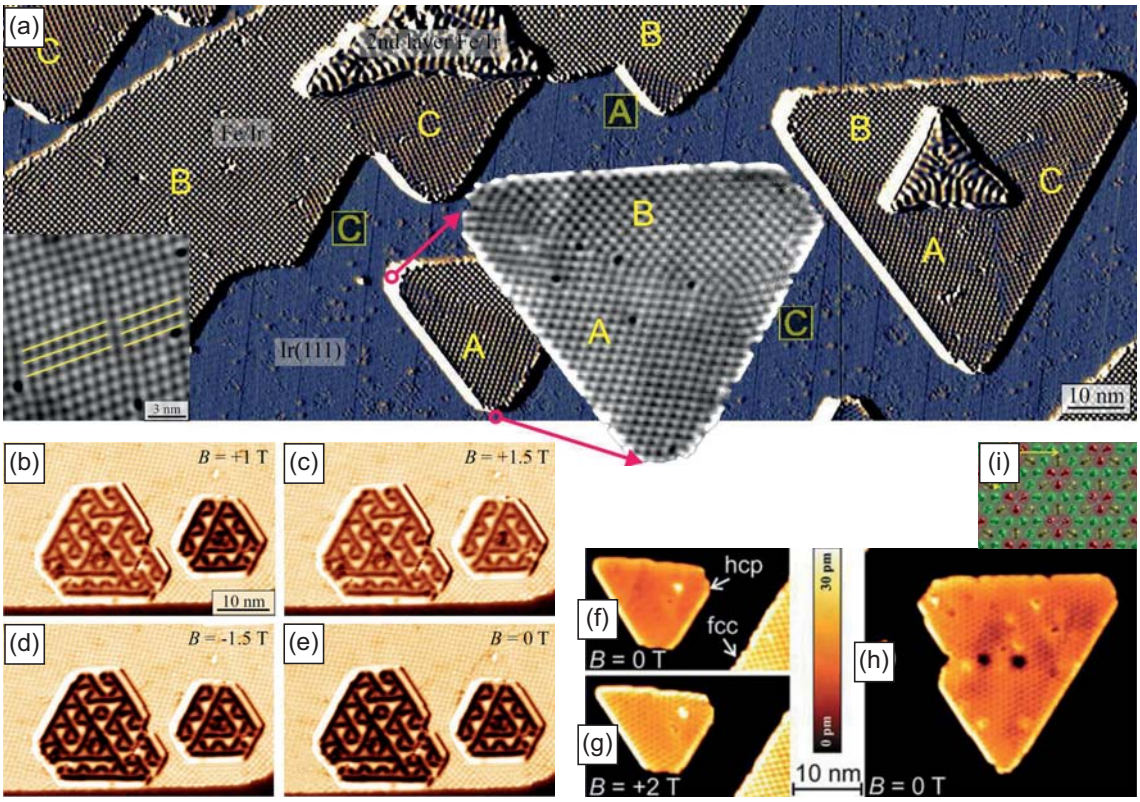

Figure 3.6: Nanoskyrmion lattices in the Fe monolayer on Ir(111). (a) Overview SP-STM image of fcc Fe monolayer stripes and islands, the three possible rotational magnetic domains are labeled. The coupling of the skyrmion lattice to the edges of triangular islands leads to frustration and multi-domain states. (b)-(e) Ferromagnetic Ni islands on the fcc Fe monolayer at different external magnetic fields as indicated; in the vicinity to the ferromagnetic NiFe bilayer patches the nanoskyrmion lattice rotates due to coupling. (f),(g) hcp Fe monolayer island without and with applied magnetic field, demonstrating the susceptibility of the hexagonal nanoskyrmion lattice ground state to thermal fluctuations and external magnetic fields. (h) Larger hcp Fe islands are magnetically stable. (i) Sketch of the hexagonal 12 atom magnetic nanoskyrmion lattice.

exhibits a nanoskyrmion lattice ground state, but the symmetry is hexagonal, in contrast to the roughly square lattice in fcc monolayers [10]. This results in only one rotational domain and the emergence of an effective magnetic moment of the nanoskyrmion lattice. At a measurement temperature of 8 K the magnetic state of small islands is found to fluctuate, but it can be fixed in an applied magnetic field, see images of the same island in Fig. 3.6(f) and (g). Larger islands are stable against thermal switching also in the absence of external magnetic fields, see (h). The proposed magnetic ground state is sketched in Fig. 3.6(i), and from symmetry considerations an energy contribution due to the DMI in a three-site hopping mechanism is inferred [10].

3.2.4 PdFe on Ir(111): spin spirals and magnetic skyrmions

N. Romming, C. Hanneken, L. Schmidt, P.-J. Hsu, A. Kubetzka, K. von Bergmann, and R. Wiesendanger

Single magnetic skyrmions in the PdFe bilayer on Ir(111) can be imaged with SP-STM [11]: for out-of-plane sensitive magnetic tips, see sketch in Fig. 3.7(a), they appear rotationally symmetric as in the measurement shown in (b), whereas a two-lobe structure is observed when the tip is sensitive to the in-plane magnetization of the sample as in (c),(d). The fact that all skyrmions in a PdFe sample imaged with the same in-plane tip show the same appearance demonstrates their unique rotational sense, which is imposed by the DMI. When the external magnetic field that stabilizes the individual skyrmions is inverted also the magnetic contrast inverts when measurements are performed with Cr tips that are insensitive to applied magnetic fields, compare Fig. 3.7(c) and (d). The magnetic field dependent lifetimes of single magnetic skyrmions have been investigated experimentally and by

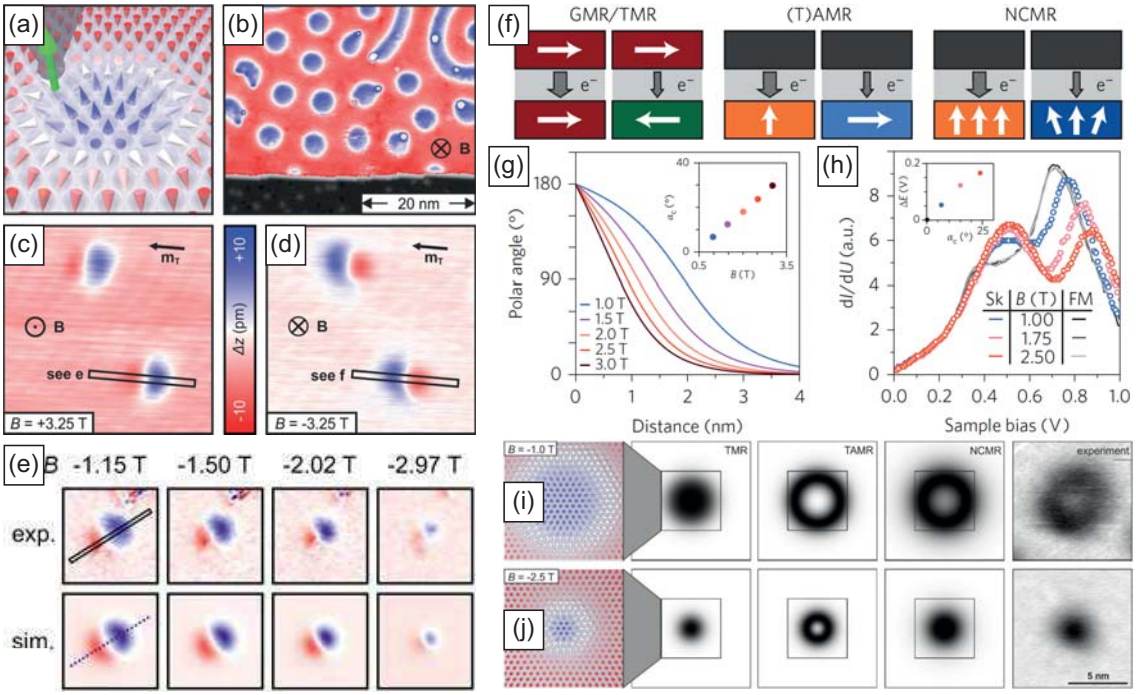

Figure 3.7: Magnetic skyrmions in the PdFe bilayer on Ir(111): magnetic field dependence and all-electrical detection. (a) Sketch of a magnetic skyrmion, colorized according to the observed SP-STM signal with out-of-plane magnetized magnetic tip. (b) SP-STM measurement with out-of-plane magnetic tip. (c),(d) Two magnetic skyrmions in opposite external magnetic out-of-plane fields imaged with the same in-plane magnetized Cr tip. (e) Magnetic field dependent SP-STM measurements (top) and simulations (bottom) of a magnetic skyrmion. (f) Magnetoresistance effects that can contribute to the total resistance. (g) Experimentally determined magnetic field dependent size and shape of a magnetic skyrmion in PdFe. (h) Spectra of differential conductance taken in the center of a skyrmion and outside at different magnetic fields. (i),(j) Spin structure, simulations of different magnetoresistive effects, and experimental data for a skyrmion at 1 T and at 2.5 T, respectively.

Monte-Carlo (MC) simulations [12], see Chapt. 3.3.1.3 for more details.

The spin structure across a skyrmion was found to nicely follow the spin structure of two overlapping 180° domain walls [11]. A fit of such a profile for field-dependent measurements of an individual skyrmion, see Fig. 3.7(e) top and comparison with the energy functional for magnetic skyrmions, yields the material parameters for the PdFe bilayer on Ir(111) such as exchange stiffness, DMI, and magnetocrystalline anisotropy. Micromagnetic simulations using these experimentally derived values as input parameters show very nice agreement with the real-space images, compare Fig. 3.7(e) top and bottom.

Spatially-resolved scanning tunnel spectroscopy revealed that in addition to the tunnel magnetoresistance (TMR) and tunnel anisotropic magnetoresistance (TAMR) also the non-collinearity can have a contribution to the total magnetoresistance, see sketches in Fig. 3.7(f) [13]. This non-collinear magnetoresistance (NCMR) could be identified by comparison of the experimentally determined magnetic field dependent size and shape of individual skyrmions [11] and local scanning tunnel spectra [13], see Fig. 3.7(g) and (h). Sketches of magnetic skyrmions at 1 T and 2.5 T and the respective simulations for the different contributions to magnetoresistance are sketched in Fig. 3.7(i) and (j) in comparison to the experimentally obtained data.

This NCMR is very sensitive to local changes in the spin texture as it roughly scales with the angle between nearest neighbor magnetic moments. Because of the significant magnetocrystalline anisotropy of the PdFe bilayer on Ir(111) [11] the zero magnetic field spin spiral ground state is not homogeneous, but the magnetic moments relax to have larger out-of-plane components and a faster rotation of spins in the in-plane regions, giving rise to a NCMR signal with half the magnetic period, see Fig. 3.8(a). When magnetic fields are applied in the magnetic film plane, a different behavior is observed depending on the direction of the magnetic field relative to the spin spiral propagation direction: for parallel alignment a superstructure with the magnetic period is observed due to a distortion of the in-plane regions of the spin spiral, see (b) [14]; for a magnetic field perpendicular to the spin spiral propagation direction the periodicity does not change and micromagnetic simulations show a distortion of all spins towards a conical spin spiral state.

This different behavior originates from the different energies which can be exploited to reorient spin spirals in magnetic field cooling experiments as shown in Fig. 3.8(c) and (d) [14]: the spin spirals tend to orient their propagation direction perpendicular to the external magnetic field. However, this favorable orientation has to compete with a rather strong coupling of the spin spiral propagation direction to the edge of the nanostructure, which prefers a parallel alignment. Magnetic skyrmions can exist in canted magnetic fields, however, they are slightly distorted as evident from the STM images with NCMR contrast in Fig. 3.8(e) and (f) [14]. Combining the observed asymmetry of the line profiles across the data with the knowledge of the direction of the external magnetic field enables a determination of the absolute rotational sense of the spin texture and their cycloidal nature, see sketch in Fig. 3.8(g) [14].

SP-STM measurements on the PdFe bilayer on Ir(111) demonstrate that single atomic defects in the Pd layer, see Fig. 3.8(h), modify the potential landscape for the existence of a skyrmion, Sk and FM in Fig. 3.8(i): at magnetic fields in which

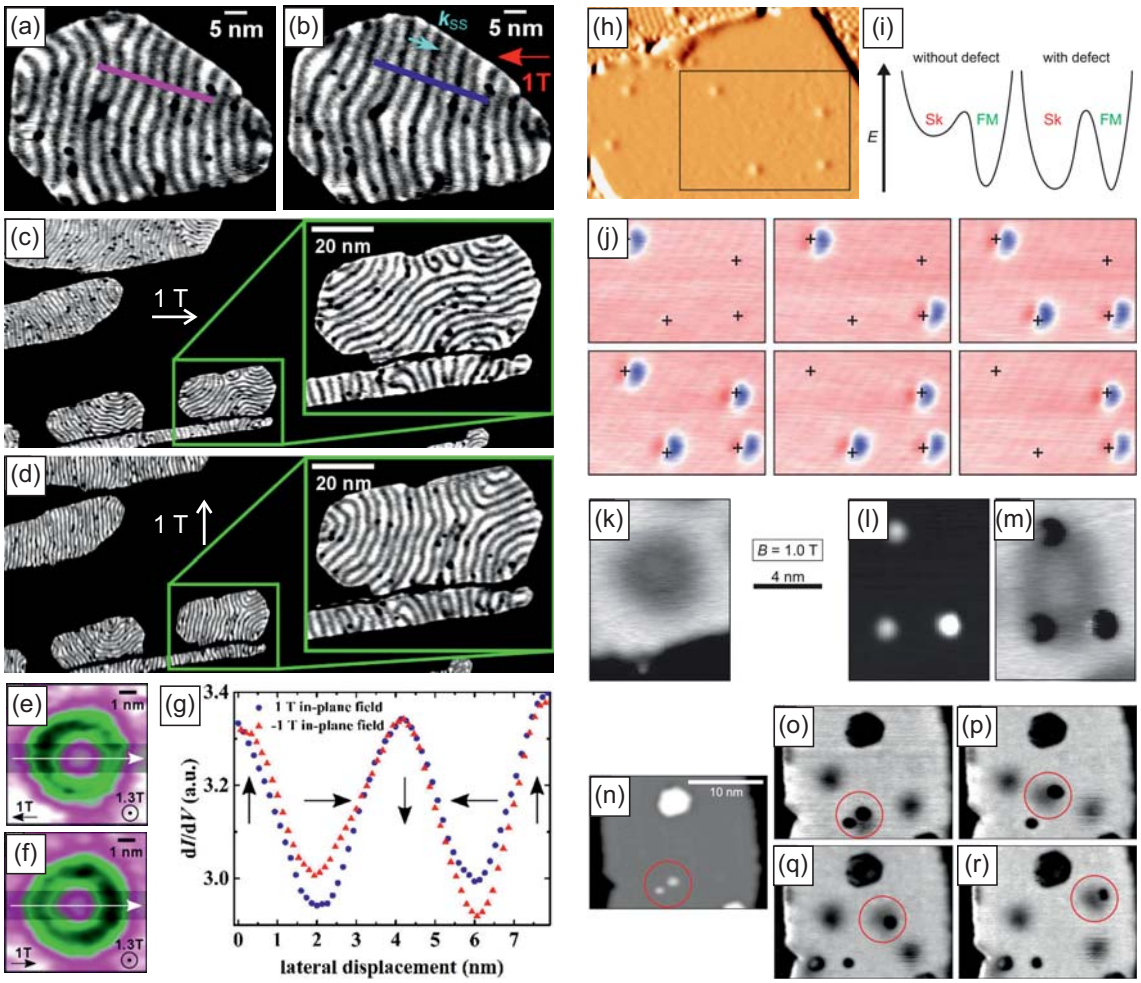

Figure 3.8: Distortion of magnetic states in PdFe and pinning. (a) The observation of NCMR with half the magnetic period demonstrates that the spin spiral is inhomogeneous due to magnetocrystalline anisotropy. (b) Magnetic fields along the spin spiral propagation direction distort the spin spiral, recovering the magnetic periodicity. (c),(d) Magnetic field cooling experiments can be used to reorient the spin spirals, however, also the edges of the nanostructure prefer a certain alignment. (e),(f) Large magnetic skyrmions appear as a ring in NCMR imaging and are distorted in canted magnetic fields. (g) Line profiles across the distorted skyrmions and sketch of the local magnetization direction. (h) Differentiated topography, highlighting four atomic defects in the Pd layer. (i) Sketch of the double well potential for a skyrmion and the ferromagnetic state, without and with a defect. (j) Writing and deleting individual magnetic skyrmions at the defect positions. (k) Typical size of a magnetic skyrmion at 1 T. (l),(m) Topography and NCMR image of a distorted skyrmion that is pinned to three Co clusters. (n) Topography and (o)-(r) NCMR images of a measurement series, in which a Co cluster is manipulated across the PdFe film and a pinned skyrmion is following.

skyrmions make a transition to the ferromagnetic state such single atomic defects can rearrange the energy of the states, leading to a degeneracy of the two magnetic states. This enables the local switching between a skyrmion and the collinear state at the positions of single atomic defects, see Fig. 3.8(j) [15]. Clusters of Co atoms on top of the PdFe film can be used to pin the spin texture near the in-plane region of the skyrmion, as demonstrated by the strong distortion of the skyrmion

in Fig. 3.8(l),(m), compared to the typical size at the same magnetic field as shown in Fig. 3.8(k). Manipulation of such a Co cluster with the tip of the STM enables a concurrent movement of a pinned skyrmion, as shown in the sequence of STM images in Fig. 3.8(n)-(r) [15].

3.2.5 Fe double- and triple-layer on Ir(111): spin states and electric field switching

P.-J. Hsu, A. Finco, N. Romming, L. Schmidt, A. Kubetzka, K. von Bergmann, and R. Wiesendanger

The Fe monolayer on Ir(111) is pseudomorphic with a two-dimensional magnetic state on the order of 1 nm, whereas the addition of another Fe layer leads to strain

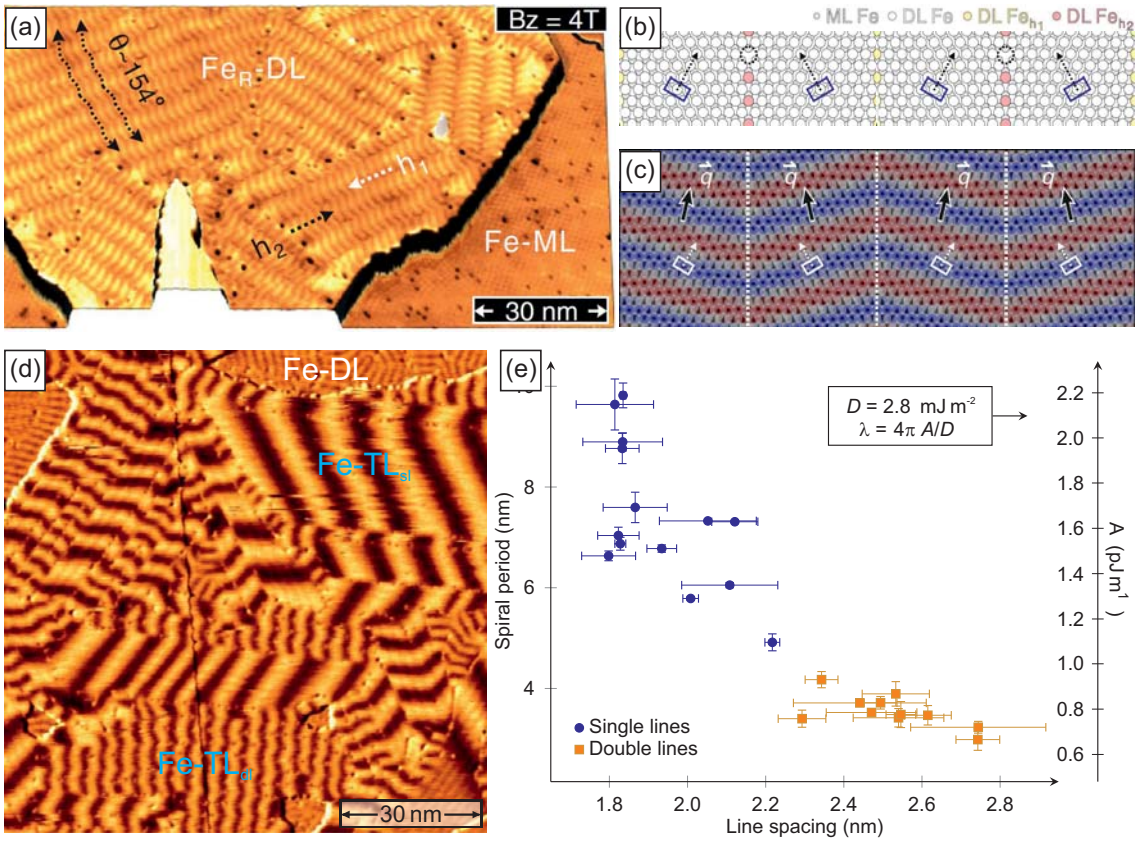

Figure 3.9: The spin spirals in the double-layer (DL) and triple-layer (TL) Fe on Ir(111). (a) The SP-STM measurement shows three rotational domains of the zigzag spin spiral in the Fe-DL. (b) The structure model of the Fe-DL can explain the zigzag shape of the wavefronts; the spin spiral favors a propagation along the bcc[001]-like atomic rows. (c) Sketch of the zigzag spin spiral; also the spins are canted with respect to the dislocation lines, presumably to increase the energy gain due to DMI. (d) The Fe-TL shows two similar reconstructions: one exhibits spin spirals with straight wavefronts, the other one spin spirals with a shorter wavelength and zigzag wavefronts. (e) The spin spiral period decreases with increasing line spacing of the reconstruction, which is attributed to a concurrent change in effective exchange stiffness A.

release and dislocation line formation, see Fig. 3.9(a). The magnetic state is a spin spiral with a period on the order of about 1.5 nm, which exhibits a zigzag wavefront and propagates along the dislocation lines in the three symmetry-equivalent $\langle 1\bar{1}2 \rangle$ directions. The origin of the zigzag shape of the cycloidal spin spiral wavefront is the underlying atomic structure, see Fig. 3.9(b). Figure 3.9(c) shows a model of the spin state: not only the wavefront is canted with respect to the dislocation lines, but also the spins within the spiral are canted, presumably to enhance the energy gain due to DMI in a cycloidal configuration [16].

The triple layer of Fe on Ir(111) also shows dislocation lines and a spin spiral, however, two different reconstructions are found and the magnetic period has increased to $4 - 9$ nm, see Fig. 3.9(d) [17]. In accordance with their atomic structure models one of the reconstruction types has a straight wavefront, which is canted with respect to the dislocation lines, whereas the other one exhibits a zigzag wavefront. The fact that the spin spiral period decreases with increasing line spacing, see Fig. 3.9(e), is attributed to a change of the effective exchange stiffness with the variation of the strain within the Fe-film [17].

The spin spiral in the Fe-TL shown in Fig. 3.10(a) is modified in an external out-of-plane magnetic field and breaks up into small bean-shaped magnetic objects,

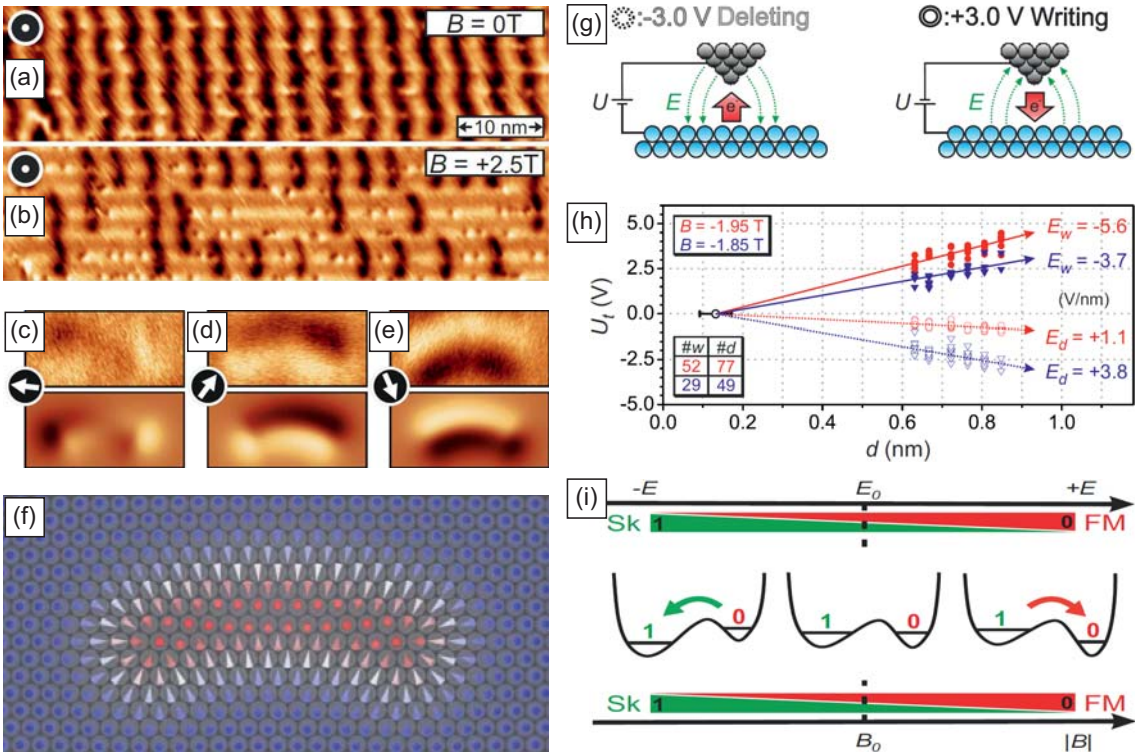

Figure 3.10: Magnetic skyrmions in the triple-layer Fe on Ir(111) and switching with electric fields. (a) The zero magnetic field spin spiral ground state. (b) At 2.5 T magnetic skyrmions are formed. (c),(d),(e) Three rotated magnetic skyrmions were imaged with the same in-plane magnetic tip (top). The bottom row displays SP-STM simulations of the spin structure sketched in (f). (g) Electric field in an STM setup. (h) Critical electric fields derived from tip-sample distance dependent measurements of writing and deleting of individual skyrmions with a W tip. (i) Sketch of the modification of the double-well potential of skyrmion and ferromagnet by global magnetic or local electric fields.

see Fig. 3.10(b). An evaluation of measurements with a tip sensitive to the in-plane component of the sample magnetization, see Fig. 3.10(c)-(e), demonstrates that the magnetic objects are topologically distinct skyrmions; a model of the spin state is shown in Fig. 3.10(f) and SP-STM simulations thereof are in nice agreement with the experimental data, compare Fig. 3.10(c)-(e) top and bottom [18].

Writing and deleting of these magnetic skyrmions was realized with local voltage pulses between tip and sample, see Fig. 3.10(g). Measurements with an unpolarized W tip could directly rule out spin-transfer torque as switching mechanism. An investigation of the threshold voltages for creation and annihilation at different tip-sample distances demonstrated the decisive role of the electric field for the switching between these topologically distinct states, Fig. 3.10(h). Thus, simultaneously to a global control of the energy levels of skyrmion and ferromagnet in an external magnetic field, a local tuning of the relative energy levels is possible, Fig. 3.10(i) [18].

References

[1] K. von Bergmann, A. Kubetzka, O. Pietzsch, and R. Wiesendanger, Interface-induced chiral domain walls, spin spirals and skyrmions revealed by spin-polarized scanning tunneling microscopy, J. Phys.: Condens. Matter **26**, 394002 (2014).

[2] R. Wiesendanger, Nanoscale magnetic skyrmions in metallic films and multilayers: a new twist for spintronics, Nature Reviews Materials **1**, 16044 (2016).

[3] B. Dupé, J. E. Bickel, Y. Mokrousov, F. Otte, K. von Bergmann, A. Kubetzka, S. Heinze, and R. Wiesendanger, Giant magnetization canting due to symmetry breaking in zigzag Co chains on Ir(001), New J. Phys. **17**, 023014 (2015).

[4] M. Menzel, A. Kubetzka, K. von Bergmann, and R. Wiesendanger, Parity effects in 120° spin spirals, Phys. Rev. Lett. **112**, 047204 (2014).

[5] S. Ouazi, T. Pohlmann, A. Kubetzka, K. von Bergmann, and R. Wiesendanger, Scanning tunneling microscopy study of Fe, Co and Cr growth on Re(0001), Surf. Sci. **630**, 280 (2014).

[6] S. Ouazi, A. Kubetzka, K. von Bergmann, and R. Wiesendanger, Enhanced Atomic-Scale Spin Contrast due to Spin Friction, Phys. Rev. Lett. **112**, 076102 (2014).

[7] A. Palacio-Morales, A. Kubetzka, K. von Bergmann, and R. Wiesendanger, Coupling of Coexisting Noncollinear Spin States in the Fe Monolayer on Re(0001), Nano Lett. **16**, 6252 (2016).

[8] J. Hagemeister, D. Iaia, E.Y. Vedmedenko, K. von Bergmann, A. Kubetzka, and R. Wiesendanger, Skyrmions at the edge: Confinement effects in Fe/Ir(111), Phys. Rev. Lett. **117**, 207202 (2016).

[9] D. Iaia, A. Kubetzka, K. von Bergmann, and R. Wiesendanger, Structural and magnetic properties of Ni/Fe nanostructures on Ir(111), Phys. Rev. B **93**, 134409 (2016).

[10] K. von Bergmann, M. Menzel, A. Kubetzka, and R. Wiesendanger, Influence of the Local Atom Configuration on a Hexagonal Skyrmion Lattice, Nano Lett. **15**, 3280 (2015).

[11] N. Romming, A. Kubetzka, C. Hanneken, K. von Bergmann, and R. Wiesendanger, Field-Dependent Size and Shape of Single Magnetic Skyrmions, Phys. Rev. Lett. **114**, 177203 (2015).

[12] J. Hagemeister, N. Romming, K. von Bergmann, E.Y. Vedmedenko, and R. Wiesendanger, Stability of Single Skyrmionic Bits, Nat. Commun. **6**, 8455 (2015).

[13] C. Hanneken, F. Otte, A. Kubetzka, B. Dupé, N. Romming, K. von Bergmann, R. Wiesendanger, and S. Heinze, Electrical detection of magnetic skyrmions by tunnelling non-collinear magnetoresistance, Nat. Nanotechn. **10**, 1039 (2015).

[14] L. Schmidt, J. Hagemeister, P.-J. Hsu, A. Kubetzka, K. von Bergmann, and R. Wiesendanger, Symmetry breaking in spin spirals and skyrmions by in-plane and canted magnetic fields, New J. Phys. **18**, 075007 (2016).

[15] Ch. Hanneken, A. Kubetzka, K. von Bergmann, and R. Wiesendanger, Pinning and movement of individual nanoscale magnetic skyrmions via defects, New J. Phys. **18**, 055009 (2016).

[16] P.-J. Hsu, A. Finco, L. Schmidt, A. Kubetzka, K. von Bergmann, and R. Wiesendanger, Guiding Spin Spirals by Local Uniaxial Strain Relief, Phys. Rev. Lett. **116**, 017201 (2016).

[17] A. Finco, P.-J. Hsu, A. Kubetzka, K. von Bergmann, and R. Wiesendanger, Tailoring non-collinear magnetism by misfit dislocation lines, Phys. Rev. B **94**, 214402 (2016).

[18] P.-J. Hsu, A. Kubetzka, A. Finco, N. Romming, K. von Bergmann, and R. Wiesendanger, Electric-field-driven switching of individual magnetic skyrmions, Nat. Nanotechn. doi:10.1038/nnano.2016.234 (advanced online publication).

3.3 Theoretical studies of topological magnets

E. Y. Vedmedenko and R. Wiesendanger

Exotic topological phases of condensed matter recently became a central topic of international scientific activity. Often these phases correspond to non-trivial metastable excitations. Among these (quasiparticle) excitations are three- or two-dimensional magnetic skyrmions, one-dimensional topological solitons/helices and zero-dimensional monopoles, which can also be bound by one-dimensional Dirac strings. Once created, these magnetic objects can only be erased with effort from a surface. This makes them valuable for the application in future data storage devices but also poses fundamental questions about the microscopic reasons for the stability. During the past three years we addressed several aspects of the stability of non-trivial magnetic states by means of analytical and numerical analysis: Which metastable configurations can be achieved in topological magnets? What are the lifetimes of those metastable states? How do the boundaries influence the formation of topological magnetic structures? To answer these questions several investigations on phase diagrams, statics and dynamics of magnetic helices, magnetic skyrmions, and magnetic monopoles in spin ice have been performed. Due to these investigations we were able to show that energy can be stored in metastable states of nontrivial topological matter. The description of our activities will start with skyrmions and then continue with topological helices and monopoles.

3.3.1 Magnetic skyrmions

3.3.1.1 Phase Diagrams

A. Siemens, Y. Zhang, J. Hagemeister, E. Y. Vedmedenko, and R. Wiesendanger

Phase diagrams showing conditions under which multiple phases co/exist in equilibrium are indispensable for a systematic description of any physical system. For topological magnets they are particularly important because this exotic phase of matter appears in a rather narrow range of thermodynamic parameters. This can be seen at the example of skyrmions in a universal phase diagram for bulk chiral material. The skyrmion lattice (SkX) in this diagram occupies a tiny pocket between much larger spin spiral (SS) and ferromagnetic (FM) phases, i.e. for very specific temperature (T) and magnetic field (B) values. While all phase diagrams of skyrmionic matter distinguish between SS, SkX and FM states, there is a large diversity in the coordinates of those phases. There are three main reasons for this strong diversity. One of the reasons is that phase boundaries in one and the same skyrmionic system are multi-dimensional. They might be driven by temperature, strength of DM interaction, strength of applied magnetic field, pressure etc. There are also differences of the thermodynamic behavior for different lattice symmetries, thereby making the diversity of phases even larger. Hence, to investigate the stability of those non-collinear configurations, systematic studies of phase diagrams are extremely important and are the subject of ongoing scientific discussion.

For skyrmionic systems the B-D diagram (magnetic field-Dzyaloshinskii Moriya

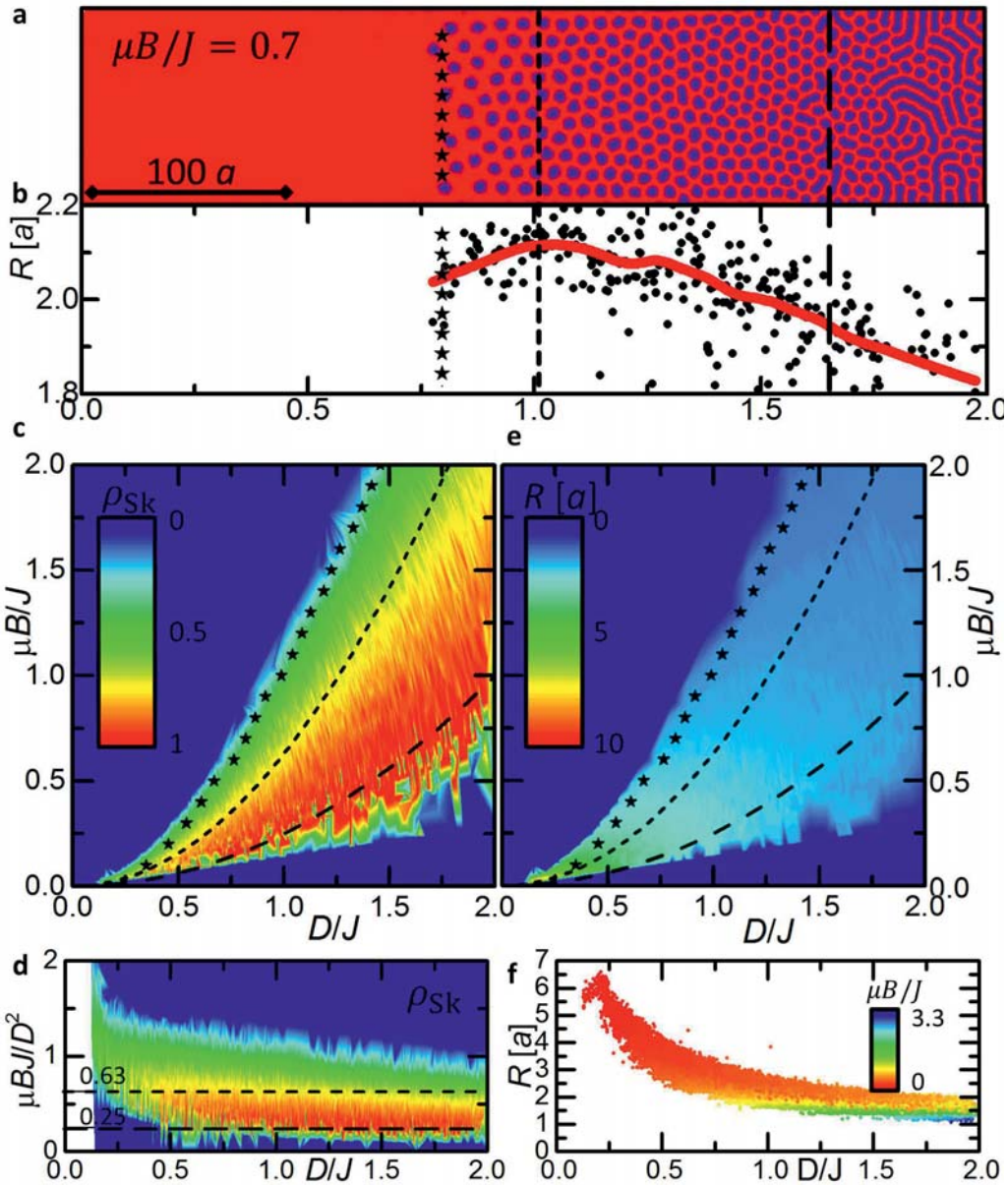

Figure 3.11: (a) Equilibrium micromagnetic configuration obtained in MC simulations at $\mu B/J = 0.7$ and $k_{\mathrm{B}}T/J = 8.5 \cdot 10^{-3}\, J$ with a gradient of the DM interaction strength along the x-axis enforcing a transition from the FM state to the spiral state. (b) Visualization of the corresponding skyrmion radii. Points represent the numerical data, while the solid line is the averaged R value. (c,d) Phase diagrams using the skyrmion density ρ as an order parameter. (e,f) The skyrmion radii as a function of the position in phase space.

(DM) interaction strength) plays a central role, because it permits to characterize the skyrmion formation in different materials. Each material class has a characteristic value of the D/J ratio. In [1] we have calculated a B-D diagram for ultrathin films with interfacial DM interaction. This diagram is shown in Fig. 3.11. The originality of our phase diagram lies in the used order parameters. Besides the standard winding number Q, the density order parameter ρ has been defined in [1]. The density parameter gives the ratio between an effective area occupied by skyrmions and the area occupied by a closed packed lattice of skyrmions having the same radius R.

Additionally, to obtain the phase diagrams very large samples (on the order of 10^6 sites) of rectangular shape, with a D/J gradient along the x-axis, have been equilibrated at various magnetic fields B. The advantage of the method of gradients is the possibility of a direct visualization of the magnetic microstructure as a function of the interaction strength.

Due to the novel order parameter and the gradient method we were able not only to distinguish between the skymionic, ferromagnetic, and the spiral phases, but also define the transition from the phase of the isolated skyrmions to the skyrmion lattice. Particularly, we observe a drastic change in the behavior of the skyrmion radius: it increases with the strength of the DM interaction for $D/J < 1.05$ in the single skyrmion regime, while it decreases with the DM interaction for $D/J < 1.05$ in the skyrmion lattice regime.

3.3.1.2 Minimal size and shape of skyrmions

A. Siemens, Y. Zhang, J. Hagemeister, E. Y. Vedmedenko, and R. Wiesendanger

The calculations [1] show that skyrmions with a radius less than a certain critical value R_c do not exist in discrete systems. At this specific skyrmion size the system overcomes the separating energy barrier and inevitably relaxes into the ferromagnetic state. With increasing strength of DM interaction R_c decreases and eventually reaches its ultimate limit. For interfacial magnetic systems like Pd/Fe/Ir(111) the minimal skyrmion radii are very small and lie in the region of (0.5 - 1)a. These data are in very good agreement with a recent experimental study presented in the Chapter 3.2.4.

Until now spherically symmetric skyrmions have mainly been addressed as only in this case the skyrmion radius unambiguously defines its geometrical properties. However, various experimentally feasible material systems naturally exhibit spatially anisotropic behaviour. This phenomenon is particularly strong at interfaces. An example relevant for interfacial anisotropic skyrmionic systems is given by the double and triple atomic layers of Fe on Ir(111) as shown in Chapter 3.2.5. A systematic theoretical investigation of the skyrmion formation in systems with anisotropic environment is presented in our paper [2]. This investigation shows that spatial modulations of the exchange interaction and the anisotropy energy in combination with an isotropic DM interaction lead to the formation of deformed skyrmionic objects.

The shape and the size of deformed skyrmions strongly depend on the particular energy landscape. An example of a non-trivial deformed skyrmion obtained with the help of Monte-Carlo simulations is analyzed in Fig.3.12. In this case a spatial modulation of magnetocrystalline anisotropy between the in-plane and the out-of-plane orientation has been considered to account for the skyrmion deformation (see Fig.3.12 (a)). Such a modulation might occur, for instance, due to stress induced surface reconstructions. Additionally, it is known that the exchange interaction parameters J_{ij} might be modulated as a function of the orientation of the respective bond and also of the bond position in the lattice. Fig.3.12 (b)-(c) show the skyrmionic structures for two different magnetic fields with such a spatial modulation of the exchange parameters, but without any anisotropy modulation. One observes ordered bent non-collinear spin states with a non-vanishing topologi-

cal charge. Fig.3.12(d)-(e) show the corresponding equilibrium structure if a spatial modulation of anisotropy has been taken into account. The distorted skyrmionic objects remain but become ordered along linear tracks. The detailed spin structure of the deformed skyrmions is shown in Fig. 3.12(f).

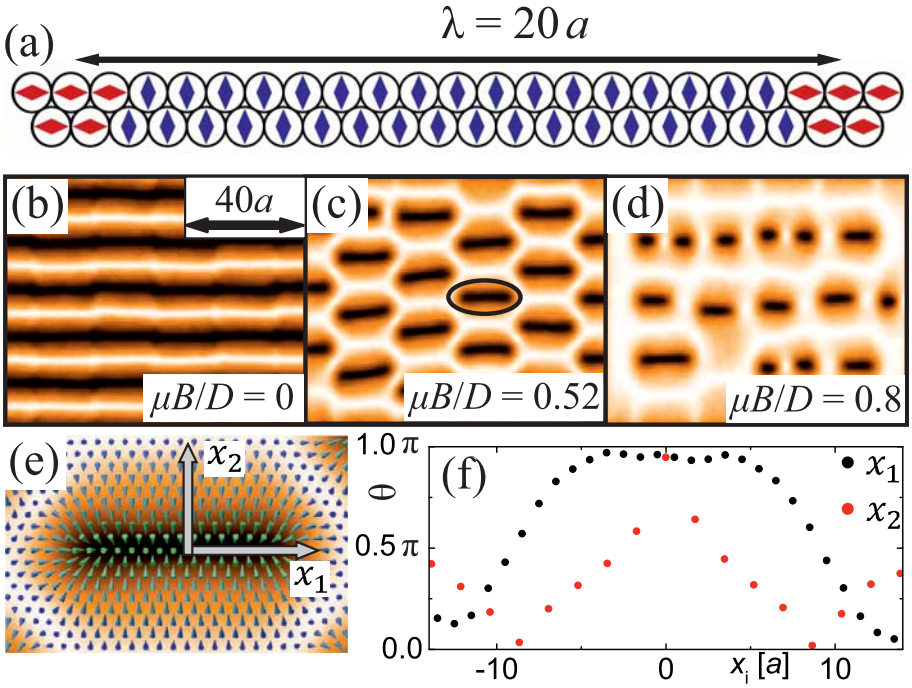

Figure 3.12: (a) Sketch of the atomic lattice indicating the spatial modulation of the direction of the easy anisotropy axis. (b, c) Color maps of the perpendicular component of the magnetization of equilibrium skyrmionic states for different strengths of magnetic field and spatial modulation of the exchange interaction corresponding to 3 ML Fe on Ir(111). (d, e) The same as in (b, c) with an additional modulation of the anisotropy according to the scheme outlined in panel (a). (f) Spin structure and local density of the topological charge for a deformed magnetic skyrmion.

3.3.1.3 Stability of skyrmions

J. Hagemeister, N. Romming, K. von Bergmann, E. Y. Vedmedenko, and R. Wiesendanger

In many cases isolated magnetic skyrmions correspond to metastable states, which can be deleted or created by fields or currents. This metastability permits the use of topologically distinct skyrmionic and ferromagnetic states as information bits. The critical parameter for any bit of information is its stability. The stability of any state can be quantified by measuring its lifetime. The lifetimes of metastable states in turn depend on temperature, external magnetic field, and other intrinsic or extrinsic parameters. At zero temperature a skyrmion might possess an infinite lifetime. At higher temperatures the thermal energy has to be compared with the height of the energy barrier between the two states. Therefore, the interesting question is how the lifetimes of the skyrmionic and ferromagnetic states depend

on the field and temperature. We addressed this important issue in [3]. In these investigations the lifetimes of the skyrmionic states have been studied by means of Monte-Carlo simulations. It has been found that the skyrmion lifetime follows the Arrhenius-like law. This conclusion is in good agreement with other investigations of this subject. The originality of our approach was two-fold. First, we were able to determine the energy barriers between the skyrmionic and the ferromagnetic states. By that means we were able to quantify the attempt frequencies and the lifetimes of skyrmion and ferromagnet. The ratio of the attempt frequencies for the FM and the Sk states obtained from the Arrhenius fit is on the order of inverse time units (Monte Carlo steps) throughout the whole range of explored magnetic fields and temperatures.

Secondly, we were able to demonstrate that this large difference results from the higher entropy of the skyrmionic state. This led us to the conclusion that the simple Arrhenius behavior can not explain the high skyrmion stability. To understand why the increased entropy leads to higher attempt frequencies one has to consider the Eyring equation, as a more general form of the Arrenius law:

$$\tau = \tau_0 \cdot e^{\Delta S/k_B} \cdot e^{\Delta E/k_B T} = \tau_{eff} \cdot e^{\Delta E/k_B T} \tag{3.1}$$

Thirdly, by mapping our numerical results to experimental data described in Section 3.2.4. we were able to quantify the exchange and DM parameters (7 meV and 2.2 meV respectively) and lifetimes for Pd/Fe/Ir(111) biatomic layers. Additionally, we have identified the critical fields B_c at which the lifetimes of skyrmionic and ferromagnetic states are identical.

3.3.1.4 Annihilation of skyrmions

J. Hagemeister, N. Romming, K. von Bergmann, A. Siemens, Y. Zhang, E. Y. Vedmedenko, and R. Wiesendanger

While the MC simulations of [3] concern the equilibrium skyrmion sizes, the dynamical simulations of Ref. [1] are concentrated on unstable isolated skyrmions at the very moment, when a skyrmion is dynamically annihilated. The annihilation of a single skyrmion was achieved using a magnetic field B being greater than or equal to the critical field B_c defined at the end of the previous paragraph. The dynamical evolution of the skyrmion radius as a function of time for different field strengths is shown in Fig.3.13. According to atomistic simulations at zero temperature the dynamics of the skyrmion annihilation follows the same scenario for any field strength. It consists of two dynamical stages: continuous contraction and discontinuous annihilation of isolated skyrmions. The discontinuous phase starts as soon as the skyrmion radius reaches its minimal value R_{min}. While the duration of the contraction phase decreases with increasing field, the duration of the annihilation phase is practically independent of the field strength. This two-phase transition has also been observed for skyrmions annihilated by the use of spin-polarized currents. The inset in the bottom panel of Fig.3.13 shows the minimal skyrmion radius. In accordance with MC simulations discussed above the ultimately small skyrmion consists of four or seven atomic spins only. This value corresponds to $R_{min} \approx 2.35$, which is close to recent experimental results.

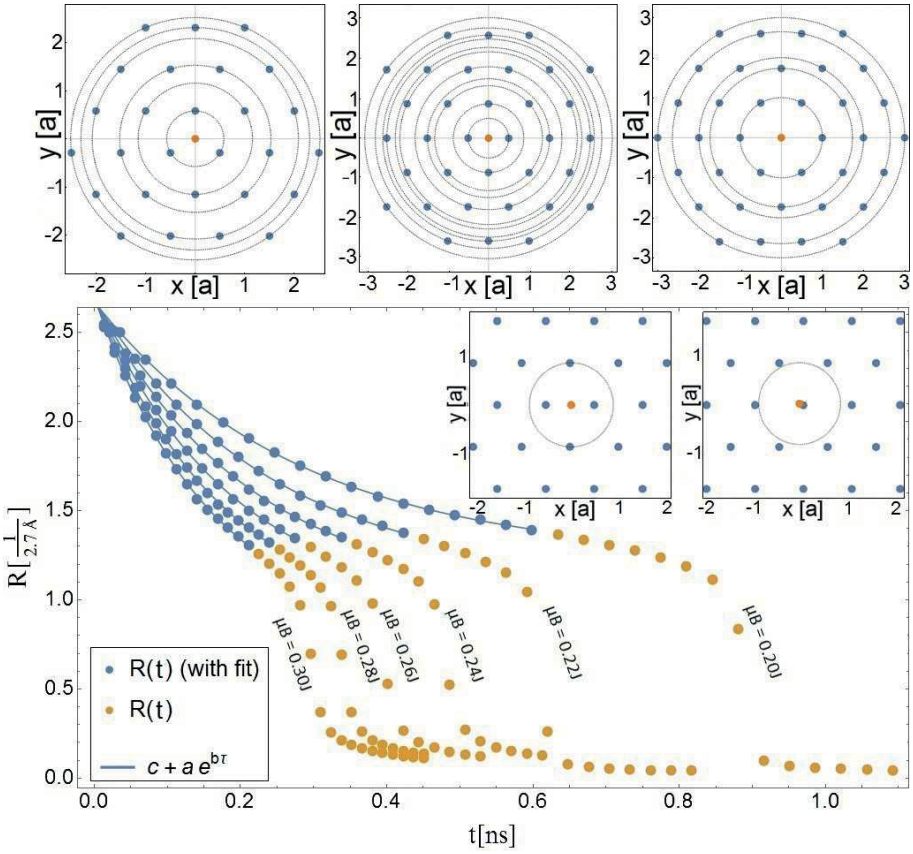

Figure 3.13: Upper panels show schematics of three possible rotationally symmetric configurations of a smallest possible skyrmion on a hexagonal lattice. Bottom panel shows the numerically calculated time evolution (points) and fits (solid lines) of the skyrmion radius at different applied magnetic fields B at zero temperature. The part of numerical data used for fits is darker. Field values are expressed in units of the exchange interaction constant J. The insets in the bottom panel show smallest skyrmions obtained in LLG spin dynamics.

3.3.1.5 Skyrmion's confinement

J. Hagemeister, D. Iaia, E. Y. Vedmedenko, K. von Bergmann, A. Kubetzka, and R. Wiesendanger

In view of the application aspects of skyrmionic systems, theoretical investigations exploring the effect of boundaries and confinement become more and more important, as can be seen by the contemporary literature. Particularly, it has recently been shown that the confinement of a skyrmion in a circular nanoisland may lead to its isolation because of the specific boundary conditions induced by the Dzyaloshinskii-Moriya interaction. All above mentioned publications concentrated on individual skyrmions. A first investigation of the interplay between a skyrmion lattice, as found in the Fe/Ir(111) system, and the confined geometry of nanoscale islands has recently been reported. A strong coupling of one diagonal of the square magnetic unit cell to the close-packed edges of Fe nanostructures has been observed experimentally by means of Spin-Polarized Scanning Tunneling Microscopy and the-

oretically by means of Monte-Carlo simulations [4]. The details of the theoretically calculated micromagnetic structure are presented in Fig. 3.14. A clear trend of close-packed edges favouring one of the three rotational domains of the skyrmionic lattice can be seen in Fig. 3.14 (c). However, in an island of triangular shape it is impossible to orient the diagonal of a square nanoskyrmion lattice along all three edges of the island simultaneously. The mismatch of the symmetries of the skyrmionic lattice and the shape of the island leads to frustration and triple-domain states as visualized in Fig. 3.14 (a). On the other hand, the formation of domain walls (Fig. 3.14 (a)) is accompanied by an energy increase with respect to a monodomain state (Fig. 3.14 (b)).

To determine the energy at edges and within domain walls, and to identify the contributions of the different energy terms to the total energy of the system, spatially resolved energy maps of the triangular islands have been analyzed. The result of this analysis can be appreciated in Fig. 3.14, where the average energy cost per atom with respect to the corresponding value in the interior of a very large sample in the nth atomic row parallel to the edge for favourable and unfavourable edges are plotted. Surprisingly, the monodomain state has lower internal energy than the triple domain state. However, despite the lower energy of the single-domain state, multi-domain configurations show up in experiments and numerical simulations due to the combined effect of entropy and an intrinsic domain wall pinning, which results from the skyrmionic character of the spin texture.

3.3.2 Topologically stable magnetic helix

E. Y. Vedmedenko and D. Altwein

In addition to interfacial magnetic films discussed in previous section a variety of one-dimensional magnetic chain or ring structures with different anisotropy axes can be experimentally produced. This list includes atomic spin ensembles , magnetic nanoarrays and molecular structures. Obtained experimental data are partially still not understood. Particularly, the hysteresis curved measured on open and closed atomic magnetic chains show much higher disorder than the applied Ising model. Hence, the question arises whether the topological magnetism can be achieved in closed linear structures with periodic or non-periodic boundaries and whether it can be responsible for the deviations of experiments from the prediction by standard models. Another important question is what is the role of the free energy in formation of topological states?

As reported in [5] we have performed analytical and numerical analysis of the size dependent properties of magnetic chains that are coupled via either exchange or long-range dipolar or Ruderman-Kittel-Kasuya-Yosida interactions. These calculations have shown that in linear as well as nonlinear chains there are metastable magnetic configurations with long lifetimes for certain boundary conditions. They correspond to helices with integer number of π-twists, that are commensurate with the chain's length. In some cases, for example for antiferromagnetic interactions or the dipolar coupling with easy plane anisotropy topologically stable double-helices are observed. An example of such double-helix is given in Fig. 3.15.

The double-helices are similarly to skyrmions and domain walls topologically

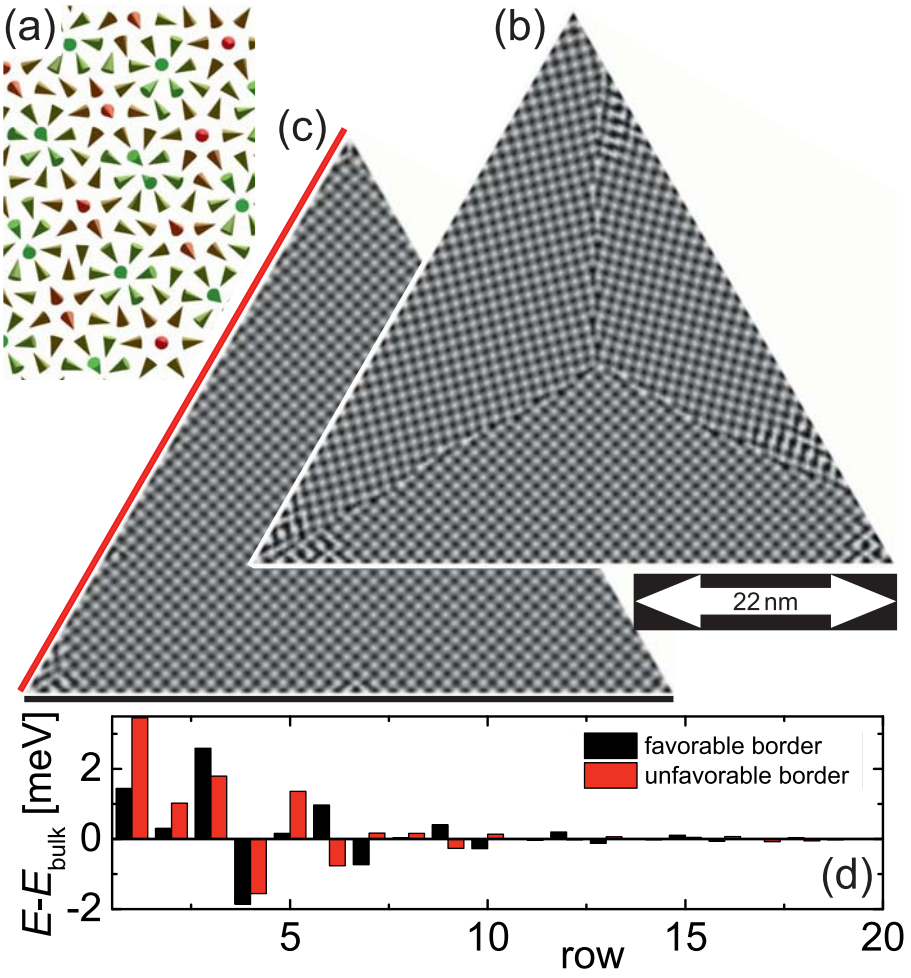

Figure 3.14: (a) An excerpt of the spin structure of the nanoskyrmion lattice at T = 1K as obtained by MC calculations. (b), (c) Islands with triangular boundary shape and open boundary conditions exhibiting multi-domain and single domain nanoskyrmion lattice states. (d) Average energy cost with respect to the bulk per atom which belongs to the n-th atomic row parallel to the boundary. The energetically (un)favorable border is marked in (red) black in (c).

non-trivial objects. In continuous matter, once created they would be stable for infinite times. In discrete systems their lifetimes are finite. In contrast to two-dimensional skyrmions topological helices are one-dimensional objects. In [5] we proposed to use the metastable helix configurations with integer number of revolutions for an energy storing element that uses spins only. To store energy one has to rotate one of the end-nanomagnets in a chain until the helix will click into place. At the later time the magnet may be released to deliver the energy on demand. The longer is a chain, the larger amount of rotations can be stored. The stable magnetic helices can be also used to transfer the information. To do so, one has to read out when a knot, created at one end of the chain will arrive at the other chain's end. The main advantage of the proposed concept is it's scalability from the macro- to the atomic scale and applicability to the great diversity of systems like e.g. magnetic multilayers, magnetic or molecular nanoarrays, colloids, Bose-Einstein condensates, and atomic ensembles.

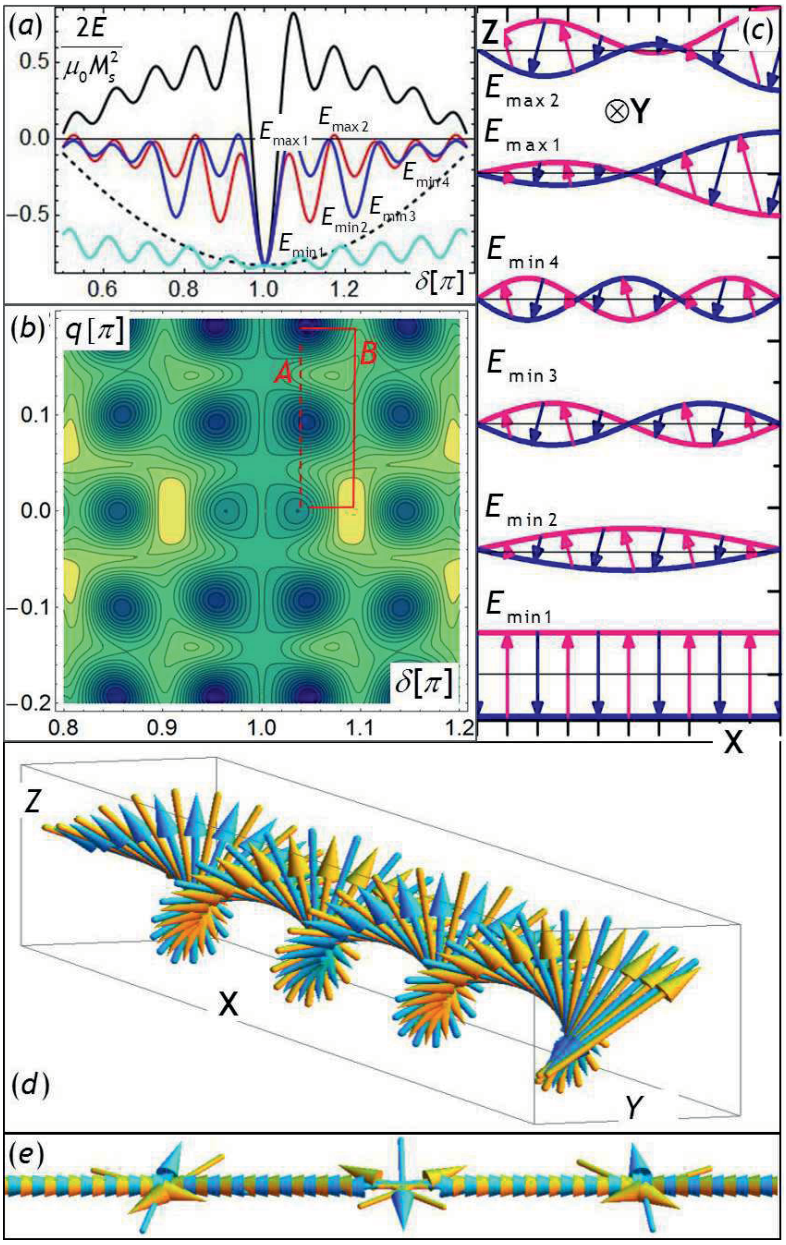

Figure 3.15: (a,b) One- and two-dimensional representation of the energy of modulated helices in a dipolar chain consisting of ten moments as a function of two wave vectors δ and q; (c) vertical magnetization component $S_z(r)$ for several energy levels. The thick lines in (c) show the envelope lines of double-helices. The dashed parabola in (a) corresponds to the energy of the harmonic spiral; the black, red, and blue curves correspond to $E(\delta)$ of modulated helices with K=0 and $q = 0$, $q = \frac{\pi}{N}$, and $q = \frac{2\pi}{N}$ respectively, while the cyan line shows $E(\delta)$ for $q = \frac{\pi}{N}$ and $K = 2.5D$. (d) Three-dimensional representation of an intermediate helix state found for a chain consisting of 81 spins at zero temperature. (e) End-configuration of SD-simulations for $K = 0$ and starting configuration identical to (d).

3.3.3 Energy storage in Dirac strings and bound magnetic monopoles

E. Y. Vedmedenko

After discussing two- and one-dimensional magnetic topological quasiparticles we come to our recent publication on zero-dimensional topological objects known as "emerging magnetic monopoles". Emerging monopoles appear in spin-ice. Magnetism of two-dimensional dipolar spin ice (2D-DSI), artificial counterparts of three-dimensional spin ice in magnetic arrays on lattices of different symmetry including quasicrystals [6], is an exploding and innovative field of science. Recent developments in 2D-DSI research concern the metastable defects also known as “emerging magnetic monopoles” arising at the ends of a line of reversed magnetic dipoles known as Dirac string. The ultimate goal of investigations on 2D-DSI is the magnetic analog of spintronics using magnetic monopoles and Dirac strings as acting elements. From the point of view of physics, the majority of investigations on 2D-DSI is concentrated on the behavior of unbound magnetic monopoles with vanishing tension of Dirac strings. In our recent investigation [7], the complete phase space defined by the Dirac string’s tension has been investigated. It has been shown that in the regime of bound monopoles (BM) one-dimensional Dirac strings rather than point-like monopoles are effective degrees of freedom. Particularly, BMs do not obey the Coulomb law. BMs of opposite sign can be attracted or repulsed depending on the Dirac string tension-to-mass ratio. The Dirac string tension in strongly coupled 2D-DSI is found to be a fundamental quantity, which is determined by the fine-structure constant and lattice specific parameters only. A measurable prediction of path-time dependence of endpoints of stretched and then released Dirac strings has been made and verified via simulations. It has been demonstrated that this kind of string dynamics may be used to achieve spontaneous currents of confined monopoles. This is important because until now only field driven currents have been reported and because spontaneous currents can be used to store energy in Dirac strings. Interestingly, the current duration can be increased by geometrical means, e.g. increasing the length of a sample. Similarly to the example of topological helices, this effect can be used to store energy in Dirac strings.

3.4 Numerical and analytical investigations of quantum and classical dynamics of effective spins and clusters at the interfaces

3.4.1 Switching of a molecular spin by the tip of a Magnetic Exchange Force Microscope

K. Them, T. Stapelfeldt, E. Y. Vedmedenko, and R. Wiesendanger

In the previous three-year period we have studied theoretically interactions between the tip of a magnetic exchange force microscope (MExFM) and a magnetic substrate in dissipative and non-dissipative regimes. In the current three-year period we have extended these investigations exploring the possibilities to switch the magnetization of a magnetic atom or cluster between different stable states by the exchange coupling with a magnetic tip (see Fig. 3.16) as described in [8]. This method seems to be promising on insulating substrates, for which the spin-polarized currents are inapplicable. A combination of first-principles calculations and spin dynamics simulations has been used. A magnetic tip has been supposed to operate in the dynamic mode of an MExFM. The exchange interaction between the tip and the molecule was evaluated quantitatively by plotting the exchange energy which is the difference between the total energy of the FM and AFM orientation of the magnetization at the tip and that of the molecule. The difference between the forces in the two configurations constituted the magnetic exchange force measured by MExFM. It has been concluded that the exchange energies are large enough in static DFT calculation to overcome the magneto-crystalline anisotropy barrier. To clarify the question of how a switching process can be observed in the dynamic mode of a MExFM experiment additional spin dynamics simulations have been performed.

In these simulations the molecule on the substrate has been treated as an effective quantum-mechanical spin and the tip magnetization as an effective classical spin vector. Within this approximation the exchange interaction acts as a time dependent external field. The quantum-mechanical Heisenberg Hamiltonian includes anisotropy contributions to the molecule-tip interactions. The parameters for the model have been taken from the DFT calculations described above. Using the time-dependent Schrödinger equation as equation of motion we have calculated numerically the time dependence of the expectation values of magnetization of the molecule and defined the regimes, in which the magnetization switching is achievable [8].

Particularly, we could show that the assumed conditions play an important role. There are at least eight different scenarios depending on the occurrence of relaxation and quantum tunneling. As a consequence of the Bethe–Slater-like exchange interaction and the existence of a minimal tip position d_{min}, we saw that a system without the appearance of quantum tunneling shows a controlled switching of the molecule from an antiparallel spin alignment of the tip and the sample (molecule) to a parallel one if d_{min} is larger than the distance d_c where the ferromagnetic exchange turns to its antiferromagnetic counterpart. If $d_{min} < d_c$ the molecule switches back to the antiparallel spin alignment caused by the changing exchange interaction.

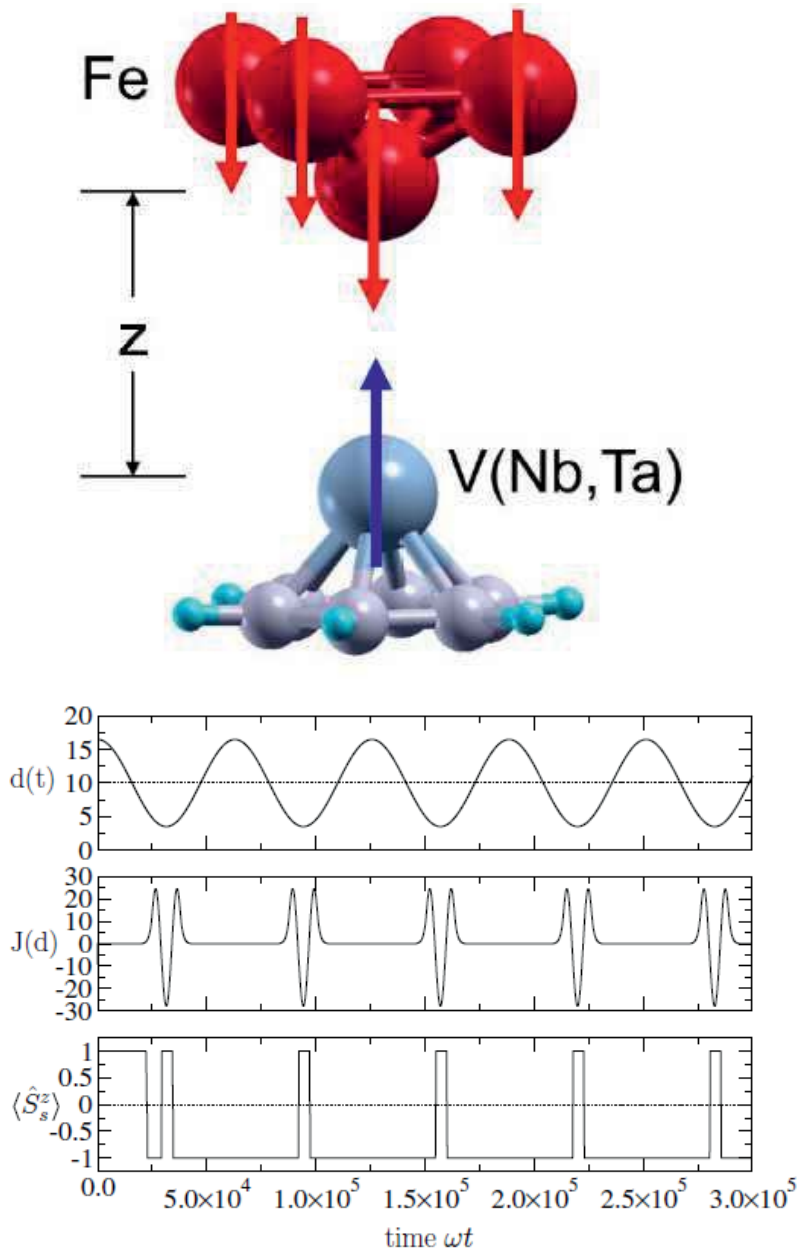

Figure 3.16: Schematics of a magnetic Fe tip and a magnetic V-benzene molecule used in our study. Tip–sample distance $d(t)$, exchange interaction $J(d)$ in meV, and the quantum mechanical expectation value of the magnetization of the molecule for the mean tip-molecule distance of 6.5 Å.

3.4.2 Switching of a molecular or atomic spin by the tip of a Spin-Polarized Scanning Tunneling Microscope (SP-STM)

K. Them, E. Y. Vedmedenko, K. Fredenhagen, and R. Wiesendanger

When the tip of a Spin-Polarized Scanning Tunneling Microscope (SP-STM) comes toward an atom or a cluster under study, the Hamilton operator of the sys-

tem changes due to interactions with tunneling electrons, in contrast to non-contact MExFM, which doesn't change the Hamiltonian of a sample. The perturbed dynamics drives the state out of equilibrium and the ergodicity is not a priori ensured. A related problem is the so-called 'return to equilibrium', also referred to as relaxation. The relaxation of an excited system depends on its initial state. There might exist some initial states from which the system can return to equilibrium, and there might exist some other initial states from which this process will not happen. To study the dynamics of single quantum spins during and after SP-STM measurements at finite temperatures we have separated the thermal equilibrium Gibbs states and the time evolution of the system during SP-STM experiments using the methods described in [9]. To do so we have plugged in the perturbed dynamics into the unperturbed equilibrium state.

The SP-STM set-up is approximated by (in general) two different Hamiltonians in our approach. There is a Hamiltonian H for the free system and, if a measurement is started, we get an additional Hermitian operator P for the interaction between the tip and the sample. Hence, if the tip is moved towards the surface, the system switches from H to $H + P$ because of the sudden emergence of tunneling electrons causing the interaction between the tip and the sample. The STM-tip can be used to prepare a system with desired expectation values. For the corresponding state we choose a perturbed KMS state $\omega^{\beta P}$.

A mixed (or normal) state ω is described as a normalized positive linear functional over the matrix algebra $\mathcal{A}$ and is given by a density matrix ρ.

$$\omega : \mathcal{A} \to \mathbb{C}, \quad A \mapsto \omega(A) = Tr(\rho A) \tag{3.2}$$

The dynamical evolution of an observable $A \in \mathcal{A}$ for a system with Hamiltonian $H = H^* \in M_n$ can be described by the Heisenberg relations

$$\tau_t : \mathcal{A} \to \mathcal{A}, \quad A \mapsto \tau_t(A) = e^{\frac{itH}{\hbar}} A\, e^{-\frac{itH}{\hbar}}. \tag{3.3}$$

Thus, the map $t \in \mathbb{R} \mapsto \tau_t$ is a one-parameter group of *-automorphisms of the matrix algebra $\mathcal{A}$. In our formalism the Hamiltonian H describes a "free" quantum system without any interaction with the magnetic tip. When the spin-polarized current starts to flow through the system under investigation, the interaction between the tip and the sample is described by the perturbed Hamiltonian $H + P$. A perturbed dynamical evolution can be introduced by

$$\tau_t^P : \mathcal{A} \to \mathcal{A}, \quad A \mapsto \tau_t^P(A) = e^{\frac{it(H+P)}{\hbar}} A\, e^{-\frac{it(H+P)}{\hbar}}. \tag{3.4}$$

Thermal equilibrium at inverse temperature β is modeled by the Gibbs canonical ensemble state which is also the unique (τ, β)-KMS state, denoted by ω^β and given by

$$\omega^\beta(A) = \frac{Tr(e^{-\beta H} A)}{Tr(e^{-\beta H})}. \tag{3.5}$$

These states are invariant under the action of τ, i.e. $\omega^\beta(\tau_t(A)) = \omega^\beta(A)$, but in general not invariant under the action of τ^P. A corresponding perturbed (τ^P, β)-KMS state can be introduced by

$$\omega^{\beta P}(A) = \frac{Tr(e^{-\beta(H+P)} A)}{Tr(e^{-\beta(H+P)})}. \tag{3.6}$$

Now we can plug the perturbed dynamics into the unperturbed equilibrium state [9]

$$\omega^{\beta}(\tau_t^P(A)) \equiv \langle A \rangle_1(t). \tag{3.7}$$

The brackets $\langle ... \rangle(t)$ shall mean that we calculate the time evolution of an expectation value for the observable A. This corresponds to the situation when the spin-polarized tunneling current is switched on at the time $t = 0$ and the system was in thermal equilibrium for $t < 0$. The function (3.7) is used to model the process of a measurement of a magnetization curve. We can also plug the unperturbed dynamics into the perturbed equilibrium state [9]

$$\omega^{\beta P}(\tau_t(A)) \equiv \langle A \rangle_2(t). \tag{3.8}$$

In this case a spin-polarized current is switched off at the time $t = 0$.

Our calculations have shown that the relaxation times of effective quantum objects on different substrates lie in the femto-, pico- or nanosecond regime. It means that in many cases even short-time calculations can give a good approximation of the long-time behavior for certain classes of real finite systems. To check whether the short-time dynamics has a reliable behavior, the calculated relaxation time has been compared with experimentally determined lifetimes for single spins [10]. A good agreement with experimental data for Fe adatoms on InSb and Co adatoms on Pt(111) has been obtained. We have also derived ground states in the zero-temperature limit and compared them with known analytical results. The results demonstrate that even a weak perturbation due to tunneling electrons initiates a quantum tunneling in otherwise diagonal systems and, hence, can explain the magnetization switching of effective quantum spins even for very high anisotropy barriers.

The numerical investigation of many-body quantum systems usually requires different kinds of physical approximations. Using the approach described above [9] we have later examined an upper bound on expectation values for small quantum subsystems embedded in the large quantum subsystem [11]. This calculation enabled us to make the estimation of the maximum error that is made by physical approximations outside the subsystem (for example by approximation of a bath with simplified interactions). This is important because the error which is made by these approximations is difficult to estimate and remains unknown in most cases. The limits in which a small quantum system can be used instead of a large one have been critically discussed in [11].

3.4.3 Quantum revivals and magnetization tunneling in effective spin systems

M. Krizanac, D. Altwein, E. Y. Vedmedenko, and R. Wiesendanger

In view of the importance of the quantum-mechanical tunneling for the magnetization dynamics we went a step further and investigated the quantum revival time and its relation to the magnetization tunneling. The quantum revival time has been initially defined as the recurrence time of a total wave-function. In our recent investigation [12] we have shown that the quantum revivals of wave-functions and expectation values in spin systems may be quite different which gives rise to

a more sophisticated definition of the quantum revival within the realm of experimental research. Particularly, the revival times for wave-functions and expectation values for integer spins coincide, which is not the case for half-integer spins. Furthermore, the quantum revival is found to be shortest for integer ratios between the on-site anisotropy and an external magnetic field paving the way to novel methods of anisotropy measurements. Additionally, it has been shown that the quantum tunneling of magnetization at avoided level crossing is coherent to the quantum revival time of expectation values, leading to a connection between these two fundamental properties of quantum mechanical spins [12].

3.4.4 Thermal switching of coupled magnetic nanoparticles

A. Neumann, D. Altwein, C. Thönnißen, R. Wieser, A. Berger, A. Meyer, E. Y. Vedmedenko, and H. P. Oepen

In previous sections we were mainly concerned with the magnetization dynamics of effective spins, which are coupled by the short-range interactions to the tip of a magnetic tip based microscope and/or to the surrounding. In many cases, however, the long-range interactions are also present. Long-range interactions can be particularly important in storage media, because the ultimate goal of any storage concept is to go for the highest packing density, which requires a minimal distance in between dots or grains. In the latter situation the system becomes unstable against temporal changes in residual magnetic fields created in the surrounding. In particular it means that magnetic properties of nanodots in ensembles, e.g. either superparamagnetic features or switching field distributions in arrays of ferromagnetic dots, are strongly dependent on the magnetic environment. While the static properties of this kind of systems have been broadly studied in the past, their dynamic behaviour is still under discussion.

To get better insight into the highly complex energy landscape of a multi-dot system we have performed a combined experimental and theoretical study of the dots' switching dynamics [13]. The theoretical investigations have been performed in the framework of Landau–Lifshitz–Gilbert spin dynamics. The dots have been treated as macroscopic dipoles subject to the interdot dipole-dipole coupling, on-site magnetic anisotropy and external magnetic field. Exactly the same arrangement of Co/Pt nanodots as in the experimental set-up has been modeled (see Fig. 3.17) and the dynamics of the switching behavior analyzed. In accordance with the experimental results it has been found that the dynamical behavior of the four dots is very different from that expected due to the energy barriers determined from the temperature dependent coercive fields of individual magnetic particles. The predominantly populated state is the one which minimizes the dipolar coupling and corresponds to the middle panel of Fig. 3.17(b). The calculations, however, revealed that this state is temporally degenerated with respect to the orientation of the dots D and C. In other words, on the timescale at which the dots A and B remain stable, their D and C counterparts perform many switching events between the configurations of the upper and middle panels of Fig. 3.17(b). This finding raised an exciting question of whether this instability may explain the deviation of the energy barriers from those of individual, non-coupled dots. Generally, to answer this question one has to know

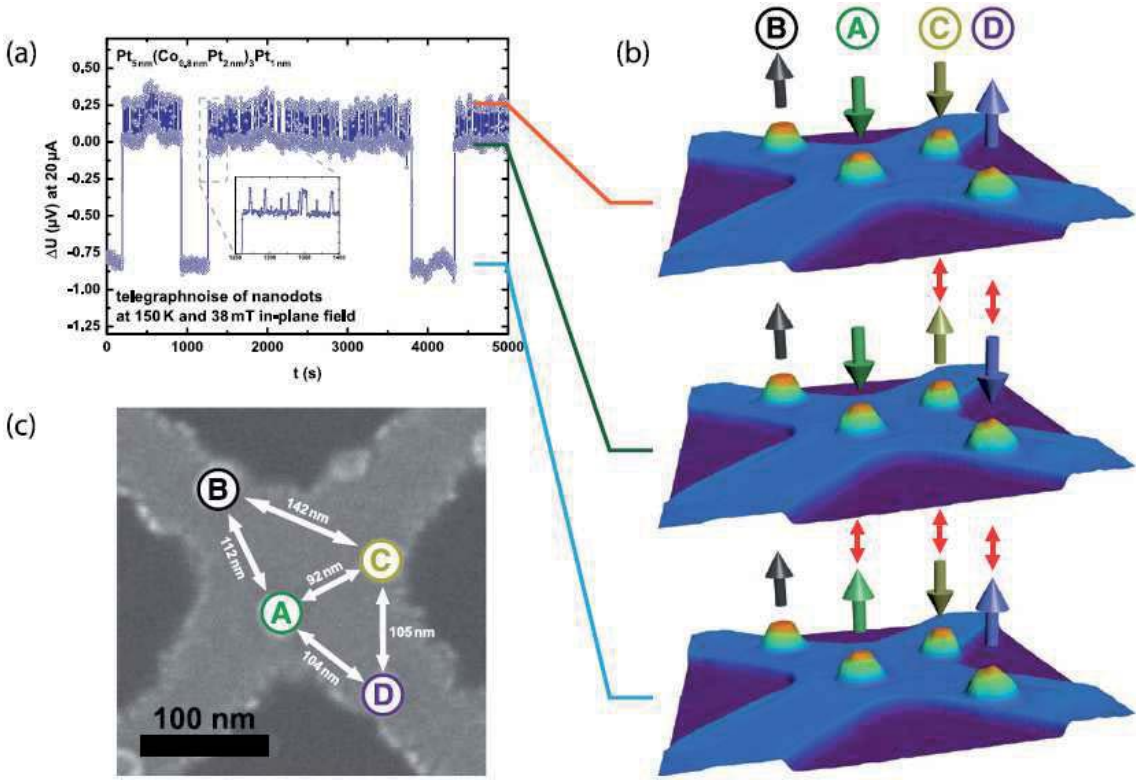

Figure 3.17: Telegraph noise and the corresponding states of the system consisting of four nanodots. (a) Telegraph noise obtained in an in-plane field of 38 mT over an expanded time period. It becomes evident that the signal reveals switching between three different levels. Detailed analysis of the jump heights leads to a scenario that is sketched in (b). (c) Scanning Electron Microscope micrograph of the cross.

the time dependent evolution of the complete energy landscape. The latter is a tremendous task, because the energy landscape is nine-dimensional (the magnetization of each macroscopic dipole i can be described by two spherical coordinates plus time. The best way to solve this problem is to analyze the dynamical correlation function $C_{\mathrm{dyn}} = 1/T \int_{\infty}^{-\infty} dt S_{z,t}(t) S_{z,t}(t+s)$ between pairs of magnetic moments i and j, where S_z is the z-component of magnetization of moments i and j at times t and $t+s$, respectively. This function gives the information whether a given state is still correlated after a delay time s. Hence, $C_{\mathrm{dyn}} \to 1$ corresponds to the correlated, in-phase switching, while $C_{\mathrm{dyn}} \to 0$ to stochastic noise. In the simulations this function was evaluated for vanishing delay $s = 0$ and variable center-to-center distances r_{ij} to check for the degree of correlation for simultaneous switching. The dependence of the function $C_{\mathrm{dyn}}(r_{ij}^3)$ on dot separation shows that the dynamical correlation C_{dyn} decreases much slower than the static dipolar coupling. For the separation of dots C and D of 105 nm the correlation function is still more than 0.8 and thus correlated switching will be found. Hence, these two dots are switching in-phase and the stability of the anti-parallel configuration is increased. Even the farther separated dots ($r_{ij} > 4d \approx 140nm$) show strong correlations which is responsible for the occasional switching of dot A although its anisotropy energy is much larger than the dipolar energy. The physical reason for the long range phenomenon is the minimization of

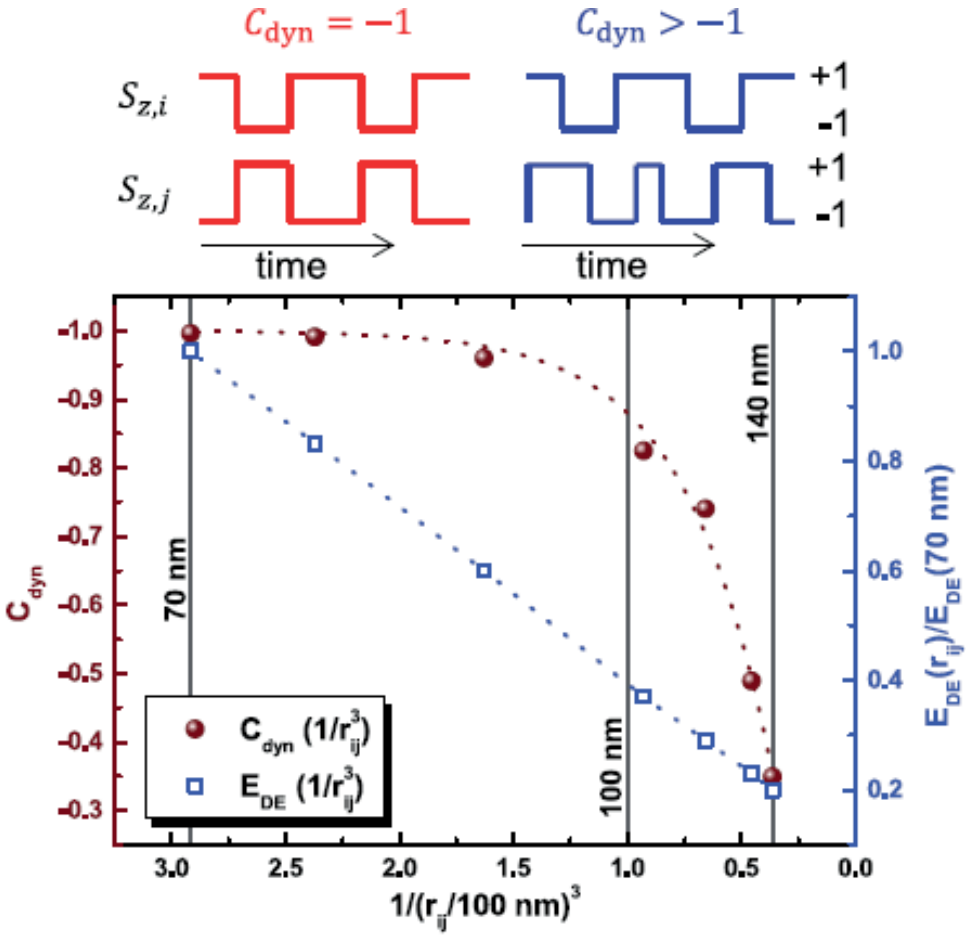

Figure 3.18: Dynamical correlation-function C_{dyn} and dipolar energy as a function of dot separation. Comparison between the two-dot dynamical correlation-function (spheres) and the normalized dipolar energy E_{DE} between to dipoles (open squares, normalized to the value at 70 nm) as a function of $1/r_{ij}^3$ normalized to 100 nm. It is evident that the correlation-function decreases more slowly than the dipolar energy.

the time-averaged or -integrated total potential energy of all dots. This manifests in the many-body dynamical correlations and prevents the magnetic moments from the dephasing. In other words the many-body dynamical effects, described here experimentally and theoretically, correspond to a minimization of a dynamical quantity - the spin dynamical version of the action - rather than to a mere minimization of single particle energies in a static viewpoint for individual dots [13].

These data show that magnetostatic interactions can play an important role in the dynamic reversal process of magnetic dots even when the system is mainly determined by anisotropy barriers. The observed switching behavior demonstrates that correlations determine the switching. Dynamical processes have been observed that are in contradiction to a single particle scenario. The correlations can cause erroneous interpretations when only single particles are studied, neglecting the temporal behavior of the surroundings. The spin-dynamical simulations and the calculation of the dynamical correlation function prove that dynamic correlations open up new reversal paths through the multidimensional energy landscape [13].

References

[1] A. Siemens, Y. Zhang, J. Hagemeister, E. Y. Vedmedenko and R. Wiesendanger, Minimal Size of magnetic Skyrmions: STatics and Dynamics, New J. Phys. **18**, 045021 (2016).

[2] J. Hagemeister, E. Y. Vedmedenko and R. Wiesendanger, Pattern formation in skyrmionic materials with anisotropic environments, Phys. Rev. B **94**, 104434 (2016).

[3] J. Hagemeister, N. Romming, K. von Bergmann, E. Y. Vedmedenko, and R. Wiesendanger, Stability of SIngle Skyrmionic Bits, Nat. Commun. **6**, 8455 (2015).

[4] J. Hagemeister, D. Iaia, E. Y. Vedmedenko, K. von Bergmann, A. Kubetzka, R. Wiesendanger, Skyrmions at the Edge: Confinement Effects in Fe/Ir(111), Phys. Rev. Lett. **117**, 207202 (2016).

[5] E. Y. Vedmedenko and D. Altwein, Topologically Protected Magnetic Helix for All-Spin-Based Applications, Phys. Rev. Lett. **112**, 017206 (2014).

[6] Quasicrystals: Magnetism. In: Reference Module in Materials Science and Materials Engineering, Elsevier, Oxford (2016).

[7] E. Y. Vedmedenko, Dynamics of Bound Monopoles in Artificial Spin Ice: How to Store Energy in Dirac Strings, Phys. Rev. Lett. **116**, 077202 (2016).

[8] R. Wieser, V. Cacius, C. Lazo, H. Hölscher, E. Y. Vedmedenko, and R. Wiesendanger, A theoretical study of the dynamical switching of a single spin by exchange forces, Phys. Rev. Lett. **15**, 013011 (2013).

[9] O. Bratelli and D. W. Robinson, Operator Algebras and Quantum Statistical Mechanics II (Berlin: Springer, 1981)

[10] A. A. Khajetoorians *et al.*, Nature **467**, 1084 (2010).

[11] K. Them, E. Y. Vedmedenko, K. Fredenhagen, and R. Wiesendanger, Bounds on expectation values of quantum subsystems and perturbation theory, J. Phys. A: Mathematical and Theoretical **48**, 075301(2015).

[12] M. Krizanac, D. Altwein, E. Y. Vedmedenko, and R. Wiesendanger, Quantum revivals and magnetization tunneling in effective spin systems, New J. Phys. **18**, 033029 (2016).

[13] A. Neumann, D. Altwein, C. Thönnißen, R. Wieser, A: Berger, A. Meyer, E. Y. Vedmedenko, and H. P. Oepen, Influence of long-range interactions on the switching behavior of particles in an array of ferromagnetic nanostructures, New J. Phys. **16**, 083012 (2014).

3.5 Magnetization dynamics and current-induced magnetization switching studied by SP-STM

S. Krause and R. Wiesendanger

Magnetic skyrmions are promising candidates for future spintronic applications using particle-like winding spin configurations as carriers and storage units for digital information. So far the smallest skyrmions have been observed in the Fe/Ir(111) system. Here, the interface-induced Dzyaloshinskii-Moryia interaction stabilizes a lattice of nanoskyrmions in the Fe monolayer. Whereas the experiments have been performed at very low temperature, the stability against thermal agitation is crucial for the development of future skyrmion-based devices working under ambient conditions. In our study we show that the skyrmion lattice in Fe/Ir(111) is stable up to about 30 K. This finding disqualifies the nanoskyrmion lattice for the direct implementation in new spintronic devices – however, knowledge about the exact transition temperature is very important for the theoretical understanding of skyrmions, which is crucial for the engineering of future skyrmionic systems.

Another prerequisite for the industrial mass production of skyrmionic devices is the compatibility with today's silicon-based fabrication techniques. So far, interface-induced skyrmions on the atomic scale have only been observed on bulk crystal surfaces, but fabrication in semiconductor industry is conventionally based on a layer-by-layer growth approach. In our experimental study in cooperation with the University of Augsburg we demonstrate the realization of a nanoskyrmion lattice on Si-wafer based multilayer system being terminated by a single Fe monolayer.

The most fundamental processes of magnetization reversal are nucleation, annihilation and domain wall propagation. Understanding these mechanisms is crucial for the development of high-speed spintronic applications for data storage, information transmission and sensing. In our experimental studies we extend the temporal resolution of SP-STM by the application of pump-probe schemes. This allows to investigate processes that are far beyond the temporal resolution of conventional transimpedance amplifiers. We investigate the switching behavior of individual Fe/W(110) nanomagnets over a very wide temperature regime, spanning up to nine orders of magnitude of each nanomagnet's switching rate. The data shows a clear transition between two Arrhenius regimes when considerably changing the system temperature. A four-state hopping model for magnetization reversal is developed to understand the switching behavior for low and high temperature, showing that the effective switching rate of a nanomagnet is the result of the temperature-dependent underlying microscopic processes of nucleation, annihilation and domain wall propagation.

3.5.1 Thermal stability of an interface-stabilized skyrmion lattice

A. Sonntag, J. Hermenau, S. Krause, and R. Wiesendanger

At surfaces or interfaces, inversion symmetry of lattices is broken or lacking. Here, interfacial Dzyaloshinskii-Moriya (DM) interactions can be significant, resulting in the energetic stabilization of magnetic skyrmions, i.e. chiral spin structures with a whirling configuration [1,2]. Skyrmions are in the focus of current research because they could pave the way to a new field of spintronic applications, using them as carriers of digital information [3]. Recently, an atomic-scale two-dimensional skyrmion lattice that is stabilized by an interface has been discovered using spin-polarized scanning tunneling microscopy (SP-STM) [4]. Moreover, the selective writing and deleting of individual skyrmions by injecting a spin-polarized tunnel current into a bilayer system has been demonstrated [5]. It was reported that very low current densities are sufficient to move a skyrmion, compared to the current-induced movement of a domain wall [6, 7]. However, for technical applications the stability against thermal agitation is crucial. Whereas a temperature stability near room temperature was observed for a bulk-like skyrmionic system stabilized by an external magnetic field [8], the temperature dependence of atomic-scale skyrmions stabilized by an interface is yet unexplored. In a previous investigation combining SP-STM experiments and theory, a large interaction energy of 17 meV/atom has been reported for magnetic skyrmions stabilized at the interface of an Fe monolayer on Ir(111) [4]. Consequently, it was speculated that this system could show a correspondingly high thermal stability, possibly up to near room temperature [3]. Here, we present a temperature-dependent SP-STM study of the Fe/Ir(111) system to test the skyrmion lattice for its robustness against thermal agitation.

The experiments were performed under ultra-high vacuum conditions with a pressure below $1 \cdot 10^{-8}$ Pa using a home-built spin-polarized scanning tunneling microscope (SP-STM) at variable temperatures. Within our experimental setup, the entire microscope including the tip is cooled to maximize the thermal stability. In direct vicinity of the sample, a GaAs/GaAlAs diode is mounted, serving as a temperature sensor. A continuous flow He cryostat with a PID-controlled resistive heating at the cooling finger allows for a precise adjustment of the system temperature to any setpoint between 27 K and 300 K. The Ir(111) surface was prepared by annealing an Ir single crystal under oxygen atmosphere at 1600 K, followed by a high temperature flash (1800 K). Sputtering with Ar^+ ions at room temperature was used to remove deposited metal films. The iron monolayer was deposited by molecular beam epitaxy at elevated substrate temperature (450 K), leading to step-flow growth in fcc stacking configuration [9, 10]. For the SP-STM experiments, antiferromagnetic bulk Cr tips were used to avoid an undesired dipolar coupling with the sample [11]. The experiments have been performed in absence of any external magnetic field.

Figure 3.19(a) shows a constant-current SP-STM image of the Fe/Ir(111) monolayer taken at a temperature $T = 27.42$ K. A superstructure with square lattice symmetry is observed although the Ir(111) surface exhibits hexagonal atomic lattice symmetry. In SP-STM, the spin-polarized tunnel current depends on the relative orientation between the tip and local sample magnetization. Consequently, the

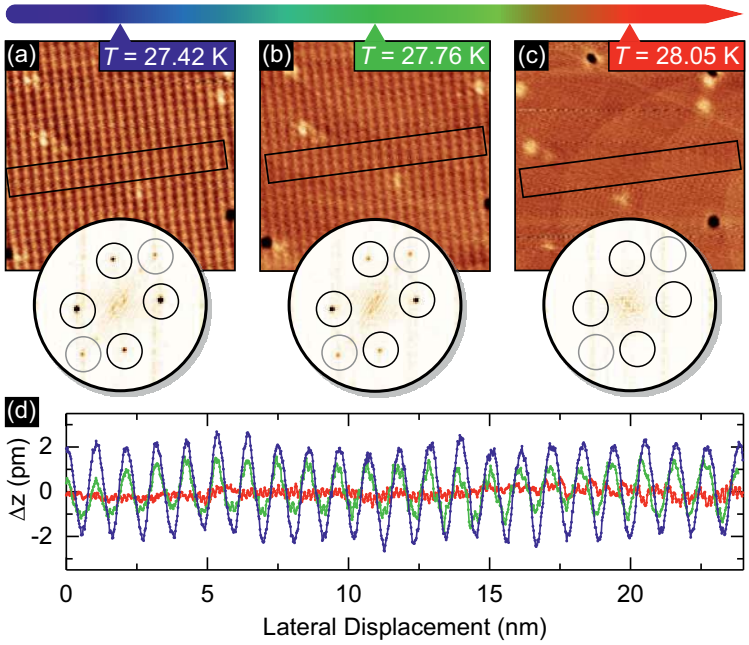

Figure 3.19: (color online) (a-c) SP-STM data of Fe/Ir(111) at different temperatures. For all images the same color scale and tunneling parameters were used ($25 \times 25\,\mathrm{nm}^2$, $U = 10\,\mathrm{mV}$ $I = 4\,\mathrm{nA}$). The insets show the corresponding Fourier transforms. Black circles mark the contribution from the magnetic unit cell and grey circles the spots caused by the TAMR effect. (d) Line profiles along the direction indicated in (a-c).

variation of the tip-sample distance in constant-current SP-STM experiments on an electronically homogeneous system reflects the magnetic structure of the surface. As we know from previous investigations, the observed square lattice can be assigned to a skyrmion lattice that is stabilized by the interface between Fe and Ir(111) [4]. The corresponding incommensurate magnetic unit cell has a size of approximately $1 \times 1\,\mathrm{nm}^2$ and consists of about 15 atoms. Both the observed angle between the lattice vectors $\theta = (91 \pm 2)^\circ$ as well as the lattice constant $(1.00 \pm 0.05)\,\mathrm{nm}$ are well in agreement with previous investigations at lower temperatures.

The inset in Fig. 3.19(a) shows the Fourier transform (FT) of the SP-STM data, revealing six distinct spots. The spots marked with black circles correspond to the magnetic contrast and thus resemble the unit cell of the skyrmion lattice. The spots marked in grey circles indicate a periodicity that is reduced by a factor of $\sqrt{2}$ compared to the magnetic unit cell. They are attributed to a contribution of the tunneling anisotropic magnetoresistance (TAMR) effect that can be observed at low bias voltages [4, 12, 13]. Note that the measured corrugation along the horizontal direction is stronger than along the vertical direction in our experiment, which is attributed to a canted tip magnetization [11]. In the FT, this results in a variation of the magnetic contrast spot intensities.

To study the response of the skyrmion lattice to thermal agitation, we carefully increased the system temperature. The respective SP-STM images for $T = 27.76\,\mathrm{K}$ and $T = 28.05\,\mathrm{K}$ are shown in Figs. 3.19(b) and (c). For comparison, we applied the same color-scale to all three images. Obviously, the measured corrugation of the skyrmion lattice as well as the respective FT spots fade away with increasing

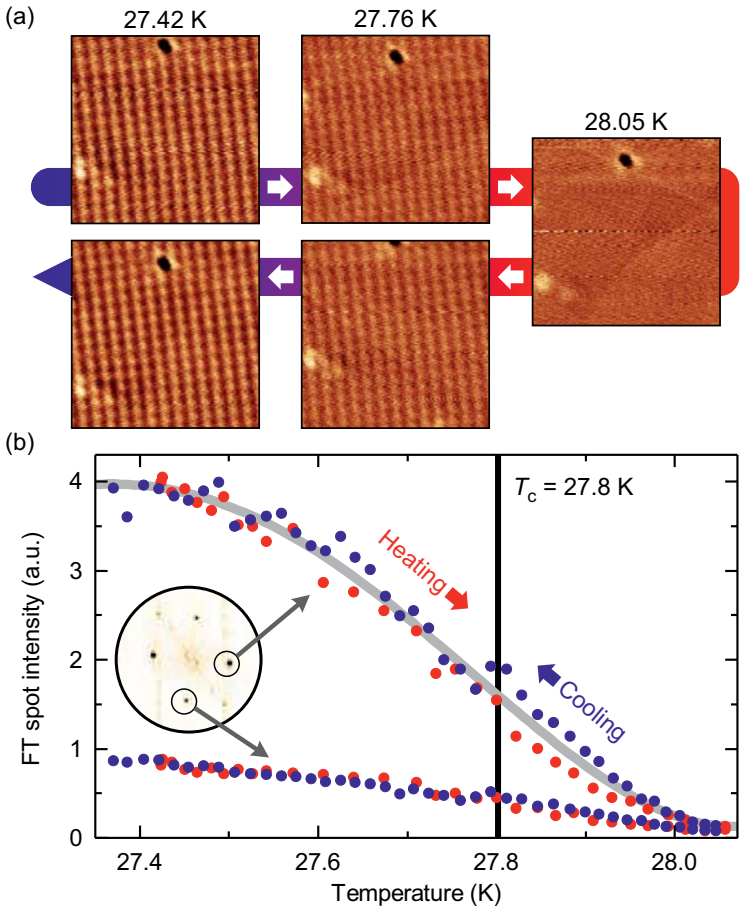

Figure 3.20: (color online) (a) SP-STM images acquired while ramping the temperature ($15 \times 15\,\mathrm{nm}^2$, $U = 10\,\mathrm{mV}$ $I = 4\,\mathrm{nA}$). (b) FT-spot intensity of the skyrmion lattice as a function of temperature (blue: cooling; red: heating), and curve fitting with a polynomial of degree four (grey) for estimating the critical temperature T_c. The data were measured with a slew rate of 80 mK/h.

T. In Fig. 3.19(d), line-profiles along the direction marked in the SP-STM images are shown for the three temperature setpoints. At $T = 27.42\,\mathrm{K}$, the peak-to-peak corrugation is on the order of 4 pm. It is reduced significantly upon increasing the temperature to $T = 27.76\,\mathrm{K}$, and at $T = 28.05\,\mathrm{K}$ the square lattice completely disappears, resulting in a smooth line profile with no magnetic contrast. The experiments show a vanishing magnetic contrast above a critical temperature $T_\mathrm{c} \approx 28\,\mathrm{K}$, thereby indicating magnetic disorder above T_c.

In order to study this transition in detail, we slowly ramped T between 27.40 K and 28.10 K while recording SP-STM images on the very same spot. After each image, the temperature setpoint was increased by 15 mK before starting the acquisition of the next image. This procedure results in a T sweep rate of approximately 80 mK/h. Post-processing by linewise flattening of the SP-STM images was necessary to compensate for thermal drift. Figure 3.20(a) shows five exemplary SP-STM topographies that were acquired during the temperature ramp. Again, the skyrmion lattice vanishes smoothly upon heating the sample to $T = 28.05\,\mathrm{K}$. Reducing the temperature results in the lattice reappearing, and the original magnetic state is restored. To evaluate the corrugation for the whole image, the Fourier transform of

each image was calculated. A measure of the magnetic corrugation is given by the intensity of the distinct magnetic spots in Fourier space. To account for the finite spot-width and lateral thermal drift, we average the intensity over a small area covering the spot. Figure 3.20(b) shows the intensities of the magnetic FT spots as a function of T. As described above, the intensity of the two magnetic spots differs due to an in-plane component of the tip magnetization. Nevertheless, the same qualitative behavior can be found for both spots. At temperatures below 27.5 K a large corrugation is observed, indicating the robust presence of the skyrmion lattice. Above $T = 27.5\,\mathrm{K}$ the corrugation significantly decreases with increasing temperature and ultimately disappears within the noise level. As no hysteresis between heating and cooling is observed, we conclude that the sweep rate is slow enough to ensure the microscope being in thermal equilibrium at all times. Hence, the experiments indicate a relatively sharp transition with increasing temperature. A differential method for estimating the critical temperature T_c seeks the maximum curvature in the thermomagnetic curve. Therefore, the experimental data shown in Fig. 3.20(b) have been fitted by a polynomial of degree four, and its point of inflection has been determined, resulting in $T_\mathrm{c} = 27.8\,\mathrm{K}$.

Figure 3.21(a) shows an SP-STM image of the Fe/Ir(111) surface in the vicinity of a second-layer iron island, taken below T_c. The bright part on the very left side of the image reflects the edge of the island. As before, the periodic superstructure of the skyrmion square lattice is observed far away from the island. Close to the island, the skyrmion lattice is distorted, as denoted by the arrows. This finding indicates an interaction between the skyrmion lattice and the island, most likely due to exchange coupling. Figure 3.21(b) shows the same sample area, now imaged at a temperature above T_c. Far away from the second-layer island the skyrmion lattice has vanished. However, the magnetic order persists close to the island, being most pronounced directly at the island edge and decaying with increasing distance. In Fig. 3.21(c), two line sections along the direction marked in the SP-STM images are shown. For temperatures below T_c, the skyrmion lattice leads to a periodic variation of the apparent height with a constant amplitude. At 28.07 K, on the other hand, the corrugation decreases continuously with increasing distance from the island. Within $6-7$ magnetic lattice constants the periodic corrugation completely vanishes. Note that the same periodicity is observed below and above T_c.

Obviously, the same magnetic order is observed close to the second monolayer Fe island even above T_c of the extended film. This finding proves the tunneling tip being magnetically sensitive at all temperatures investigated here. Moreover, the experiments show that the skyrmion lattice is strongly pinned to the second-layer island, resulting in a locally enhanced stabilization of the magnetic order. The persistence of the pinning at the nanoisland indicates that a depinning of the whole skyrmion lattice is not the cause for the vanishing corrugation above T_c. Consequently, T_c is not related to the pinning potential but to the intrinsic properties of the skyrmion lattice.

Considering the scenario of a transition into a ferromagnetic phase, we expect an out-of-plane magnetization above T_c, due to the out-of-plane easy axis of the system [4]. Consequently, the apparent height of the extended film should nearly resemble the maximum or minimum apparent height on the skyrmion lattice that is pinned by the second-layer island at $T = 28.07\,\mathrm{K}$. As can be seen from the SP-STM

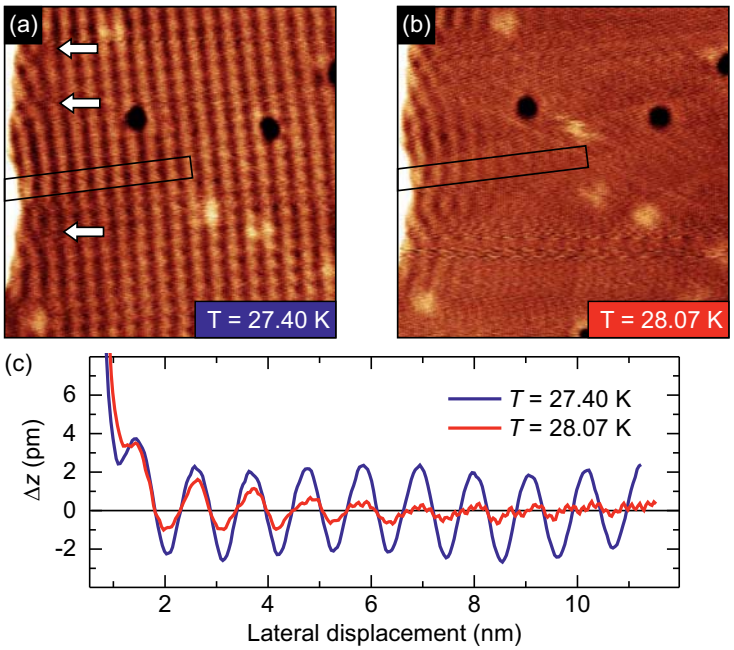

Figure 3.21: (color online) Pinning of the skyrmion lattice at a second monolayer iron island. (a) and (b) show SP-STM data below and above T_c, respectively. The second monolayer island is on the far left of the image. (c) Line sections along the area marked in (a) and (b).

image in Fig. 3.21(b) and the corresponding linesection in Fig. 3.21(c), this is not the case.

Hence we conclude that the magnetic order on the extended Fe/Ir(111) system is destroyed at T_c, whereas in the vicinity of a second-layer Fe nanoisland it is stabilized even above T_c. Note that the magnetic correlation between neighboring spins does not necessarily have to vanish completely above T_c, as shown by a theoretical study on the system of bi-atomic Fe chains on a $(5 \times 1)-$Ir(001) surface, exhibiting a 120° spin-spiral [14]. Here, a short-range spin-spiral order was found even at temperatures where the overall magnetization of the chains is destroyed. Consequently, both a melting transition, for example into a skyrmion liquid phase, as well as a transition into a paramagnetic phase could explain our experimental findings. Theoretical investigations could provide a deeper insight into the microscopic details of the phase transition.

In Ref. [4], the energy gain due to the formation of the skyrmion lattice was calculated from first principles to 17 meV per atom. Due to this large interaction energy one would expect a high thermal stability for the Fe/Ir(111) skyrmion lattice. Our experiments, however, indicate a rather low transition temperature of the system. The question remains open how this finding can be understood from a theoretical point of view. Up to now there is no theory regarding the temperature dependency of non-collinear magnetism including the diverse interactions that play a role in the formation of the skyrmion lattice. In particular, Dzyaloshinskii-Moriya (D), four-spin (K_4) and biquadratic (B) interactions and their different angle dependencies have to be considered for an appropriate theoretical approach for the quasi-2D skyrmion system. Here, small angle perturbations driven by thermal fluc-

tuations could be energetically favored by D and K_4. Therefore, temperature may affect the skyrmion lattice much stronger compared to a system solely driven by exchange interaction. Additionally, one may speculate that the interaction energies of individual spins on particular lattice sites significantly vary within the magnetic unit cell. Consequently, spins with lower interaction energies may be very susceptible to thermal fluctuations, resulting in an overall easier destabilization of the lattice by thermal agitation.

In order to roughly estimate the stabilization energy for our system, we consider D, K_4 and B counteracting the exchange interaction, thereby destabilizing collinear magnetic order. Taking into account the negative sign of the destabilizing interactions, we compare the sum of all magnetic interactions with the thermal energy of the system at the critical temperature T_c', where the magnetic order gets lost:

$$\sum_i J_i N_i + N_1 \left(D + K_4 + B\right) = k_\mathrm{B} T_\mathrm{c}', \tag{3.9}$$

with J_i being the i^{th} nearest neighbor exchange energy, and N_i is the number of i^{th} nearest neighbors. Using the values from first principles calculations in Ref. [4] we find $T_\mathrm{c}' = 51\,\mathrm{K}$, corresponding to an effective stabilization energy of 4.4 meV per atom. Although this simple estimation does not account for the real complexity of all the different magnetic interactions, it is in a quite good agreement with our findings, which indicate an effective stabilization energy of 2.4 meV per atom as calculated from T_c of the experiment. More sophisticated methods like, for example, Monte-Carlo simulations could help to clarify the details of the phase transition of the skyrmion lattice [15], but are beyond the scope of this paper.

In summary, our experimental SP-STM study demonstrates that the skyrmion lattice stabilized by the Fe/Ir(111) interface is much more susceptible to thermal agitation than expected from previous investigations. At T_c =27.8 K, the skyrmion lattice vanishes, indicating a loss of long-range magnetic order. The low energy scale of this transition is attributed to the complex relation between Dzyaloshinskii-Moriya, four-spin and biquadratic interactions and their different angle dependencies, as well as to a non-homogeneous distribution of the interaction energy within the magnetic unit cell. At second-layer Fe nanoislands, however, pinning stabilizes the magnetic order locally even above the transition temperature of the extended film.

References

[1] S. Mühlbauer, B. Binz, F. Jonietz, C. Pfleiderer, A. Rosch, A. Neubauer, R. Georgii, and P. Böni, Science **323**, 915 (2009).

[2] N. Nagaosa and Y. Tokura, Nature Nanotech. **8**, 899 (2013).

[3] A. Fert, V. Cros, and J. Sampaio, Nature Nanotech. **8**, 152 (2013).

[4] S. Heinze, K. von Bergmann, M. Menzel, J. Brede, A. Kubetzka, R. Wiesendanger, G. Bihlmayer, and S. Blügel, Nature Phys. **7**, 713 (2011).

[5] N. Romming, C. Hanneken, M. Menzel, J. E. Bickel, B. Wolter, K. von Bergmann, A. Kubetzka, and R. Wiesendanger, Science **341**, 636 (2013).

[6] X. Yu, N. Kanazawa, W. Zhang, T. Nagai, T. Hara, K. Kimoto, Y. Matsui, Y. Onose, and Y. Tokura, Nat. Commun. **3**, 988 (2012).

[7] J. Sampaio, V. Cros, S. Rohart, A. Thiaville, and A. Fert, Nature Nanotech. **8**, 839 (2013).

[8] X. Z. Yu, N. Kanazawa, Y. Onose, K. Kimoto, W. Z. Zhang, S. Ishiwata, Y. Matsui, and Y. Tokura, Nature Mater. **10**, 106 (2011).

[9] K. von Bergmann, S. Heinze, M. Bode, E. Y. Vedmedenko, G. Bihlmayer, S. Blügel, and R. Wiesendanger, Phys. Rev. Lett. **96**, 167203 (2006).

[10] K. von Bergmann, S. Heinze, M. Bode, G. Bihlmayer, S. Blügel, and R. Wiesendanger, New J. Phys. **9**, 396 (2007).

[11] A. Schlenhoff, S. Krause, G. Herzog, and R. Wiesendanger, Appl. Phys. Lett. **97**, 083104 (2010).

[12] M. Bode, S. Heinze, A. Kubetzka, O. Pietzsch, X. Nie, G. Bihlmayer, S. Blügel, and R. Wiesendanger, Phys. Rev. Lett. **89**, 237205 (2002).

[13] K. von Bergmann, M. Menzel, D. Serrate, Y. Yoshida, S. Schröder, P. Ferriani, A. Kubetzka, R. Wiesendanger, and S. Heinze, Phys. Rev. B **86**, 134422 (2012).

[14] M. Menzel, Y. Mokrousov, R. Wieser, J. E. Bickel, E. Vedmedenko, S. Blügel, S. Heinze, K. von Bergmann, A. Kubetzka, and R. Wiesendanger, Phys. Rev. Lett. **108**, 197204 (2012).

[15] N. S. Kiselev, D. S. G. Bauer, and S. Blügel, presentation at the DPG Spring Meeting, Dresden (2014).

3.5.2 A magnetic nano-skyrmion lattice observed in a Si-wafer based multilayer system

A. Schlenhoff, P. Lindner, J. Friedlein, S. Krause, and R. Wiesendanger

Magnetic skyrmions are localized spin configurations with a whirling configuration [1, 2]. They are extremely well defined, since they always occur with a specific rotational sense. In addition, they are topologically stable: they cannot be deformed to a ferromagnetic or other magnetic state without overcoming an energy barrier. Due to this robustness, these particle-like skyrmions offer new exciting possibilities for spintronic applications, using them as carriers of digital information [3, 4]. Recently, an atomic-scale two-dimensional magnetic skyrmion lattice that is stabilized by Dzyaloshinskii-Moriya interactions at the Fe/Ir(111) interface has been discovered using spin-polarized scanning tunneling microscopy (SP-STM) [5]. The selective writing and deleting of individual nano-skyrmions by injecting a spin-polarized tunnel current into a bilayer metal system has already been demonstrated [6]. It was also reported that very low current densities are sufficient to move a skyrmion, compared to the current-induced movement of a domain wall [7, 8].

Up to now, interface-stabilized nano-skyrmion lattices in metal films have only been studied on metallic bulk single crystal substrates [5, 6, 9, 10]. Like for the Si-based technology of today, an important prerequisite for future skyrmion-based spintronic applications is the mass production of skyrmionic devices using multilayer growth. In the last years, heteroepitaxial growth of Ir on Si(111) with an yttria-stabilized zirconia (YSZ) buffer layer has been developed [11, 12]. Using Si wafers as substrates, this technique can be easily implemented into standard Si-based fabrication. Ir/YSZ/Si(111) wafers of up to 4 inch diameter have already been prepared and characterized, revealing basically twin-free heteroepitaxial Ir(111) films on the YSZ/Si(111) support with low mosaic spread ($\leq 0.2°$) [12, 13].

In our study we epitaxially grow Fe onto the Ir/YSZ/Si(111) surface and test the system for a magnetic nano-skyrmion lattice. After depositing nominally 0.8 atomic layers (AL) of Fe on the substrate, the sample was inserted into the microscope and cooled down to our measurement temperature of 26.4 K.

Methods

The experiments were performed under ultra-high vacuum conditions with a pressure below $1 \cdot 10^{-8}$ Pa using a home-built spin-polarized scanning tunneling microscope at variable temperatures. Within our experimental setup, the entire microscope including the tip is cooled to maximize the thermal stability. For the SP-STM experiments, antiferromagnetic bulk Cr tips were used to avoid an undesired dipolar coupling with the sample [18]. All experiments presented in this paper have been performed at a temperature of 26.4 K and in absence of any external magnetic field. The Ir/YSZ/Si(111) multilayer system was prepared in Augsburg according to a previously described method [12]. A (111)-oriented Si wafer was first covered by an YSZ layer with a thickness of 150 nm by means of pulsed laser deposition from a ZrO_2 target containing 6.5 mol% $YO_{1.5}$ [21]. The YSZ serves as buffer layer preventing silicide formation of the metal with the subjacent silicon. In addition, it

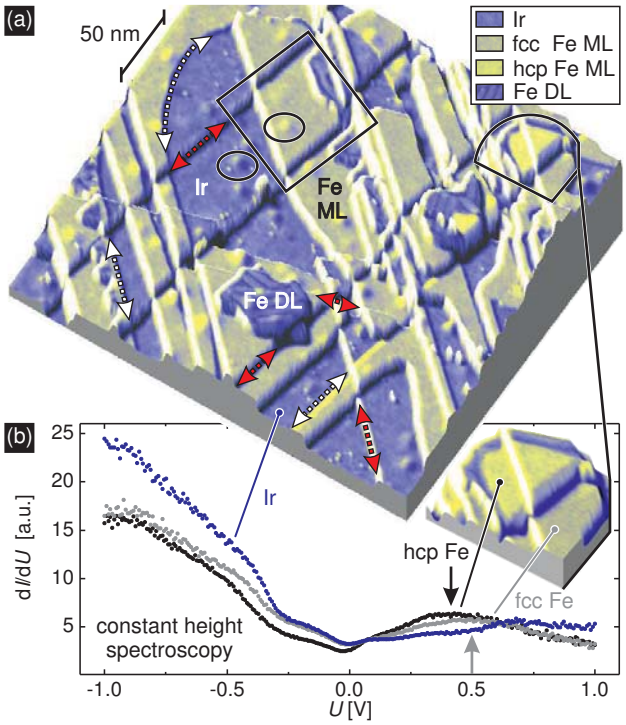

Figure 3.22: **(a)** Topography of 0.8 AL Fe on Ir/YSZ/Si(111) overlaid with the simultaneously recorded $\mathrm{d}I/\mathrm{d}U$ signal ($U = 260\,\mathrm{mV}$, $I = 1\,\mathrm{nA}$). The Fe ML grows at the intrinsic step edges and the slip lines of the Ir surface (white arrows). Small Fe DL islands are visible. Slip lines that evolve when cooling down the system for the experiments break up the already-grown Fe film (red arrows). Defects resulting from sputtering of the substrate are visible on Ir and Fe (encircled). **(b)** Constant height spectroscopy above Ir, hcp and fcc Fe ML (stabilization parameters: $I = 1\,\mathrm{nA}$, $U = 1\,\mathrm{V}$). A typical peak at $U \approx +350\,\mathrm{mV}$ is visible for the hcp stacking, whereas it is located at $U \approx +500\,\mathrm{mV}$ for the fcc stacking (positions marked by arrows). Inset: Closer view of the area marked in (a) showing both types of ML areas.

transfers the epitaxial orientation from the Si single crystal to the metal film. On top of the YSZ layer a 600 nm thick Ir film was deposited by molecular beam epitaxy. The first 20 nm were grown with a rate of 0.004 nm/s at 920 K. For the remaining 580 nm the growth rate was increased to 0.02 nm/s and the temperature decreased to 820 K. This procedure guaranteed flat films with high structural perfection as proven by a polar and azimuthal mosaic spread of 0.089° and 0.075°, respectively. For the present experiments the high total thickness facilitated repeated sputtering and annealing cycles. However, for future applications an identical functionality can be achieved with Ir film thicknesses well below 100 nm. (10x10) mm^2 pieces were cut from the wafers, mounted to sample holders and introduced into the UHV chamber in Hamburg. The Ir/YSZ/Si(111) substrate was then prepared *in situ* by sputtering with Ar^+ ions at room temperature, annealing under oxygen atmosphere at 820 K, followed by a high temperature flash (1060 K). Iron was deposited by molecular beam epitaxy at elevated substrate temperature (450 K).

Results and Discussion

A topography overview of a typical sample is shown in Fig. 3.22(a). A small ac modulation voltage ($U_{\mathrm{mod}} = 40\,\mathrm{mV}$, $f = 4.333\,\mathrm{kHz}$) was added to the applied sample bias voltage U in order to record the spatially resolved differential tunneling conductance $\mathrm{d}I/\mathrm{d}U$ by lock-in technique simultaneously to the constant current topography image. The topography is overlaid with the $\mathrm{d}I/\mathrm{d}U$ signal in Fig. 3.22(a). Regions of monolayer (ML) coverages coexist with regions of the bare Ir surface. The $\mathrm{d}I/\mathrm{d}U$ signal reveals an electronic contrast between them. Small double layer (DL) areas are also present. While the Fe ML appears flat, the Fe DL shows a reconstruction due to strain relaxation [14].

The Fe grows mainly at the step edges of the Ir surface, as it is also known from the step-flow growth mode on the Ir(111) bulk single crystal [14, 15]. Beside an intrinsic curved step at the top of the image, straight steps running along the main crystallographic directions can be observed, being characteristic for the underlying Ir/YSZ/Si(111) surface [16]. These steps of atomic height are slip lines that result from gliding processes or dislocation movements in the Ir film occuring during the thermal treatment of the Ir/YSZ/Si(111) substrate. They arise due to the different thermal expansion coefficients of the individual components of the Ir/YSZ/Si(111) multilayer system. The directions of the slip lines reflect the hexagonal sample symmetry. Since the Fe grows at all these step edges, they lead to multiple growth directions of the Fe film. Likewise, additional slip lines evolve when cooling down to low temperature for the SP-STM experiments, resulting in multiple break-ups of the Fe ML and DL patches, as is observable in Fig. 3.22(a).

On the Ir surface, as well as on the Fe ML, shallow protrusions are visible. These defects that have been found on the bare substrate before originate from sputtering during sample preparation [16]. They are most likely caused by Ar^+ ions incorporated into the Ir film. For Ir(111) single crystals these volume defects can be removed by flash annealing after sputtering at temperatures between 1350 K and 1800 K [10, 15]. In case of Ir/YSZ/Si(111), temperatures above $\approx 1300\,\mathrm{K}$ cannot be applied because they result in a dewetting of the metal film [16].

Besides the electronic contrast between Fe and Ir, the signal of the differential tunneling conductance $\mathrm{d}I/\mathrm{d}U$ in Fig. 3.22(a) reveals two different types of Fe ML areas. A closer view of an area that exhibits both types of ML patches is shown in the inset of Fig. 3.22(b). For Fe/Ir(111) it is known, that the ML grows in two different in-plane commensurate stackings, fcc and hcp [14, 15]. They can be distinguished by their different electronic structure. In Figure 3.22(b) constant-height $\mathrm{d}I/\mathrm{d}U$ spectroscopy curves taken on the Ir/YSZ/Si(111) surface and the two different types of Fe ML areas are shown. For both types of ML areas a broad empty-state peak at positive sample bias voltage is observed. The predominant type exhibits a peak at $U \approx +500\,\mathrm{mV}$, which is typical for the fcc stacking, as has been observed in experimental spectra for Fe on Ir(111) [14]. For the scarce ML patches the peak is shifted to $U \approx +350\,\mathrm{mV}$, which is also consistent with experimental spectra taken on hcp stacked Fe on the Ir(111) single crystal [14]. We conclude, that the bright Fe ML patches in Fig. 3.22(a) grow in hcp stacking, whereas all the other areas of ML coverage exhibit an fcc stacking. The preference of the fcc stacked regions result from the high density of slip lines where Fe continues the arrangement of the Ir atoms and therefore grows in fcc stacking. Summing up, our

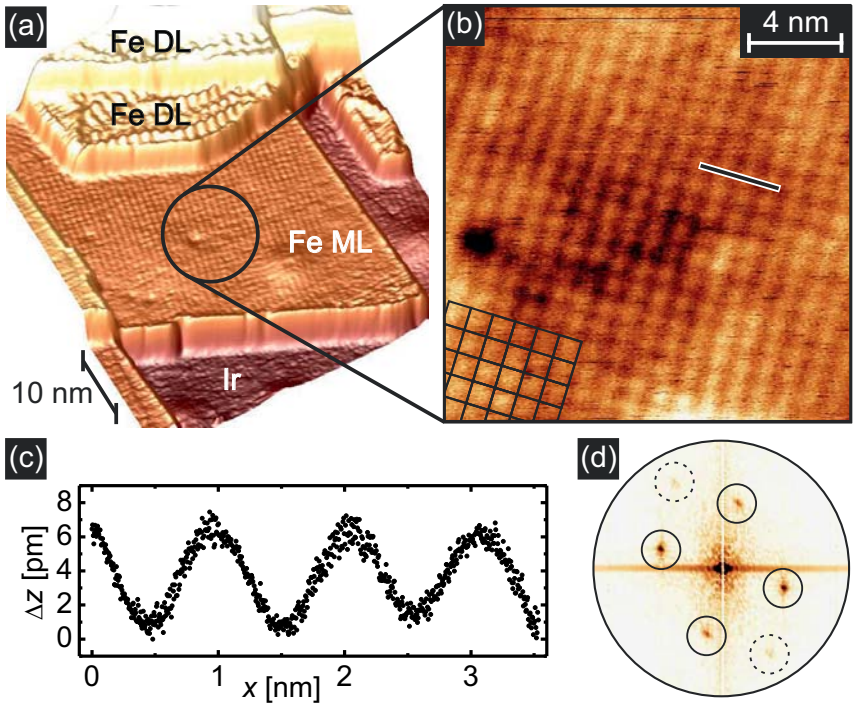

Figure 3.23: **(a)** Constant-current SP-STM image of the sample area marked in Fig. 3.22(a). **(b)** Closer view of the fcc Fe ML area marked in (a). A square lattice is visible. The inset shows a schematic. **(c)** Line profile along the direction indicated in (b). **(d)** Fourier transform of (b). Black circles mark the contribution from the magnetic unit cell and dashed circles the spots caused by the TAMR effect. ($U = 10\,\mathrm{mV}$, $I = 4\,\mathrm{nA}$, $T = 26.4\,\mathrm{K}$.)

measurements show that the electronic properties of a submonolayer coverage of Fe on Ir/YSZ/Si(111) are equivalent to those on the (111) surface of Ir bulk single crystals, despite of substantial variations in surface topography depending on the sample preparation.

The observed electronic equivalence raises the question about the magnetic properties of the Fe/Ir/YSZ/Si(111) multilayer system in comparison to the topographically much simpler Fe/Ir(111) bulk single crystal system. A closer view of the area marked in Fig. 3.22(a) is shown in Fig. 3.23(a). The constant-current SP-STM image shows an extended fcc stacked Fe ML film that is broken by two slip lines running from the bottom to the top of the image. At the top of the image an Fe DL region with its reconstruction is observable. It is broken by a slip line that runs, in this case, horizontally through the image. At the bottom, a small region of the bare Ir surface is visible. On the Fe ML a regular superstructure is observable. In SP-STM, the spin-polarized tunnel current depends on the relative orientation between the tip and the local sample magnetization [17]. Consequently, the variation of the tip-sample distance in constant-current SP-STM experiments on an electronically homogeneous system reflects the magnetic structure of the surface. In Fig. 3.23(b) a zoom in on the Fe ML is shown. It reveals a square lattice symmetry of the superstructure. The line profile in Fig. 3.23(c) taken along the direction indicated in (b) reveals a periodicity of about 1 nm and a corrugation of about 6 pm. Figure 3.23(d) shows the Fourier transform (FT) of the SP-STM data of Fig. 3.23(b), revealing

six distinct spots. The spots marked with black circles correspond to the square lattice shown in the inset of Fig. 3.23(b), with an observed angle between the lattice vectors $\theta = (91 \pm 3)^\circ$ and a lattice constant (1.02 ± 0.08) nm. The observed square lattice resembles the magnetic contrast that has been found for the Fe ML on Ir(111) single crystals [5, 9, 10]. It can be assigned to a skyrmion lattice that is stabilized at the interface between Fe and Ir(111). The corresponding magnetic unit cell is known to have a size of approximately (1x1) nm^2 and consists of about 15 atoms. Both the observed angle between the lattice vectors as well as the lattice constant reproduce well the experimental findings on the Ir(111) bulk single crystal [5, 9, 10]. Note that the measured corrugation along the horizontal direction is stronger than along the vertical direction in our experiment, which is attributed to a canted tip magnetization [18]. In the FT shown in Fig. 3.23(d), this results in a variation of the magnetic contrast spot intensities. The FT spots marked in dashed circles indicate a periodicity that is reduced by a factor of $\sqrt{2}$ compared to the magnetic unit cell. They are attributed to the tunneling anisotropic magnetoresistance (TAMR) effect that can be observed at low bias voltages [5, 19, 20]. In summary, our experiments demonstrate that the magnetic ground state of the Fe ML on a Ir/YSZ/Si(111) substrate is identical to that on the (111) surface of Ir bulk single crystals. The magnetic nano-skyrmion lattice of the Fe ML is also observable on a Si-wafer based multilayer system that is fabricated by industrial preparation techniques.

Zooming out of the sample area of Fig. 3.23(a) reveals the magnetic square lattice evolving also on the upper left and lower right Fe ML area, as shown in Fig. 3.24(a). As mentioned before, they are separated from the middle Fe ML patch by slip lines. On each ML patch, a sputtering defect is visible, causing a local protrusion. Interestingly, the magnetic square lattice is observable even on these local defects. A closer view of the middle ML area with the sputtering defect is shown in Fig. 3.24(b). The square unit cell of the superstructure, that resembles the unit cell of the magnetic skyrmion lattice, is clearly visible all over the defect, and even on top of it. No distortion of the magnetic skyrmion lattice is observable. The line profile in Fig. 3.24(c), taken along the direction indicated in (b), reveals that the defect exhibits a maximum height of $h \approx 43$ pm and is about 8 nm wide. Taking the interatomic distance $a/\sqrt{2}$ with the lattice constant $a = 2.22$ Å of Ir into account, the local stress is relieved over approximately 25 atoms in horizontal direction. Hence, the vertical lattice displacement between next neighbours can be estimated to 1.7 pm, which is about 1 % of the distance of the (111) planes in Ir. Obviously, the skyrmion lattice is robust against local atomic lattice distortions induced by structural point defects.

Conclusions

In summary, our SP-STM experiments at low temperature show that a magnetic nano-skyrmion lattice is formed in the Fe ML on the Ir/YSZ/Si(111) multilayer system. Despite substantial variations in surface topography like volume defects, slip lines and multiple growth directions induced by multilayer preparation, the electronic and magnetic properties of the Fe ML on the Si-wafer based substrate are comparable to those that have been observed on the Fe ML on Ir(111) bulk single crystals. Our experimental results pave the way for the use of multilayer substrates in magnetic surface studies by SP-STM, that are based so far on single

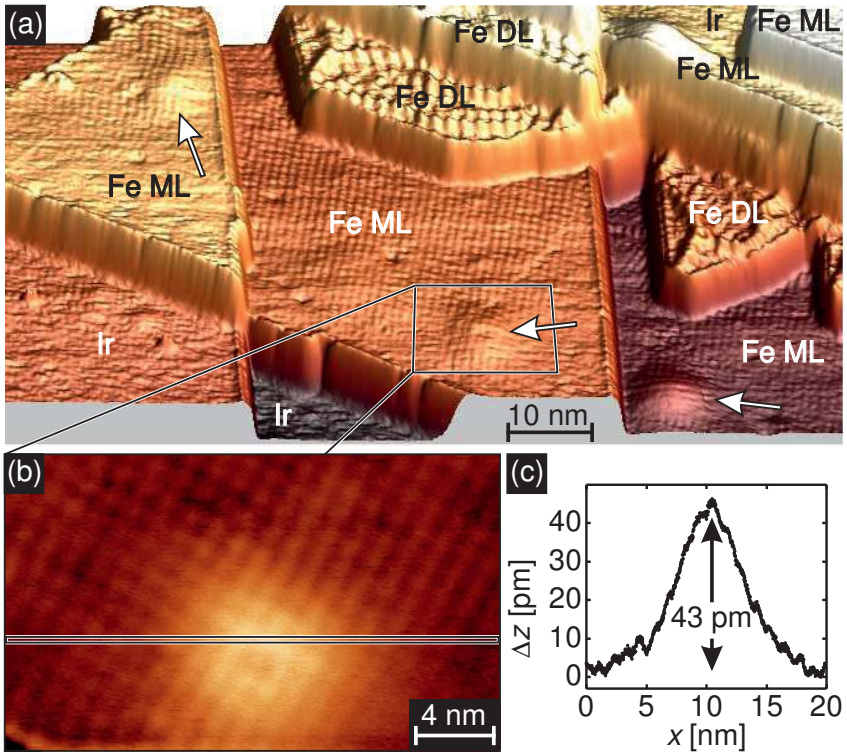

Figure 3.24: **(a)** Constant-current SP-STM image of the sample around the area shown in Fig. 3.23(a). On the Fe ML sputtering defects are visible (marked by arrows). **(b)** Closer view of the area marked in (a). Also on the sputtering defect the square lattice is visible. **(c)** Line profile along the direction indicated in (b). The maximum height of the defect is $\approx 43\,\mathrm{pm}$. ($U = 10\,\mathrm{mV}$, $I = 4\,\mathrm{nA}$, $T = 26.4\,\mathrm{K}$.)

crystal metal substrates. Being performed on an up-scalable Si-based substrate, our work promotes spintronic applications of nano-skyrmions as carriers of digital information that can be fabricated on a wafer scale by industrial processes being fully compatible with standard semiconductor technology.

References

[1] S. Mühlbauer, B. Binz, F. Jonietz, C. Pfleiderer, A. Rosch, A. Neubauer, R. Georgii, P. Böni, Science **323**, 915 (2009).

[2] N. Nagaosa and Y. Tokura, Nature Nanotech. **8**, 899 (2013).

[3] A. Fert, V. Cros, and J. Sampaio, Nature Nano **8**, 152 (2013).

[4] N. S. Kiselev, A. N. Bogdanov, R. Schaefer, and U. K. Rößler, J. Phys. D: Appl. Phys. **44**, 392001(2011).

[5] S. Heinze, K. von Bergmann, M. Menzel, J. Brede, A. Kubetzka, R. Wiesendanger, G. Bihlmayer, and S. Blügel, Nature Physics **7**, 713 (2011).

[6] N. Romming, C. Hanneken, M. Menzel, J. E. Bickel, B. Wolter, K. von Bergmann, A. Kubetzka, and R. Wiesendanger, Science **341**, 636 (2013).

[7] X. Yu, N. Kanazawa, W. Zhang, T. Nagai, T. Hara, K. Kimoto, Y. Matsui, Y. Onose, and Y. Tokura, Nat. Commun. **3**, 988(2012).

[8] J. Sampaio, V. Cros, S. Rohart, A. Thiaville, and A. Fert, Nature Nanotech. **8**, 839 (2013).

[9] K. von Bergmann, A. Kubetzka, O. Pietzsch, and R. Wiesendanger, J. Phys.: Condens. Matter **26**, 394002 (2014).

[10] A. Sonntag, J. Hermenau, S. Krause, and R. Wiesendanger, Phys. Rev. Lett. **113**, 077202 (2014).

[11] S. Gsell, M. Fischer, R. Brescia, M. Schreck, P. Huber, F. Bayer, B. Stritzker, and D. G. Schlom, Appl. Phys. Lett. **91**, 061501 (2007).

[12] S. Gsell, M. Fischer, M. Schreck, and B. Stritzker, J. Cryst. Growth **311**, 3731 (2009).

[13] M. Fischer, S. Gsell, M. Schreck, R. Brescia, and B. Stritzker, Diamond Relat. Mater. **17**, 1035 (2008).

[14] K. von Bergmann, S. Heinze, M. Bode, G. Bihlmayer, S. Blügel, and R. Wiesendanger, New Journal of Physics **9**, 396 (2007).

[15] K. von Bergmann, S. Heinze, M. Bode, E. Y. Vedmedenko, G. Bihlmayer, S. Blügel, and R. Wiesendanger, Phys. Rev. Lett. **96**, 167203 (2006).

[16] P. Zeller, S. Dänhardt, S. Gsell, M. Schreck, and J. Wintterlin, Scalable Surf. Sci. **606**, 1475 (2012).

[17] R. Wiesendanger, Rev. Mod. Phys. **81**, 1495 (2009).

[18] A. Schlenhoff, S. Krause, G. Herzog, and R. Wiesendanger, Appl. Phys. Lett. **97**, 083104 (2010).

[19] M. Bode, S. Heinze, A. Kubetzka, O. Pietzsch, X. Nie, G. Bihlmayer, S. Blügel, and R. Wiesendanger, Phys. Rev. Lett. **89**, 237205 (2002).

[20] K. von Bergmann, M. Menzel, D. Serrate, Y. Yoshida, S. Schröder, P. Ferriani, A. Kubetzka, R. Wiesendanger, and S. Heinze, Phys. Rev. B **86**, 134422 (2012).

[21] S. Gsell, M. Fischer, T. Bauer, M. Schreck, and B. Stritzker, Diamond Relat. Mater. **15**, 479 (2006).

3.5.3 High frequency magnetization dynamics of individual atomic-scale magnets

S. Krause, A. Sonntag, J. Hermenau, J. Friedlein, and R. Wiesendanger

Nucleation, annihilation and domain wall propagation are the most fundamental microscopic processes of magnetization reversal [1, 2]. Understanding and controlling the mechanisms that favor or hinder magnetization reversal is crucial for the development of high-speed spintronic applications for data storage, information transmission and sensing.

In previous spin-polarized scanning tunneling microscopy (SP-STM) studies it was shown that the thermally activated magnetization reversal of Fe/W(110) nanomagnets consisting of less than 100 atoms is realized by nucleation and propagation instead of a coherent rotation of all magnetic moments of the nanomagnet [3–5]. Here, the domain wall behaves like a quasi-particle moving along the [001] direction. Although the monodomain state is not present during the magnetization reversal, the temperature dependent switching rate can be described by an Arrhenius law. The experiments in Refs. [3–5] were all based on real-time recording of the telegraphic noise of the spin-polarized tunnel current I. A typical telegraphic noise measurement is shown in Fig. 3.25(a). As I depends on the relative orientation between tip and sample magnetization [6, 7], switching between antiparallel (state **0**) or parallel (state **1**) orientation between the sample and fixed tip magnetization generates a two-state signal. This is reflected by a modulation of the tip-to-sample distance z in the constant current mode of SP-STM. The temporal resolution of this method is ultimately limited by the bandwidth of the transimpedance amplifier (TIA), being typically in the kHz regime. Consequently, only the lifetime *between* two switching events is readily accessible, whereas the dynamics of the microscopic processes *during* magnetization reversal is hidden.

Pump-probe schemes allow the observation of processes that are much faster than the temporal resolution of the TIA. In combination with STM, a temporal resolution down to the low ps or even fs regime has successfully been realized with electrical or optical pumping [8, 9]. In the pioneering work of Loth *et al.*, SP-STM experiments have been combined with an all-electronic pump-probe scheme, thereby achieving a temporal resolution in the low ns regime, while maintaining magnetic and atomic resolution [10]. Within the present study we use SP-STM to investigate the magnetic ground state dynamics of a single nanomagnet with uniaxial magnetic anisotropy over a wide temperature and switching rate regime. The experimental data are interpreted in terms of an analytical hopping model, thereby providing new insight into the microscopic processes during magnetization reversal. Switching is hindered at low temperature by a high annihilation rate after nucleation, whereas the switching rate is comparable to the nucleation rate at high temperature.

Experimental setup

Our experiments were performed under ultrahigh vacuum conditions with a pressure below 1×10^{-8} Pa using a home-built SP-STM at variable temperatures with coaxial cabling for the sample bias voltage line (bandwidth ≈ 100 MHz). Within our

experimental setup, the entire microscope including the tip is cooled to maximize the thermal stability. In the direct vicinity of the sample, a GaAs/GaAlAs diode is mounted, serving as a temperature sensor. A continuous flow He cryostat with a PID-controlled resistive heater at the cooling finger allows for a precise adjustment of the system temperature T to any set-point between 27 K and 300 K. Bulk Cr tips [11] as well as Fe coated W tips [7] served as magnetic probes. The W(110) substrate was prepared by annealing in oxygen atmosphere and subsequent high temperature flashes [12]. Depositing Fe onto this substrate leads to the pseudomorphic formation of atomic-scale monolayer nanoislands that are found to be ferromagnetic at cryogenic temperatures [4]. They exhibit an in-plane uniaxial magnetic anisotropy with the easy axis of magnetization lying in the $[1\bar{1}0]$ direction [13, 14]. Due to thermal activation, the nanomagnets frequently switch their magnetization between the two ground states **0** and **1**, being in the mean state $1/2$ when integrating over time.

Real-time observations during pump-probe experiments

In the work of Loth *et al.*, the spin relaxation times of Fe-Cu dimers were probed [10]. A magnetic field was used to align the spin of the dimer, and pumping into the excited state was achieved by a voltage pulse via inelastic scattering of tunneling electrons. The relaxation into the ground state was probed by a second voltage pulse which was applied with varying delay time Δt after the pump-pulse. In contrast to the scheme of Loth *et al.*, we measure the transition rate between the two energetically degenerate ground states of an individual nanomagnet, implying that no magnetic field is applied. Moreover, a high tunnel current of spin-polarized electrons is used for pumping.

The basic idea of this spin-transfer torque based pump-probe scheme is illustrated in the following. In Fig. 3.25 (a), the tip-to-sample distance variation $z(t)$ is shown for an individual nanomagnet at closed feedback loop for $I = 1\,\mathrm{nA}$ and $I = 800\,\mathrm{nA}$, respectively. At low I, the nanomagnet is in thermal equilibrium, being in a mean state $1/2$, as can be seen from the upper graph of Fig. 3.25(a). When I is on the order of a few hundred nA, as shown in the lower graph of Fig. 3.25(a), the spin-transfer torque generated by a high spin-polarized tunnel current forces the magnetization of the nanomagnet into one of the two states [3, 5, 15].

In order to record the telegraphic noise during and after the injection of a high spin-polarized tunnel current, a periodic modulated bias voltage U (with period T_p) is applied between the nanomagnet and the magnetic SP-STM tip being held at constant distance. In Fig. 3.25(b), the results of such an experiment are exemplarily shown for $T_\mathrm{p} = 0.7\,\mathrm{s}$. Every cycle starts by setting the bias to $U_\mathrm{high} = 100\,\mathrm{mV}$ for 0.2 s. This generates a short high spin-polarized tunnel current of $I = 850\,\mathrm{nA}$. The pulse is followed by a period of low bias $U_\mathrm{low} = 25\,\mathrm{mV}$ for 0.5 s, resulting in a reduced spin-polarized tunnel current of $I = 250\,\mathrm{nA}$. Within the low-current and high-current sequences, a two-level modulation of the spin-polarized tunnel current is observed on a much smaller scale, reflecting the switching behavior of the nanomagnet. Analyzing the telegraphic noise at low I, the intrinsic mean lifetime τ_tn between two consecutive switching events can directly be determined [4], resulting in $\tau_\mathrm{tn} = (76 \pm 4)\,\mathrm{ms}$ for the given nanomagnet.

In Fig. 3.25(c), $I(t)$ has been averaged to $I_\mathrm{avg}(t)$ over numerous cycles. Here, no telegraphic noise is visible any more. However, an exponential decay is found

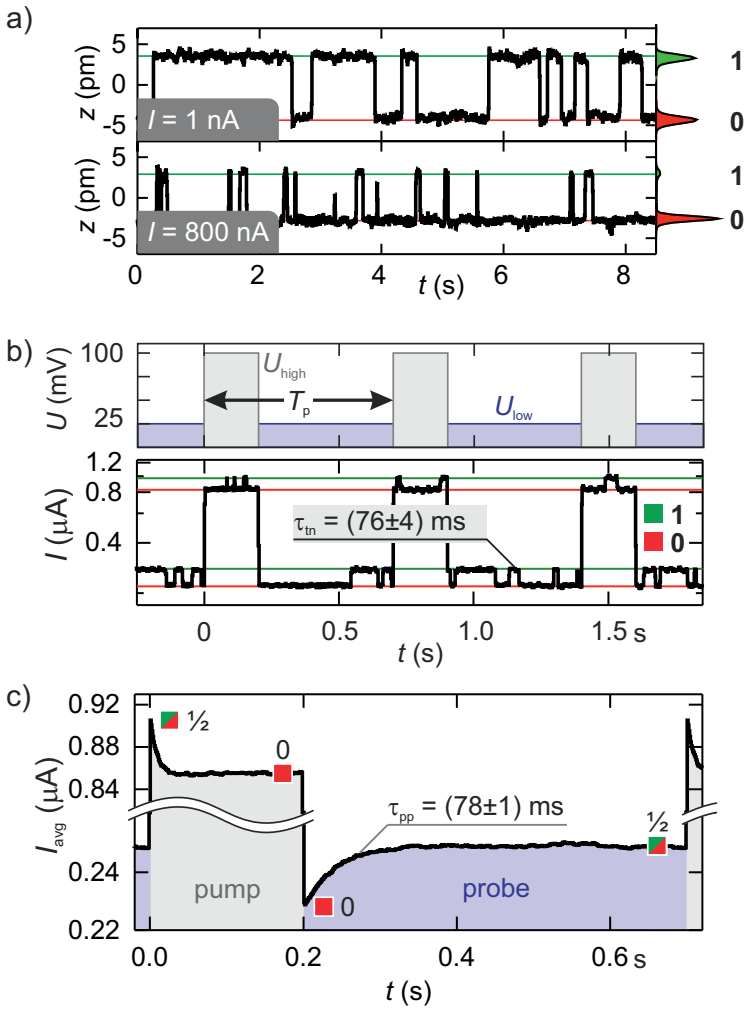

Figure 3.25: (color online) (**a**) Telegraphic noise $z(t)$ on a nanomagnet at low and high I at closed feedback loop, and respective data histograms. ($U = 100\,\mathrm{mV}$, $T = 45\,\mathrm{K}$) (**b**) Top: periodic sequence of high and low tunnel bias. Bottom: Resulting noise I on a thermally switching nanomagnet at constant tip-sample distance. (**c**) Averaged noise signal during one cycle, calculated from $I(t)$ in (b).

in $I_{\mathrm{avg}}(t)$ whenever U is changed. This behavior reflects the alignment and thermal relaxation of the sample magnetization when changing from the low to the high I regime and vice versa in each cycle. At $t = 0$, the nanomagnet is in thermal equilibrium (state $^1/_2$). During the pulse of high I it is driven into the magnetic state **0**, as indicated by the significant decrease of I_{avg} during the pulse. When the pulse ends (at $t = 0.2\,\mathrm{s}$), the nanomagnet thermally relaxes back into the state $^1/_2$, as can be seen from the temporal evolution of I_{avg}. Consequently, the nanomagnet is pumped into one preferred state during the high I pulse, and its relaxation back into its thermal equilibrium state is probed after the pulse at low I. Note that the decay time during pumping is much smaller than for probing, reflecting the higher switching rate of the nanomagnet at high I due to significant Joule heating. As can be shown from solving the rate equations within a model of a simple two-state system reversing its magnetization by surmounting one single activation energy barrier, the characteristic magnetic decay time λ after pumping is given by the intrinsic mean

lifetime τ of the nanomagnet: $\lambda = \tau/2$. From the data in Fig. 3.25(c) a mean lifetime from the pump-probe experiment $\tau_{\mathrm{pp}} = (78 \pm 1)\,\mathrm{ms}$ is found for the relaxation into thermal equilibrium.

Both values, τ_{tn} and τ_{pp}, are in perfect agreement with each other. Consequently, the intrinsic mean lifetime τ can be determined either by real-time telegraph noise experiments (τ_{tn}) or by applying pump-probe schemes (τ_{pp}). In the latter, no real-time observation is necessary, making this method suitable for systems exhibiting magnetic ground state dynamics that cannot be resolved by telegraphic noise experiments.

Pump-probe experiments on fast switching nanomagnets

In our pump-probe experiments on nanomagnets with switching rates that exceed the bandwidth of our TIA, we apply a pump-probe scheme that is schematically depicted in Fig. 3.26(a). Within each pump-probe cyle, a pump pulse forces the nanomagnet out of thermal equilibrium (state 1/2) into one preferred magnetic state, e.g. state **0**. After pumping the nanomagnet stochastically relaxes back into state 1/2. A probe pulse is applied after varying Δt to map the evolution of the magnetic state.

The experimental realization of this pump-probe scheme with SP-STM is depicted in Fig. 3.26(b). Initially, the tip-to-sample distance is adjusted at closed feedback loop. Here, the tunnel current setpoint equals the desired pump pulse amplitude I_{pump}. Once the distance is adjusted, the feedback loop is switched off and U is set to zero. Consecutively, a pump pulse is generated, followed by a probe pulse of low I at a given delay time Δt. This pump-probe cycle is repeatedly applied to the tunnel junction. The short spin-polarized tunnel current pulses are not resolved individually due to the limited bandwidth of the TIA, and the average during the cycle is measured. To isolate the contribution of the probe pulse and to increase the signal-to-noise ratio, a differential measurement is realized. The sequence of pump-probe cycles is followed by a sequence of pump-only cycles in which the probe pulse is left out. The averaged spin-polarized tunnel current is now lower compared to the full pump-probe cycle due to the missing contribution of the probe pulse. Therefore, I is modulated by ΔI at the chopping frequency f_{mod}. Since ΔI is the average spin-polarized tunnel current during the probe pulse, it gives a measure of the alignment between tip and sample magnetization averaged over the (fixed) probe pulse length. The pulse pattern is generated by a two-channel pulse generator (Agilent 81130A or 88150A). The first channel is used to generate the pump pulses, while the second generates the probe pulses that are chopped with f_{mod}. Both channels are added using a signal adder, and the pulse pattern is fed to the sample via a remote-controlled RF switch. The resulting modulation of I is measured by a lock-in amplifier.

To map the evolution of the magnetic state after pumping, the experiment is repeated for different Δt. From $\Delta I(\Delta t)$, the characteristic magnetic decay time λ can be extracted by fitting an exponential.

An exemplary pump-probe measurement on a nanomagnet is shown in Fig. 3.26(c). Pump and probe spin-polarized tunnel current pulses were injected into the nanomagnet, and the variation in I was recorded as a function of Δt. The results for $\Delta I(\Delta t)$ show a characteristic triangular-shape feature when pump and

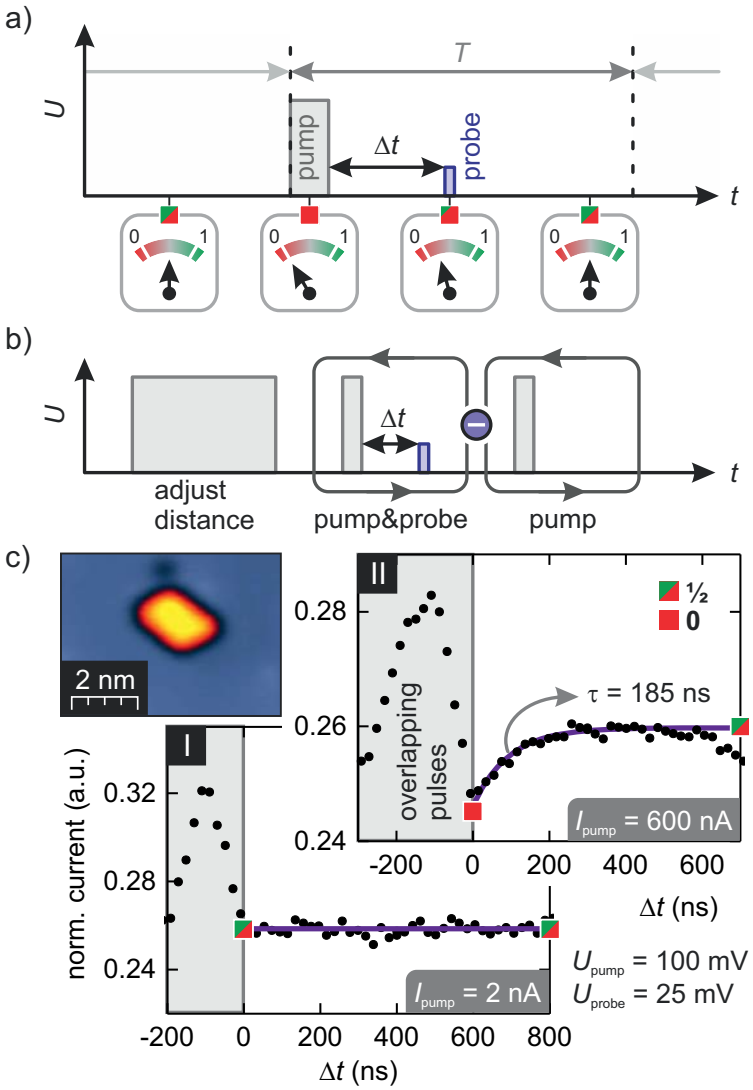

Figure 3.26: (color online) (**a**) Basic idea of the spin-transfer torque driven pump-probe scheme. (**b**) Experimental realization of the pump-probe scheme with SP-STM (see text for details). **(c)** Pump-probe experiment on a nanomagnet (inset: topography). (I) Low pumping current I_{pump}: No relaxation is observed. (II): High I_{pump}: A relaxation into thermal equilibrium is observed. Fitting the data yields the mean lifetime τ. ($T = 42\,\mathrm{K}$).

probe pulses overlap, resulting from the non-linearity in the $I(U)$ curve of the tunnel junction [8, 10]. For $\Delta t > 0$, the pulses do not overlap, and ΔI is given by the average current during the probe pulse. In Fig. 3.26(c) I, the spin-polarized pump pulse amplitude is set to $I_{\mathrm{pump}} = 2\,\mathrm{nA}$. A flat line is observed for $\Delta t > 0$, indicating the nanomagnet being in the mean state $1/2$ throughout the experiment. Hence, the nanomagnet has not been affected by the pump pulse and remains in thermal equilibrium. In Fig. 3.26(c) II, I_{pump} was increased by a factor of 300 with respect to the situation in I. Now an exponential decay is observed after the pump pulse. The combined action of spin-transfer torque and Joule heating during the pump pulse forces the nanomagnet into the state **0**, and it decays back into thermal equilibrium (mean state $1/2$) for $\Delta t > 0$. Fitting the data with an exponential reveals $\tau = 185\,\mathrm{ns}$. In this experiment I during the probe pulse is sufficiently high that pumping into

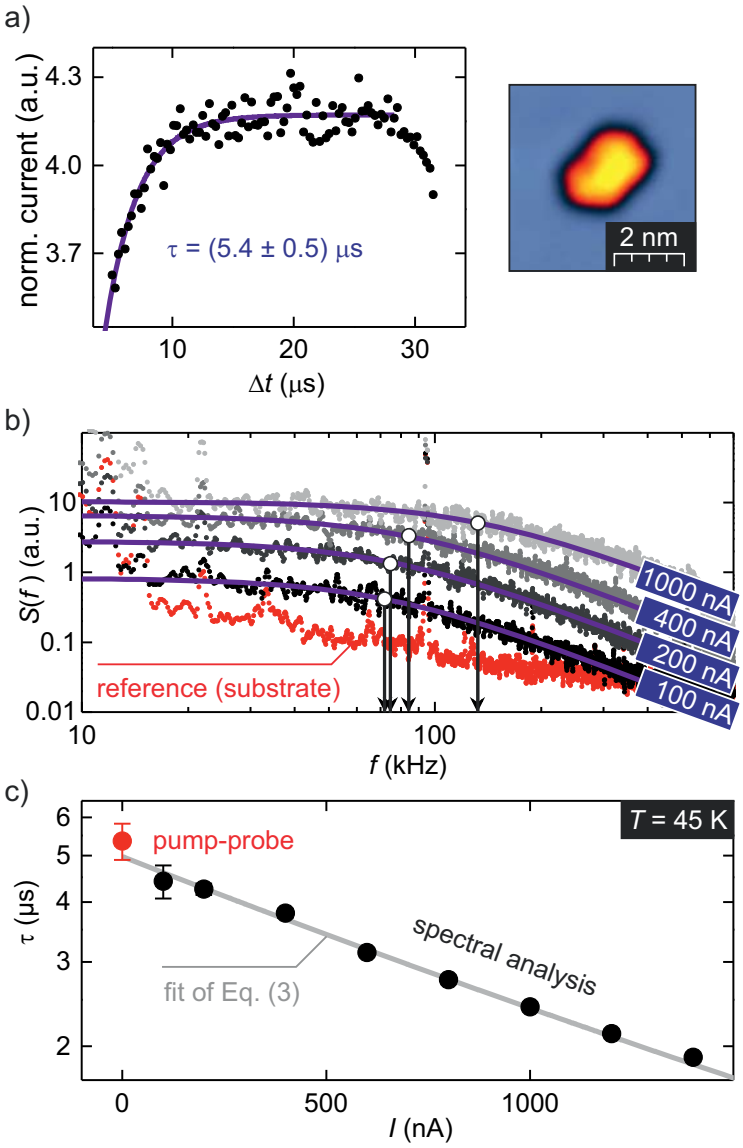

Figure 3.27: (color online) (**a**) Pump-probe measurement on the island shown in the inset, $T = 45\,\mathrm{K}$. (**b**) Power spectral density measured as a function of tunnel current ($U = 100\,\mathrm{mV}$). (**c**) Comparison between results obtained using the pump-probe and the power spectral measurement. A fit is used to extrapolate the spectral analysis to $I = 0$.

state **0** cannot be neglected, resulting in the decrease of ΔI for $\Delta t > 600\,\mathrm{ns}$. In this regime, the excitation is probed by the pump pulse that is applied shortly following the probe pulse.

Quantitative validation of the experiments

A direct comparison between pump-probe experiments and real-time telegraphic noise observation for the validation of the experimental findings is not possible as the latter technique can only be used for lifetimes larger than a few milliseconds. The identification of individual switching events of shorter lifetimes is mainly hindered by mechanical noise in the kHz regime (e.g. the resonance frequencies of the scanner) overlaying the telegraphic signal. However, the mean lifetime τ between two

consecutive switching events of a random telegraph signal can be determined in frequency space. To obtain the lifetime using spectral analysis, we measure the power spectral density $S(f)$ of I using a HP 89410A spectral analyzer. For a symmetric random telegraph signal $S(f)$ is given by [16]:

$$S(f) \propto \frac{1}{1+\left(\frac{f}{f_\mathrm{c}}\right)^2}. \tag{3.10}$$

Consequently, $S(f)$ is constant for frequencies f much smaller than the characteristic frequency f_c and decays with f^{-2} for $f \gg f_\mathrm{c}$. The characteristic frequency is related to τ by

$$f_\mathrm{c} = \frac{1}{\pi\tau}. \tag{3.11}$$

To compare the two methods we choose a superparamagnetic nanoisland that is expected to have a lifetime of a few μs at the measurement temperature of $T = 45\,\mathrm{K}$, so that both the spectral analysis and the pump-probe method are applicable. Figure 3.27(a) shows a pump-probe experiment performed on the nanomagnet. Its topography is shown in the inset. From the data, an exponential decay of the normalized tunnel current is observed as a function of Δt. Fitting yields a mean lifetime of $\tau_\mathrm{pp} = (5.4 \pm 0.5)\,\mu\mathrm{s}$.

To measure such a short lifetime with the spectral measurement, a bandwidth of the TIA on the order of 500 kHz is needed. In the present setup, this bandwidth can be achieved when the gain of the TIA is reduced to $10^4\,\mathrm{V/A}$. However, due to the small gain, the tunnel current has to be increased to a few hundred nA to achieve a reasonable signal-to-noise ratio. Consequently, current-induced effects are expected not to be negligible. Current dependent spectral measurements are shown in Fig. 3.27(b). Compared to the reference spectrum that was taken with the tip positioned above the substrate ($I = 200\,\mathrm{nA}$), a significantly higher $S(f)$ is obtained when the tip is positioned above the nanomagnet. The increase on the island is caused by its thermal magnetization switching, as can be concluded from the characteristic $S(f)$ shape (rf. Eq. 3.10). Below 15 kHz considerable noise is found, which is attributed to mechanical vibrations inside the STM. The strong peak at 90 kHz is caused by electrical noise, probably from a power supply.

Fitting the experimental data with Eq. 3.10, the characteristic frequency $f_c(I)$ is obtained. The fits and corresponding $f_c(I)$ are indicated in Fig. 3.27(b). The mean lifetime $\tau(I)$ was calculated from $f_c(I)$ according to Eq. 3.11. They are shown in Fig. 3.27(c). Obviously, τ decreases with increasing tunnel current. Joule heating is not negligible for the tunnel currents used in this experiment, which thus significantly shortens the mean lifetime. Additionally, the switching behavior of the nanomagnet at high I is expected to be asymmetric due to the spin-transfer torque of the tunneling electrons. However, this effect only slightly affects the mean lifetime $\tau(I)$. Using a Néel-Brown model, the lifetimes were fitted, taking into account Joule heating that is linear in I [5] and omitting the influence of the spin transfer torque:

$$\tau(I) = \nu_0^{-1} \exp\left(\frac{E_b}{k_\mathrm{B}(T + c_T I)}\right), \tag{3.12}$$

with E_b being the effective activation energy barrier, ν_0 is the effective attempt frequency, k_B is the Boltzmann factor, and c_T is a constant that reflects the effective

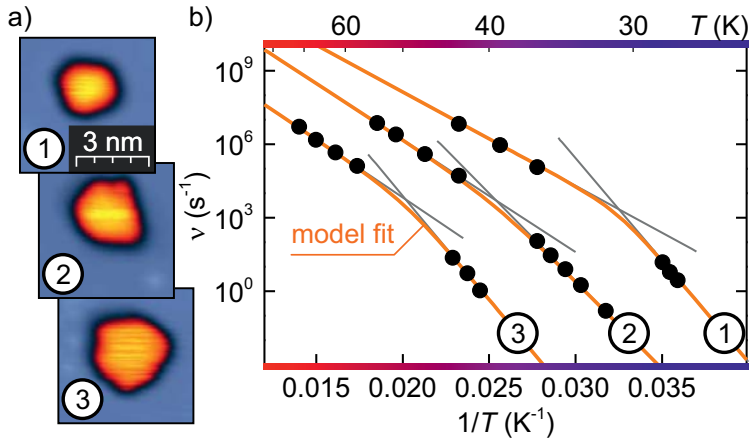

Figure 3.28: (color online) (**a**) The nanomagnets under investigations. (**b**) T dependent switching rates of each nanomagnet. A crossover between two Arrhenius regimes is observed. Orange: four-state hopping model fit.

differential heating of the nanomagnet (in K/nA). The fit is used to extrapolate to $I = 0$, yielding an intrinsic mean lifetime of $(5.0 \pm 0.2)\,\mu$s. Within the error bars, this is in very good agreement with the finding of the pump-probe method.

The Arrhenius behavior of the lifetimes as function of temperature and the perfect agreement between the two experimental methods show that the pump-probe scheme yields reliable results that are quantitatively comparable to results obtained with conventional methods. Consequently, combining pump-probe SP-STM experiments and real-time observation enables the determination of lifetimes ranging from hours to nanoseconds and thereby allows to study the lifetime of an individual nanomagnet over a wide temperature range.

Experimental results

Such experiments were performed for three different nanomagnets shown in Fig. 3.28(a). For each nanomagnet τ has been determined via real-time telegraphic noise observations in the low switching rate regime ($\tau > 10^{-2}$ s) and pump-probe experiments for high switching rates ($\tau < 10^{-4}$ s). For $10^{-4}\,\text{s} < \tau < 10^{-2}$ s the determination of τ is hindered due to the low signal-to-noise ratio of the system in this frequency band. In Fig. 3.28(b), the respective T dependent switching rates $\nu = \tau^{-1}$ are shown in an Arrhenius plot for all three nanomagnets. As can be seen from the data, each of the nanomagnets shows a characteristic switching behavior, with the data points lying on two crossing straight lines. In the Arrhenius plot, the slope of the lines corresponds to the effective activation energy barrier E_b for magnetization reversal. From the data it is obvious that E_b of every nanomagnet is constant within the low and the high T range, respectively, and undergoes a transition within a T window of about 10 K. Moreover, ν at high T is generally found to be by orders of magnitude lower than expected from extrapolating the Arrhenius behavior at low T.

It is known that material parameters like magnetic exchange and anisotropy can change with T. A smooth deviation from the Arrhenius behavior can be expected in this case, but not a sharp transition within a window of a few Kelvin, as observed in

our experiments. A sudden change of magnetic exchange or anisotropy with drastic consequences for the magnetic properties with increasing T is unlikely. Moreover, no significant variations in the magnetic properties of a closed monolayer film of Fe/W(110) have been observed in a much broader T window [13], so we exclude T dependent material parameters to be the origin of the experimental findings. In a theoretical investigation using Monte-Carlo calculations, a transition from a one-droplet to a multi-droplet nucleation was observed with increasing T, resulting in two distinct Arrhenius regimes [17]. In the situation of multi-droplet nucleation, a second domain wall is created before the first domain wall is annihilated. Both domain walls can interact with each other, thereby changing the Arrhenius switching behavior. In our experiments, the characteristic time scale of the transition between the two Arrhenius regimes is on the order of milliseconds. Consequently, one domain wall has to be trapped inside the island for about a millisecond before it can interact with the second domain wall. To our opinion this is unlikely since the microscopic processes are known to happen on a much faster timescale of pico- or even femtoseconds [18]. Within the original model for the coherent rotation of all magnetic moments, a $\sqrt{T}$ temperature dependence of the attempt frequency is predicted [19, 20]. This T dependence is omitted in most studies, as it usually changes insignificantly compared to the exponential term. When the T dependence is taken into account, the lifetimes at higher temperature are increased compared to the case where the temperature dependence is neglected, which is in qualitative agreement with our experimental findings. We included the temperature dependence and fitted the model to our data. It turned out that the fit with or without the temperature dependence gives almost the same results. Consequently, even when taking into account the temperature dependent attempt frequency, the model of a single activation energy barrier cannot be used to describe our observations. In summary, none of these theoretical approaches correctly describes our experimental findings.

4-state hopping model

Based on simple arguments, we developed an analytical four-state hopping model that accounts for all the microscopic processes that are involved in the magnetization reversal: nucleation, annihilation and propagation. Its scheme is depicted in Fig. 3.29(a). In the model, the nanomagnet can be found at any time in one of four magnetic states **0**, **01**, **10** and **1** with probabilities P_0, P_1, P_{01} and P_{10}, respectively. Here, **0** and **1** are the two monodomain ground states. **01** and **10** are metastable states where the magnetization within a nucleus volume is reversed with respect to the rest of the nanomagnet. Nucleation, annihilation and propagation is modelled by hopping between the states at intrinsic rates ν_n, ν_a and ν_p, respectively. They follow Arrhenius laws:

$$\nu_i = \nu_{0,i} \exp\left(-\frac{E_i}{k_\mathrm{B}T}\right) \qquad i = \mathrm{n}, \mathrm{a}, \mathrm{p}. \tag{3.13}$$

Here, $\nu_{0,\mathrm{n}}, \nu_{0,\mathrm{p}}, \nu_{0,\mathrm{a}}, E_\mathrm{n}, E_\mathrm{p}$ and E_n are the effective attempt frequencies and activation energy barriers. The potential landscape for the magnetization reversal within our hopping model is shown in Fig. 3.29(b). It is known that the magnetocrystalline anisotropy can be drastically higher at the rim of a nanomagnet due to the reduced

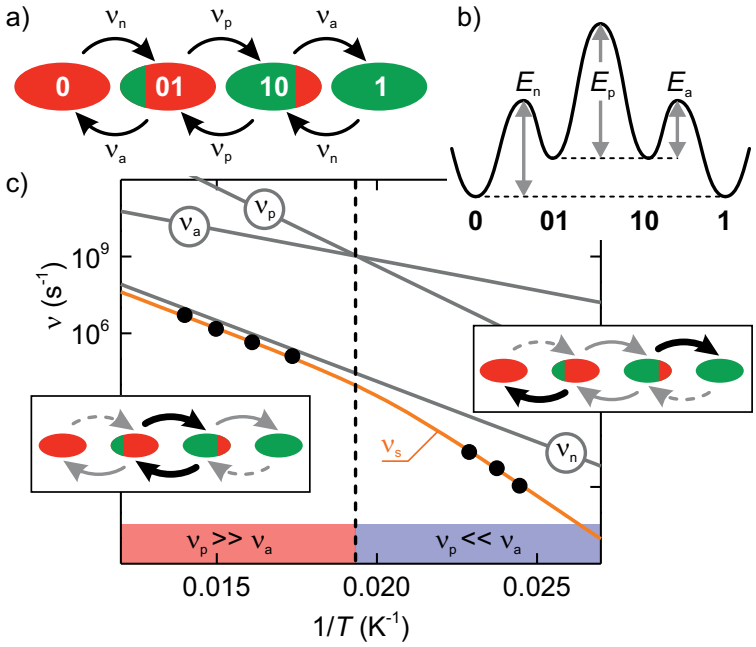

Figure 3.29: (color online) **(a)** Schematics and **(b)** energy landscape of the four-state hopping model. **(c)** Experimental data for nanomagnet "3", fitted by the hopping model (orange), and respective rates ν_n, ν_a and ν_p. Insets: Dominating hopping paths (thick arrows) at low and high T, respectively.

coordination of the rim atoms [21]. This hinders the formation as well as the annihilation of a nucleus. Hence, in our model the effective activation energy barriers E_n for nucleation and E_a for annihilation are introduced. The domain wall propagation inside the nanomagnet is a very complex process. We implement an effective activation barrier E_p and attempt frequency $\nu_{0,\mathrm{p}}$ in our model to mimic the microscopic details of the domain wall propagation between nucleation and annihilation. Magnetization reversal is triggered by nucleation, implying that $\nu_\mathrm{n} \ll \nu_\mathrm{a}$ and $\nu_\mathrm{n} \ll \nu_\mathrm{p}$. We calculate the effective switching rate ν_s between the two ground states **0** and **1** by solving the rate equations, yielding

$$\nu_\mathrm{s} = \left(2 + \frac{\nu_\mathrm{a}}{\nu_\mathrm{p}}\right)^{-1} \nu_\mathrm{n}. \tag{3.14}$$

Hence, ν_s is given by ν_n reduced by a factor that depends on the ratio $\nu_\mathrm{a}/\nu_\mathrm{p}$. We find the asymptotic limits for low and high T:

$$\text{low } T: \quad \nu_\mathrm{s}^\mathrm{low} = \nu_0^\mathrm{low} \exp\left(-\frac{E^\mathrm{low}}{k_\mathrm{B}T}\right) \tag{3.15}$$

$$\text{high } T: \quad \nu_\mathrm{s}^\mathrm{high} = \frac{1}{2}\nu_\mathrm{n} \tag{3.16}$$

Here, $E^\mathrm{low} = E_\mathrm{n} - E_\mathrm{a} + E_\mathrm{p} = E_\mathrm{act}$ is the overall activation energy barrier for magnetization reversal, and $\nu_0^\mathrm{low} = \frac{\nu_{0,\mathrm{n}}\nu_{0,\mathrm{p}}}{\nu_{0,\mathrm{a}}}$ is the effective attempt frequency at low T. A distinct Arrhenius behavior is found for each T regime, in perfect agreement with our experimental results. The experiments in Ref. [4] have been performed in the low T regime and therefore address the magnetization reversal over an effective

			①	②	③
E^{low}	$= E_{\mathrm{act}}$	(meV)	165	142	168
E^{high}	$= E_{\mathrm{n}}$	(meV)	76	91	94
ν_0^{low}	$= \frac{\nu_{0,\mathrm{n}}\nu_{0,\mathrm{p}}}{\nu_{0,\mathrm{a}}}$	(s^{-1})	2.4×10^{30}	7.7×10^{21}	6.7×10^{20}
$2\nu_0^{\mathrm{high}}$	$= \nu_{0,\mathrm{n}}$	(s^{-1})	1.3×10^{16}	4.6×10^{15}	4.0×10^{13}

Table 3.1: Results of fitting the four-state hopping model to the experimentally obtained data for each nanomagnet.

activation barrier given by E_{act}. Note that the parameters E_{p}, E_{a}, $\nu_{0,\mathrm{p}}$ and $\nu_{0,\mathrm{a}}$ cannot explicitly be determined from the experiments in the low T regime, because the effective switching rate results from the complex interplay between nucleation, annihilation and propagation. In our model, $\nu_{\mathrm{s}}^{\mathrm{high}}$ directly reflects the nucleation rate of the nanomagnet, implying that the effective attempt frequency and activation energy barrier for nucleation can directly be determined experimentally from the Arrhenius behavior in the high T regime.

Fitting the experimental data

Using the model, the experimentally obtained $\nu(T)$ for each nanomagnet are fitted. The resulting fit parameters are summarized in Tab. 3.1, and the model fit curves are added to Fig. 3.27(b). The data for the nanomagnets ② and ③ in the low T regime are in perfect agreement with the results of Ref. [4] in terms of activation energy barrier and attempt frequency, whereas nanomagnet ① deviates. In the high T regime, E_{n} and $\nu_{0,\mathrm{n}}$ are determined from the model. For all three nanomagnets, the nucleation process can be described by an effective activation energy barrier between 75 meV and 95 meV, and the respective attempt frequency for nucleation varies between $10^{13}\,\mathrm{s}^{-1}$ and $10^{16}\,\mathrm{s}^{-1}$.

To illustrate the model interpretation of the experimental findings, the fit results for the nanomagnet ③ are shown in Fig. 3.29(c). For exemplification, the open parameters are set to $\nu_{0,\mathrm{a}} = \nu_{0,\mathrm{n}}$ and $E_{\mathrm{a}} = E_{\mathrm{n}}/2$. At high T, $\nu_{\mathrm{p}} \gg \nu_{\mathrm{a}}$, implying that a nucleation event is immediately followed by the propagation of a domain wall. Annihilation is hindered, so the domain wall undergoes numerous backscattering events. Because of this annihilation site uncertainty, $\nu_{\mathrm{s}} = \nu_{\mathrm{n}}/2$. At low T, $\nu_{\mathrm{p}} \ll \nu_{\mathrm{a}}$. Propagation is hindered, and the nucleus is very likely to annihilate at its nucleation site. Only in very rare events, the domain wall can propagate through the nanomagnet, finally resulting in a magnetization reversal. Consequently, $\nu_{\mathrm{s}} \ll \nu_{\mathrm{n}}$, but again follows an Arrhenius law, as can be seen from Fig. 3.29(c).

Summary

In summary, we investigated the magnetization dynamics of individual nanomagnets over a wide temperature and switching rate range using SP-STM telegraphic noise experiments and applying pump-probe schemes. The finite and distinct effective activation energy barriers and attempt frequencies for the microscopic processes involved in the magnetization reversal are found to have drastic consequences for the T dependent switching behavior of atomic-scale magnets. Our study reveals that the switching behavior does not follow one single Arrhenius law. Instead, a

transition between two Arrhenius regimes is observed with increasing T, and the switching rate at high T is found to be orders of magnitude smaller than expected from an extrapolation from the low T regime. An analytical four-state hopping model is developed to interpret the experimental results, indicating that ν at high T reflects the nucleation rate, whereas ν at low T results from the complex interplay between nucleation, annihilation and propagation which drastically reduces the effective switching rate of the nanomagnets compared to the nucleation rate.

References

[1] W. Wernsdorfer, B. Doudin, D. Mailly, K. Hasselbach, A. Benoit, J. Meier, J.-P. Ansermet, and B. Barbara, Phys. Rev. Lett. **77**, 1873 (1996).

[2] S. S. P. Parkin, M. Hayashi, and L. Thomas, Science **320**, 190 (2008).

[3] S. Krause, L. Berbil-Bautista, G. Herzog, M. Bode, and R. Wiesendanger, Science **317**, 1537 (2007).

[4] S. Krause, G. Herzog, T. Stapelfeldt, L. Berbil-Bautista, M. Bode, E. Y. Vedmedenko, and R. Wiesendanger, Phys. Rev. Lett. **103**, 127202 (2009).

[5] S. Krause, G. Herzog, A. Schlenhoff, A. Sonntag, and R. Wiesendanger, Phys. Rev. Lett. **107**, 186601 (2011).

[6] R. Wiesendanger, H. J. Güntherodt, G. Güntherodt, R. J. Gambino, and R. Ruf, Phys. Rev. Lett. **65**, 247 (1990).

[7] R. Wiesendanger, Rev. Mod. Phys. **81**, 1495 (2009).

[8] G. Nunes and M. R. Freeman, Science **262**, 1029 (1993).

[9] O. Takeuchi, M. Aoyama, R. Oshima, Y. Okada, H. Oigawa, N. Sano, H. Shigekawa, R. Morita, and M. Yamashita, Appl. Phys. Lett. **85**, 3268 (2004).

[10] S. Loth, M. Etzkorn, C. P. Lutz, D. M. Eigler, and A. J. Heinrich, Science **329**, 1628 (2010).

[11] A. Schlenhoff, S. Krause, G. Herzog, and R. Wiesendanger, Appl. Phys. Lett. **97**, 083104 (2010).

[12] M. Bode, S. Krause, L. Berbil-Bautista, S. Heinze, and R. Wiesendanger, Surf. Sci. **601**, 3308 (2007).

[13] U. Gradmann, G. Liu, H. J. Elmers, and M. Przybylski, Hyperfine Interact. **57**, 1845 (1990).

[14] H. J. Elmers, J. Hauschild, H. Höche, U. Gradmann, H. Bethge, D. Heuer, and U. Köhler, Phys. Rev. Lett. **73**, 898 (1994).

[15] G. Herzog, S. Krause and R. Wiesendanger, Appl. Phys. Lett. **96**, 102505 (2010).

[16] M. J. Kirton and M. J. Uren, Adv. Phys. **38**, 367 (1989).

[17] U. Nowak and D. Hinzke, J. Appl. Phys. **85**, 4337 (1999).

[18] H. Stoll, M. Noske, M. Weigand, K. Richter, B. Krüger, R. M. Reeve, M. Hänze, C. F. Adolf, F.-U. Stein, and G. Meier, Frontiers in Physics **3**, 26 (2015).

[19] M. L. Néel, Ann. Géophys. **5**, 99 (1949).

[20] W. F. Brown, Phys. Rev. **130**, 1677 (1963).

[21] P. Gambardella, A. Dallmeyer, K. Maiti, M. C. Malagoli, W. Eberhardt, K. Kern, and C. Carbone, Nature **416**, 301 (2002).

3.6 Topological insulators and graphene

J. Wiebe and R. Wiesendanger

Topological insulators (TIs) feature metallic surface states with a helical spin structure on the surface of a semiconducting bulk material. They are therefore regarded as possible candidates for spintronics applications. The unique property of the topological surface states is topological protection, which means that the topological surface states cannot be destroyed by perturbations that do not break time reversal symmetry [1]. It is often argued that this protection is caused by the spin structure which suppresses backscattering events as this requires a spin flip which is not possible for non-magnetic scattering centers. While this explanation is certainly valid for case of the one-dimensional edge states of ideal two-dimensional TIs, for the two-dimensional surface states of real three-dimensional TI materials, additional effects need to be investigated in view of potential applications: As a matter of small angle scattering, there is additional phase-space available which might disturb the protection. The energetic overlap of the topological surface state with bulk bands due to doping effects can introduce interband scattering of the topological surface state into the bulk bands.

Additionally, introducing magnetic impurities to the surface of TIs promises interesting effects both from an application and from the fundamental physics point of view. A band gap opening at the Dirac point of the topological surface state which is theoretically expected for a magnetic exchange field of a particular orientation could introduce mass to the topological surface state electrons and, moreover, should enable to realize the quantum anomalous Hall effect.

Within this triannual research period, we investigated the morphology, electronic and magnetic properties of different TI materials and of Bi-intercalated graphene by a combination of STM based methods, angle-resolved photoelectron spectroscopy (ARPES), x-ray magnetic circular dichroism (XMCD) measurements, and comparison to $ab-initio$ density functional theory (DFT) based calculations, as described in the following.

3.6.1 Electron scattering in a bismuth bilayer on Bi_2Se_3

A. Eich, M. Michiardi, G. Bihlmayer, X.-G. Zhu, J.-L. Mi, Bo B. Iversen, R. Wiesendanger, Ph. Hofmann, A. A. Khajetoorians, and J. Wiebe

The band structure and intra- and interband scattering processes of the electrons at the surface of a bismuth bilayer on Bi_2Se_3 have been experimentally investigated by low-temperature Fourier-transform scanning tunneling spectroscopy [2]. The observed complex quasiparticle interference patterns shown in Fig.3.30(a,b,c) were compared to a simulation based on the spin-dependent joint density of states approach using the surface-localized spectral function calculated from first principles and fitting to the ARPES band structure as the only input Fig. 3.30(d). Thereby, the origin of the quasiparticle interferences was traced back to intraband scattering in the bismuth-bilayer valence band and Bi_2Se_3 conduction band and to interband scattering between the two-dimensional topological state and the bismuth-bilayer va-

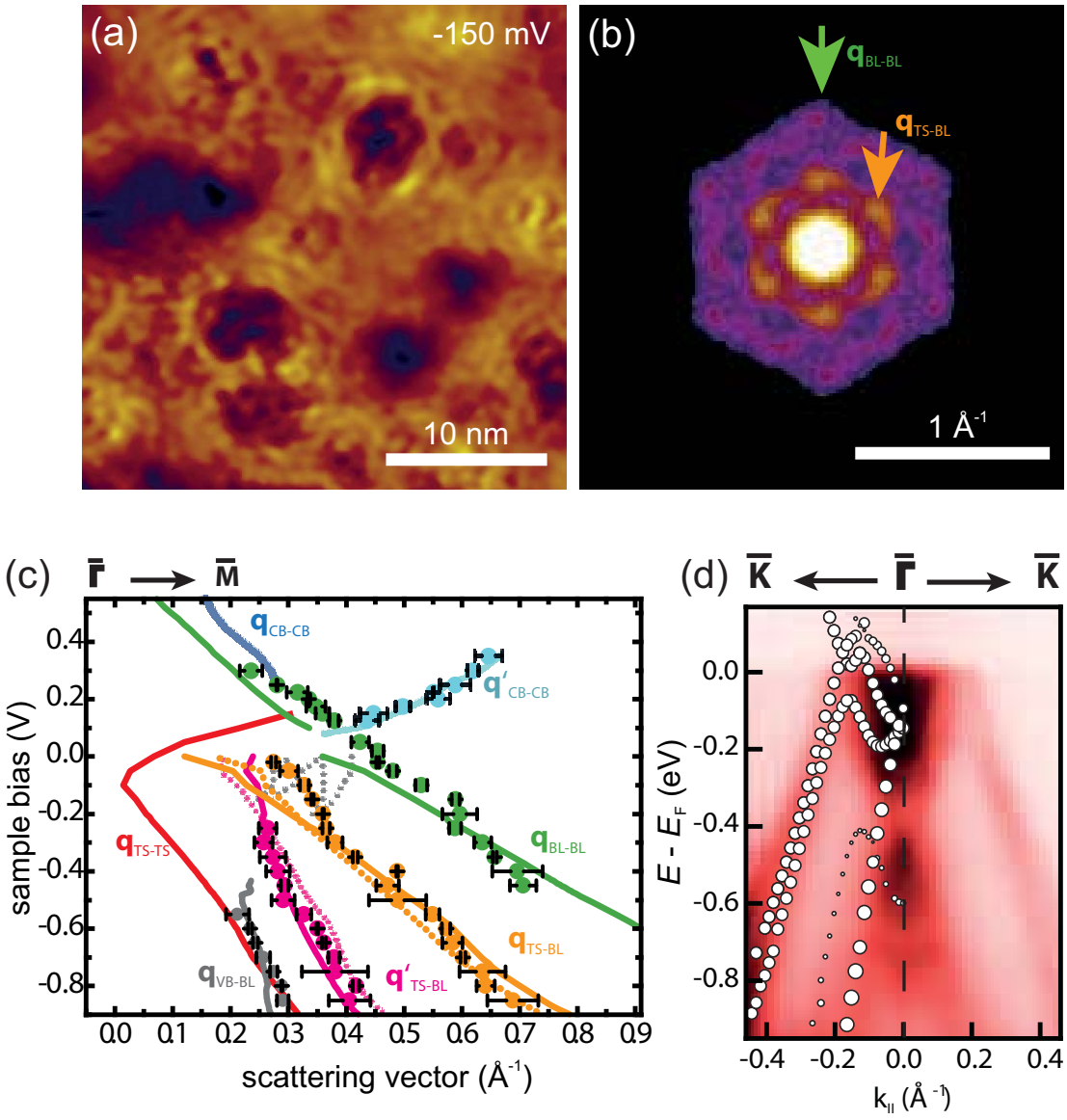

Figure 3.30: Intra- and interband scattering of the two-dimensional topological surface state of the hybrid topological insulator Bi bilayer (BL) on Bi_2Se_3 [2]. (a) STS image and (b) FT-STS image of the quasiparticle interference patterns taken at the indicated bias voltage. The arrows in (b) indicate the hexagonal features stemming from intraband scattering in the Bi-BL valence band (q_{BL-BL}) and interband scattering between BL valence band and topological surface state (q_{TS-BL}). The energy-dependent determination of all such scattering vectors shown by dots in (c) fits nicely to the simulated scattering vectors (solid lines) determined from ARPES (d) together with the *ab-initio* calculated band structure (dots,d).

lence band. The investigation revealed that the bilayer band gap, which is predicted to host one-dimensional topological states at the edges of the bilayer, is pushed several hundred meV above the Fermi level. This result was rationalized by an electron transfer from the bilayer to Bi_2Se_3 which also leads to a two-dimensional electron state in the Bi_2Se_3 conduction band with a strong Rashba spin splitting, coexisting with the topological state and the bilayer valence band.

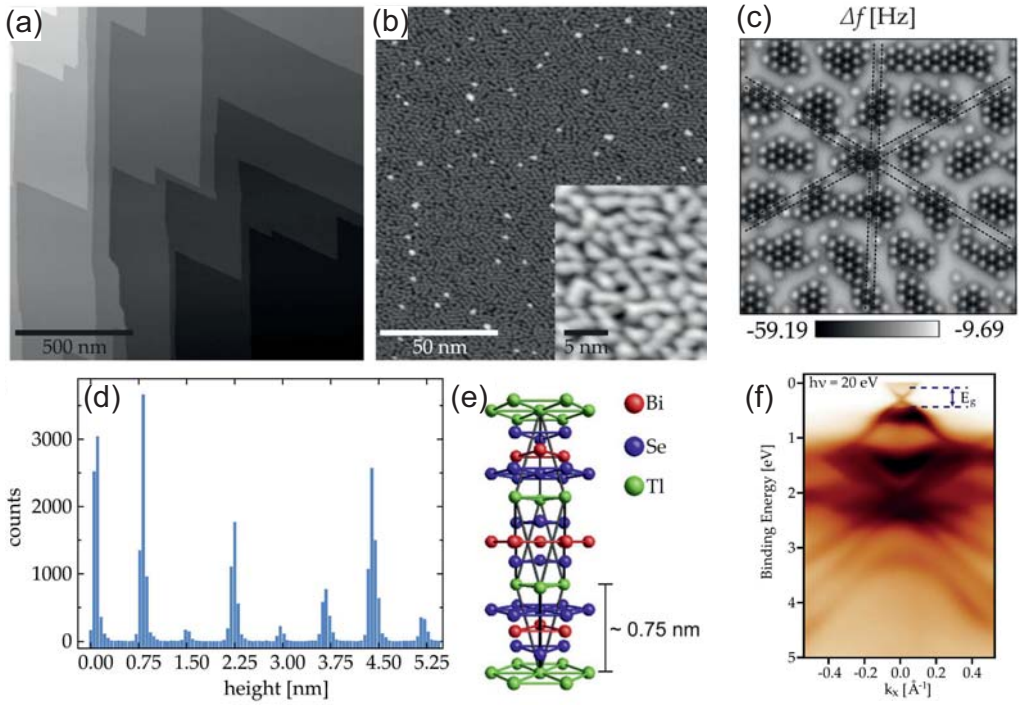

Figure 3.31: Investigation of the surface morphology and electronic structure of cleaved $TlBiSe_2$ [1]. (a) Large scale STM image and (b) zoom on one of the terraces of the cleaved surface of $TlBiSe_2$. (c) Constant height mode frequency shift image (AFM) of a similar area as in the inset of (b) showing atomic resolution in the irregular islands. (d) Histogram of step height distribution in (a). The peaks are all spaced by multiples of the Tl–Tl distance of about 0.75 nm. (d) Crystal structure model of $TlBiSe_2$. (f) ARPES band map of cleaved $TlBiSe_2$ along the $\Gamma - M$ direction measured at the indicated photon energy. The dashed blue lines indicate the bulk band gap E_g with the topological surface state.

3.6.2 Effect of surface disorder on the topological surface state

F. Pielmeier, G. Landolt, B. Slomski, S. Muff, J. Berwanger, A. Eich, A. A. Khajetoorians, J. Wiebe, Z. S. Aliev, M. B. Babanly, R. Wiesendanger, J. Osterwalder, E. V. Chulkov, F. J. Giessibl, and J. H. Dil

Through a combination of experimental techniques [1] we have shown that the topmost layer of the topological insulator $TlBiSe_2$ as prepared by cleavage (Fig.3.31(a,d)) is formed by irregularly shaped Tl islands at cryogenic temperatures (Fig.3.31(b,c)) and by mobile Tl atoms at room temperature. With APRES at low temperatures no trivial surface states are observed (Fig.3.31(f)), which suggests that these islands cannot be regarded as a clear surface termination. The topological surface state is, however, clearly resolved in photoemission experiments (Fig.3.31(f)). This is interpreted as direct evidence of its topological self-protection, i.e. that the topological surface state is pushed from the surface layers further into the bulk (Fig.3.31(e)), which shows the robust nature of the Dirac cone-like surface state to strong surface perturbations.

3.6.3 Topological insulator homojunctions

M. Vališka, J. Warmuth, M. Michiardi, M. Vondráček, A. S. Ngankeu, V. Holý, V. Sechovský, G. Springholz, M. Bianchi, J. Wiebe, P. Hofmann, and J. Honolka

Homojunctions between Bi_2Se_3 and its magnetically (Mn)-doped phase were investigated as an optimally suited sample geometry to study the influence of spin degrees of freedom on TI properties [3]. n quintuple layers of Bi_2Se_3 were grown on top of Mn-doped Bi_2Se_3 by molecular beam epitaxy for $0 \leq n \leq 30$ quintuple layers (Fig.3.32(a)-(c)). This enabled us to unhamperedly monitor the development of the electronic and topological properties by the surface sensitive technique ARPES (Fig.3.32(d)-(g)). With increasing n, a Mn induced gap at the Dirac point (E_{DP}) is gradually filled in an "hourglass" fashion to reestablish a topological surface state at $n \approx 9$ quintuple layers. Our results suggest a competition of upward and downward band bending effects due to the presence of an $n-p$ type interface, which can be used to tailor topological and quantum well states independently.

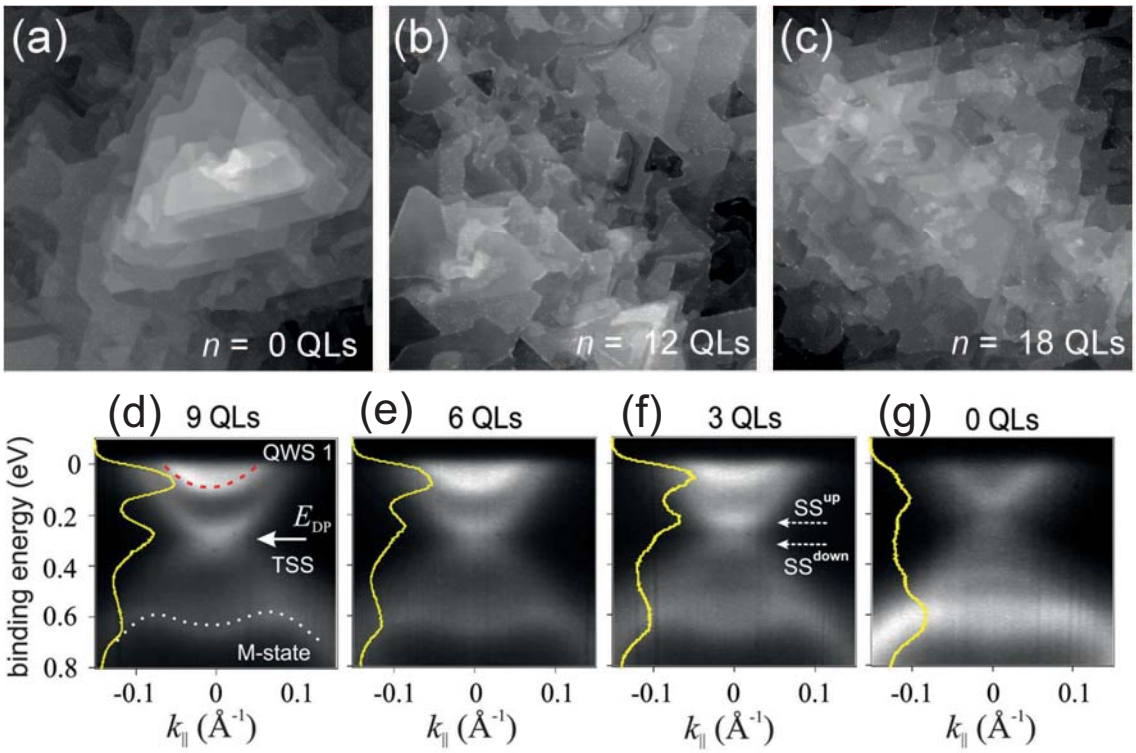

Figure 3.32: Electronic structure of n quintuple layers of Bi_2Se_3 grown on Mn-doped Bi_2Se_3 [3]. (a)–(c) AFM topography (image size $3\mu\mathrm{m} \times 3\mu\mathrm{m}$) of the terraced surfaces of the heterostructures for different n as indicated. ARPES data of heterostructures with the indicated numbers n of quintuple layers along the $\mathrm{M}-\Gamma-\mathrm{M}$ direction. Overlaid are energy distribution curves derived from the k-interval $[-0.01\text{Å}^{-1}, 0.01\text{Å}^{-1}]$ at respective binding energies.

3.6.4 Magnetic adatoms on topological insulators

M. Vondráček, L. Cornils, J. Minár, J. Warmuth, M. Michiardi, C. Piamonteze, L. Barreto, J. A. Miwa, M. Bianchi, Ph. Hofmann, L. Zhou, A. Kamlapure, A. A. Khajetoorians, R. Wiesendanger, J.-L. Mi, B.-B. Iversen, S. Mankovsky, St. Borek, H. Ebert, M. Schüler, T. Wehling, J. Wiebe, and J. Honolka

We investigated the magnetic and electronic properties of Ni and Fe adatoms on the TIs Bi_2Te_3 and Bi_2Te_2Se by a combination of STM (Fig.3.33(a)), ARPES (Fig.3.33(b)-(e)), XMCD measurements (Fig.3.33(f),(g)) and DFT calculations (Fig.3.33(f),(g)) [4]. We revealed a quenching of the magnetic moments of single Ni adatoms adsorbed at the surface of both TIs. The effect is noted as a missing XMCD signal for resonant $L_{3,2}$ transitions (Fig.3.33(f)) into partially filled Ni $3d$ states of theory-derived occupancy $n_d = 9.2$. On the basis of a comparative study of Ni and Fe using scanning tunneling microscopy and DFT calculations, we were able to relate the element specific moment formation to a local Stoner criterion. Our theory shows that while Fe adatoms form large spin moments of $m_s = 2.54\mu_B$ with out-of-plane anisotropy due to a sufficiently large density of states at the Fermi energy, Ni remains well below an effective Stoner threshold for local moment formation. With the Fermi level remaining in the bulk band gap after adatom deposition, as revealed by ARPES (Fig.3.33(b)-(e)), nonmagnetic Ni and preferentially out-of-plane oriented magnetic Fe with similar structural properties on Bi_2Te_3 surfaces constitute a perfect platform to study the off-on effects of time-reversal symmetry breaking on topological surface states.

3.6.5 Bismuth intercalation into graphene on iridum(111)

J. Warmuth, A. Bruix, M. Michiardi, T. Hänke, M. Bianchi, J. Wiebe, R. Wiesendanger, B. Hammer, Ph. Hofmann, and A. A. Khajetoorians

Finally, we also investigated the structural and electronic properties of a single bismuth layer intercalated underneath a graphene layer grown on an Ir(111) single crystal [5]. STM images (Fig.3.34(a),(b)) revealed a hexagonal surface structure and a dislocation network upon Bi intercalation, which we attributed to a $\sqrt{3} \times \sqrt{3}R30°$ Bi structure on the underlying Ir(111) surface. Our DFT calculations indeed substantiate that the intercalated Bi structure shown in Fig.3.34(d) is the most energetically favorable and illustrate that STM measurements are most sensitive to C atoms in close proximity to intercalated Bi atoms. Additionally, Bi intercalation induces a band gap at the Dirac point of graphene and an overall n doping as seen in ARPES (Fig.3.34(c)). We attribute the emergence of the band gap to the dislocation network which forms favorably along certain parts of the Moiré structure induced by the graphene/Ir(111) interface.

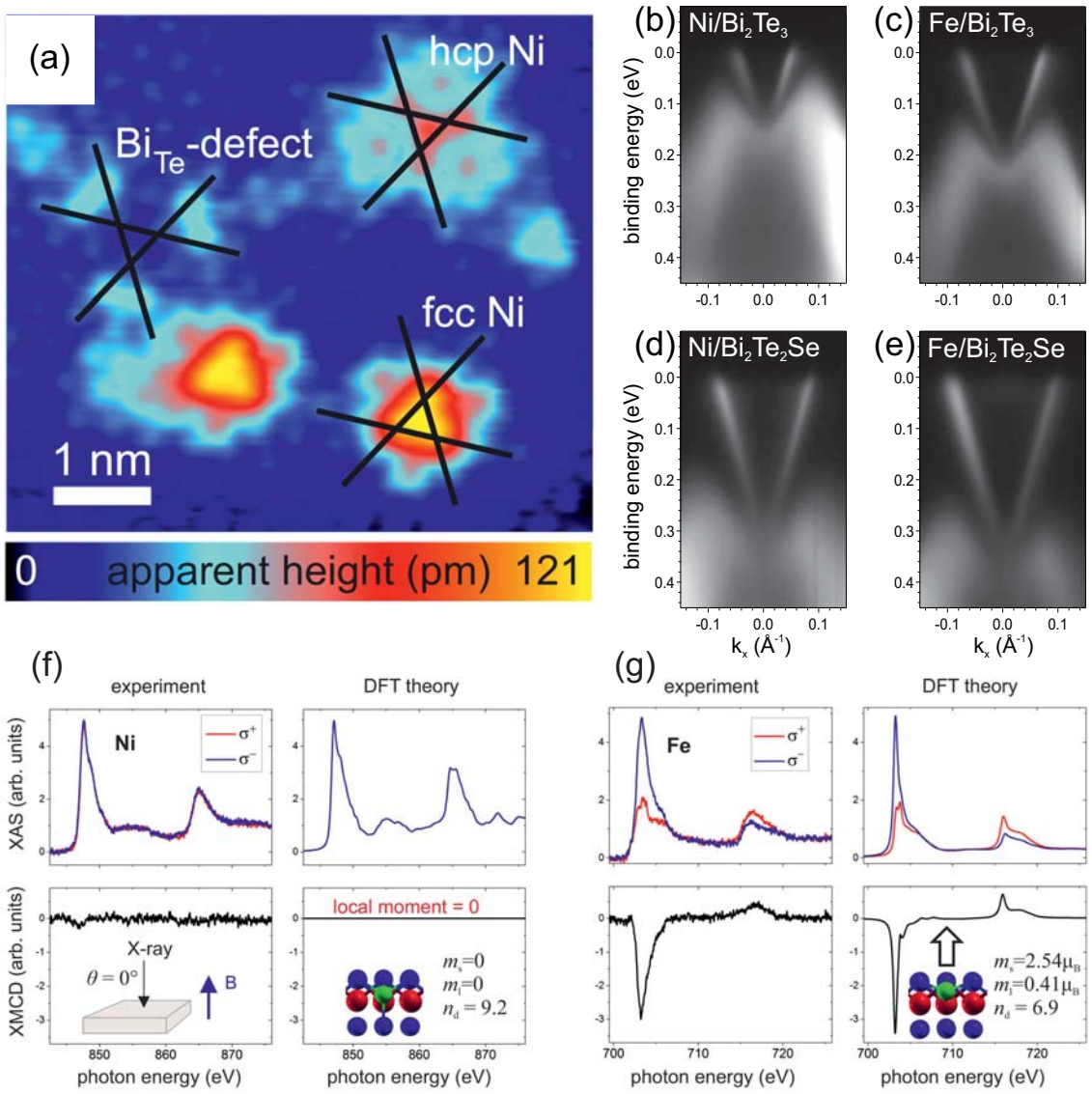

Figure 3.33: Investigation of the magnetism of Fe and Ni adatoms on Bi_2Te_3 and Bi_2Te_2Se [4]. (a) Atomically resolved STM image of $\approx$ 1% ML Ni on Bi_2Te_3 with single Ni atoms occupying the two different adsorption sites and a subsurface Bi_{Te} antisite defect. The lines trace the surface Te atom rows. (b)-(e) ARPES data for 0.3 % ML Ni on (b) Bi_2Te_3 and (d) Bi_2Te_2Se, respectively, and 0.2 % ML Fe on (c) Bi_2Te_3 and (e) Bi_2Te_2Se, respectively. (f) and (g) Ni and Fe $L_{2,3}$ XAS data on Bi_2Te_2Se for positive (σ^+) and negative (σ^-) circular polarization in polar geometry and the resulting XMCD signals below (left panels). Measurements were done at low temperatures of $T = 2$ K and polar fields of $B = 6.8$ T. Right panels show respective spectra calculated for Bi_2Te_3 on the basis of DFT theory using the relaxed fcc geometry shown as insets. Ni and Fe both show partially filled d shells but only Fe develops finite local orbital and spin moments.

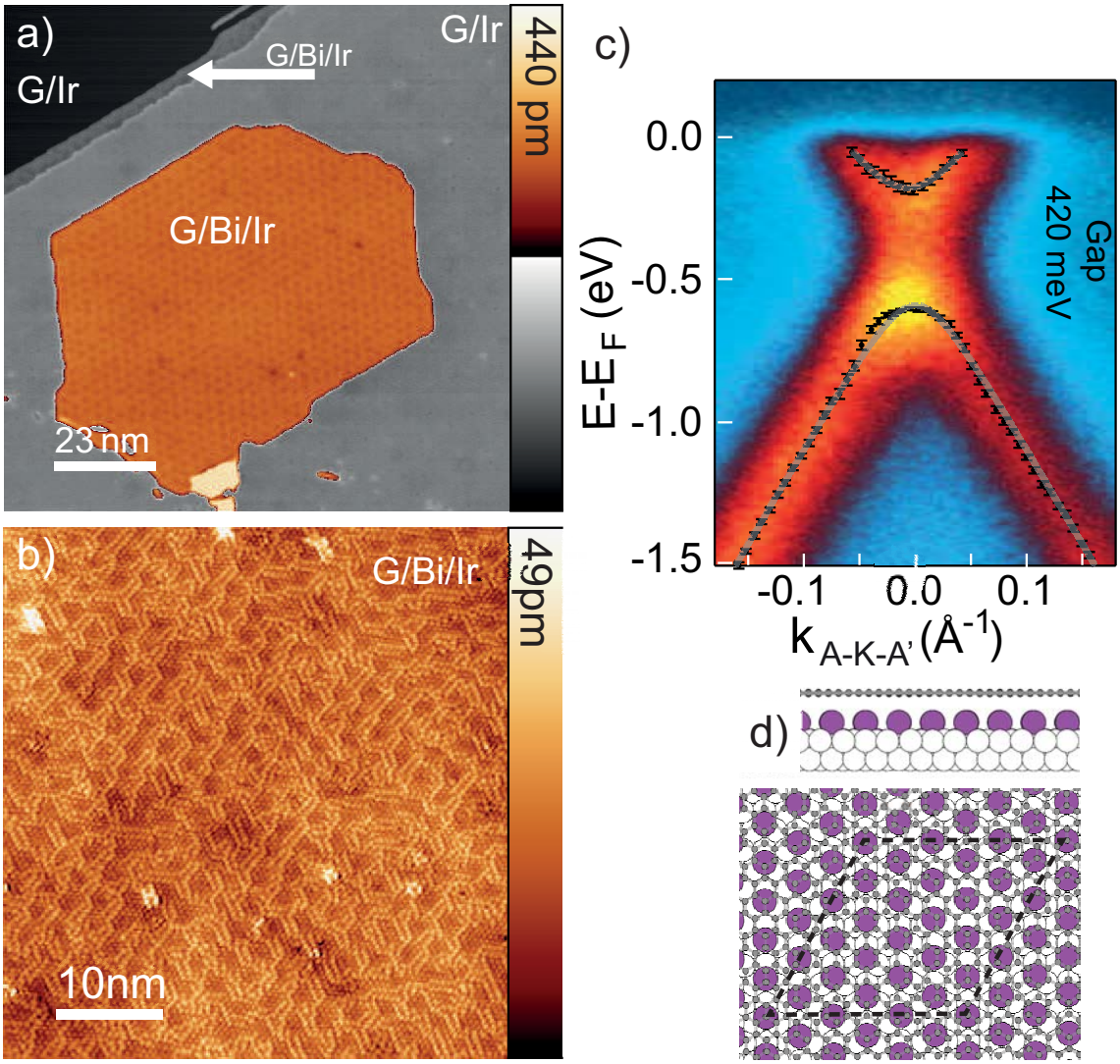

Figure 3.34: Investigation of the morphology and electronic structure of Bi intercalation of graphene (G) on Ir(111) [5]. (a) STM image of a G/Bi/Ir island and a thin G/Bi/Ir terrace (on the low side of the iridium step edge) on a G/Ir background. (b) STM image resolving the $(\sqrt{3} \times \sqrt{3})$ structure, the dislocation network and the Moiré superstructure at the surface of a G/Bi/Ir island. (c) ARPES of the Dirac cone of 0.95% G/Bi/Ir along the $A - K - A'$ direction. A 0.42 eV energy gap is opened at the Dirac point. The symbols on top of the spectrum show the location of the energy distribution curve maxima. The solid lines show the hyperbolic fitting on the upper and lower cones. (d) Ball-stick model of the most probable structure of the Bi layer underneath G.

References

[1] F. Pielmeier, G. Landolt, B. Slomski, S. Muff, J. Berwanger, A. Eich, A. A. Khajetoorians, J. Wiebe, Z. S. Aliev, M. B. Babanly, R. Wiesendanger, J. Osterwalder, E. V. Chulkov, F. J. Giessibl, and J. H. Dil, Response of the topological surface state to surface disorder in $TlBiSe_2$, New Journal of Physics **17**, 023967 (2015).

[2] A. Eich, M. Michiardi, G. Bihlmayer, X.-G. Zhu, J.-L. Mi, Bo B. Iversen, R. Wiesendanger, Ph. Hofmann, A. A. Khajetoorians, and J. Wiebe, Intra- and interband electron scattering in a hybrid topological insulator: Bismuth bilayer on Bi_2Se_3, Physical Review B **90**, 155414 (2014).

[3] M. Vališka, J. Warmuth, M. Michiardi, M. Vondráček, A. S. Ngankeu, V. Holý, V. Sechovský, G. Springholz, M. Bianchi, J. Wiebe, P. Hofmann, and J. Honolka, Topological insulator homojunctions including magnetic layers: The example of n-p type (n-QLs Bi_2Se_3/Mn-Bi_2Se_3) heterostructures, Applied Physics Letters **108**, 262402 (2016).

[4] M. Vondráček, L. Cornils, J. Minár, J. Warmuth, M. Michiardi, C. Piamonteze, L. Barreto, J. A. Miwa, M. Bianchi, Ph. Hofmann, L. Zhou, A. Kamlapure, A. A. Khajetoorians, R. Wiesendanger, J.-L. Mi, B.-B. Iversen, S. Mankovsky, St. Borek, H. Ebert, M. Schüler, T. Wehling, J. Wiebe, and J. Honolka, Nickel: The time-reversal symmetry conserving partner of iron on a chalcogenide topological insulator, Physical Review B **94**, 161114(R) (2016).

[5] J. Warmuth, A. Bruix, M. Michiardi, T. Hänke, M. Bianchi, J. Wiebe, R. Wiesendanger, B. Hammer, Ph. Hofmann, and A. A. Khajetoorians, Band-gap engineering by Bi intercalation of graphene on Ir(111), Physical Review B **93**, 165437 (2016).

3.7 Fundamental studies of superconductivity

R. Wiesendanger

Our experimental investigations concentrate on *model-type systems* which are prepared and thoroughly characterized with *atomic level precision. Atomic-scale characterization at low energy-scales* is performed by low-temperature spin-resolved elastic and inelastic scanning tunnelling microscopy (STM) and spectroscopy (STS). Transport experiments are conducted by a four-probe STM setup under well-defined ultra-high vacuum conditions.
The following model-type systems have been investigated in the reporting period:

- *metal-based superconductors including superconductor-magnet hybrid systems,*
- *ultrathin Fe-chalcogenide films epitaxially grown on Bi-based topological insulators,*
- *oxide-based systems epitaxially grown on elemental superconductors.*

3.7.1 Metal-based superconductors

T. Eelbo, H. Kim, P. Löptien, A. Palacio-Morales, J. Wiebe, V. Zdravkov, L. Zhou, and R. Wiesendanger

The first type of model systems we have studied in the reporting period consist of *metal-based superconductors*. We focussed on lanthanum (La), a rare earth element with a reasonably high bulk superconducting transition temperature T_c. In order to tailor T_c of this material we first investigated the growth and superconducting properties of thin films of La on the (110) surface of tungsten [1]. The W(110) substrate is ideally suited for the well-defined growth of clean lanthanides, as our group already showed in the 1990s. We focussed on the Stranski-Krastanov-growth of La on W(110) resulting in the formation of a La wetting layer and three-dimensional islands with lateral sizes much larger than the bulk superconducting coherence length and a large thickness range. This enabled us to investigate the superconducting properties of La in the thin film regime, i.e. where the thickness is on the order of the coherence length, to the bulk regime where the thickness is much larger than the coherence length. We found a suppression of superconductivity by the boundary conditions for the superconducting wave function at the surface and the W/La interface, leading to the usual linear decrease of T_c as a function of the inverse film thickness. Interestingly, in extremely pure La films, T_c increased by 40% with respect to the bulk value. Previous studies using spatially averaging techniques as, e.g., planar tunnelling, point contact spectroscopy, or transport measurements, reported $T_c = 4.9$ K for the stable hexagonal phase of La. Our local STS study of the superconducting energy gap enabled an in-situ correlation of the material's purity, which is quantified by the intensity of the surface state present at the (0001) surface of La, and T_c. Thereby, we showed that T_c can get as high as 7

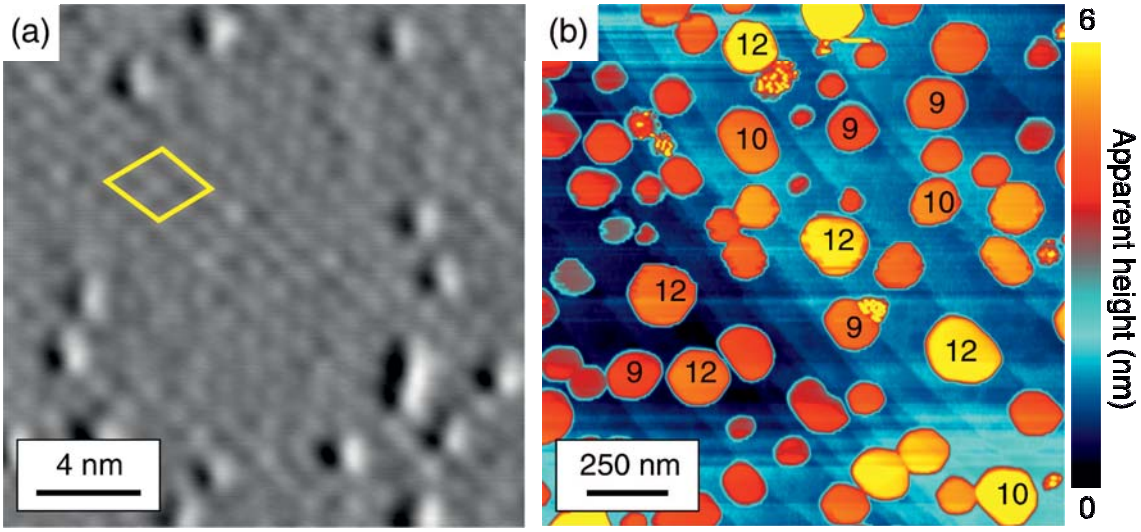

Figure 3.35: STM topographs of La/W(110) (I=100 pA,V=1 V). (a) Laterally differentiated topograph of the wetting layer between the La islands with the rhombic unit cell indicated in yellow. (b) Islands of a 1st generation sample with heights in ML, as depicted by the numbers (I=200 pA,V=1 V).

K for the cleanest samples we were able to grow, while T_c was considerably smaller for dirtier samples, and close to the previously reported values.

Moreover, the gap spectra taken on the thin La films revealed an extraordinarily large broadening of the coherence peaks. We were able to show that the observed broadening corresponds to very short electron-like quasiparticle lifetimes in the tunnelling process [2]. A thorough analysis considering the different relaxation processes revealed that the dominant mechanism is an efficient quasiparticle relaxation at the interface between the superconducting film and the underlying sub-strate. This process is of general relevance to scanning tunnelling spectroscopy studies on thin superconducting films and principally enables measurements of film thicknesses via a spectroscopic method.

Furthermore, we studied *superconductor-magnet hybrid systems* where the superconductor is an elemental material with large spin-orbit coupling, e.g. Fe on Ta(110), Fe on Ta(001), and Fe on Re(0001). Tantalum is an elemental superconductor with a relatively large T_c of about 4.5 K. However, it has proven to be extremely difficult in the past to prepare clean Ta surfaces or thin films free of contaminations. The successful preparation of clean Ta(110) surfaces and the subsequent epitaxial growth of two-dimensional Fe islands has now been achieved and reported in [3]. Low-temperature STS studies for that system are currently in progress. For the case of ultrathin Fe films epitaxially grown on Re(0001) several different types of non-collinear spin states, including Néel states and spin spiral states, could be revealed by spin-polarized scanning tunnelling microscopy (SP-STM) [4]. This sample system appears to be particularly promising for studies of exotic phases, including theoretically predicted unconventional superconducting phases in hybrids of non-collinear spin textures and superconducting substrates.

3.7.2 Ultrathin Fe-chalcogenide films

L. Cornils, T. Hänke, A. Kamlapure, S. Manna, U. R. Singh, J. Warmuth, J. Wiebe and R. Wiesendanger

The second kind of model systems explored in the reporting period are ultrathin Fe-chalcogenide films epitaxially grown on Bi-based topological insulator substrates such as Bi_2X_3(111) (X=Se,Te). The discovery of a very high superconducting transition temperature above 100K in single unit cell thick FeSe layers on $SrTiO_3$ substrates by Chinese research groups has motivated fundamental studies of how the superconductivity in Fe-chalcogenides evolves from bulk to ultra-thin films, but also lead to a renewal of the idea of tailoring the electron pairing by interfacial engineering in order to achieve high-temperature superconductivity. Many unconventional superconductors, including the well-known Fe-chalcogenide superconductors, possess a phase diagram in which superconductivity emerges from an antiferromagnetic parent compound. The strength of the antiferromagnetic exchange coupling in the magnetic state is, in some theoretical models, related to the Cooper pairing energy in the superconducting state. Achieving a microscopic picture of the relation between these two properties is believed to be the key towards a fundamental insight into the physics of unconventional superconductivity. However, experiments on rather complex material systems often suffer from material imperfections or from a lack of control of materials properties within a wide range. Our experimental studies are focussed on model-type systems which have been prepared and thoroughly characterized with atomic level precision. We have achieved defect-free ultrathin Fe-chalcogenide films, i.e. $FeTe_{1-x}Se_x$ (x = 0, 0.5), by growing small amounts of Fe on top of various Bi_2X_3 substrates. Despite the different lattice symmetries (six-fold for Bi_2X_3(111) and four-fold for FeX) and the relatively large lattice mismatch, the heteroepitaxial growth was found to be of very high quality, resulting in an atomically sharp and defect-free interface. In contrast to the surface of bulk FeX, the surfaces of our ultrathin FeX films do not show any excess Fe atoms, indicating a stoichiometric FeX layer. We have characterized these samples by low-temperature spin-polarized scanning tunnelling microscopy (SP-STM) and spectroscopy (SP-STS). The experimental method of SP-STS allowed us to investigate superconductivity and magnetism simultaneously at the same sample spot down to the atomic scale.

In order to study the superconducting properties of one unit-cell thick $FeTe_{1-x}Se_x$ (x = 0, 0.5), we performed differential tunnelling conductance (dI/dU) measurements at a temperature down to 1 K. We observed fully developed U-shaped superconducting gaps (δ= 2.2meV) in $FeTe_{0.5}Se_{0.5}$ layers of one unit-cell thickness with a transition temperature (T_c) of ~11 K, close to the one of the corresponding bulk system (Tc ~ 4.5 K). The temperature-dependence of the dI/dU spectra as well as the derived T_c value in the framework of BCS theory provided strong evidence that the observed gap feature arises from superconductivity in the ultrathin $FeTe_{0.5}Se_{0.5}$ film grown on $Bi_2Te_{1.8}Se_{1.2}$ [5]. Spatially resolved tunnelling spectroscopy data showed a strong inhomogeneity in the gap magnitude which varies from 1mV up to 3mV. This gap inhomogeneity indicated that the interlayer

coupling with the substrate is important.

Interestingly, we also found clear evidence for superconductivity up to T_c ~ 6.5K for one unit-cell thick FeTe layers grown on Bi_2Te_3(111) substrates, in contrast to the non-superconducting FeTe bulk compound which exhibits bi-collinear antiferromagnetic (AFM) order up to 70 K [5]. The spatial variation of the superconducting gap at the interface of FeTe and Bi_2Te_3 confirms that the previously reported 2D superconductivity in FeTe/Bi_2Te_3 heterostructures is associated with the presence of a superconducting layer of FeTe located at the interface. It has been an open question whether the bi-collinear AFM order of bulk FeTe is suppressed in the ultrathin FeTe layer grown on Bi_2Te_3, or whether it can co-exist with the superconducting correlations we observed. In order to answer this question, we simultaneously characterized the local superconducting correlations and the atomic-scale spin structure of the ultrathin FeTe films grown on Bi_2Te_3 by SP-STS using a spin-polarized bulk Cr-tip. Remarkably, we could resolve for the first time directly in real-space the bi-collinear AFM order of an Fe-chalcogenide compound at the limit of single unit-cell film thickness. Most interestingly, our temperature-dependent SP-STM data demonstrated that the bi-collinear AFM order is unaffected by the onset or suppression of superconducting correlations

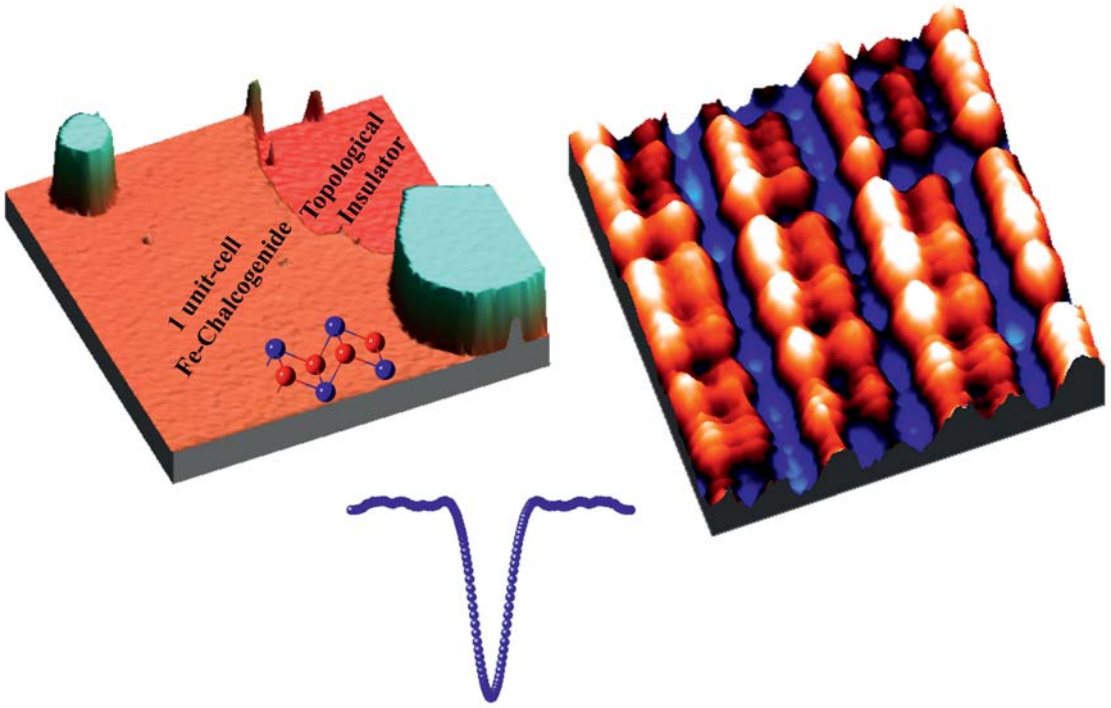

Figure 3.36: (left) Scanning tunneling microscopy (STM) image (perspective view) of a heterostructure interface consisting of two non-superconducting materials, namely a topological insulator as substrate and an ultrathin film of iron-telluride grown on top. The unit-cell high layer of FeTe exhibits simultaneously bi-collinear antiferromagnetic order as revealed by spin-resolved STM (right) and superconducting properties at the same location as measured by the spectroscopic STM mode (bottom).

below or above 6.5 K and remarkably persists up to 75 K in single unit-cell thick FeTe layers. Therefore, our experimental results do not support the previously published claim by other authors that one kind of order emerges at the expense of the other, nor does our data provide any indication for a microscopic phase separation between regions with superconducting and magnetic order. Our findings for single unit-cell thick FeTe layers on Bi_2Te_3 therefore challenge the common belief that optimal superconducting pairing sets in when long-range AFM order is suppressed in the parent compound. In conclusion, we were able to observe the coexistence of superconductivity and magnetic order for the first time at the same sample location at the atomic scale using spin-resolved scanning tunnelling microscopy and spectroscopy [5].

In another in-depth study making use of 3D-vector-resolved SP-STM, we have found a reorientation of the spin direction in the bi-collinear AFM state at the surface of atomic layers of FeTe epitaxially grown on Bi_2Te_3 [6]. In particular, we have found a strong contribution of the surface spin component in the out-of-plane direction along the c-axis, in addition to an in-plane component which deviates from the b-axis direction. Neutron scattering, which is sensitive to the bulk spin structure, previously revealed a dominant spin direction of the bi-collinear antiferromagnetic structure along the b-axis. In contrast, our SP-STM experiments indicated a strong component of the surface spins away from the b-axis direction. Our findings might have implications for related sample systems, e.g. spin-polarized STM studies could offer insight into the origin of the strongly increased Tc of the FeSe monolayer grown on $SrTiO_3$ compared to bulk FeSe. Although bulk FeSe does not show static magnetic order, spin fluctuations are known to exist and are coupled to the superconducting pairing.

Finally, we have studied the effect of doping by K-atoms on ultrathin FeTe films grown on $Bi_2Te_3(111)$ in order to study a possible change in spin order and a possible enhancement of superconducting correlations. We found a strong Coulomb repulsion between ionized adsorbed K-atoms indicating a significant charge transfer to FeTe, which has been verified by tunnelling spectroscopy. The electron donation effect can clearly be observed in the spectra as a systematic change of valence band features and a significant change in the density of states at the Fermi level in a potassium coverage regime from 0.025 to 0.40 ML.

For the system of $FeSe_{0.5}Te_{0.5}$ epitaxially grown on $Bi_2(Se,Te)_3$ we found strong evidence for a two-fold symmetric superconducting gap [7]. Spatially resolved tunnelling spectroscopic data showed a strong spatial inhomogeneity in the superconducting gap magnitude. Despite this inhomogeneity, all spectra could successfully be fitted with an anisotropic s-wave gap function. Interestingly, we observed two gap features on Te rich patches. Such spectra could be fitted with a two-gap model. We also observed a large variation in the degree of anisotropy in the spectra, reflecting a large variation of gap structure, from nodal to nodeless. The Fourier transform analysis of high resolution tunnelling spectroscopy data reveals Bogoliubov quasiparticle interference patterns with distinct C2-symmetry at all bias values, indicating a two-fold gap symmetry in our $FeSe_{0.5}Te_{0.5}$ thin films.

In addition, we observe orbital ordering in the spectral maps, where unidirectional stripe-like pattern can be observed. We propose that such a pronounced C2-symmetry in our $FeSe_{0.5}Te_{0.5}$ thin films is the result of strong spin-orbital coupling possibly due to the presence of the topological insulator underneath [7].

The simplicity of our growth procedure enables us to study ultrathin Fe-chalcogenide films with different concentrations of Se and Te, and to explore the nature of superconductivity as a function of chemical composition.

We also successfully prepared the system of FeSe epitaxially grown on $Bi_2Se_3(111)$. In order to probe the electronic properties including a potential superconducting state of ultrathin FeSe layers on $Bi_2Se_3(111)$, we performed tunnelling spectroscopic measurements at low temperatures. However, there was always a finite density of states at the Fermi level down to 6 K, indicating the absence of a superconducting gap. Tunnelling spectra measured on two unit-cell thick FeSe were found to be identical to the ones taken on one unit-cell thick FeSe layers. Both surfaces of one and two unit-cell thick FeSe layers were found to be electronically homogeneous [8]. This experimental result is in strong contrast to the relatively large T_c-values reported by other groups for ultrathin FeSe films epitaxially grown on $SrTiO_3$ substrates.

3.7.3 Oxide-based systems

L. Cornils, A. Kamlapure, J. Wiebe, L. Zhou and R. Wiesendanger

As a third type of model systems we started to investigate oxide-based systems epitaxially grown on elemental superconductors with strong spin-orbit coupling. Tantalum being a superconductor with $T_c = 4.5$ K allows us to study the interaction between a superconductor and localized magnetic moments through a well-ordered surface oxide in a controlled way. The Ta(001) surface was prepared by first Ar^+-ion sputter cleaning followed by repeated cycles of annealing in the presence of oxygen and high temperature flashes, until a well-ordered oxygen-induced (3 x 3) reconstructed surface was formed. Low-temperature tunnelling spectra acquired on such oxygen-reconstructed Ta(001) surfaces exhibit a superconducting gap at the Fermi level being homogeneous all over the surface. The spectra can be described perfectly using BCS-Dynes density of states with an energy gap of $\Delta = 0.63$ meV at $T = 1.1$ K. Subsequently, Fe atoms were deposited at low temperature. Depending on the Fe adsorption site and its coupling to the local environment, we observed mainly two different features in the differential tunnelling spectra acquired on the Fe atoms: (i) spin excitations with additional peaks outside the superconducting gap, and (ii) intra-gap bound states, called Yu-Shiba-Rusinov states, resulting from a weak interaction between the Fe atoms with the Ta substrate.

References

[1] P. Löptien, L. Zhou, A. A. Khajetoorians, J. Wiebe, and R. Wiesendanger, Superconductivity of lanthanum revisited: enhanced critical temperature in the clean limit, J. Phys.: Condens. Matter **26**, 425703 (2014).

[2] P. Löptien, L. Zhou, A. A. Khajetoorians, J. Wiebe, and R. Wiesendanger, Tunneling into thin superconducting films: Interface-induced quasiparticle lifetime reduction, Surf. Sci. **643**, 6 (2016).

[3] T. Eelbo, V. Zdravkov, and R. Wiesendanger, STM study of the preparation of clean Ta(110) and the subsequent growth of two-dimensional Fe islands, Surf. Sci. **653**, 113 (2016).

[4] A. Palacio-Morales, A. Kubetzka, K. von Bergmann, and R. Wiesendanger, Coupling of Coexisting Non-Collinear Spin States in the Fe Monolayer on Re(0001), Nano Lett. **16**, 6252 (2016).

[5] S. Manna, A. Kamlapure, L. Cornils, T. Hänke, J.-L. Mi, M. Bremholm, B. B. Iversen, Ph. Hofmann, J. Wiebe, and R. Wiesendanger, Evidence for interfacial superconductivity in a bi-collinear antiferromagnetically ordered FeTe monolayer on a topological insulator, Nature Commun. **8**, 14074 (2017).

[6] T. Hänke, U. R. Singh, L. Cornils, S. Manna, A. Kamlapure, J. Wiebe, R. Wiesendanger, J.-L. Mi, B. B. Iversen, Ph. Hofmann, J. Hu, and Z. Mao, Reorientation of the bi-collinear antiferromagnetic structure at the surface of bulk and thin films of $Fe_{1+y}Te$, Nature Commun. **8**, 13939 (2017).

[7] A. Kamlapure, S. Manna, L. Cornils, T. Hänke, M. Bremholm, Ph. Hofmann, J. Wiebe, and R. Wiesendanger, Spatial variation of the two-fold anisotropic superconducting gap in a monolayer of $FeSe_{0.5}Te_{0.5}$ on a topological insulator, submitted.

[8] U. R. Singh, J. Warmuth, V. Markmann, J. Wiebe, and R. Wiesendanger, Structural and electronic properties of ultrathin FeSe films grown on Bi_2Se_3(0001) studied by STM/STS, J. Phys.: Condens. Matter **29**, 025004 (2017).

3.8 Towards molecular spintronic devices

M. Bazarnik and R. Wiesendanger

With increasing degree of miniaturization the current density increases and heat dissipation becomes a major problem. Spintronic devices, based on the manipulation of spin states rather than charge flow of electrons, could offer energy-efficient solutions for future smart information and communication technologies. Spins can either be employed as classical bits of information [1] or as qubits in quantum computing [2–4].

In particular, molecular spintronic devices offer great potential for future energy efficient nanoelectronics due to their small size, potentially high switching rates, and multi-functionality. Progress in this field relies on the realization of all necessary building blocks, such as molecular wires conducting spin information, molecular junctions and switches. An all-spin based logic device has recently been built using single iron atoms deposited on a Cu(111) surface and arranged into a desired device structure using the atomic manipulation capabilities of the scanning tunneling microscope (STM) [5]. Each individual Fe atom behaves paramagnetically on this Cu surface, even at very low temperatures. However, thanks to indirect magnetic exchange interactions mediated by electrons of the Cu substrate, the magnetic moments of the Fe atoms can be aligned antiferromagnetically by tuning those interactions via position control of single Fe atoms on the Cu surface [6]. As a result, several different types of logic gates could be realized [5].

The use of single atoms for logic operations represents the true limit of miniaturization; however, it has its limitations. Firstly, atoms have to be arranged on the surface one-by-one and they have to retain their positions for long periods of time which requires temperatures lower than 4 K for metallic substrates such as Cu(111). Secondly, the indirect magnetic exchange interaction employed in the previous work of our group is very weak, on the order of J = 0.1 meV for Fe adatoms on a Cu surface [6], which limits the operation temperature of the atomic-scale device even further, below 1 K. Thirdly, the ultimate size of devices made of individual atoms is limited since neighboring atomic- and nano-scale structures being too close will interact with the single atoms making up the device. To tackle those problems we propose to use planar magnetic molecules instead of single atoms.

In this area of research we focus on the magnetic properties of molecular and carbon based systems. In particular in the last three year period we focused on the combination of the carbon based pi-system with ultra-thin iron films grown on Iridium(111) surfaces, and the construction of salophene based spintronic devices. Among the highlights of our efforts is the on-surface synthesis of metal-organic hybrid systems interacting with the non-collinear magnetic structure of 1ML Fe on Ir(111) [6], the development of our own Electrospray Deposition System and the successful on-surface synthesis of a prototype all-spin molecular device [7].

3.8.1 Multi-layer and multi-component intercalation of magnetic transition metals at the graphene/Ir(111) interface

M. Bazarnik, R. Decker, J. Brede, and R. Wiesendanger

We performed a scanning tunneling microscopy studies of iron- and cobalt-intercalated graphene / Ir(111. In both cases, the intercalation leads to well-defined epitaxial layers and the intercalated areas are characterized by a moiré pattern, which adopts the same symmetry and periodicity as the graphene / Ir(111) [8].
The formation of Fe and Co nanostructures or layers at the interface between graphene and Ir(111) shows many similarities with the growth of metal species on metallic surfaces without graphene via the thermally-assisted diffusion of atoms. These atoms eventually form critical immobile nuclei, which then act as nucleation centers for larger structures by attachment of further atoms. However, this intercalation process differs from the usual growth, since it implies two distinct migration paths for the adatoms: the migration on graphene and the subsequent migration at the interface. The latter migration becomes possible by the penetration of metal adatoms through defects in graphene. Experimentally, adatoms are deposited on the metal substrate covered by graphene. The intercalation is activated by annealing of the sample during or after the deposition of adatoms on the decorated surface. The former procedure is more effective, because it prevents the formation of large and stable structures on top of graphene. During our experiments, we noticed that the intercalation process is facilitated and the range of useful temperatures is wider if instead of a full graphene layer, we have graphene islands [6, 9, 10]. This is explained by the opening of a new penetration pathway starting from the edges of the graphene islands.

3.8.2 Local tunnel magnetoresistance of an iron intercalated graphene-based heterostructure

R. Decker, M. Bazarnik, N. Atodiresei, V. Caciuc, S. Blügel, and R. Wiesendanger

We have studied the local properties of a well-defined and new graphene-based TMR heterostructure by Spin-Polarized Scanning Tunneling Microscopy (SP-STM). In order to realize a graphene-based spin valve device, we used an Fe-coated STM tip on one side and graphene / 1ML Fe / Ir(111) on the other side. A spatially varying spin-polarization is observed above the graphene layer with a TMR ratio exceeding 100%. In order to understand the origin of these observations, the spin-resolved electronic structure of the graphene / 1 ML Fe / Ir(111) and of the graphene – Fe interfaces has to be considered.
We have observed that the magnetoresistance at valleys is higher than the one at hills (1 time to 5 times higher, depending on the bias). In particular, all our data show a considerable reduction in the magnetoresistance at hills in the vicinity of the Fermi energy. Such a site dependence in the magnetoresistance can only be explained by the difference in charge transfer between graphene and Fe at hills and valleys.

3.8.3 Long-range magnetic coupling between nanoscale organic–metal hybrids mediated by a nanoskyrmion lattice

J. Brede, N. Atodiresei, V. Caciuc, M. Bazarnik, A. Al-Zubi, S. Blügel, and R. Wiesendanger

We have fabricated organic-metal hybrids with tunable lateral dimensions on the nanoscale by depositing sp2-conjugated organic carbon systems, i.e. single coronene (Cor) molecules or graphene (Gr) islands, on a magnetic skyrmion lattice (SkX) [11] of a single atomic layer of Fe on an Ir(111) substrate [6]. While the SkX does not exhibit a net magnetic moment and thus does not align with an external magnetic field, the strong interaction between the Fe-atoms and the organic material leads to the formation of local organic-ferromagnetic (organic-FM) units that can be switched with an external field [6]. Controlling the lateral dimensions of the organic carbon systems enables tuning the experimentally determined switching fields of the nanoscale organic-metal hybrids by SP-STM. State-of-the-art first principles calculations elucidate how the exchange coupling, magnetic moment, as well as magnetocrystalline anisotropy energy can be controlled on the atomic scale, with magnetic moments from few tens up to several thousand Bohr magnetons (μB) and magnetocrystalline anisotropy energies of few millielectronvolt up to several electronvolt. When the magnetocrystalline anisotropy energy is tailored to match the exchange coupling of the nanoscale organic-metal hybrid to its surrounding, we find a correlated magnetization reversal behavior of individual organic-metal hybrids, indicating long-range magnetic coupling mediated by the chiral nanoskyrmion lattice, thereby opening up new avenues to control, couple, and manipulate spin properties of metal-organic hybrid systems at the nanoscale.

A representative overview image is shown in Figure 3.37 (a). The bare iron monolayer exhibits a square lattice with a periodicity of about one nanometer. This checkerboard pattern is characteristic for the SkX imaged with an out-of-plane magnetized SP-STM probe tip [11]. The experimentally deduced adsorption geometry of coronene molecules is depicted in the inset of Figure 3.37 (a)). We will refer to a coronene molecule together with the underlying twelve Fe-atoms as a Cor-FM unit from now on. Cor-FM units exhibit a binary (red/green) contrast in SP-STM images. The contrast corresponds to a magnetization direction parallel or antiparallel with respect to the tip magnetization direction, respectively. The response of the sample to an external out-of-plane magnetic field H is evaluated as follows: In Figure 3.37 (b) a typical SPSTM image of a Cor-FM unit at H= 1 T is presented and the SkX unit cell as well as two sub-units are indicated by the squares and triangles, respectively. By increasing H to 1.5 T and subsequently recording another SP-STM image (Figure 3.37 (c)), an increase of the apparent height of the Cor-FM unit and an inversion of the contrast of the SkX are clearly visible . The changes in apparent height due to magnetization reversal are conveniently visualized in the difference image in Figure 3.37 (d): blue/red areas indicate a switching of the magnetization. The apparent height changes derived from Figures 3.37 (b) and (c) as a function of the externally applied field yield magnetization curves as displayed in Figure 3.37 (e). The black(blue) traces correspond to a measurement series with

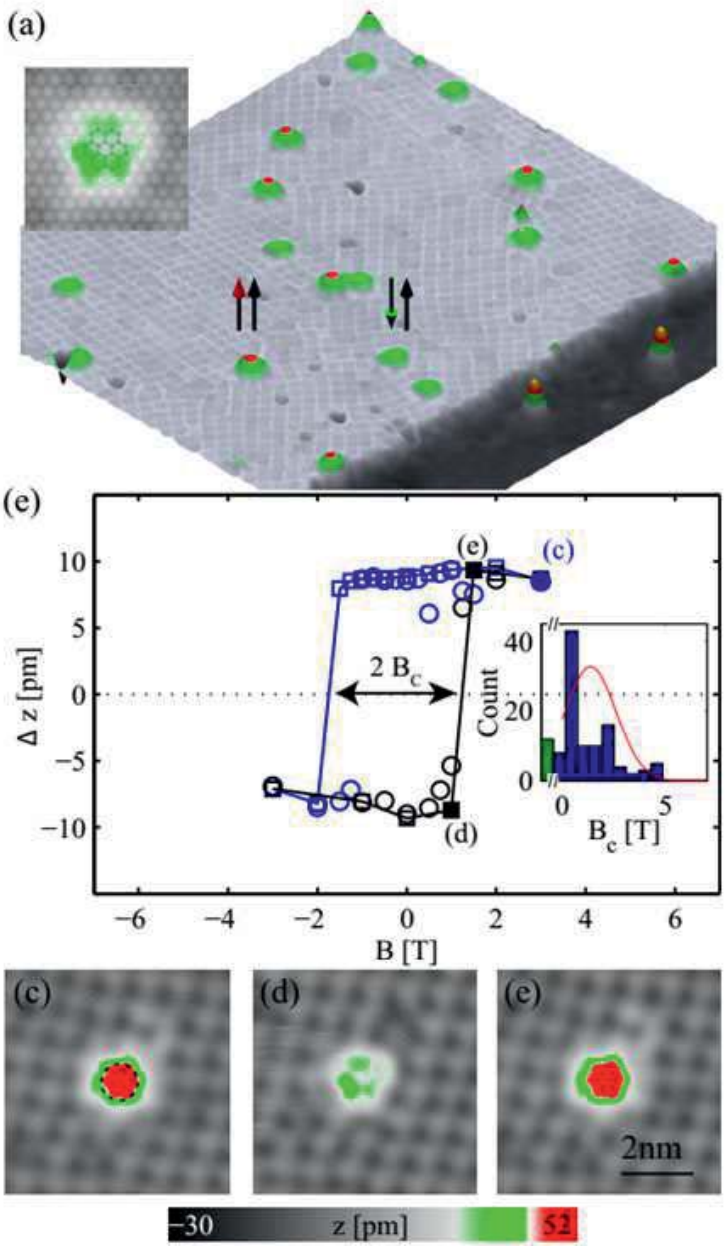

Figure 3.37: SP-STM image of Cor-Fe-units embedded in the magnetic skyrmion lattice of 1 ML Fe/Ir. (a) Pseudo three-dimensional representation of Cor-Fe-units (the red and white protrusions) within the skyrmion lattice. Two different Cor-Fe-units are clearly identified: the difference in apparent height corresponds to a magnetization direction either parallel or anti-parallel with respect to the tip as schematically depicted by the green-black - and red-black arrows, respectively. (c)-(e) SPSTM images of a Cor-Fe-unit for different external magnetic fields (B_{ext}) applied. The mean apparent height of the Cor-Fe-units is plotted in (b). The black (blue) trace is for subsequently increasing (decreasing) B_{ext}-values. The inset shows the distribution of switching field values obtained for more than 100 different Cor-Fe-units. The red curve shows a normal distribution.

increasing(decreasing) field H. On the one hand, the SkX (squares) does not show a net change in magnetization, on the other hand, the two SkX sub-units (upward and downward triangles) show hysteretic behavior due to shifting of the SkX by half a unit cell. The shifting correlates with a magnetization reversal of the Cor-FM unit 3 (circles). A schematic side view representation of the changes in the local magnetization for the atoms indicated by the circles in Figure 3.37 (b) through (d) are depicted in Figure 3.37 (e). The full spatial information of the magnetization-reversal is clearly seen in the difference image (Figure 3.37 (d)): (i), a uniform contrast at the Cor-FM unit site due to a flipping of the Cor-FM unit's magnetization direction, and (ii), an alternating contrast giving rise to a checkerboard pattern for the SkX due to a shift of half a unit cell.

3.8.4 Toward tailored all-spin molecular devices

M. Bazarnik, B. Bugenhagen, M. Elsebach, E. Sierda, A. Frank, M. H. Prosenc, and R. Wiesendanger

Complex molecular structures such as functioning devices cannot be deposited onto substrates in a clean and controlled way. Therefore, a bottom-up approach is required involving the deposition of different molecular building blocks onto a surface and an in situ on-surface chemical synthesis of the molecular device. Salophene molecules are very promising in view of future molecular spintronic devices because they are planar, they can be substituted at the foremost ends by Br to enable on-surface Ullmann coupling [12], and they can incorporate a number of transition metals as magnetic ions. These molecules can easily be prepared in situ under ultra-high vacuum (UHV) conditions via thermal sublimation. A triple-salophene molecule, which includes three magnetic ions, is also planar and can be used as a 3-terminal junction within a molecular device. It can be substituted with three Br atoms for on-surface Ullmann coupling. These multi-center molecules, however, cannot easily be handled under UHV conditions. Thermal sublimation does not work, since these larger molecules decompose before they sublime. Therefore, we exploited a different approach, that is electrospray deposition [7]. The molecules were dissolved in water free pyridine in a concentration of 1 mM. We obtained stable spray action with a flow rate set between 0.5 μL/minute and 0.9 μL/minute and 1.9 kV voltage applied between the needle and the capillary. During the deposition we monitored the ion current on the substrate, and calibrated the coverage of the sample vs. total charge registered during deposition, yielding $6 * 104$ ML/C. The typical ion current registered during deposition is on the order of 100-150 fA. Most experiments were carried out with a coverage of 0.05 ML, therefore the deposition time ranged from 1 h to 6 h, varying from experiment to experiment mainly due to the exact position of the needle vs. the capillary.
Some molecules got fragmented due to the impact on the surface. Therefore, we made use of a soft landing approach and decelerated the molecules in the final 1 cm of their flight. By analyzing the ion current as a function of decelerating voltage we determined the kinetic energy of the molecules landing on the surface to be (25.8 ± 3.1) eV per charge. In our experiments we reduced the kinetic energy of the molecules to 5 eV. This way we increased the percentage of intact molecules

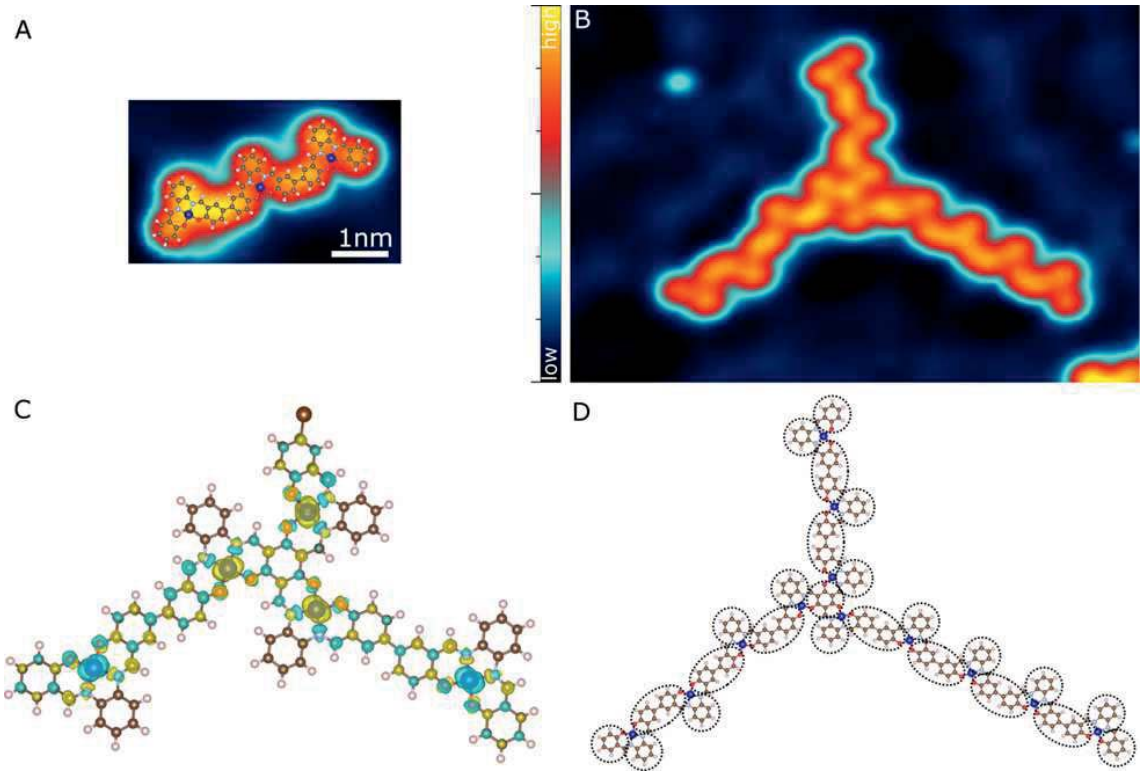

Figure 3.38: Design of an all-spin based logic gate built of covalently bound molecules. (a) STM image along with a ball-and-stick model of a molecular chain with antiferromagnetically coupled Co centers and hydrogen terminations at both ends. (b) STM image of a molecular arrangement. (c) Ball-and-stick model of the DFT calculated structure with spatial distribution of the spin densities plotted on top. Blue and yellow colors correspond to opposing spin directions. (d) Ball-and-stick model of a molecular device structure corresponding to the STM image in (b). Dotted circles and ellipses depict parts of molecules from which high intensities in the STM image arise.

landing on the surface to over 80%, while still conserving a reasonable deposition rate (sufficient ion current).

An STM image of the final product of an Ullmann reaction of subsequently deposited tri-bromo-triplecobaltsalophene, 5,5'-dibromosalophenato-cobalt(II), and 5-bromo-salophenato-cobalt(II) molecules on the Au(111) surface in a 1:6:3 ratio is shown in Figure 3.38 (b). The supramolecular structure consists of a Br_3Co_3 molecule, one two-block long chain in the upper part of the image, one three-block long chain on the left, and a four-block long chain extending to the right. As in the case of simple molecular wires, two covalently bound carbon rings form an elongated ridge. This is also the case for the Br_3Co_3 molecule bound to the molecular chains. Therefore, at low bias a triplecobaltsalophene molecule embedded in a supramolecular structure is imaged as a central round protrusion, three elevations in topography are corresponding to $N_2C_6H_4$ bridges, and three elongated ridges are corresponding to outermost carbon rings bound to side rings of salophenato-cobalt(II). By changing the ratio of the tri-bromo-triplecobaltsalophene, 5,5'-dibromosalophenato-cobalt(II), and 5-bromo-salophenato-cobalt(II) molecules, the shape and extension of the resulting molecular structure can be tailored. The molecular structure model

is shown in Figure 3.38 (d). While not yet proven to operate the designed and on-surface synthesized molecular assembly is an important milestone on the way towards a working all-spin molecular device.

References

[1] S. A. Wolf, D. D. Awschalom, R. A. Buhrman, J. M. Daughton, S. von Molnár, M. L. Roukes, A. Y. Chtchelkanova, and D. M. Treger, Spintronics: A Spin-Based Electronics Vision for the Future, Science **294**, 1488-1495 (2001).

[2] W. Wernsdorfer, and R. Sessoli, Quantum phase interference and parity effects in magnetic molecular clusters, Science **284**, 133–135 (1999).

[3] M.N. Leuenberger, and D. Loss, Quantum computing in molecular magnets, Nature **410**, 789–793 (2001).

[4] F. Troiani, A. Ghirri, M. Affronte, S. Carretta, P. Santini, G. Amoretti, S. Piligkos, G. Timco, and R. E. P. Winpenny, Molecular Engineering of Antiferromagnetic Rings for Quantum Computation, Phys. Rev. Lett. **94**, 207208 (2005).

[5] A. A. Khajetoorians, J. Wiebe, B. Chilian, and R. Wiesendanger, Realizing All-Spin Based Logic Operations Atom by Atom, Science **332**, 1062?1064 (2011).

[6] J. Brede, N. Atodiresei, V. Caciuc, M. Bazarnik, A. Al-Zubi, S. Blügel, and R. Wiesendanger, Long-range magnetic coupling between nanoscale organic–metal hybrids mediated by a nanoskyrmion lattice, Nature Nanotechnology **9**, 1018 (2014).

[7] M. Bazarnik, B. Bugenhagen, M. Elsebach, E. Sierda, A. Frank, M. H. Prosenc, and R. Wiesendanger, Toward Tailored All-Spin Molecular Devices, Nano Lett. **16** 577 (2016).

[8] M. Bazarnik, R. Decker, J. Brede, and R. Wiesendanger, Multi-layer and multi-component intercalation at the graphene/Ir(111) interface, Surf. Sci. **639** 70 (2015).

[9] R. Decker, J. Brede, N. Atodiresei, V. Caciuc, S. Blügel, and R. Wiesendanger, Atomic-scale magnetism of cobalt-intercalated graphene, Phys Rev. B **87**, 041403(R) (2013).

[10] R. Decker, M. Bazarnik, N. Atodiresei, V. Caciuc, S. Blügel, and R. Wiesendanger, Local tunnel magnetoresistance of an iron intercalated graphene-based heterostructure, J. Phys.: Condens. Matter **26** 394004 (2014).

[11] S. Heinze, K. von Bergmann, M. Menzel, J. Brede, A. Kubetzka, R. Wiesendanger, G. Bihlmayer, and S. Blügel, Spontaneous atomic-scale magnetic skyrmion lattice in two dimensions, Nature Physics **7** 713-718 (2011).

[12] A. DiLullo, S.-H. Chang, N. Baadji, K. Clark, J.-P. Klöckner, M. H. Prosenc, S. Sanvito, R. Wiesendanger, G. Hoffmann, and S.-W. Hla, Molecular Kondo chain, Nano Lett. **12** 3174 (2012).

3.9 Revealing atoms and molecules on insulating substrates by atomic force microscopy

3.9.1 Set-up of a ^{3}He/10T atomic force microscope

A. Schwarz, K. Ruschmeier, H. von Allwörden, A. Köhler, T. Eelbo, G. Fläschner, and R. Wiesendanger

We built a ^{3}He evaporation based low temperature atomic force microscope equipped with a 10 T superconducting magnet. The set-up is dedicated to magnetic exchange force microscopy (MExFM) [1] and spectroscopy (MExFS) [2] experiments on single magnetic atoms and molecules deposited on well-defined substrates and described in Ref. [3]. More specifically, we intend focussing on insulating substrates, where spin flip scattering processes, which destabilize the atomic magnetic moments even in the presence of a large anisotropy energy and are induced by the conduction electrons of metallic substrates, are absent.

The experiment is set up in a two-storey laboratory shown in Fig. 3.39(a). The upper floor contains the data acquisition system and provides access to supply the Dewar with cryogenic liquids. The UHV system with the cryostat on top is mounted on a frame that is supported by air damping legs, which rest on a separate foundation in the lower floor. Using a bakeout tent the entire system including the insert inside the cryostat can be heated to 120°. Scroll pumps, turbo-molecular pumps, ion getter pumps and non-evaporable getter pumps are used to generate ultrahigh vacuum (UHV) conditions with pressures of about 1×10^{-10} hPa. Standard surface science tools (LEED, AES, Ar ion gun, heaters, evaporators etc.) are at hand to prepare and characterize samples as well as tips. Wobble sticks and magnetically driven transfer rods are used to move tips and samples between load lock, preparation chamber, analysis chamber and the central cryostat chamber. The insert with the microscope body can be moved into the cryostat chamber so that tip and sample can be exchanged *in-situ*. In this position it is also possible to deposit single atoms and molecules directly onto a cold substrate inside the microscope body.

The cryostat is based on a commercial UHV-compatible Heliox system from Oxford Instruments [4]. It utilizes ^{3}He evaporation as described in Refs. [5, 6]. However, instead of an internal spindle mechanism an edge welded bellow is used as a z-shift. A cross sectional view is depicted in Fig. 3.39(b). It shows the Dewar with the outer liquid nitrogen tank (capacity: 75 l, hold time: about 10 days), the main liquid helium tank (capacity: 100 l, hold time: about 6 days) with the superconducting 10 T magnet made from NbTi and Nb_3Sn and the central cryostat tube with the motor-driven z-shift on top used to move the insert up and down. The cryostat tube itself is multi-walled, so that hot gaseous nitrogen can be circulated during bake out to heat up the innermost wall while keeping the outermost wall cold. To further protect the magnet from overheating during bake-out, it has to be immersed in liquid nitrogen. During low temperature operation a needle valve allows to fill the multi-walled tube with ^{4}He from the main tank.

The ^{3}He unit is composed of the 1-K-pot and the ^{3}He-pot with the charcoal sorption pump used to achieve about 300 mK by pumping on the liquid ^{3}He. To

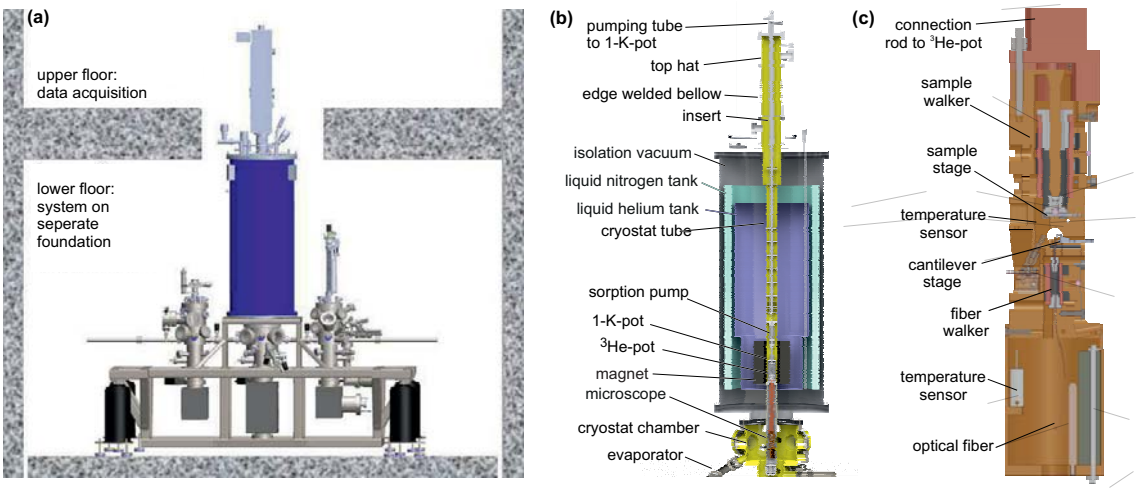

Figure 3.39: **(a)** Layout of the UHV-system in the two-story lab. The UHV system is mounted on a frame that is supported by four passive damping legs that stand on a separate foundation in the lower floor. The three main chambers are aligned symmetrically in a row with the cryostat depicted in **(b)** placed on top of the central vessel. The microscope shown in **(c)** is attached to a copper rod that serves as a thermal link between the small ^{3}He-pot and the microscope body. Cooling is performed by pumping with a sorption pump attached to the 1-K-pot on the ^{3}He-pot. Using a motor driven bellow the insert can be moved between the central chamber, where tip and sample can be exchanged *in-situ*, and the measurement position in the center of the 10 T superconducting magnet. Additionally, the flexible bellow allows aligning the insert, so that it does not touch the walls of the cryostat tube.

microscope is attached to the ^{3}He-pot via a copper rod. Microscope body, copper rod and 1-K-pot are surrounded by a radiation shield fixed to the 1-K-pot. The radiation shield features a rotating shutter that can be opened to exchange tip and sample, if the microscope is lowered into the cryostat chamber. The insert is connected to the top flange of a small chamber on top of the z-shift via the central 1-K-pot pumping tube. Radiation baffles fixed to the insert prevent room temperature radiation from entering the ^{3}He unit from above. Room temperature radiation from below is blocked by spring loaded flaps which are thermally anchored to the liquid nitrogen tank. They automatically open or close, when the insert is moved down or up.

To replenish the 1-K-pot with helium it is connected via a flexible spiraled capillary to the main helium tank. The flow can be adjusted via a needle valve. All electrical wires required to operate the microscope and the ^{3}He unit as well as the glass fiber are brought into the cryostat via feedthroughs attached to this small chamber. The wires are thermally anchored at the sorption pump, which is connected to the 1-K-pot, and at the copper rod between ^{3}He-pot and microscope body. To increase the thermal path from the ^{4}He bath and the liquid nitrogen tank to the outer walls at room temperature and to compensate for any differential thermal expansion between 4 K (low temperature operation) and 400 K (bake-out temperature), a hydro-formed bellow assembly is implemented.

To monitor the temperature several Cernox and RuO_2 temperature sensors are mounted to the microscope body, the ^{3}He-pot, the 1-K-pot and the sorption pump.

condition	t_h	T_b
^{3}He-pot without microscope, continuous operation	42 h	307 mK
^{3}He-pot without microscope, single shot operation	21 h	333 mK
^{3}He-pot with microscope, single shot operation, laser off	12 h	350 mK
^{3}He-pot with microscope, single shot operation, laser on	7 h	500 mK

Table 3.2: Hold times t_h and base temperatures T_b for different conditions. Continuous (single shot) operation means that the 1-K-pot is pumped (not pumped). AFM experiments can only be performed without pumping the 1-K-Pot and of course with laser on (last row). Here, T_b and t_h are limited by stray light, which can be reduced by mirror coating the fiber end as well as the cantilever backside.

Heaters at the ^{3}He-pot and the sorption pump allow to perform temperature dependent experiments. The result of the hold time tests and base temperature in different set-ups are summarized in table 3.2. Single shot mode indicates that the 1-K-pot is not pumped, which increases the hold time and the base temperature, but reduces the level of vibrational noise. Only in this mode of operation high resolution is possible.

The microscope displayed in Fig. 3.39 (c) is conceptually very similar to earlier designs [7, 8]: It features a Rugar-type interferometer set-up [9] and utilizes two Pan-type piezo-driven stepper motors to approach the fiber end to the backside of the cantilever as well as to approach the sample to the tip. However, several modifications were introduced. To reduce the thermal load caused by the wiring, we selected the stick-slip configuration (one wire plus ground for each stepper motor) and not the walker configuration (six wires for each plus ground for each stepper motor). To facilitate fast thermalization the microscope body is not made from MACOR but from phosphorous bronze. The cantilever stage can also accommodate a wire tip holder to perform scanning tunneling microscopy (STM) and appropriate wiring using shielded twisted pair cables for low noise tunneling current measurement using a preamplifier outside the UHV system.

We conducted several test measurements to demonstrate the performance of the microscope at cryogenic temperatures. The results are shown in Fig. 3.40. As insulating test system we prepared NaCl(001) by *in-situ* cleavage. In (a), recorded at 519 mK, the typical stepped surface structure of NaCl(001) is visible. In (b) atomic resolution is demonstrated on the same sample at 548 mK. The oscillations visible in both images stem from low frequency vibrations that appear, when the insert touches the cryostat tube.

As a metallic test sample a submonolayer Mn on W(110) was prepared. Regarding cleanliness, it is a more demanding test system because it is prone to contaminations, if the pressure during preparation or transfer is too high. On the other hand, it is a magnetically interesting sample, as a monolayer Mn on W(110) exhibits an out-of-plane antiferromagnetic spin spiral in the $[1\bar{1}0]$ direction with a periodicity of about 12 nm and a relative spin orientation of adjacent Mn atoms of 173° [10]. The W(110) crystal was cleaned by repeated cycles of oxygen glowing at about 1500 K for 30 minutes and flashing at a temperature of 2200 K for 15 s. Subsequently, Mn was evaporated from a crucible onto the W(110) substrate. The temperature of the crystal was kept constant at 110°C during evaporation and the following annealing

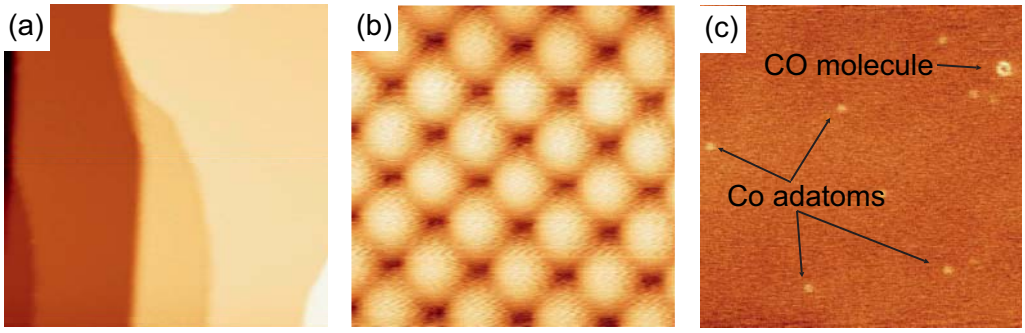

Figure 3.40: **(a)** 500 nm × 500 nm topography of a cleaved NaCl(001) sample recorded at 519 mK. Clean terraces are separated by steps with a height of one or more interlayer distances $a/2 \approx 282$ pm). **(b)** Atomically resolved NaCl(001) of an area of 2 nm × 2 nm recorded at 548 mK. **(c)** 50 nm × 50 nm topography of a Mn covered area on a W(110) substrate after deposition of Co atoms onto the cold surface. Individual Co adatoms are clearly visible with only one contamination feature that can be identified as a CO molecule.

process, which lasted 10 min. The pressure of the system during Mn evaporation did not exceed $2.9 \cdot 10^{-10}$ hPa. Afterwards, the sample was transferred to the cryostat chamber and inserted into the microscope in order to check the quality of the sample preparation. Subsequently, the microscope was lowered into the cryostat chamber and Co atoms were evaporated from an electron beam evaporator attached to the cryostat chamber onto the cold Mn/W(110) ($T \approx 30$ K) sample inside the microscope. The result is displayed in Fig. 3.40(c). Small randomly distributed protrusions indicate the positions of individual Co adatoms. The image shows eight well separated Co atoms within an area of 50 nm × 50 nm and one CO contamination that can be identified by its peculiar donut shaped appearance [11].

To determine the fundamental force sensitivity of our microscope, the cantilever temperature is the figure of merit [12]. Since the cantilever is illuminated by light, its temperature can differ from the temperature measured by the thermometers attached to the microscope body. In principle, the cantilever temperature can be determined by measuring the thermal noise power spectrum, fitting a Lorentzian line shape to the resonance peak at the eigenfrequency $f_0 = 2\pi\omega_0$ and applying the equipartition theorem [13, 14]. However, as we discuss in a joint publication with theoretical support from R. Bakhtiari and M. Thorwart (I. ITP, University of Hamburg) [17], it turns out that the situation is more complex. First, it is important to distinguish between the *mode temperature* T_m of the cantilever eigenfrequency and the *phonon temperature* T_ph of the cantilever material defined by the occupation of its phonon density of states. T_ph would be measured with a conventional resistive thermometer, while a thermal noise spectrum yields T_m. For interferometric detection schemes these two temperatures are not necessarily identical, because interaction with light due to radiation pressure or photothermal effects can influence the cantilever dynamics significantly [15, 16]. We further find that for low light powers, which are desirable in cryogenic environments, intensity noise can alter the cantilever dynamics dramatically.

First, one has to consider that the incident laser beam hits the cantilever at its free end, while the heat has to be carried away via the clamped end at the environmental temperature T_env. Therefore, a temperature gradient $T(x)$ develops, which

depends on the laser power P, absorption coefficient α_λ at the laser wavelength λ, thermal conductivity $\Lambda(T)$ and on the cantilever dimensions ($L \times W \times T$), and can be simulated using finite element calculus as shown in Fig. 3.41(a). As we demonstrate in Ref. [17] such a temperature gradient can be represented by a cantilever with a homogeneous temperature $T_{\rm eff}$ that would experience the same thermal drive. Note that this $T_{\rm eff}$ temperature is related to $T_{\rm ph}$ and not $T_{\rm m}$. However, $T_{\rm ph}$ and $T_{\rm m}$ are interrelated via $T_{\rm m}/T_{\rm ph} = Q_{\rm m}/Q_0$, where Q_0 is the intrinsic mechanical quality factor of the cantilever without the influence of light and $Q_{\rm m}$ is the mechanical quality factor that belongs to $T_{\rm m}$ and can be determined from the width of the resonance peak. To obtain $T_{\rm ph}$ using the above formula one has to find a way to determine Q_0.

A method to obtain Q_0 by measuring $Q_{\rm m}(D)$ was suggested by Hölscher et al. [16]. This method utilizes the fact that $Q_{\rm m}$ (as well as $T_{\rm m}$) depends on the distance D between cantilever back-side and fiber end. Figure 3.41(b) shows the

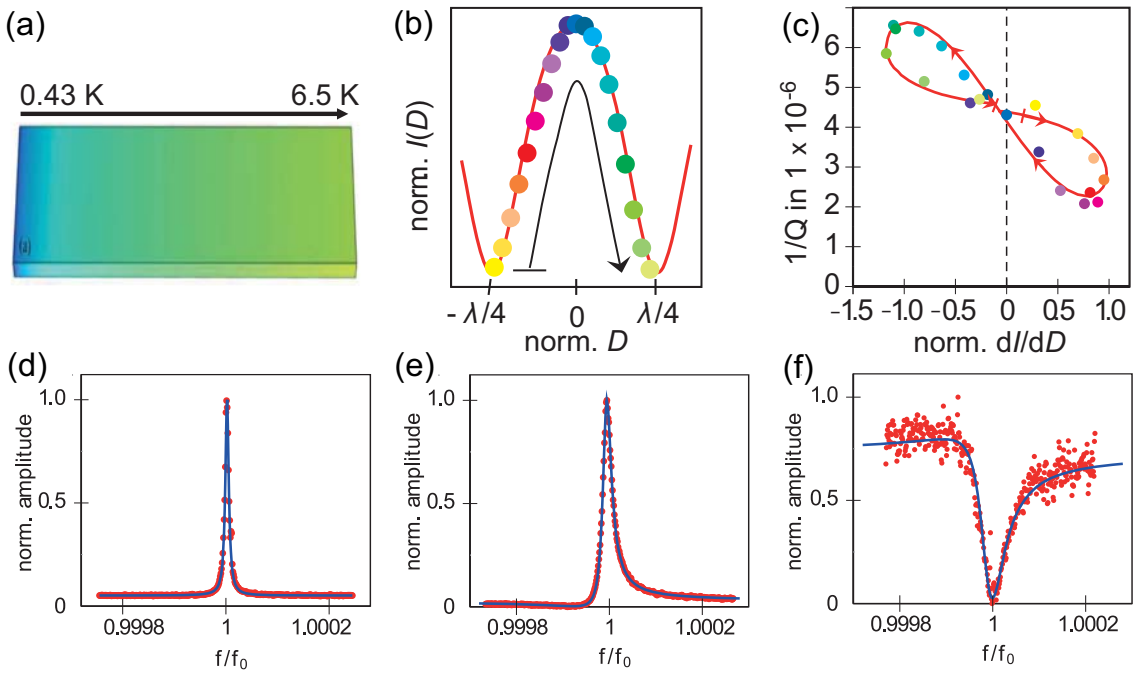

Figure 3.41: **(a)** Color-coded temperature gradient $T(x)$ of a cantilever simulated using the finite element based simulation tool COMSOL [18]. The left side is attached to a temperature bath with $T_{\rm env} = 430$ mK while the right side is heated by a laser with an incident power of 29.1 μW. **(b)** Distance dependent periodic interferometer signal $I(D)$ with D normalized by λ. Arrows and colored dots indicate the positions, where $Q_{\rm m}(D)$ data points were recorded. **(c)** $Q_{\rm m}^{-1}$ vs. $\mathrm{d}I/\mathrm{d}D$ plot using measured $Q_{\rm m}(D)$ data. Q_0 is obtained at the y-intersection. The solid line is a fit according to our model, which assumes that radiation pressure alters the cantilever dynamics. **(d)** Symmetric resonance peak that can be fitted with a Lorentzian line shape to determine the mode temperature $T_{\rm m}$ and the corresponding Q-factor $Q_{\rm m}$. Note that in general $T_{\rm m}$ and $Q_{\rm m}$ are different on the positive and negative slope of the interferometer signal. **(e)** Asymmetric resonance peak that cannot be fitted with a Lorentzian line shape but with a Fano line shape. **(f)** Asymmetric antiresonance recorded a the negative slope of the interferometer signal, which can also be fitted to a Fano line shape. For the same cantilever and the same optical power an asymmetric resonance peak like in **(e)** was observed.

distance dependence $I(D)$ of the interferometer signal, which exhibits a $\lambda/2$ periodicity. Depending on the slope, the interaction between light and cantilever increases or decreases Q_m (and T_m). The magnitude of the effect is largest, where the slope is largest. The effect vanishes at the maxima and minima of the interferometer signal, but since the slope is zero it is impossible to measure the deflection of the cantilever at these points. However, the y-intersection of a Q_m^{-1} vs. $\mathrm{d}I/\mathrm{d}D$ plot corresponds to $1/Q_0$. As explained above no data points can be taken at the y-intersection, but if the cantilever dynamics is altered by photothermal forces it can be shown that the plot results in a straight line. Hence, $1/Q_0$ can be obtained from a fit [16].

Following this idea, we measured $Q_\mathrm{m}(D)$ from resonance curves obtained by exciting the cantilever with a dither piezo. The different positions in which the resonance curves were recorded are indicated by the colored dots in Fig. 3.41(b). We do not find a straight line but a peculiar tilted eight shape in the Q_m^{-1}-$\mathrm{d}I/\mathrm{d}D$-plot as shown in Fig. 3.41(c). A thorough analysis of the equation of motion for the cantilever in the presence of light reveals that such a shape occurs, if the cantilever dynamics is altered exclusively by radiation pressure [17]. If radiation pressure and photothermal forces are present, the eight shape gets squeezed until it becomes a straight line, if the latter dominates. In any case, $1/Q_0$ can always be determined at the y-intersection. Note that the fundamental limit of the force sensitivity of a cantilever depends on the ratio $\sqrt{T/Q}$ [12]. If the cantilever is cooled by the interaction with light, meaning $T_\mathrm{m} < T_\mathrm{ph}$, the corresponding Q_m gets smaller so that the ratio $T_\mathrm{m}/Q_\mathrm{m} = T_\mathrm{ph}/Q_0$ stays constant. Thus, the force sensitivity cannot be increased by lowering the mode temperature, because Q_m gets smaller by the same factor.

To achieve the highest force sensitivity, the cantilever temperature should be as small as possible. If light absorption takes place, it is beneficial to use low light powers. However, we find that small light powers can result in peculiar line shapes. Figure 3.41 (d)-(f) displays three thermal noise spectra recorded with different light powers at environmental temperatures $T_\mathrm{m} \approx 500$ mK of the microscope body. Only the curve in (d) is symmetric and can be fitted with a Lorentzian line shape to determine T_m, while the curve in (e) is clearly asymmetric and in (f) even an antiresonance is visible.

As we discuss in detail in Ref. [17] the asymmetric line shapes in (e) and (f) are the result of a superposition of a continuum of states provided by the photon number fluctuation noise of the laser light and the discrete states of the cantilever eigenmodes. This general phenomenon occurs in many different areas of physics and has been first described by Fano [19]. This Fano resonance converges into a Lorentzian line shape, if the coupling between discrete and continuum states is weak, i.e., in our case, if the laser noise is negligible. Reducing the laser power by reducing the driving current leads to a larger relative laser noise. This modifies the cantilever dynamics and renders the cantilever resonances asymmetric. Even antiresonances can appear at the position of the cantilever eigenfrequency. In any case, a Fano line shape can be fitted to such data as demonstrated in (e) as well as (f) by the red curves. In principle it is possible to determine the cantilever temperature T_ph from such a fit. However, in our experimental set-up too many parameters are not very well known. Therefore, it is not possible to obtain a reliable fit.

References

[1] U. Kaiser, A. Schwarz and R. Wiesendanger, Nature **446**, 522 (2007).

[2] R. Schmidt, U. Kaiser, C. Lazo, A. Schwarz, R. Wiesendanger, and S. Heinze, Phys. Rev. Lett. **106**, 257202 (2011).

[3] H. von Allwörden, K. Ruschmeier, A. Köhler, T. Eelbo, A. Schwarz, and R. Wiesendanger, Rev. Sci. Instrum., **87**, 073702 (2016).

[4] Heliox type insert from Oxford Instruments, Tubney Woods (UK); www.oxford-instruments.com.

[5] M. Kugler, C. Renner, V. Mikheev, and G. Batey, Rev. Sci. Instrum. **71**, 1475 (2000).

[6] J. Wiebe, A. Wachowiak, F. Meier, D. Haude, T. Foster, M. Morgenstern and R. Wiesendanger, Rev. Sci. Instrum. **75**, 4871 (2004).

[7] W. Allers, A. Schwarz, U. D. Schwarz, and R. Wiesendanger, Rev. Sci. Instrum. **69**, 221 (1998).

[8] M. Liebmann, A. Schwarz, S. M. Langkat, and R. Wiesendanger, Rev. Sci. Instrum. **73**, 3508 (2002).

[9] D. Rugar, H. J. Mammin, and Guethner, Appl. Phys. Lett. **55**, 2588 (1989).

[10] M. Bode et al., Nature **447**, 190 (2007).

[11] A. Schwarz, A. Köhler, J. Grenz, and R. Wiesendanger, Appl. Phys. Lett. **105**, 011606 (2014).

[12] T. R. Albrecht, Pr. Grütter, D. Horne, and D. Rugar, J. Appl. Phys. **69**, 668 (1991).

[13] H. J. Mamin and D. Rugar, Appl. Phys. Lett. **79**, 3358 (2001).

[14] J. Welker, F. de Faria-Elsner, and F. J. Giessibl, Appl. Phys. Lett. **99**, 084102 (2011).

[15] C. H. Metzger and K. Karrai, Nature **432**, 1002 (2004).

[16] H. Hölscher, P. Milde, U. Zerweck, L. M. Eng, and R. Hoffmann, Appl. Phys. Lett **94**, 223514 (2009).

[17] G. Fläschner, K. Ruschmeier, A. Schwarz, M. R. Bakhtiari, M. Thorwart, and R. Wiesendanger Appl. Phys. Lett. **106**, 123102 (2015).

[18] www.comsol.de.

[19] U. Fano, Phys. Rev. **124**, 1866 (1961).

3.9.2 Utilizing the permanent electrostatic dipole moment of metallic tips for high resolution imaging

A. Schwarz, J. Grenz, A. Köhler, and R. Wiesendanger

Together with D. Z. Gao, M. B. Watkins, F. F. Canova from the group of Prof. Shluger at the UCL we studied the role of the electrostatic properties of an atomically sharp metallic tip apex [1,2]. We found that due to the Smoluchowski effect [3] such tips exhibit a permanent electrostatic dipole moment that points with its positive end towards the sample surface. This dipole moment can be utilized for atom identification on polar surfaces [4] and is very important to understand the contrast formation on polar molecules

Figure 3.42(a) shows two models of close-packed metallic pyramidal tip apices. They can be classified by the number of layers. According to density functional theory (DFT) calculations larger pyramids, i.e., sharper tip apices possess larger total dipole moments. Expectedly, their magnitudes eventually saturate for large pyramids. The dipole moment is positive, meaning that the positive pole is pointing towards the surface. The calculation has been performed for Cr, but due to the universality of the Smoluchowski effect similar results are expected for all close-packed metal tips. However, if the atoms at the apex are not close-packed or if the tip apex is made of different chemical species, the dipole moment could also point in the opposite direction. It should be noted that also non-metallic tips can possess an electrostatic dipole moment, e.g., oxygen terminated silicon tips (oxygen has a larger electronegativity than silicon) or tips functionalized with carbon monoxide (CO is a polar molecule). In the inset of (b) the color-coded electrostatic potential emanating from a three-layer close-packed Cr pyramid with a total dipole moment

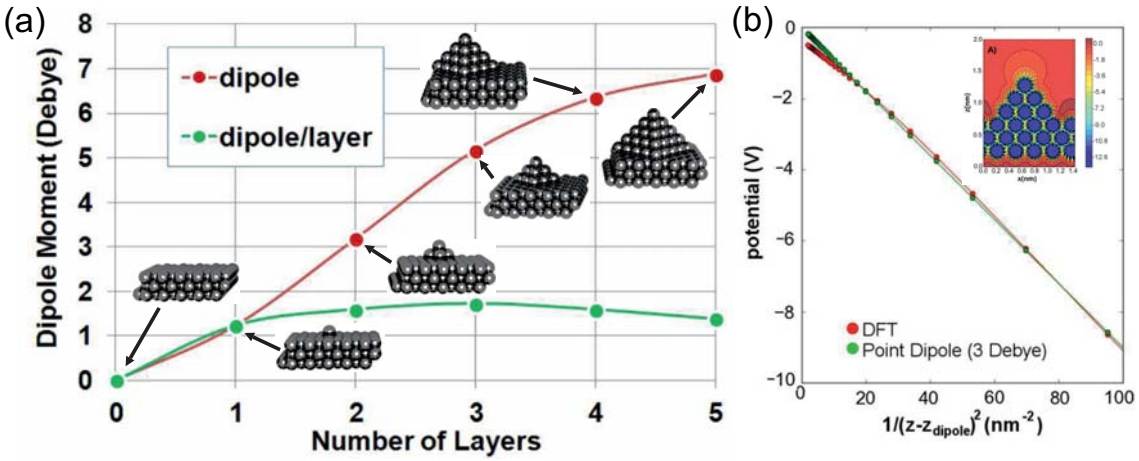

Figure 3.42: **(a)** The total dipole moment of various pyramidal Cr tip apices as a function of pyramid height. The dipole moment found at the tip apex of these asperities increases with pyramid size and eventually converges to a maximum value. **(b)** Demonstration that a 3 D point dipole positioned at the atomic coordinates of the apex atom (green) is able to reproduce the local electrostatic potential obtained from DFT calculations (red). The inset shows the color-coded electrostatic potential emanating from a 3-layer close-packed Cr tip pyramid.

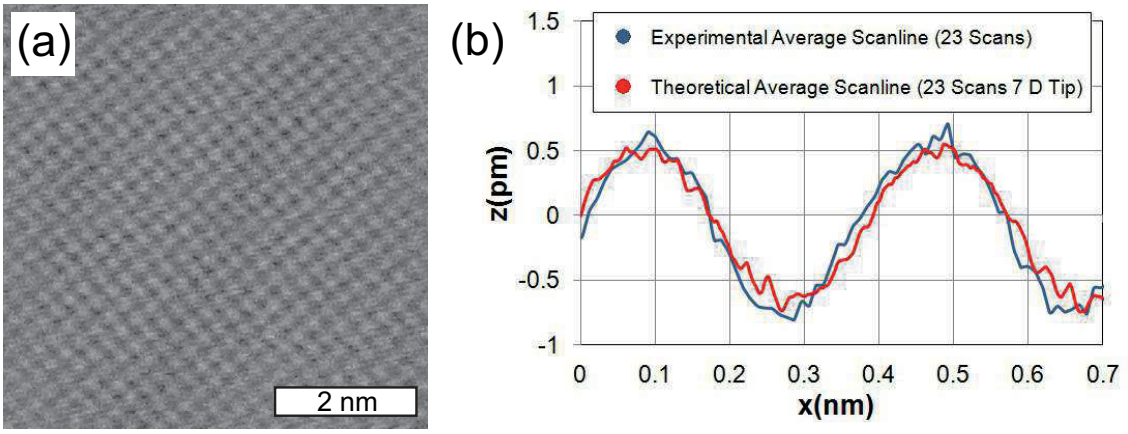

Figure 3.43: **(a)** Atomically resolved NiO(001) using a Cr coated tip recorded at 8 K. Protrusions (bright) and depressions (dark) correspond to the positions of oxygen and nickel ions, respectively. **(b)** Averaged atomic corrugation along the [001]-direction (blue) and a virtual-AFM simulation using the point-dipole approximation (red).

of 5 D is shown. The electrostatic potential emerging from such a tip can well be simulated by a simple electrostatic dipole moment as demonstrated in (b). The plot shows the electrostatic potential with respect to distance away from the tip apex according to DFT calculations and the corresponding electrostatic potential of a 3 D point-dipole positioned at the atomic coordinates of the foremost tip atom.

We tested the model on NiO(001), a well-defined ionic surface. Figure 3.43(a) shows an atomically resolved image recorded with a Cr coated tip. In (b) the average of 23 experimental scan lines across minima and maxima in the [100]-direction is displayed together with a simulated scan line using a virtual AFM (vAFM) code [5]. Note that the vAFM code does not only integrate the equation of motion of the cantilever, but also models the feedback loops and thus provides a full simulation of the real experiment including noise. For the simulation the long-range van der Waals interaction between tip and sample were taken into account as well. The parameters were obtained by fitting an experimental force-distance curve recorded with the same tip up to a distance of 10 nm away from the surface and assuming a spherical mesoscopic tip shape. Note that long-range electrostatic forces are negligible, because during all measurement the average local contact potential difference was nullified by applying an appropriate bias voltage. Further, the short-range van der Waals interaction between nano-tip and surface turned out to be negligible in our case as well. Although the agreement between experimental and theoretical scan-lines for this dipole moment value is remarkably good, it should be stressed that magnitude and position of the point dipole are interrelated and cannot be uniquely defined. They provide only plausible information about the actual atomic structure of the tip.

To further demonstrate the feasibility of our model we used exactly the same nano-tip to image carbon monoxide (CO) adsorbed on NiO(001). In the gas phase CO possesses a permanent electrostatic dipole moment of about 0.1 D with its positive pole at the oxygen atom. If such a polar molecule is imaged with a metallic tip the dipole-dipole interaction is certainly important for the contrast formation during imaging.

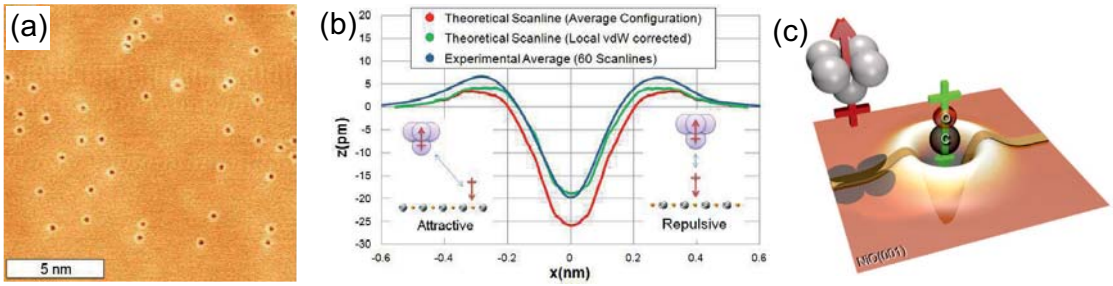

Figure 3.44: **(a)** CO molecules on the NiO (100) surface imaged at 8 K with the same nano-tip as in Fig. 3.43. They appear as bright rings with a central depression (donuts). **(b)** Representative averaged experimental scan line in the [100] direction of 60 CO molecules (blue curve). The theoretical curve (red) was obtained by using the same point-dipole parameters as for the simulation in Fig. 3.43. Including local van der Waals (vdW) interactions (green curve) improves the agreement with the experiment. The inset explains the transition from a repulsive electrostatic interaction above the center of the CO molecule to an attractive interaction in its periphery. **(c)** Rendered model of imaging a CO molecule with a metallic tip apex.

According to theoretical calculations and experimental results, CO adsorbs with its carbon atom above Ni sites and possesses an enhanced dipole moment of 0.4 D that points with its positive pole away from the surface [1, 6, 7]. Figure 3.44 (a) shows an overview topography, in which the CO molecules appear as bright rings with dark depressions in the center. In (b) a representative averaged scan line across 60 of these donut-like contrast patterns along the [001]-direction of the substrate is compared with a theoretical scan line (red), which was obtained employing exactly the same point-dipole parameters used to simulate the atomic corrugation on NiO(001). As indicated by the inset, which sketches the relative alignment between tip and CO dipole moment, the electrostatic interaction between tip and sample is repulsive directly above the CO molecule (parallel alignment of dipoles; central dark depression), but becomes attractive, if the distance is increased laterally (more antiparallel alignment; bright ring). The remaining discrepancy can be explained by local short-ranged van der Waals forces between the CO-molecule and the nano-tip. If this contribution is taken into account applying a semi-empirical method [8] the agreement is excellent (green curve).

The fact that the local van der Waals interaction plays a role for the contrast formation is demonstrated in Fig. 3.45 (a)-(c), where CO molecules on Cu(111), NiO(001) and Mn/W(001) are imaged at relatively large (upper row) and small (lower row) tip-sample distances. Rather far away the attractive van der Waals force dominates and a CO-molecule appears as a protrusion. Only at a sufficiently small tip-sample distance the characteristic donut-like shape evolves. This transition can also be seen as a crossover of two $\Delta f(z)$-spectroscopy curves as displayed in (d). The blue curve was recorded on the bare Mn/W(001) substrate and the red curve directly on top of a CO molecule. Subtracting both curves from each other (inset) yields the pure interaction between tip and molecule alone. The curve has the appearance of a Lennard-Jones type interaction, but in this case the repulsion stems from electrostatic repulsion and not from Pauli repulsion. Note that at smaller distance the much stronger Pauli-repulsion would become dominant. In this case the

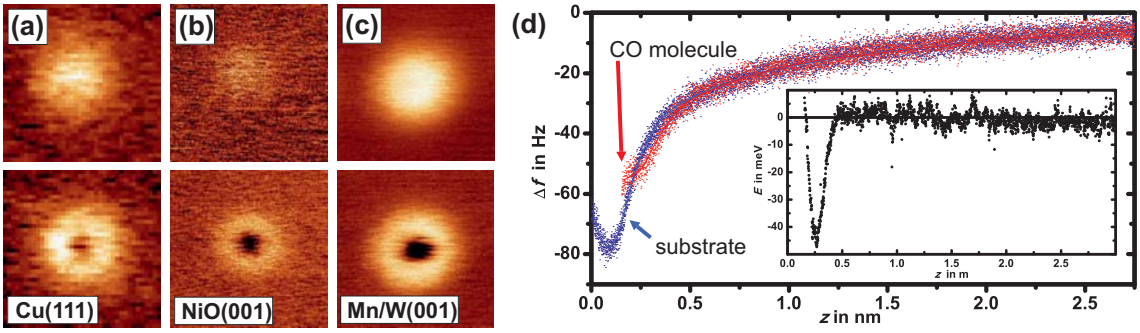

Figure 3.45: Images of single CO molecules on **(a)** Cu(111), **(b)** NiO(001), and **(c)** Mn/W(001). Images in the lower row are recorded at about 0.2 nm smaller tip-sample separations. **(d)** $\Delta f(z)$ recorded above the bare Mn/W(001) substrate (blue) and above the CO molecule (red). The difference $\Delta f_{\mathrm{CO}}(z) = \Delta f_{\mathrm{S}}(z) - \Delta_{\mathrm{M}} f(z)$ was used to calculate the pure tip-molecule interaction energy $E_{\mathrm{CO}}(z)$ shown in the inset.

CO molecule would bend sideways first - an effect that has been recently studied for CO-functionalized tips [9] - and at even smaller separations would leave its adsorption site. Such a tip induced lateral manipulation is well known, e.g., for CO on Cu(111) [10].

Our finding demonstrates that the simple point-dipole model with the inclusion of short-ranged van der Waals forces is sufficient to explain the contrast formation on polar molecules qualitatively. Even very good quantitative agreement can be achieved by *calibrating* the dipole moment of a tip apex on a well-defined polar surface. Such a calibration should be very useful to investigate the charge distribution of polar molecules adsorbed on surfaces, which usually leads to a rearrangement of charges that is different from the intramolecular charge distribution in the gas phase.

References

[1] D. Z. Gao, J. Grenz, M. B. Watkins, F. F. Canova, A. Schwarz, R. Wiesendanger, and A. L. Shluger, ACS Nano **8**, 5339 (2014).

[2] A. Schwarz, A. Köhler, J. Grenz, and R. Wiesendanger, Appl. Phys. Lett. **105**, 011606 (2014).

[3] R. Smoluchowski, Phys. Rev. **60**, 661 (1941).

[4] G. Teobaldi, K. Lämmle, T. Trevethan, M. Watkins, A. Schwarz, R. Wiesendanger, and A. L. Shluger, Phys. Rev. Lett. **106**, 216102 (2011).

[5] F. F. Canova, A. S. Foster, M. K. Rasmussen, K. Meinander, F. Besenbacher, and J. V. Lauristen, Nanotechnology **23**, 325703 (2012).

[6] W. Wang, J. Li, and Y. Zhang, Appl. Surf. Sci. **252**, 2673 (2006).

[7] M. Kittel, J. T. Hoeft, S. Bao, M. Polcik, R. L. Toomes, J.-H. Kang, D. P. Woodruff, M. Pascal, and C. L. A. Lamont, Surf. Sci. **499**, 1 (2002).

[8] S. Grimme, J. Comput. Chem. **27**, 1787 (2006).

[9] H. Prokop, G. Kichin, C. Wagner, F. S. Tautz, R. Temirov, and P. Jelinek, Phys. Rev. B **90**, 085421 (2014).

[10] M. Ternes, C. P. Lutz, C. F. Hirjibehedin, F. J. Giessibl, and A. J. Heinrich, Science **319**, 1066 (2008).

3.10 Towards an atom-membrane hybrid quantum system

A. Schwarz, H. Zhong, G, Fläschner, R. Wiesendanger, C. Becker, A. Bick, C. Staarmann, P. Christoph, T. Wagner and K. Sengstock

Together with the group of Prof. Sengstock (ILP and ZOQ, University of Hamburg) we constructed an apparatus designed to realize a hybrid quantum system (HQS) comprised of a cryogenically cooled mechanical oscillator and ultra-cold ^{87}Rb atoms coupled via light [12]. The arrangement of the experiment in its dedicated laboratory is shown in Fig. 3.46. The outstanding feature of our instrument is an *in-situ* adjustable mode-matched asymmetric all-fiber membrane-in-the-middle (MiM) cavity located inside an ultra-high vacuum dilution refrigerator (DR) based cryostat. At this point we are able to prepare ^{87}Rb Bose-Einstein condensates (BEC) of $N = 2 \times 10^6$ atoms in less than 20 s and achieve a single photon optomechanical coupling strength of $g_0 = 2\pi \times 9\,\mathrm{kHz}$ employing a high-stress Si_3N_4 membrane with a mechanical quality factor $Q_\mathrm{m} > 10^7$ at a temperature of $T_\mathrm{MiM} = 480\,\mathrm{mK}$.

In general a HQS consists of two (or more) different physical quantum objects. Ideally, they combine complementary functionality in terms of e.g., manipulation, storage and detection of quantum states. The advent of quantum optomechan-

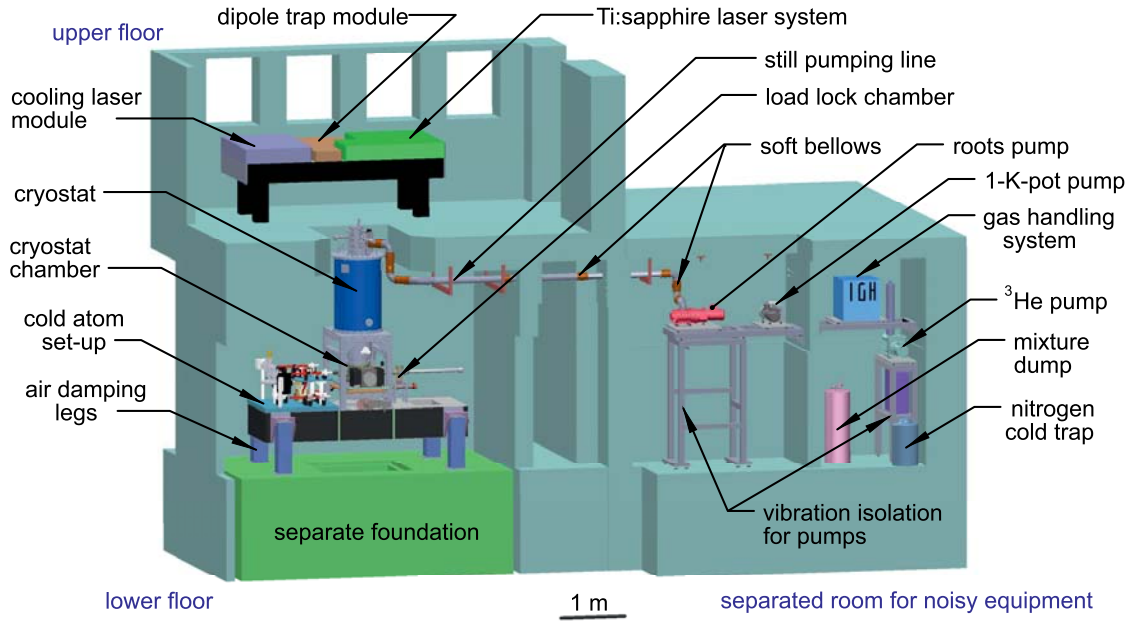

Figure 3.46: Overview of the laboratory with the experimental set-up. The UHV cryostat with the all-fiber MiM cavity inside, the cold atom set-up, and the homodyne detection scheme are placed on an optical table in the lower floor. To further reduce vibrational perturbations the table itself stands on a separate foundation. The coupling and detection laser system is assembled on a second optical table that is located in the upper floor, together with the experimental control and data acquisition system. All mechanical pumps used to run the DR as well as its gas handling system, the ^{3}He/^{4}He-mixture dump and the nitrogen cold trap are kept in a separate side room.

ics [1] with the possibility to cool mechanical oscillators to their quantum ground state [2–4], has opened up new perspectives to use them as one integral part of such HQS owing to the inherent ability of mechanical motion being able to 'interact with everything'. Once realized, such devices can be utilized, e.g., for highly sensitive optical detection of small forces and displacements, for manipulation and detection of mechanical motion in the quantum regime or as a coherent light-matter interface for quantum information processing [1]. Another particularly interesting class of objects for a HQS are atomic systems such as trapped ions or cold atoms [5, 6]. Due to their weak interaction with the environment, atomic systems possess very long coherence times. Hence, several proposals have been put forward for coupling cold atoms with mechanical oscillators, such as the interaction of the magnetic moments of a Bose-Einstein condensate (BEC) with a nanomagnet on a cantilever [7], or coupling a vibrating mirror to atoms in an optical lattice, which can drive the transition between a Mott insulator and a superfluid state [8]. One of the most intruiging possibilities of an atom-membrane HQS is the realization and detection of entanglement between microscopic and macroscopic degrees of freedom [9], either for studying the quantum to classical transition or for quantum information applications. Up to date the quantum ground state of a mechanical oscillator has been either reached by cryogenically cooling a GHz resonator [2], or by resolved sideband cooling of integral nanomechanical structures in optomechanical systems, both in the microwave [3] and optical [4] domain.

Resonant coupling of the motional degrees of freedom of cold atoms trapped in an optical lattice to the motion of a mechanical oscillator practically limits the frequency of the employed resonator to $f < 400\,\mathrm{kHz}$ [5, 6]. For such low-frequency mechanical oscillators cryogenic cooling alone is not sufficient to reach the quantum ground state. To accomplish this, further optomechancial cooling schemes have to be applied. To achieve strong coupling between a mechanical oscillator and atoms, the total decoherence rate in the combined system has to be sufficiently small. Main contributions to that rate include resonant light scattering at the atoms, cavity loss and heating the mechanical oscillator by light absorption and light pressure shot noise.

We decided for Si_3N_4 membranes as mechanical oscillator in our system because they are readily available, exhibiting low optical absorption and high mechanical Q factors. For the atomic part we selected ^{87}Rb atoms, because they can be very well controlled and possess suitable external and internal degrees of freedom for our envisaged coupling experiments. A thorough analysis reveals that for this HQS an optimal regime exists for a cavity finesse of $F \approx 500$. Taking into account the very short cavity length of a mode-matched all-fiber cavity ($L_{\mathrm{cav}} \approx 25\,\mu\mathrm{m}$) [10] and the corresponding very large free spectral range (FSR $\approx 6\,\mathrm{THz}$), the typical linewidth of such a medium finesse all-fiber cavity is very broad ($\Delta\nu \approx 12\,\mathrm{GHz}$). Thus, we are well outside the so-called 'resolved sideband regime' and the corresponding optomechanical cooling schemes [3,4] cannot be applied efficiently for our system. However, ground state cooling of a low-frequency mechanical oscillator can be achieved by active feedback cooling [11], if the environmental temperature is low enough. In our experiment this requirement is fulfilled by placing the MiM cavity set-up in a DR. With this cooling scheme minimal temperatures below 10 mK can be realized.

Details of the whole set-up including all parts visible in Fig. 3.46 are detailed

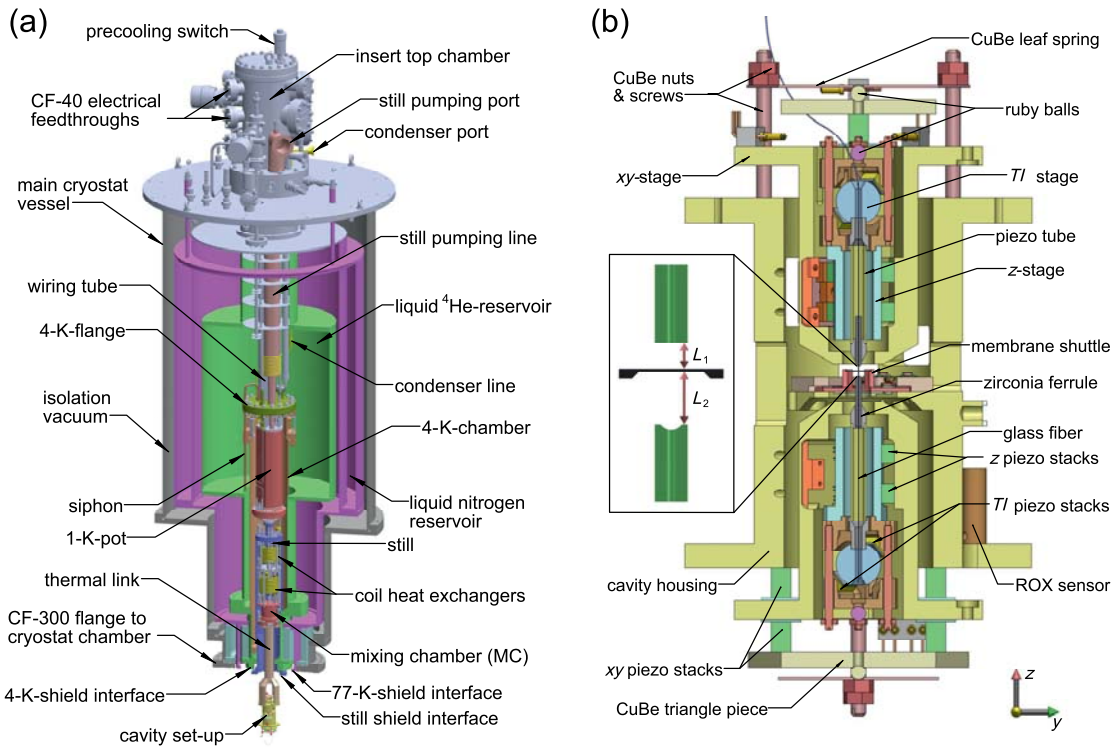

Figure 3.47: **(a)** Section view of the cryostat. It comprises a main vessel with the insulation vacuum ($p < 10^{-4}$ mbar), the liquid nitrogen reservoir (purple), the liquid ^{4}He-reservoir (green) and the insert with a small chamber on top. The DR unit (including 1-K-pot, still, two stainless steel coil heat exchangers and the MC) are located directly below the 4-K-flange. The cavity set-up is mounted to the MC via a thermal link, so that it is, surrounded by a set of radiation shields, situated in the center of the cryostat chamber. **(b)** Section view of the all-fiber MiM cavity set-up. The cavity housing encloses two identical piezo-driven positioning stages with a z-, xy-, and $\theta\phi$-stepper motor, which provide five degrees of freedom for each fiber. The membrane receptacle is located between them. Both fibers are glued into a piezo tube to fine adjust their z-positions and to scan the cavity length L_{cav} as well as the fiber-membrane spacings L_1 and L_2. The MiM cavity temperature T_{MiM} is measured with a ROX sensor as well as with a Cernox sensor attached to the cavity housing.

in Ref. [12]. Figure 3.47(a) shows the crystat with the DR-unit. The MiM cavity set-up attached via a thermal link to the mixing chamber (MC) is shown in (b). The thermal link is used to bring the cavity set-up down to a vacuum chamber below the cryostat, where it is surrounded by a set of three radiation shields at 77 K, 4 K and 0.7 K respectively. Four apertures in the shield assembly allow for visual inspection of the *in-situ* fiber alignment procedure. A fifth aperture is avaiable to *in-situ* exchange membranes using a wobble stick (new membranes can be introduced into the UHV-system via a load lock). A rotational shutter assembly that can be moved with the wobble stick allows to open and close the apertures.

The planar-concave mode-matched all-fiber MiM cavity is the central component of the optomechanical part of our experiment. It is an asymmetric cavity with different reflectivities of the dielectric coatings at the fiber ends, respectively [10]. Each fiber is glued into a zirconia (ZrO_2) ferrule, which in turn is glued to the free

end of a piezo tube, which is used to fine-adjust or to scan the cavity length. The lateral and angular fiber alignment is performed with high accuracy (better than 1 nm and 0.1°, respectively) using two piezo-driven 5-axes (x, y, z, θ, and ϕ) alignment stages described in Ref. [13]. The total cavity length L_{cav} as well as the distance between both fibers and the membrane L_1 and L_2 can be determined with nanometer precision using white light interferometry or by measuring the distance between successive cavity resonances generated with the laser system shown in Fig. 3.47.

To achieve a coupling between the membrane and the ultra-cold atomic cloud, we use a titanium-sapphire laser operated at a wavelength close to the ^{87}Rb D2 line at a wavelength of $\lambda = 780\,\mathrm{nm}$. This laser can be widely tuned and Pound-Drever-Hall-locked to an external Fabry-Pérot transfer cavity with a free spectral range (FSR) of 1GHz, which is referenced to the ^{87}Rb cooling laser system. The light is divided into four different branches that serve as the coupling beam, the homodyne detection beam to determine the membrane motion, the Pound-Drever-Hall-locking beam for the fiber Fabry-Pérot cavity of the MiM set-up and the feedback beam for active feedback cooling of the membrane. The coupling and detection beams are coupled into the MiM setup from the planar side to allow optimal mode match and thus minimized losses [10]. For the less critical feedback and Pound-Drever-Hall beams we choose an incoupling from the curved side of the cavity.

The coupling beam is focused onto the atomic cloud with a waist size of $w_0 = 68\,\mu\mathrm{m}$ and then coupled into the MiM set-up. Afterwards, the reflected light from the MiM set-up interferes with the incoming beam and forms a 1D optical lattice at the position of the atoms providing the basis of the coupling scheme. To produce ultra-cold ^{87}Rb atoms visible in Fig. 3.47 a dedicated apparatus has been constructed and placed next to the cryostat on the same optical table in the lower floor. The set-up is based on a scheme consisting of a two-dimensional magneto-optical trap (2D-MOT) to catch atoms from a background gas and a 3D-MOT operating at pressures below 1×10^{-11} mbar. The two different vacuum glass cells are connected via a differential pumping stage allowing for pressure that can differ by a factor of 10^3. This setup has the advantage of providing extremely good optical access to the lower 3D-MOT glass cell allowing for different kinds of optical trapping, manipulation and detection schemes, such as optical lattices of different dimensionality, Raman laser configurations or momentum resolved Bragg spectroscopy.

In a typical experimental sequence we start by loading the 3D MOT for 10 s resulting in atom numbers of $N = 10^{10}$ at temperatures of $T \approx T_D =$ where $T_D = 146\,\mu\mathrm{K}$ is the Doppler temperature of ^{87}Rb. Subsequently, the atoms can be further cooled in an optical molasses reducing the temperature to $T_{\mathrm{min}} = 10\,\mu\mathrm{K}$, which amounts to several times the ^{87}Rb recoil temperature of $T_{\mathrm{rec}} = 362\,\mathrm{nK}$. For the purpose of generating a Bose-Einstein condensate (BEC), we load our atoms in a magnetic trap of hybrid cloverleaf 4D type. Forced evaporation cooling for less than 20 s allows producing Bose-Einstein condensates of $N_{\mathrm{BEC}} \approx 2 \times 10^6$ particles without any discernible amount of thermal atoms.

For continuous experiments our setup is equipped with a crossed optical dipole trap derived from a Nd:YAG laser operated at 1064 nm with circular beam waists of $52\,\mu\mathrm{m}$ and $242\,\mu\mathrm{m}$. The maximum available optical power at the experiment is 8 W per beam. The BEC inside this dipole trap has an elongated cigar like shape and corresponding trapping frequencies $(\omega_y, \omega_z) = 2\pi \times (85, 62)$ Hz, where

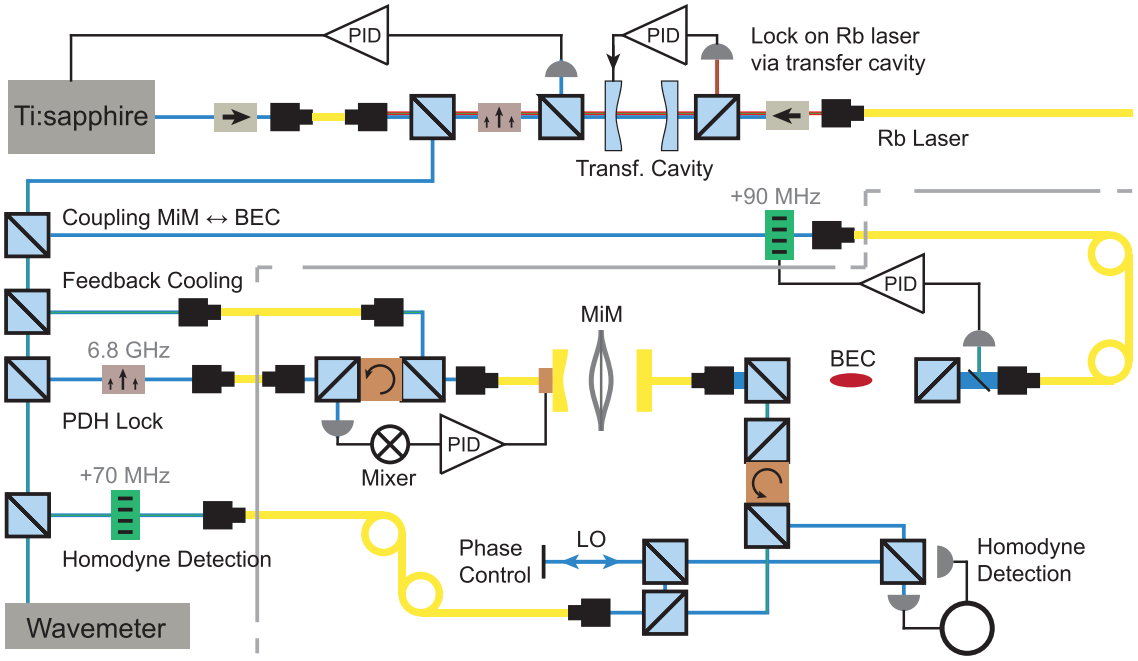

Figure 3.48: Coupling and detection laser system based on a titanium-sapphire laser locked via a transfer cavity to the ^{87}Rb laser cooling system. Four different beam branches are derived by polarizing beam-splitter cubes and are guided to the lower floor laboratory using polarization maintaining fibers (yellow lines). The coupling beam is frequency shifted and intensity controlled by an acousto-optic modulator (AOM; green rectangle), passes the atomic cloud (indicated by the red ellipse), and is then coupled into the cavity via the planar fiber. The homodyne detection beam is superimposed with the coupling lattice beam and also coupled to the MiM cavity from the planar side owing to the much better mode match. LO denotes the local oscillator beam of the homodyne detection. The Pound-Drever-Hall (PDH) locking beam is phase modulated with an electro-optical modulator (EOM; light gray box) and superimposed with the feedback cooling beam using an optical isolator (brown square with circular arrow) and coupled into the cavity via the curved fiber end.

gravity points along the z-direction. The beam with the larger beam waist can be used to tune ω_x between $2\pi \times (1 \ldots 20)$ Hz. Thereby we can vary the elongation of the atomic cloud along the direction of the coupling lattice or coupling Raman beams, respectively. For experiments aiming at coupling internal atomic degrees of freedom to the motional state of a mechanical oscillator it is necessary to trap the atoms in a potential that is independent of the particular internal state, which is guaranteed by a far detuned optical dipole potential. From the same laser we also derive a two-dimensional optical lattice perpendicular to the coupling lattice that enables us to confine the atoms in a three-dimensional periodic potential and to freeze out all continuous degrees of freedom. The properties of the cold atom sample are detected using a flexible absorption imaging system allowing for different magnification ranging from 0.5 to 10.

The asymmetric mode-matched cavity consists of a planar fiber end with a nominal reflectivity $|r_1|^2 = 0.907$ (for incoupling) and a curved fiber end (radius of curvature $r_{\mathrm{ROC}} \approx 50\ \mu$m) with a nominal reflectivity $|r_2|^2 = 0.995$ (for outcoupling). After thorough alignment of the cavity, typical empty cavity power transmission

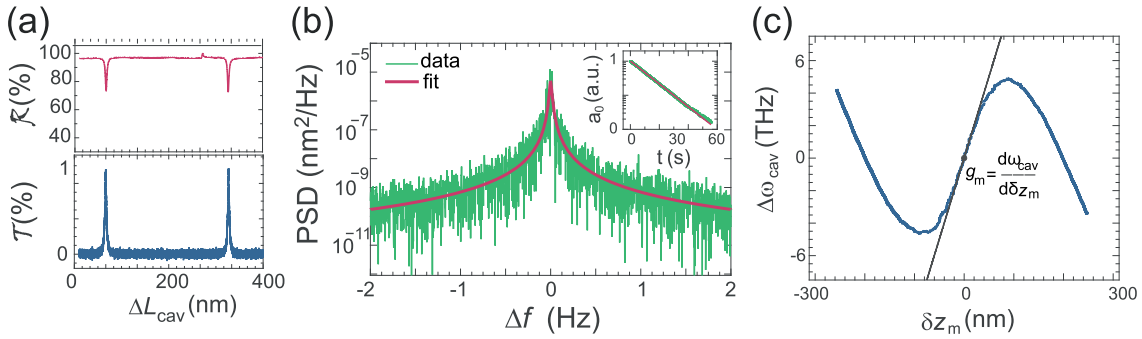

Figure 3.49: **(a)** Empty cavity power transmission $\mathcal{T}$ and power reflection $\mathcal{R}$ at about 25 K as function of cavity length L_{cav}. **(b)** Power spectral density around the thermal peak of the (1,1)-eigenmode at $f_(1,1) = 283.8$ kHz of a high-stress Si_3N_4 membrane at $T_{\mathrm{MiM}} = 485$ mK (green). From a Lorentzian fit (red line) a mode temperature $T_{1,1} = 3.623$ K is determined. The inset shows a logarithmic plot of a ring-down measurement (green) recorded at $T_{\mathrm{MiM}} = 485$ mK using the same membrane. From the ring-down time $\tau = (12,982 \pm 0.002)$ s, we obtain $Q_{1,1} = 10,757,900 \pm 1500$. **(c)** Measured detuning of the cavity resonance $\Delta\omega_{\mathrm{cav}}$ from its mean value in dependence of the membrane position change δz_{m}. We arbitrarily choose the zero point $z_{\mathrm{m},0} = 0$ where the optomechanical coupling, i.e., the derivative of the data displayed, is largest.

$\mathcal{T}$ and power reflection $\mathcal{R}$ signals as visible in Fig. 3.49(a) are obtained. The on-resonance reflectivity is about 75%. We determined an empty cavity finesse $F \approx 60$, which is found to be unchanged up to a cavity length of 25 μm. To insert a membrane, both fibers must be retracted and afterwards reapproached. Only minimal lateral and no angular adjustments are required after this procedure to again obtain a properly aligned MiM cavity.

Figures 3.49 (b) and (c) show two characterization measurements performed with our set-up using the fundamental eigenmode $f_{1,1} = 283.8$ kHz of a high-stress square Si_3N_4 membrane (nominal dimensions: 1.5 mm × 1.5 mm × 50 nm) from Norcada [14]. We determined its position in the cavity to be at $L_1 \approx 5.8$ μm and $L_2 = 17.9$ μm, respectively. The noise floor of our homodyne detection system of about 0.3 fm/$\sqrt{\mathrm{Hz}}$ around $f_{1,1}$ is on the same order of magnitude as the laser shot noise equivalent of 0.13 fm/$\sqrt{\mathrm{Hz}}$ for our set-up at 5 μW detection power. For the realization of an atom-membrane HQS the mode temperature $T_{1,1}$ (related to the mean phonon occupation number) and the corresponding mechanical quality factor $Q_{1,1}$ (related to the mechanical decoherence rate $n_{\mathrm{m}}\gamma_{1,1} = k_{\mathrm{B}}T_{1,1}/\hbar Q_{\mathrm{m}}$) are of key importance. The temperature can be determined using the equipartition theorem according to $T_{1,1} = k\langle x^2\rangle / k_{\mathrm{B}}$, where $k = (2\pi f_{1,1})^2 \cdot m_{\mathrm{eff}}$ is the spring constant of the membrane with an effective mass $m_{\mathrm{eff}} = 9.7 \times 10^{-11}$ kg [11]. $\langle x^2\rangle = (1/2\pi) \times \int_0^\infty S_x(\omega)d\omega$ is obtained by integrating the measured power spectral density $S_x(\omega)d\omega$ shown in Fig. 3.49(b). As result we obtain a mode temperature $T_{1,1} = 3.623 \pm 0.023$ K. $T_{1,1}$ is larger than the environmental temperature $T_{\mathrm{MiM}} = 480$ mK. Similar deviations have been observed before [4, 15–17]. In our case one possible reason for that deviation is local heating of the membrane due to heat radiation from the two fiber ends caused by insufficient thermal anchoring. The inset in Fig. 3.49(b) shows the normalized ring down curve obtained at $T_{\mathrm{MiM}} = 485$ mK. Fitting an exponential decay function to the data we find a decay time $\tau = (12.982 \pm 0.002)$ s, which corresponds to

$Q_{1,1} = \pi f_{1,1}\tau = 10,757,900 \pm 1500$. Similar large Q-factors for high-stress Si_3N_4 membranes in this temperature regime have been reported recently [16, 18]. The resulting mechanical decay rate reads $\gamma_m = \omega_m/Q_m = 2\pi \times 0.024\,\mathrm{Hz}$.

Since our envisaged HQS relies on coupling ultra-cold atoms to a membrane via light, the strength of the optomechanical coupling is a crucial parameter. For a Fabry-Pérot cavity of length L_{cav} with a moving end mirror, the optomechanical coupling strength is given by $G = \omega_{cav}/L_{cav}$, where the cavity frequency ω_{cav} is equal to the laser frequency ω_L and L_{cav} is the cavity length. In the MiM configuration the optomechanical coupling strength depends on the membrane position with respect to the cavity center z_m and is given by $g_m = -\partial\omega_{cav}/\partial z_m$ [19]. Figure 3.49(c) displays the cavity resonance frequency shift $\delta\omega_{cav}$ when the membrane is moved by δz_m relative to its rest position $z_{m,0}$. From its derivative displayed, we find a maximum single photon optomechanical coupling strength $g_0 = 2\pi \times 9$ kHz.

References

[1] M. Aspelmeyer, T. J. Kippenberg, and F. Marquardt, Rev. Mod. Phys. **86**, 1391 (2014).

[2] A. D. O'Connell, and M. Hofheinz, M. Ansmann, R. C. Bialczak, M. Lenander, E. Lucero, M. Neeley, D. Sank, H. Wang, M. Weides, J. Wenner, J. M. Martinis and A. N. Cleland, Nature **464**, 697(2010).

[3] J. D. Teufel, T. Donner, D. Li, J. W. Harlow, M. S. Allman, K. Cicak, A. J. Sirois, J. D. Whittaker, K. W. Lehnert and R. W. Simmonds, Nature **475** 359 (2011).

[4] J. Chan, T. P. M. Alegre, A. H. Safavi-Naeini, J. T. Hill, A. Krause, S. Gröblacher, M. Aspelmeyer and O. Paiter, Nature **478**, 89 (2011).

[5] B. Vogell, K. Stannigel, P. Zoller, K. Hammerer, M. T. Rakher, M. Korppi, A. Jöckel, and P. Treutlein, Phys. Rev. A **87** 023816(2013).

[6] A. Jöckel, A. Faber, T. Kampschulte, M. Korppi, M. T. Rakher, and P. Treutlein, Nat. Nanotech. **10** 55(2015).

[7] P. Treutlein, D. Hunger, S. Camerer, T. W. Hansch, and J. Reichel, Phys. Rev. Lett. **99** 140403(2007).

[8] J. Larson, B. Damski, G. Morigi, and M. Lewenstein, Phys. Rev. Lett. **100**, 050401 (2008).

[9] M. Asjad and F. Saif, Phys. Rev. A **84** 033606 (2011).

[10] A. Bick, C. Staarmann, P. Christoph, O. Hellmig, J. Heinze, K. Sengstock, and C. Becker, Rev. Sci. Instrum. **87**, 013102 (2016).

[11] M. Poot and H. S. J. van der Zant, Phys. Rep. **511**, 273 (2012).

[12] H. Zhong, G. Fläschner, A. Schwarz, R. Wiesendanger, P. Christoph, R. Wagner, A. Bick, C. Staarmann, B. Abeln, K. Sengstock, and C. Becker, http://arxiv.org/abs/1611.03406.

[13] H. Zhong, A. Schwarz, and R. Wiesendanger, Rev. Sci. Instrum. **85**, 045006 (2014).

[14] Norcada Inc., Edmonton, AB T6E 5B6, Canada.

[15] M. Poggio, C. L. Degen, H. J. Mamin, and D. Rugar, Phys. Rev. Lett. **99**, 017201 (2007).

[16] M. Yuan, M. A. Cohen and G. A. Steele, Appl. Phys. Lett. **107**, 263501 (2015).

[17] D. L. McAuslan, G. I. Harris, C. Baker, Y. Sachkou, X. He, E. Sheridan, and W. P. Bowen, Phys. Rev. X, **6**, 021012 (2016).

[18] A. M. Jayich, J. C. Sankey, K. Borkje, D. Lee, C. Yang, M. Underwood, L. Childress, A. Petrenko, S. M. Girvin, J. G. E. Harris, New J. Phys. **14**, 115018 (2012).

[19] J. D. Thompson, B. M. Zwickl, A. M. Jayich, F. Marquardt, S. M. Girvin, and J. G. E. Harris, Nature **452** 72 (2008).

3.11 Theoretical study of collective magnetism in arrays of spinor Bose-Einstein condensates

E. Y. Vedmedenko, M. Schult, J. Kronjäger, R. Wiesendanger, K. Bongs, and K. Sengstock

Dipolar magnetism in solid state systems has triggered curiosity and applications from the compass to data storage. While in solid state systems the long-range dipolar interaction is often overwhelmed by the Heisenberg exchange interaction, there are system classes, in which this kind of interactions can dominate. Particularly, Meystre and co-workers showed recently how the individual magnetic moments of mini-Bose-Einstein condensates (BEC) arranged in a lattice can be enhanced. In these investigations, the BEC-condensate at each lattice site has been described as a point magnetic dipole [1]. However, the dipolar physics in realistic experimental systems goes far beyond what could be anticipated within the point-dipole assumption

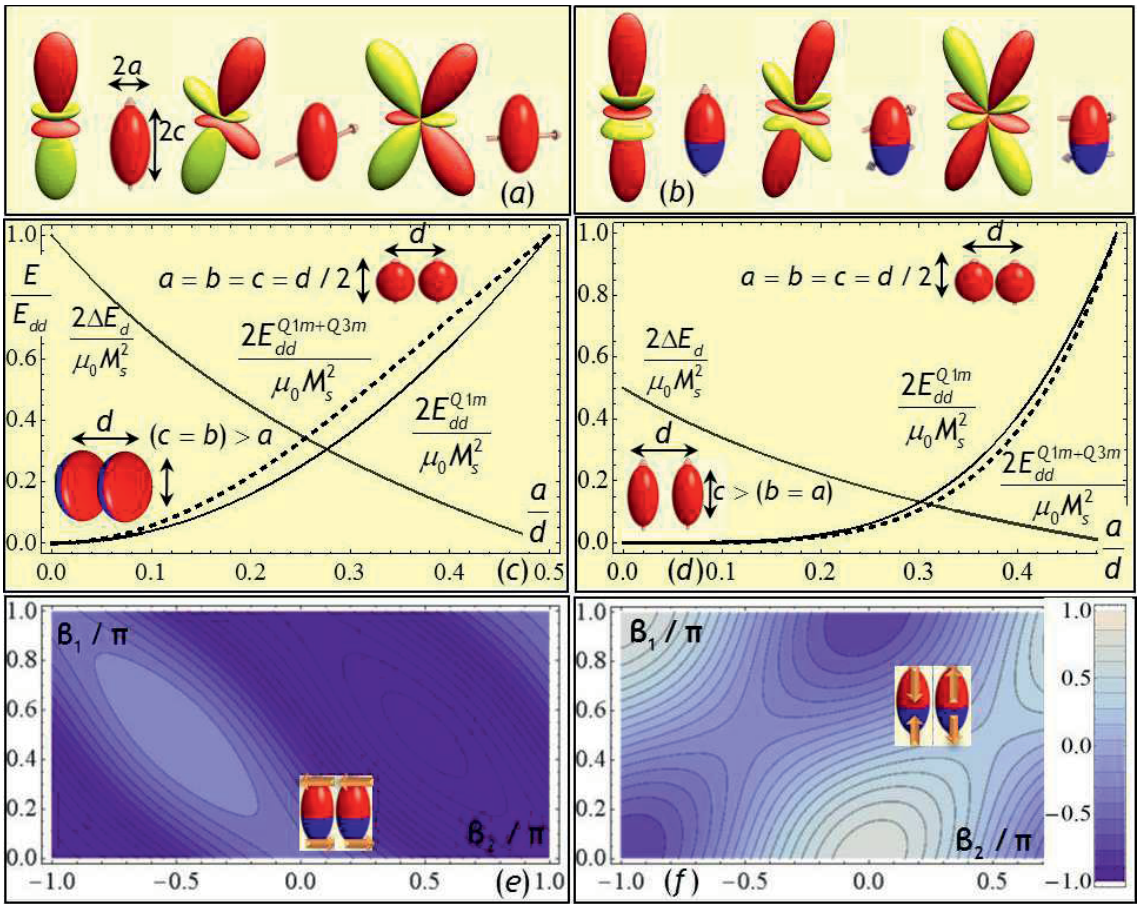

Figure 3.50: (a, b) Visualization of multipole moments for single- (a) and double-domain (b) ellipsoidal spinors. (c, d) Interaction energy E_{dd} and the shape anisotropy ΔE_d of a pair of oblate (c) and prolate (d) spheroids as a function of the aspect ratio c/d and a/d, respectively. The energy is calculated on the basis of Eq. 37 in [2] and is expressed in units of $\mu_0 M_s^2/2$. (e, f) The map of quadrupolar contribution to the E_{dd} for a pair of double-domain spheroids with $c/a = 10$ and $d = 2c$.

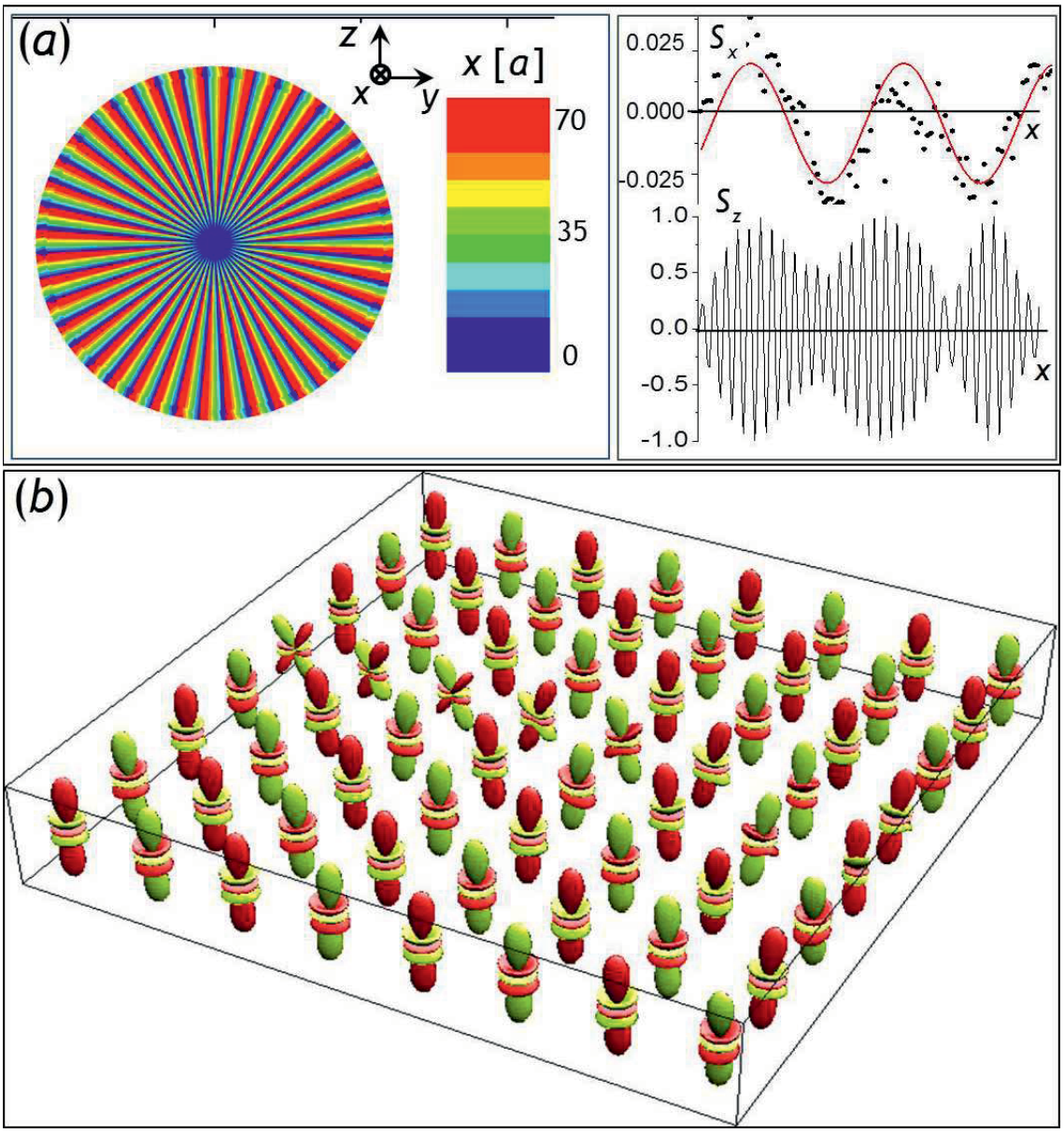

Figure 3.51: (a) A snapshot of an antiferromagnetically modulated spiral found in the Monte-Carlo simulations of a linear chain of oblate BECs with $c/a \approx 10$ at $kT < 1$K. The distance dependence of x and z magnetization components (right) as well as the side-view of the spiral in the zy plane (left) are presented. The color scheme gives the positions of magnetic moments. (b) Thermodynamically stable magnetization configuration in a square array of spin-domain condensates with $c/a = 10$ at $kT < 1$K. The individual BECs are represented by their multipole moments in the spherical harmonics representation.

made in these pioneering investigations. Because we have considerable experience in the theoretical description of magnetic moments of extended charge distributions in the solid state [2], we were interested in the application of our knowledge to this new system class. In our investigation [3] we went beyond the point-dipole approximation and have taken the higher-order multipolar contributions as well as the self-energy of individual BEC condensates into account. We were able to show that the competition of these two additional geometry-dependent energy scales adds to the richness

of the system and that the higher-order terms are not Because we have considerable experience in the theoretical description of magnetic moments of extended charge distributions in the solid state [2], we were interested in the application of our knowledge to this new system class. In our investigation [3] we went beyond the point-dipole approximation and have taken the higher-order multipolar contributions as well as the self-energy of individual BEC condensates into account. We were able to show that the competition of these two additional geometry-dependent energy scales adds to the richness of the system and that the higher-order terms are not negligible in the BEC lattices. Furthermore, we have predicted the ground state of a two-dimensional square array of spin-domain condensates [3].

The single- and two-domain BECs together with corresponding magnetization orientations (arrows) and multipole moments are shown in Fig.3.50 (a), (b). The self-energy (ΔE_d) and the pair interaction energy (E_{dd}) of single- and two-domain BECs are plotted in Fig.3.50 (c), (d) as a function of the aspect ratio of the condensates. The energy landscape of a pair of condensates with in-plane or out-of-plane orientation of magnetization directions is exemplified in Fig. 3.50 (e), (f) as a function of the azimuthal/polar angles of magnetization. Already from this analytical analysis it is clear that the competition between the self-energy and the intercondensate interaction can lead to non-trivial magnetic configurations. Monte-Carlo simulations performed for larger samples of BECs have revealed non-trivial ground states. Two of the possible non-trivial configurations are shown in Fig. 3.51. They correspond to the linear chains of pancake-like BECs (Fig. 3.51 (a)) and the two-dimensional square lattice of spherical BECs (Fig. 3.51 (b)). While in the first case a modulated noncollinear magnetization spiral has been found as a ground state, the checkerboard 2×2 out-of-plane configuration evolves in the second case.

References

[1] W. Zhang, H. Pu, C. Search, and P. Meystre, Spin Waves in a Bose-Einstein–Condensed Atomic Spin Chain, Phys. Rev. Lett. **88**, 060401 (2002).

[2] E. Y. Vedmedenko, N. Mikuszeit, Multipolar Ordering in Electro- and Magnetostatic Coupled Nanosystems, ChemPhysChem **9**, 1222 (2008).

[3] E. Y. Vedmedenko, M. Schult, J. Kronjäger, R. Wiesendanger, K. Bongs, and K. Sengstock, Collective magnetism in arrays of spinor Bose–Einstein condensates, New J. Phys. **15**, 063033 (2013).

Chapter 4

Collaborations

4.1 Research Partners

- Institute of Applied Physics, University of Hamburg:
  Prof. Dr. U. Merkt, Prof. Dr. H. P. Oepen
- I. Institute of Theoretical Physics, University of Hamburg:
  Prof. Dr. A. Lichtenstein, Prof. Dr. D. Pfannkuche, Prof. Dr. M. Potthoff, Prof. Dr. M. Thorwart, Jun.-Prof. Dr. F. Lechermann
- II. Institute of Theoretical Physics, University of Hamburg:
  Prof. Dr. K. Fredenhagen
- Institute for Laser Physics, University of Hamburg:
  Prof. Dr. K. Sengstock
- Institute for Physical Chemistry, University of Hamburg:
  Prof. Dr. H. Weller
- Institute for Inorganic and Applied Chemistry, University of Hamburg:
  Prof. Dr. J. Heck, Prof. Dr. C. Herrmann
- University of Kiel:
  Prof. Dr. R. Berndt, Prof. Dr. S. Heinze
- University of Bremen:
  Prof. Dr. T. Wehling
- HGF-Forschungszentrum Jülich:
  Prof. Dr. S. Blügel, Dr. N. Atodiresei, Dr. G. Bihlmayer, Dr. S. Lounis
- MPI for Solid State Research, Stuttgart:
  Dr. J. Smet, Dr. U. Starke
- IFW Dresden:
  Prof. Dr. A. N. Bogdanov, Dr. A. O. Leonov
- LMU München:
  Prof. Dr. H. Ebert

- University of Augsburg:
  Prof. Dr. M. Albrecht
- University of Regensburg:
  Prof. Dr. F. J. Giessibl
- TU Kaiserslautern:
  Dr. M. H. Prosenc
- University of Zurich, Switzerland:
  Prof. Dr. J. Osterwalder, Dr. J. H. Dil
- EPFL Lausanne, Switzerland:
  Prof. Dr. O. V. Yazyev
- Radboud University, Nijmegen, The Netherlands:
  Prof. Dr. A. A. Khajetoorians
- University of Aarhus, Denmark:
  Prof. Dr. Ph. Hofmann
- Poznan University of Technology, Poland:
  Prof. Dr. R. Czajka
- Institute of Physics, Czech Academy of Sciences, Czech Republic:
  Prof. Dr. J. Honolka
- University of Zaragoza, Spain:
  Prof. Dr. J. I. Arnaudas, Dr. D. Serrate
- Donostia International Physics Center, San Sebastian, Spain:
  Prof. Dr. E. V. Chulkov
- University College London, GB:
  Prof. Dr. A. Shluger
- Dalhousie University, Halifax, Canada:
  Prof. Dr. T. L. Monchesky
- Los Alamos National Laboratory, USA:
  Dr. A. V. Balatsky
- University of Tokyo, Japan:
  Dr. Y. Yoshida

Chapter 5

Theses

5.1 Bachelor Theses

1. Florian Meyer (2014):
   Implementierung einer adaptiven Entwicklungsumgebung zur Simulation von atomaren Manipulationen

2. Philipp Lindner (2014):
   Untersuchung von Wachstum und magnetischen Eigenschaften der Eisenmonolage auf Ir/YSZ/Si(111) mittels spinpolarisierter Rastertunnelmikroskopie

3. Sven Lennart Tunze (2014):
   Präparation und Charakterisierung von ultra-scharfen Spitzen für SP-STM

4. Joris Böttcher (2014):
   Integration and test of a Single-Atom-Evaporator into a low temperature AFM-System

5. Micha Elsebach (2014):
   Development and Testing of a Soft-Landing for Electrospray Deposition

6. Eugen Trapp (2014):
   Entwicklung eines UHV-Kammersystems für ein Hochfrequenz-Mehrfach-Spitzen-Rastertunnelmikroskop

7. Rafaela Friedericke Fuchs (2014):
   Test der Schwingungseigenschaften dünner Membranen mit einem Glasfaser-Fabry-Pérot-Interferometer

8. Sarah Mastracchio (2014):
   Wachstum von Fe-Phthalocyanin auf NiO(001)

9. Alexander Ilin (2014):
   Aufbau eines qPlus-Rastersondenmikroskops

10. Ansgar Siemens (2014):
    Dynamische Prozesse in nicht-kollinearen Spin-Strukturen

11. Christoph Leonhardt (2015):
Präparation und Charakterisierung supraleitender Schichten mit starker Spin-Bahn-Kopplung

12. Jan Leonard Riemann (2015):
Charakterisierung der Oberfläche von Strontiumtitanat mit Rasterkraftmikroskopie

13. Verena Markmann (2015):
Wachstumsstudie von FeSe auf Bi_2Se_3

5.2 Master Theses

1. Jonas Harm (2014):
   Konzeption eines Mehrfach-Spitzen-Rastertunnelmikroskops für spinaufgelöste Experimente mit hoher Zeitauflösung

2. Jonas Constantin Frank Michel Warmuth (2014):
   Structural and Electronic Properties of Bismuth Intercalated Graphene on Iridium

3. Davide Iaia (2014):
   Spin-polarized scanning tunneling microscopy study of structural and magnetic properties of Ni/Fe/Ir(111)

4. Maximilian Meyer (2015):
   Mikroskopische Untersuchungen metallischer Multilagensysteme mittels UHV-Rastertunnelmikroskopie

5. Yangye Zhang (2016):
   Monte-Carlo study of time-correlations and phase diagrams of magnetic systems with long and short-ranged interactions

6. David Schwickert (2016):
   Properties of Co-Salophen oligomers on a NaCl(100)-covered Au(111) surface

7. Jonas Saßmannshausen (2016):
   Rastertunnelmikroskopie ultradünner Bleischichten auf Fe/Ir(111)

8. Philipp Lindner (2016):
   Untersuchung der Interskyrmion-Wechselwirkung in Palladium-Eisen-Nanoinseln auf Ir(111) mittels zeitaufgelöster Rastertunnelmikroskopie

9. Micha Elsebach (2016):
   Electronic Properties of Tailored Co-Salophene Based Building Blocks on Ag(111)

10. Hermann Osterhage (2016):
    Calorimetric experiments on Fe/W(110) using scanning tunneling microscopy

5.3 Ph. D. Theses

1. Andreas Sonntag (2014):
   Magnetoelectric Coupling and Thermally Driven Magnetization Dynamics Studied on the Atomic Scale

2. Boris A. W. Wolter (2014):
   Magnetic Atom Manipulation and Spin-dependent Atomic Friction Investigated by Spin-polarized Scanning Tunneling Microscopy and Monte Carlo Simulations

3. Kai Ruschmeier (2014):
   Aufbau eines 300mK-10T-UHV-Kryostatsystems für die Rasterkraftmikroskopie und Analyse der Kraftsensortemperatur

4. Kolja Them (2014):
   Applications of the C-algebraic reformulation of quantum statistical mechanics to the description of experimentally investigated spin systems*

5. Andreas Eich (2014):
   Manipulation of Topological Edge States

6. Henning von Allwörden (2014):
   Aufbau und Charakterisierung eines 300mK-UHV-10T-Rasterkraftmikroskop-Systems und Messungen an Co-Salen auf Fe/W(001)

7. Christian Hanneken (2015):
   Observation of Non-Collinear Magnetoresistance by Scanning Tunneling Spectroscopy on Skyrmions in PdFe/Ir(111)

8. Josef Grenz (2016):
   Untersuchungen adsorbierter magnetischer Moleküle mittels Rasterkraftmikroskopie

Chapter 6

Scientific Publications

6.1 Book Contributions

1. A. Schwarz and S. Heinze, Non-Contact Atomic Force Microscopy Vol. 3 (ed. by S. Morita, F. J. Giessibl, E. Meyer, and R. Wiesendanger), p.111, Springer (2015) ISBN: 978-3-319-15587-6: *Magnetic Exchange Force Spectroscopy.*

2. D. Z. Gao, A. Schwarz and A. L. Shluger, Non-Contact Atomic Force Microscopy Vol. 3 (ed. by S. Morita, F. J. Giessibl, E. Meyer, and R. Wiesendanger), p.355, Springer (2015) ISBN: 978-3-319-15587-6: *Imaging Molecules on Bulk Insulators Using Metallic Tips.*

3. M. Ashino and R. Wiesendanger, Non-Contact Atomic Force Microscopy Vol. 3 (ed. by S. Morita, F. J. Giessibl, E. Meyer, and R. Wiesendanger), p.127, Springer (2015) ISBN: 978-3-319-15587-6: *Revealing Subsurface Vibrational Modes by Atomic-Resolution Damping Force Spectroscopy.*

4. E. Y. Vedmedenko, Reference Module in Materials Science and Materials Engineering Update of Encyclopedia of Materials: Science and Technology (Second Edition), 2015 (ed. by S. Hashmi), p.1-5, Elsevier (2015) ISBN: 978-0-12-803581-8: *Quasicrystals: Magnetism.*

5. J. Brede, B. Chilian, A. A. Khajetoorians, J. Wiebe, and R. Wiesendanger, Handbook of Spintronics (ed. by Y. Xu, D. Awschalom, and J. Nitta), p.757, Springer (2016) ISBN: 978-94-007-7604-3: *Atomic-Scale Spintronics.*

6. H. Fuchs and R. Wiesendanger, Wirtschaftsstandort Hamburg / Schleswig-Holstein, p.130, Europäischer Wirtschafts-Verlag (2016): *Nanotechnologie in Hamburg: neue Impulse für die Datenspeicherung der Zukunft*

6.2 Original Articles

1. H. Fuchs and R. Wiesendanger, nanoTECHNOLOGIE aktuell **8**, 28 (2014): *Neuartige Konzepte für die Informationstechnologie*

2. J. Brede, N. Atodiresei, V. Caciuc, M. Bazarnik, A. Al-Zubi, S. Blügel, and R. Wiesendanger, Nature Nanotechnology **9**, 1018 (2014): *Long-range magnetic coupling between nanoscale organic-metal hybrids mediated by a nanoskyrmion lattice*

3. A. Eich, M. Michiardi, G. Bihlmayer, X.-G. Zhu, J.-L. Mi, Bo B. Iversen, R. Wiesendanger, Ph. Hofmann, A. A. Khajetoorians, and J. Wiebe, Phys. Rev. B **90**, 155414 (2014): *Intra- and interband electron scattering in a hybrid topological insulator: Bismuth bilayer on Bi_2Se_3*

4. P. Löptien, L. Zhou, A. A. Khajetoorians, J. Wiebe, and R. Wiesendanger, J. Phys.: Condens. Matter **26**, 425703 (2014): *Superconductivity of lanthanum revisited: enhanced critical temperature in the clean limit*

5. R. Decker, M. Bazarnik, N. Atodiresei, V. Caciuc, S. Blügel, and R. Wiesendanger, J. Phys.: Condens. Matter **26**, 394004 (2014): *Local tunnel magnetoresistance of an iron intercalated graphene-based heterostructure*

6. K. von Bergmann, A. Kubetzka, O. Pietzsch, and R. Wiesendanger, J. Phys.: Condens. Matter **26**, 394002 (2014): *Interface-induced chiral domain walls, spin spirals and skyrmions revealed by spin-polarized scanning tunneling microscopy*

7. S. Ouazi, T. Pohlmann, A. Kubetzka, K. von Bergmann, and R. Wiesendanger, Surf. Sci. **630** , 280 (2014): *Scanning tunneling microscopy study of Fe, Co and Cr growth on Re(0001)*

8. A. Sonntag, J. Hermenau, S. Krause, and R. Wiesendanger, Phys. Rev. Lett. **113**, 077202 (2014): *Thermal Stability of an Interface-Stabilized Skyrmion Lattice*

9. B. Behin-Aein, J.-P. Wang, and R. Wiesendanger, MRS Bulletin **39**, 696 (2014): *Computing with spins and magnets*

10. A. Neumann, D. Altwein, C. Thönnißen, R. Wieser, A. Berger, A. Meyer, E. Vedmedenko and H.-P. Oepen, New Journ. Phys. **16**, 083012 (2014): *Influence of long-range interactions on the switching behavior of particles in an array of ferromagnetic nanostructure*

11. J. Brede and R. Wiesendanger, MRS Bulletin **39**, 608 (2014): *Spin-resolved imaging and spectroscopy of individual molecules with sub-molecular spatial resolution*

12. A. Schwarz, A. Köhler, J. Grenz, and R. Wiesendanger, Appl. Phys. Lett. **105**, 011606 (2014): *Detecting the dipole moment of a single carbon monoxide molecule*

13. A. A. Khajetoorians and J. Wiebe, Science **344**, 976 (2014): *Hitting the limit of magnetic anisotropy*

14. D. Z. Gao, J. Grenz, M. B. Watkins, F. F. Canova, A. Schwarz, R. Wiesendanger, and A. L. Shluger, ACS Nano **8**, 5339 (2014): *Using Metallic Noncontact Atomic Force Microscope Tips for Imaging Insulators and Polar Molecules: Tip Characterization and Imaging Mechanisms*

15. H. Zhong, A. Schwarz, and R. Wiesendanger, Rev. Sci. Instr. **85**, 045006 (2014): *Miniaturized high-precision piezo driven two axes stepper goniometer*

16. T. Iwasaki, A. A. Zakharov, T. Eelbo, M. Waśniowska, R. Wiesendanger, J. H. Smet, and U. Starke, Surf. Sci. **625**, 44 (2014): *Formation and structural analysis of twisted bilayer graphene on Ni(111) thin films*

17. T. Eelbo, M. Waśniowska, M. Sikora, M. Dobrzanski, A. Kozlowski, A. Pulkin, G. Autes, I. Miotkowski, O. V. Yazyev, and R. Wiesendanger, Phys. Rev. B **89**, 104424 (2014): *Strong out-of-plane magnetic anisotropy of Fe adatoms on* Bi_2Te_3

18. K. Them, Phys. Rev. A **89**, 022126 (2014): *Towards experimental tests and applications of Lieb-Robinson bounds*

19. S. Ouazi, A. Kubetzka, K. von Bergmann, and R. Wiesendanger, Phys. Rev. Lett. **112**, 076102 (2014): *Enhanced Atomic-Scale Spin Contrast due to Spin Friction*

20. P. Löptien, L. Zhou, J. Wiebe, A. A. Khajetoorians, J. L. Mi, B. B. Iversen, Ph. Hofmann, and R. Wiesendanger, Phys. Rev. B **89**, 085401 (2014): *Screening and atomic-scale engineering of the potential at a topological insulator surface*

21. M. Menzel, A. Kubetzka, K. von Bergmann, and R. Wiesendanger, Phys. Rev. Lett. **112**, 047204 (2014): *Parity effects in* 120° *spin spirals*

22. E. Y. Vedmedenko and D. Altwein, Phys. Rev. Lett. **112**, 017206 (2014): *Topologically Protected Magnetic Helix for All-Spin-Based Applications*

23. A. Sonntag, J. Hermenau, A. Schlenhoff, J. Friedlein, S. Krause, and R. Wiesendanger, Phys. Rev. Lett. **112**, 017204 (2014): *Electric-field-induced magnetic anisotropy in a nanomagnet investigated on the atomic scale*

24. J. Hagemeister, N. Romming, K. von Bergmann, E.Y. Vedmedenko, and R. Wiesendanger, Nature Communications **6**, 8455 (2015): *Stability of Single Skyrmionic Bits*

25. C. Hanneken, F. Otte, A. Kubetzka, B. Dupé, N. Romming, K. von Bergmann, R. Wiesendanger, and S. Heinze, Nature Nanotechnology **10**, 1039 (2015): *Electrical detection of magnetic skyrmions by tunnelling non-collinear magnetoresistance*

26. M. Waśniowska, M. Sikora, M. Dobrzański, T. Eelbo, M. M. Soares, M. Rams, I. Miotkowski, R. Wiesendanger, R. Berndt, Z. Kakol, and A. Kozlowski, Phys. Rev. B **92**, 115412 (2015): *Investigating the differences between Co adatoms states on surfaces of selected bismuth chalcogenides*

27. A. A. Khajetoorians, M. Valentyuk, M. Steinbrecher, T. Schlenk, A. Shick, J. Kolorenc, A. I. Lichtenstein, T. O. Wehling, R. Wiesendanger and J. Wiebe, Nature Nanotechnology **10**, 958 (2015): *Tuning emergent magnetism in a Hund's impurity*

28. K. von Bergmann, Science **349**, 234 (2015): *Magnetic bubbles with a twist*

29. A. Schlenhoff, P. Lindner, J. Friedlein, S. Krause, R. Wiesendanger, M. Weinl, M. Schreck, and M. Albrecht, ACS Nano **9**, 5908 (2015): *Magnetic Nanoskyrmion Lattice Observed in a Si-Wafer-Based Multilayer System*

30. M. Bazarnik, R. Decker, J. Brede, and R. Wiesendanger, Surf. Sci. **639**, 70 (2015): *Multi-layer and multi-component intercalation at the graphene/Ir(111) interface*

31. N. Romming, A. Kubetzka, C. Hanneken, K. von Bergmann, and R. Wiesendanger, Phys. Rev. Lett. **114**, 177203 (2015): *Field-Dependent Size and Shape of Single Magnetic Skyrmions*

32. K. von Bergmann, M. Menzel, A. Kubetzka, and R. Wiesendanger, Nano Lett. **15**, 3280 (2015): *Influence of the Local Atom Configuration on a Hexagonal Skyrmion Lattice*

33. G. Fläschner, K. Ruschmeier, A. Schwarz, R. Bakhtiari, M. Thorwart, and R. Wiesendanger, Appl. Phys. Lett. **106**, 123102 (2015): *Temperature and non-linear response of cantilever-type mechanical oscillators used in atomic force microscopes with interferometric detection*

34. R. Wieser, Eur. Phys. J. B **88**, 77 (2015): *Description of a dissipative quantum spin dynamics with a Landau-Lifshitz/Gilbert like damping and complete derivation of the classical Landau-Lifshitz equation*

35. F. Pielmeier, G. Landolt, B. Slomski, S. Muff, J. Berwanger, A. Eich, A. A. Khajetoorians, J. Wiebe, Z. S. Aliev, M. B. Babanly, R. Wiesendanger, J. Osterwalder, E. V. Chulkov, F. J. Giessibl, and J. H. Dil, New Journ. Phys. **17**, 023067 (2015): *Response of the topological surface state to surface disorder in* $TlBiSe_2$

36. K. von Bergmann, M. Ternes, S. Loth, C. P. Lutz, and A. J. Heinrich, Phys. Rev. Lett. **114**, 076601 (2015): *Spin Polarization of the Split Kondo State*

37. K. Them, E. Y. Vedmedenko, K. Fredenhagen, and R. Wiesendanger, J. Phys. A: Math. Theor. **48**, 075301 (2015): *Bounds on expectation values of quantum subsystems and perturbation theory*

38. B. Dupé, J. E. Bickel, Y. Mokrousov, F. Otte, K. von Bergmann, A. Kubetzka, S. Heinze, and R. Wiesendanger, New J. Phys. **17**, 023014 (2015): *Giant magnetization canting due to symmetry breaking in zigzag Co chains on Ir(001)*

39. M. Bazarnik, L. Jurczyszyn, R. Czajka, K. Morgenstern, Phys. Chem. Chem. Phys. **17**, 5366 (2015): *Mechanism of a molecular photo-switch adsorbed on Si(100)*

40. A. Finco, P.-J. Hsu, A. Kubetzka, K. von Bergmann, and R. Wiesendanger, Phys. Rev. B **94**, 214402 (2016): *Tailoring noncollinear magnetism by misfit dislocation lines*

41. U. R. Singh, J. Warmuth, V. Markmann, J. Wiebe, R. Wiesendanger, J. Phys.: Condens. Matter **29**, 025004 (2016): *Structural and electronic properties of ultrathin FeSe films grown on Bi_2Se_3(0001) studied by STM/STS*

42. J. Hagemeister, D. Iaia, E. Y. Vedmedenko, K. von Bergmann, A. Kubetzka, and R. Wiesendanger, Phys. Rev. Lett. **117**, 207202 (2016): *Skyrmions at the Edge: Confinement Effects in Fe/Ir(111)*

43. P.-J. Hsu, A. Kubetzka, A. Finco, N. Romming, K. von Bergmann, and R. Wiesendanger, Nature Nanotechnology (2016) (DOI: 10.1038/nnano.2016.234): *Electric-field-driven switching of individual magnetic Skyrmions*

44. M. Vondráček, L. Cornils, J. Minár, J. Warmuth, M. Michiardi, C. Piamonteze, L. Barreto, J. A. Miwa, M. Bianchi, Ph. Hofmann, L. Zhou, A. Kamlapure, A. A. Khajetoorians, R. Wiesendanger, J.-L. Mi, B.-B. Iversen, S. Mankovsky, St. Borek, H. Ebert, M. Schüler, T. Wehling, J. Wiebe, and J. Honolka, Phys. Rev. B **94**, 161114(R) (2016): *Nickel: The time-reversal symmetry conserving partner of iron on a chalcogenide topological insulator*

45. J. Hagemeister, E. Y. Vedmedenko, and R. Wiesendanger, Phys. Rev. B **94**, 104434 (2016): *Pattern formation in skyrmionic materials with anisotropic environments*

46. A. Palacio-Morales, A. Kubetzka, K. von Bergmann, and R. Wiesendanger, Nano Letters **16**, 6252 (2016): *Coupling of Coexisting Noncollinear Spin States in the Fe Monolayer on Re(0001)*

47. H. von Allwörden, K. Ruschmeier, A. Köhler, T. Eelbo, A. Schwarz and R. Wiesendanger, Rev. Sci. Instr. **87**, 073702 (2016): *Set-up of a high-resolution 300 mK atomic force microscope in an ultra-high vacuum compatible ^{3}He/10 T cryostat*

48. L. Schmidt, J. Hagemeister, P.-J. Hsu, A. Kubetzka, K. von Bergmann, and R. Wiesendanger, New Journ. Phys. **18**, 075007 (2016): *Symmetry breaking in spin spirals and skyrmions by in-plane and canted magnetic fields*

49. M. Vališka, J. Warmuth, M. Michiardi, M. Vondráček, A. S. Ngankeu, V. Holý, V. Sechovský, G. Springholz, M. Bianchi, J. Wiebe, P. Hofmann and J. Honolka, Appl. Phys. Lett. **108**, 262402 (2016): *Topological insulator homojunctions including magnetic layers: The example of n-type (n-QLs Bi_2Se_3/Mn-Bi_2Se_3) heterostructures*

50. R. Wiesendanger, Nature Reviews Materials **1**, 16044 (2016): *Nanoscale magnetic skyrmions in metallic films and multilayers: a new twist for spintronics*

51. T. Eelbo, V. Zdravkov, and R. Wiesendanger, Surf. Sci. **653**, 113 (2016): *STM study of the preparation of clean Ta(110) and the subsequent growth of two-dimensional Fe islands*

52. A. O. Leonov, T. L. Monchesky, N. Romming, A. Kubetzka, A. N. Bogdanov, and R. Wiesendanger, New Journ. Phys. **18**, 065003 (2016): *The properties of isolated chiral skyrmions in thin magnetic films*

53. Ch. Hanneken, A. Kubetzka, K. von Bergmann, and R. Wiesendanger, New Journ. Phys. **18**, 055009 (2016): *Pinning and movement of individual nanoscale magnetic skyrmions via defects*

54. J. Warmuth, A. Bruix, M. Michiardi, T. Hänke, M. Bianchi, J. Wiebe, R. Wiesendanger, B. Hammer, P. Hofmann, and A. A. Khajetoorians, Phys. Rev. B **93**, 165437 (2016): *Band-gap engineering by Bi intercalation of graphene on Ir(111)*

55. W. P. Schleich, K. S. Ranade, C. Anton, M. Arndt, M. Aspelmeyer, M. Bayer, G. Berg, T. Calarco, H. Fuchs, E. Giacobino, M. Grassl, P. Hänggi, W.M. Heckl, I. V. Hertel, S. Huelga, F. Jelezko, B. Keimer, J. P. Kotthaus, G. Leuchs, N. Lütkenhaus, U. Maurer, T. Pfau, M. B. Plenio, E. M. Rasel, O. Renn, C. Silberhorn, J. Schiedmayer, D. Schmitt-Landsiedel, K. Schönhammer, A. Ustinov, P. Walther, H. Weinfurter, E. Welzl, R. Wiesendanger, S. Wolf, A. Zeilinger, and P. Zoller, , Appl. Phys. B **122**, 130 (2016): *Quantum technology: from research to application*

56. S. Krause and R. Wiesendanger, Nature Materials **15**, 493 (2016): *Skyrmionics gets hot*

57. A. Siemens, Y. Zhang, J. Hagemeister, E. Vedmedenko, and R. Wiesendanger, New Journ. Phys. **18**, 045021 (2016): *Minimal radius of magnetic skyrmions: statics and dynamics*

58. D. Iaia, A. Kubetzka, K. von Bergmann, and R. Wiesendanger, Phys. Rev. B **93**, 134409 (2016): *Structural and magnetic properties of Ni/Fe nanostructures on Ir(111)*

59. D. Serrate, Y. Yoshida, M. Moro-Lagares, A. Kubetzka, and R. Wiesendanger, Phys. Rev. B **93**, 125424 (2016): *Spin-sensitive shape asymmetry of adatoms on noncollinear magnetic substrates*

60. M. Krizanac, D. Altwein, E. Y. Vedmedenko, and R. Wiesendanger, New Journ. Phys. **18** , 033029 (2016): *Quantum revivals and magnetization tunneling in effective spin systems*

61. A. A. Khajetoorians, M. Steinbrecher, M. Ternes, M. Bouhassoune, M. dos Santos Dias, S. Lounis, J. Wiebe, and R. Wiesendanger, Nature Communications **7**, 10620 (2016): *Tailoring the chiral magnetic interaction between two individual atoms*

62. E. Y. Vedmedenko, Phys. Rev. Lett. **116**, 077202 (2016): *Dynamics of Bound Monopoles in Artificial Spin Ice: How to Store Energy in Dirac Strings*

63. S. Krause, A. Sonntag, J. Hermenau, J. Friedlein, and R. Wiesendanger, Phys. Rev. B **93**, 064407 (2016): *High-frequency magnetization dynamics of individual atomic-scale magnets*

64. M. Steinbrecher, A. Sonntag, M. dos Santos Dias, M. Bouhassoune, S. Lounis, J. Wiebe, R. Wiesendanger, and A. A. Khajetoorians, Nature Communications **7**, 10454 (2016): *Absence of a spin-signature from a single Ho adatom as probed by spin-sensitive tunneling*

65. P.-J. Hsu, A. Finco, L. Schmidt, A. Kubetzka, K. von Bergmann, and R. Wiesendanger, Phys. Rev. Lett. **116**, 017201 (2016): *Guiding Spin Spirals by Local Uniaxial Strain Relief*

66. P. Löptien, L. Zhou, , A. A. Khajetoorians, J. Wiebe, and R. Wiesendanger, Surf. Sci. **643**, 6 (2016): *Tunneling into thin superconducting films: Interface-induced quasiparticle lifetime reduction*

67. M. Bazarnik, B. Bugenhagen, M. Elsebach, E. Sierda, A. Frank, M. H. Prosenc, and R. Wiesendanger, Nano Lett. **16**, 577 (2016): *Toward Tailored All-Spin Molecular Devices*

Chapter 7

Talks and Posters

7.1 Invited Talks

7.1.2014: N. Romming, C. Hanneken, M. Menzel, J.E. Bickel, B. Wolter, K. von Bergmann, A. Kubetzka, and R. Wiesendanger, Current-driven magnetisation dynamics workshop, Leeds (England): *Writing and deleting single magnetic skyrmions*

25.2.2014: K. von Bergmann, 5$^{\text{th}}$ International Workshop on Advanced Scanning Probe Microscopy Techniques, Karlsruhe (Germany): *Spin spirals and magnetic skyrmions studied with spin-polarized STM*

14.3.2014: R. Wiesendanger, 28$^{\text{th}}$ Int. Winterschool on Electronic Properties of Novel Materials: Molecular Nanostructures, Kirchberg i.T (Austria): *Spintronics at the single-molecule level*

1.4.2014: A. A. Khajetoorians, 78$^{\text{th}}$ Spring Conference, Deutsche Physikalische Gesellschaft, Dresden (Germany): *Manipulating the magnetic properties of single atoms on surfaces*

9.4.2014: R. Wiesendanger, Skymag 2014, Paris (France): *Interface-driven skyrmions: Observation and local manipulation by spin-polarized tunneling techniques*

13.5.2014: R. Wiesendanger, 34$^{\text{th}}$ CNLS Annual Conference on Mesoscale Science Frontiers, Santa Fe (USA): *Interface-driven skyrmions: Observation and local manipulation by spin-polarized tunneling techniques*

1.6.2014: A. A. Khajetoorians, NEVAC Utrecht, Utrecht (Netherlands): *Probing the magnetic nature of a single atom*

2.6.2014: A. A. Khajetoorians, Ameland Summer School, "Physics of single nano-objects", Ameland (The Netherlands): *Atomic LEGOs*

26.6.2014: E. Vedmedenko and D. Altwein, PM14 Conference, Poznan (Poland): *Topologically protected magnetic Helix for energy storage*

30.6.2014: R. Wiesendanger, Moscow International Symposium on Magnetism, MISM-2014, Moscow (Russia): *Interface-driven magnetism: from chiral domain walls to spin spirals and magnetic skyrmions*

1.7.2014: K. von Bergmann, Intl. School on Superconductivity and Magnetism at the Nanoscale, Stuttgart (Germany): *Spin spirals and magnetic skyrmions studied with spin-polarized STM*

7.7.2014: R. Wiesendanger, 5$^{\text{th}}$ Internat. Conf. on Nanostructures Self-Assembly, NanoSEA 2014, Marseille (France): *Spin-resolved studies of individual magnetic nanostructures formed by self-assembly*

7.7.2014: E. Y. Vedmedenko, 7$^{\text{th}}$ International Conference on Frustrated Magnetism, Cambridge (UK): *Application of string theory to the two-dimensional dipolar spin ice: how to store energy in Dirac strings?*

9.7.2014: R. Wiesendanger, Internat. Conf. on Strongly Correlated Electron Systems, SCES'14, Grenoble (France): *Interface-driven skyrmions: Observation and local manipulation by spin-polarized tunneling techniques*

12.7.2014: E. Y. Vedmedenko, International Symposium on Spin-Polarized Electron Physics and Nanomagnetism, Halle (Germany): *Spintronic Battery that stores energy magnetically*

17.7.2014: K. von Bergmann, 5$^{\text{th}}$ International Workshop on Spin-Polarized Scanning Tunneling Microscopy (SPSTM-5), Huron, Ohio (USA): *Spin spirals and magnetic skyrmions studied with spin-polarized STM*

18.7.2014: R. Wiesendanger, 5$^{\text{th}}$ International Workshop on Spin-Polarized Scanning Tunneling Microscopy (SPSTM-5), Huron, Ohio (USA): *Revealing Atomic-Scale Magnetic Interactions by Spin-Polarized STM*

24.7.2014: R. Wiesendanger, Internat. Conf. on Nanoscience and Technology, ICN+T 2014, Vail, Colorado (USA): *25 Years of Spin-Polarized STM: From Single-Atom Magnetism to Complex Spin Textures in Nanostructures*

28.7.2014: J. Wiebe, PASP VIII, Washington (USA): *Using single atom magnetometry to develop atom-scale spintronics*

28.7.2014: R. Wiesendanger, Internat. Conference on Nanoscale Spectroscopy, NSS-8, Chicago (USA): *Complex Spin States Revealed and Locally Manipulated by 3D-Vector Resolved Spin-Polarized Tunneling Techniques*

14.8.2014: R. Wiesendanger, Internat. Conference on Low Temperature Physics, LT27, Buenos Aires (Argentina): *Towards Computation with Single Skyrmions and Single Spins*

18.8.2014: N. Romming, Ch. Hanneken, M. Menzel, J.E. Bickel, B. Wolter, K. von Bergmann, A. Kubetzka, and R. Wiesendanger, SPIE NanoScience + Engineering, San Diego (USA): *Writing and deleting single magnetic skyrmions*

1.9.2014: R. Wiesendanger, Julius Springer Forum on Applied Physics, Amsterdam (The Netherlands): *Atom-by-Atom Engineering of Tailored Nanomagnets and Atomic-Scale Spintronic Devices*

11.9.2014: R. Wiesendanger, M-SNOWS'14 Conference, Nancy (France): *Towards Computation with Single Skyrmions and Single Spins*

17.9.2014: R. Wiesendanger, SFB668 Summer School: Magnetism on a Molecular Scale: Experiment and Theory, Hamburg (Germany): *Spintronics at the single-molecule level*

18.9.2014: M. Bazarnik, B. Bugenhagen, A. Frank, J. Brede, M.H. Prosenc, and R. Wiesendanger, SFB668 Summer School: Magnetism on a Molecular Scale: Experiment and Theory, Hamburg (Germany): *Addressing the Metal Centers of Single- and Multi-Spin-Center Macromolecules on Ferromagnetic Graphene Based Substrates*

7.10.2014: E. Y. Vedmedenko, MMM Conference 2014, Berkeley (USA): *Magnetic Energy Storage*

26.10.2014: J. Wiebe, Spintronics and Magnetochemistry on the Atomic and Molecular Level, Monte Veritá, Ascona (Switzerland): *Tailoring Ground States and Dynamics of Bottom-Up Engineered Arrays of Atomic Spins on Surfaces*

28.10.2014: R. Wiesendanger, SpinMol Conference, Ascona (Switzerland): *Spintronics at the single-molecule level*

4.11.2014: K. von Bergmann, 59^{th} Annual Magnetism and Magnetic Materials Conference (MMM), Honolulu, Hawaii (USA): *Manipulation of magnetic skyrmions with spin-polarized STM*

6.11.2014: R. Wiesendanger, 7^{th} Internat. Symposium on Surface Science, ISSS-7, Matsue (Japan): *25 Years of Spin-Polarized STM: Novel Insight into Atomic-Scale Magnetism*

3.12.2014: M. Bazarnik, VIII Seminar on Research Conducted Using Scanning Probe Techniques, Zakopane (Poland): *Design of a fully spin-based logic gate based on metaloorganic complexes*

4.12.2014: E. Y. Vedmedenko, Excitations in Nanomagnetism 2014, Barcelona (Spain): *Topologically protected magnetic Helix for energy storage*

19.2.2015: J. Wiebe, International Symposium on Quantum System and Nuclear Spin Related Phenomena (QSNS2015), Miyagi (Japan): *Tailoring ground states and dynamics of bottom-up engineered arrays of atomic spins on surfaces*

3.3.2015: K. von Bergmann, APS March Meeting, San Antonio, Texas (USA): *Manipulation of magnetic skyrmions with spin-polarized STM*

16.3.2015: K. von Bergmann, 79th Spring Conference, Deutsche Physikalische Gesellschaft, Berlin (Germany): *Interface-induced magnetic skyrmions studied with spinpolarized STM*

11.5.2015: R. Wiesendanger, E-MRS 2015 Spring Meeting, Lille (France): *Tailoring of nano-scale skyrmions by interface and strain engineering*

20.5.2015: N. Romming, A. Kubetzka, Ch. Hanneken, K. von Bergmann, and R. Wiesendanger, International Workshop on Topological Structures in Ferroic Materials, Sydney (Australia): *Field-dependent Size and Shape of Single Magnetic Skyrmions*

26.5.2015: R. Wiesendanger, Workshop on Topological Magnets, Wako, Saitama (Japan): *Nano-scale skyrmions in ultrathin transition metal films: From fundamentals to applications*

9.6.2015: R. Wiesendanger, International Workshop on New Perspectives in Spintronic and Mesoscopic Physics, Tokyo, Kashiwa (Japan): *Exploring spins at surfaces by spin-polarized STM*

10.6.2015: N. Romming, A. Kubetzka, Ch. Hanneken, K. von Bergmann, F. Otte, B. Dupé, S. Heinze, and R. Wiesendanger, Spin-orbit coupling in surface or interface states (SOCSIS 2015), Spetses (Greece): *Interface-induced magnetic skyrmions in ultrathin films and multilayers investigated by SP-STM*

11.6.2015: R. Wiesendanger, International Symposium on New Perspectives in Spintronic and Mesoscopic Physics, Tokyo, Kashiwa (Japan): *Complex spin states by interfacial Dzyaloshinskii-Moriya interactions: from single atoms to thin films*

24.6.2015: J. Wiebe, 7th International Conference on Scanning Probe Spectroscopy and Related Methods, Poznan (Poland): *Inelastic and spin-resolved scanning tunneling spectroscopy on arrays of coupled magnetic adatoms*

25.6.2015: R. Wiesendanger, 7th Polish Conference on Nanotechnology NANO 2015, Poznan (Poland): *From chiral spin textures towards novel nano-devices based on magnetic skyrmions*

2.7.2015: R. Wiesendanger, Summer School "Solids4Fun", Schloss Hernstein (Austria): *Exploring Magnetism in the Nanoworld*

7.7.2015: K. von Bergmann, 20th International Conference on Magnetism, Barcelona (Spain): *Manipulation of magnetic skyrmions with spin-polarized STM*

12.7.2015: R. Wiesendanger, International Summer School "New Directions in Spintronics and Nanomagnetism", Madrid (Spain): *Interface-driven magnetism: from chiral domain walls to spin spirals and magnetic skyrmions*

14.7.2015: R. Wiesendanger, Internat. Workshop on "Quantum Design", Dresden (Germany): *Nano-scale design of correlated and novel topological states and their characterization by (SP-)STM techniques*

15.7.2015: K. von Bergmann, International Colloquium on Magnetic Films and Surfaces (ICMFS), Cracow (Poland): *Interface-induced magnetic skyrmions studied with spin-polarized STM*

29.7.2015: R. Wiesendanger, Gordon Research Conference "Spin Dynamics in Nanostructures", Hong Kong (China): *Towards skyrmion-based devices*

5.8.2015: E. Y. Vedmedenko, Colloquium of the NanoGUNE, San-Sebastian (Spain): *Stability and Switching of Skyrmionic Bits*

18.8.2015: M. Steinbrecher, SPICE Workshop on Magnetic Adatoms as Building Blocks for Quantum Magnetism, Mainz (Germany): *Tuning magnetic anisotropy, Kondo screening and Dzyaloshinskii-Moriya interaction in pairs of Fe adatoms*

18.8.2015: R. Wiesendanger, SPICE Workshop on "Magnetic Adatoms as Building Blocks for Quantum Magnetism", Schloss Waldthausen, Mainz (Germany): *Revealing properties and interactions of individual magnetic adatoms and molecules by SP-STM*

8.9.2015: R. Wiesendanger, 2nd Grandmaster PhD Workshop in Physics 2015, Budapest (Hungary): *Nano-scale skyrmions in ultrathin transition metal films and multilayers: From fundamentals to potential applications*

21.9.2015: J. Wiebe, IBM Max Planck Workshop on Spins on Surfaces, Almaden, San Jose (USA): *Artificial arrays of coupled magnetic atoms on metallic surfaces*

24.9.2015: E. Y. Vedmedenko, Controlling Magnetic Nanostructures 2015, Konstanz (Germany): *Stability and Switching of Skyrmionic Bits*

3.11.2015: K. von Bergmann, 598. WE-Heraeus-Seminar on Frontiers in Scanning Probe Microscopy, Bad Honnef (Germany): *Spin friction: atom manipulation as a surface magnetism probe*

5.11.2015: J. Wiebe, 598. WE-Heraeus-Seminar: Frontiers in Scanning Probe Microscopy, Bad Honnef (Germany): *Non-collinear spin states induced by Dzyaloshinskii-Moriya type RKKY coupling*

17.11.2015: R. Wiesendanger, International Conference on "Seeing Molecules", Rome (Italy): *From spin-resolved studies of individual molecules on surfaces towards molecular spintronics*

14.12.2015: R. Wiesendanger, Distinguished Lecture Series des Center for Advancing Electronics Dresden, cfaed, Dresden (Germany): *Nanoscale Magnetic Knots – A New Twist For Spintronics*

8.2.2016: R. Wiesendanger, 31st Workshop on Novel Materials and Superconductivity, Obertraun (Austria): *Chiral spin textures in ultrathin films: From fundamentals to potential applications*

23.2.2016: A. Schwarz, International workshop High-resolution AFM/STM imaging, Pague (Czech Republic): *Contrast Formation on Adsorbed CO: Pauli-Repulsion vs. Dipole-Dipole Interaction*

3.3.2016: K. von Bergmann, Topological Phenomena in Novel Quantum Matter, Dresden (Germany): *Topological Magnetic Skyrmions investigated by STM*

7.3.2016: J. Wiebe, 80$^{\text{th}}$ Spring Conference, Deutsche Physikalische Gesellschaft, Regensburg (Germany): *Excitations and dynamics of non-collinear magnetization states in tailored adatoms arrays*

26.4.2016: A. Kamlapure, S. Manna, L. Cornils, T. Hänke, J.-L. Mi, B. B. Iversen, Ph. Hofamnn, J. Wiebe, and R. Wiesendanger, ICSM2016, Fethiye (Turkey): *Superconductivity in a Monolayer of Iron Based Superconductor $FeSe_{0.5}Te_{0.5}$*

28.4.2016: R. Wiesendanger, Akademievorlesungsreihe "Nanotechnologie in Hamburg", Hamburg (Germany): *Nanowissenschaft und Nanotechnologie: Von neuen Erkenntnissen zu innovativen Anwendungen*

2.5.2016: R. Wiesendanger, DIADEMS Summer School, Cargése, Corsica (France): *Single-atom magnetometry by spin-polarized STM*

27.5.2016: R. Wiesendanger, Julius Springer Forum on Applied Physics, Hamburg (Germany): *Nanoscale Magnetic Knots - A New Twist For Spintronics*

2.6.2016: R. Wiesendanger, NANOTECH FRANCE 2016, Courbevoie (France): *Nanoscale Magnetic Knots - A New Twist For Spintronics*

5.6.2016: A. Schwarz, 12$^{\text{th}}$ International Nanoscience and Nanotechnology Conference, Gebze (Turkey): *Magnetic Exchange Force Microscopy and Spectroscopy*

13.6.2016: E. Y. Vedmedenko, Minisymposium on Spin Dynamics, Uppsala (Sweden): *Stability of interfacial skyrmions, solitons and bound monopoles: how to store energy in topological magnetic quasiparticles*

18.6.2016: A. Kamlapure, S. Manna, L. Cornils, T. Hänke, J.-L. Mi, B. B. Iversen, Ph. Hofamnn, J. Wiebe, and R. Wiesendanger, Conference of Spectroscopies in Novel Superconductors, Stuttgart/Ludwigsburg (Germany): *Evidence for a 2 fold symmetric superconducting gap in a monolayer of $FeSe_{0.5}Te_{0.5}$*

21.6.2016: K. von Bergmann, Intl. Symposium on Metallic Multilayers MML, Uppsala (Sweden): *Magnetic Skyrmions investigated by STM*

23.6.2016: R. Wiesendanger, NanoTech Poland International Conference, Poznan (Poland): *Interface driven exotic states of nanomaterials for spintronic and energy applications*

23.6.2016: M. Bazarnik J. Brede, R. Decker, and R. Wiesendanger, NanoTech Poland 2016, Poznan (Poland): *Magnetism in graphene based hybrid systems*

27.6.2016: R. Wiesendanger, SOL-SKYMAG 2016 Conference, San Sebastian (Spain): *Nanoscale Magnetic Skyrmions - A New Twist For Spintronics*

2.7.2016: A. Finco, P.-J. Hsu, N. Romming, T. Eelbo, A. Kubetzka, K. von Bergmann, and R. Wiesendanger, Spin Orbit Coupling and Topology in Low Dimensions (SOCSIS 2016), Spetses (Greece): *Electric field switching of skyrmions and non-collinear magnetism at room temperature investigated by STM techniques*

3.7.2016: P.-J. Hsu, The 18th International Symposium on the Physics of Semiconductors and Applications 2016, Jeju island (South Korea): *Electric field driven switching of individual magnetic skyrmions*

4.7.2016: R. Wiesendanger, Internat. Workshop on "Topological Patterns and Dynamics in Magnetic Elements and in Condensed Matter", Dresden (Germany): *Nanoscale Skyrmions - A New Twist For Spintronics*

6.7.2016: R. Wiesendanger, 2016 Swiss Workshop on Materials with Novel Electronic Properties, Les Diablerets (Switzerland): *Novel interface-induced electronic and spin states revealed by spin-resolved scanning tunneling spectroscopy*

17.8.2016: R. Wiesendanger, Internat. Workshop on "Topological Structures in Ferroic Materials, TOPO 2016", Dresden (Germany): *Nanoscale Skyrmions - A New Twist For Spintronics*

23.8.2016: R. Wiesendanger, IVC-20 / ICN+T 2016, Busan (South Korea): *Nanoscale Magnetic Skyrmions - A New Twist For Spintronics*

28.8.2016: P.-J. Hsu, SPIE Optics+Photonics, San Diego (United States): *Electric field driven switching of individual magnetic skyrmions*

29.8.2016: R. Wiesendanger, SPSTM-6, Chiba (Japan): *Probing Exotic States of Condensed Matter by Spin-Polarized Scanning Tunneling Microscopy*

30.8.2016: S. Krause, SPSTM-6, Chiba (Japan): *High Frequency Magnetization Dynamics of Individual Atomic-Scale Magnets*

2.9.2016: R. Wiesendanger, ICSFS-18, Chemnitz (Germany): *Novel Interface-Induced Electronic and Spin States Revealed by Spin-Resolved Scanning Tunneling Spectroscopy*

6.9.2016: R. Wiesendanger, EPS CMD-26, Groningen (The Netherlands): *Observation and manipulation of individual skyrmions by local spin currents and electric fields*

8.9.2016: J. Wiebe, Spins on Surfaces (SoS), San Sebastian (Spain): *Heisenberg and Dzyaloshinskii-Moriya contributions to substrate-electron mediated interactions between atoms on surfaces*

12.9.2016: R. Wiesendanger, Internat. Workshop "From Electronic Correlations to Functionality", Kloster Irsee (Germany): *Observation and manipulation of individual nanoscale skyrmions by local spin currents and electric fields*

13.9.2016: A. Schwarz, 2nd German-French Summer School on noncontact atomic force microsccopy, Osnabrück (Germany): *Magnetic Sensitive Force Microscopy*

19.9.2016: E. Y. Vedmedenko, International Conference on Quasicrystals ICQ13, Kathmandu (Nepal): *Magnetic Charges in Quasiperiodic Vertex Models*

28.9.2016: R. Wiesendanger, Internat. Workshop "Emergent Relativistic Effects in Condensed Matter", Regensburg (Germany): *Interface-driven exotic spin and electronic states in ultrathin films*

29.9.2016: R. Wiesendanger, Internat. Workshop on Antiferromagnetic Spintronics, Mainz (Germany): *An SP-STM View of Antiferromagnetics: From the Smallest Building Units to Model-Type Atomic-Scale Spintronic Devices*

2.10.2016: R. Wiesendanger, 13th Annual Meeting of Science and Technology in Society Forum, Kyoto (Japan): *Future Nanomaterials*

7.11.2016: K. von Bergmann, American Vacuum Society (AVS), Nashville, Tennessee (USA): *Manipulation of Magnetic Skyrmions with STM*

30.11.2016: R. Wiesendanger, MRS Fall Meeting 2016, Boston (USA): *Observation and manipulation of individual nanoscale skyrmions by local spin currents and electric fields*

19.12.2016: R. Wiesendanger, Internat. Workshop on Technologically relevant Quantum Materials: growth, experiments and theory, Trieste (Italy): *Interface driven exotic states for spintronic and energy applications*

7.2 Conference Contributions and Talks at Other Institutes

7.2.1 Talks

9.1.2014: A. A. Khajetoorians, Universität Münster, Münster (Germany): *Probing the magnetic nature of a single atom*

30.1.2014: K. von Bergmann, 5$^{\text{th}}$-year Anniversary Nanoscience Cooperative Research Center nanoGUNE, San Sebastian (Spain): *Manipulating complex spin textures: writing and deleting single magnetic Skyrmions*

3.2.2014: A. A. Khajetoorians, KIT Seminar , Karlsruhe (Germany): *Tailoring the magnetic nature of single atoms on surfaces*

17.2.2014: N. Romming, A. Kubetzka, Ch. Hannecken, K. von Bergmann, and R. Wiesendanger, Special Seminar of. J. Sampaio, Kiel (Germany): *Skyrmions in nanostruktures towards technological applications*

4.3.2014: A. Eich, M. Michiardi, G. Bihlmayer, A. A. Khajetoorians, J. Wiebe J.L. Mi, B. B. Iversen, Ph. Hofmann and R. Wiesendanger, APS March Meeting 2014, Denver, (USA): *Experimental characterization and simulation of quasi-particle interference on* Bi/Bi_2Se_3

7.3.2014: P. Löptien, L. Zhou, J. Wiebe, A. A. Khajetoorians, and R. Wiesendanger, APS March Meeting 2014, Denver (USA): *Superconductivity of lanthanum revisited*

31.3.2014: T. Eelbo, M. Wasniowska, M. Sikora, M. Dobrzanski, A. Kozlowski, A. Pulkin, G. Autes, I. Miotkowski, O. V. Yazyev, and R. Wiesendanger, 78$^{\text{th}}$ Spring Conference, Deutsche Physikalische Gesellschaft, Dresden (Germany): *Strong out-of-Plane Magnetic Anisotropy of Fe Adatoms on* Bi_2Te_3

1.4.2014: M. Bazarnik, B. Bugenhagen, A. Frank, J. Brede, M.H. Prosenc, and R. Wiesendanger, 78$^{\text{th}}$ Spring Conference, Deutsche Physikalische Gesellschaft, Dresden (Germany): *Addressing the metal centers in multi-spin-center macromolecule on Au(111)*

2.4.2014: J. Hermenau, A. Sonntag, J. Friedlein, S. Krause, and R. Wiesendanger, 78$^{\text{th}}$ Spring Conference, Deutsche Physikalische Gesellschaft, Dresden (Germany): *Pump-probe-experiments on individual atomic-scale superparamagnets*

2.4.2014: A. A. Khajetoorians, M. Steinbrecher, M. Bouhassoune, S. Lounis, M. Ternes, J. Wiebe, R. Wiesendanger, 78$^{\text{th}}$ Spring Conference, Deutsche Physikalische Gesellschaft, Dresden (Germany): *Tracing the RKKY-interaction in pairs of adatoms via the peak splitting of a Kondo resonance*

3.4.2014: L. Cornils, R. Schmidt, A. Schwarz, and R. Wiesendanger, 78$^{\text{th}}$ Spring Conference, Deutsche Physikalische Gesellschaft, Dresden (Germany): *A 4K-UHV-Cryostat-System for Magnetic Exchange Force Microscopy with a 2-Axes-Vector-Field Magnet*

3.4.2014: S. Krause, A. Sonntag, J. Hermenau, and R. Wiesendanger, 78$^{\text{th}}$ Spring Conference, Deutsche Physikalische Gesellschaft, Dresden (Germany): *Temperature-driven phase transition of Fe/Ir(111) nanoskyrmions*

3.4.2014: J. Hagemeister, R. Wieser, E. Vedmedenko, and R. Wiesendanger, 78$^{\text{th}}$ Spring Conference, Deutsche Physikalische Gesellschaft, Dresden (Germany): *Creation and annihilation of skyrmions in ultrathin magnetic films*

4.4.2014: M. Michiardi, A. Eich, G. Bihlmayer, A. A. Khajetoorians, J. Wiebe, J. Mi, B. B. Iversen, Ph. Hofmann and R. Wiesendanger, 78$^{\text{th}}$ Spring Conference, Deutsche Physikalische Gesellschaft, , Dresden (Germany): *Experimental characterization and simulation of quasi-particle-interference in the Bi-bilayer topological insulator*

4.4.2014: A. Sonntag, J. Hermenau, A. Schlenhoff, J. Friedlein, S. Krause, and R. Wiesendanger, 78$^{\text{th}}$ Spring Conference, Deutsche Physikalische Gesellschaft, Dresden (Germany): *Electric-field induced magnetic anisotropy on the atomic scale*

4.4.2014: A. Schlenhoff, S. Krause, and R. Wiesendanger, 78$^{\text{th}}$ Spring Conference, Deutsche Physikalische Gesellschaft, Dresden (Germany): *Electron-phonon coupling of hot and low-energy electrons studied with SP-STM*

4.4.2014: S. Ouazi, A. Kubetzka, K. von Bergamnn, and R. Wiesendanger, 78$^{\text{th}}$ Spring Conference, Deutsche Physikalische Gesellschaft, Dresden (Germany): *Enhanced atomic-scale spin contrast due to spin friction*

9.4.2014: A. A. Khajetoorians, Universität Innsbruck, Innsbruck (Germany): *Probing the magnetic nature of a single atom*

14.4.2014: E. Y. Vedmedenko, J. Hagemeister, and R. Wiesendanger, Skymag 2014, Paris (France): *Magnetic Switching of Skyrmions*

9.5.2014: A. A. Khajetoorians, PGI -Kolloquium, Jülich (Germany): *Probing the magnetic nature of a single atom*

16.5.2014: R. Wiesendanger, Johns Hopkins University, Colloquium, Baltimore (USA): *Exploring Magnetism in the Nanoworld*

8.7.2014: J. P. Hermenau, A. Sonntag, A. Schlenhoff, J. Friedlein, S. Krause, and R. Wiesendanger, 20$^{\text{th}}$ International Conference on Magnetism, Barcelona (Spain): *Electric-Field-Induced Magnetic Anisotropy in a Nanomagnet Investigated on the Atomic Scale*

14.7.2014: A. Schwarz, INC Summer School "New Frontiers in Scanning Force Microscopy: From UltraHigh-Vacuum to Biological Material", Miraflores de la Sierra, Madrid (Spain): *Magnetic Sensitive Force Microscopy*

16.7.2014: S. Krause, A. Sonntag, J. Hermenau and R. Wiesendanger, 5$^{\text{th}}$ International Workshop on Spin-Polarized Scanning Tunneling Microscopy (SPSTM-5), Ohio (USA): *Temperature-driven Phase Transition of Fe/Ir(111) Nanoskyrmions*

17.7.2014: S. Krause, A. Sonntag, A. Schlenhoff, J. Hermenau, J. Friedlein, and R. Wiesendanger, SP-STM-5, Huron, Ohio (USA): *Electric-Field-Induced Magnetic Anisotropy in a Nanomagnet Investigated on the Atomic Scale*

20.7.2014: A. A. Khajetoorians, M. Steinbrecher, M. Bouhassoune, S. Lounis, M. Ternes, J. Wiebe and R. Wiesendanger, International Conference on Nanoscience and Technology , Vail, Colorado (USA): *Tracing the RKKY-interaction in pairs of adatoms via the peak splitting of a Kondo resonance*

23.7.2014: A. Schwarz, J. Grenz, A. Köhler, and R. Wiesendanger, International Conference on Nanoscience and Technology, Vail, Colorado (USA): *Detecting the Dipole Moment of a Molecule with Atomic Force Microscopy*

23.7.2014: C. Hanneken, N. Romming, M. Menzel, J. E. Bickel, B. Wolter, K. von Bergmann, A. Kubetzka, and R. Wiesendanger, ICN+T 2014, Vail (CO), (USA): *Writing and deleting single magnetic skyrmions*

24.7.2014: S. Krause, A. Sonntag, J. Hermenau, A. Schlenhoff, J. Friedlein, and R. Wiesendanger, International Conference on Nanoscience and Technology, Vail, Colorado (USA): *Electric-Field-Induced Magnetic Anisotropy in a Nanomagnet Investigated on the Atomic Scale*

24.7.2014: J. Wiebe, A. A. Khajetoorians, M. Steinbrecher, T. Schlenk, M. Valentyuk, A. Lichtenstein, and R. Wiesendanger, International Conference on Nanoscience and Technology, Vail, Colorado (USA): *Tuning Competition Between Magnetic Anisotropy and Kondo Screening in Individual Adatoms by Controlled Hydrogenation*

30.7.2014: A. A. Khajetoorians, M. Steinbrecher, M. Valentyuk, T. Schlenk, A. Lichtenstein, T. O. Wehling, J. Wiebe and R. Wiesendanger,, International Workshop on Nanoscale Spectroscopy and Nanotechnology 8, Chicago, Illinois (USA): *Tuning Magnetic Anisotropy and Kondo Screening in a Hund's Impurity by Controlled Hydrogenation*

8.8.2014: A. Schwarz, K. Ruschmeier, G. Fläschner, and R. Wiesendanger, 17^{th} International Conference on non-contact Atomic Force Microscopy, Tsukuba (Japan): *The Meaning of Temperature in Interferometric Detection Schemes*

3.9.2014: N. Romming, C. Hanneken, M. Menzel, J.E. Bickel, B. Wolter, K. von Bergmann, A. Kubetzka, and R. Wiesendanger, ALS-CXRO Wednesday seminar, Berkeley, Berkeley (USA): *Writing and deleting single magnetic skyrmions*

16.9.2014: M. Dobrzański, M. Waśnoiowska, M. Sikora, T. Elbo, M. Soarez, M. Rams, I. Miotkowski, R. Wiesendanger, Kakol, and A. Kozlowski, E-MRS 2014, Warsaw (Poland): *Surface of Bi_2Se_3-class materials probed bei Co adatoms electrical states: difference between topological and non-topological insulators*

18.9.2014: J. Wiebe, Sandbjerg Meeting, Sandbjerg (Denmark): *Introduction to Spin-Resolved Scanning Tunneling Spectroscopy*

18.9.2014: M. Steinbrecher, A. A. Khajetoorians, M. Valentyuk, T. Schlenk, A. Lichtenstein, T. O. Wehling, M. Bouhassoune, S. Lounis, J. Wiebe and R. Wiesendanger, SFB 668 Summerschool - Magnetism on a Molecular Scale: Experiment and Theory, Hamburg (Germany): *Investigating the magnetism of single Fe atoms affected by Hydrogenation*

11.11.2014: R. Wiesendanger, Veranstaltung der Universitätsgesellschaft Hamburg, Hamburg (Germany): *Informations- und Kommunikationstechnik als Basis unserer Wissensgesellschaft: Was bringt die Zukunft?*

14.11.2014: R. Wiesendanger, Veranstaltung der Akademie der Wissenschaften in Hamburg, Hamburg (Germany): *Informations- und Kommunikationstechnik als Basis unserer Wissensgesellschaft: Was bringt die Zukunft?*

29.1.2015: K. von Bergmann, Colloquium on Solid State Physics, TUM, Munich (Germany): *Manipulation of magnetic skyrmions with spin-polarized STM*

16.3.2015: S. Krause, A. Schlenhoff, P. Lindner, J. Friedlein, R. Wiesendanger, M. Weinl, M. Schreck, and M. Albrecht, 79$^{\text{th}}$ Spring Conference, Deutsche Physikalische Gesellschaft, Berlin (Germany): *A Magnetic Nano-Skyrmion Lattice observed in a Si-wafer based Multilayer System*

16.3.2015: N. Romming, A. Kubetzka, C. Hanneken, K. von Bergmann, and R. Wiesendanger, 79$^{\text{th}}$ Spring Conference, Deutsche Physikalische Gesellschaft, Berlin (Germany): *Field-dependent Size and Shape of Single Magnetic Skyrmions*

16.3.2015: J. Wiebe, A. A. Khajetoorians, M. Steinbrecher, M. Bouhassoune, S. Lounis, M. Ternes, and R. Wiesendanger, 79$^{\text{th}}$ Spring Conference, Deutsche Physikalische Gesellschaft, Berlin (Germany): *Tracing the RKKY-Interaction in Pairs of Adatoms via the Peak Splitting of a Kondo Resonance*

16.3.2015: M. Steinbrecher, A. Sonntag, M. dos Santos Dias, M. Bouhassoune, S. Lounis, J. Wiebe, R. Wiesendanger, A. A. Khajetoorians, 79$^{\text{th}}$ Spring Conference, Deutsche Physikalische Gesellschaft, Berlin (Germany): *ISTS of Ho atoms and Ho-Fe atom pairs on Pt(111) in the RKKY-coupling regime*

16.3.2015: J. Grenz, A. Schwarz, and R. Wiesendanger, 79. Frühjahrstagung der Deutschen Physikalischen Gesellschaft, Berlin (Germany): *Single Iron-Phthalocyanine molecules on Fe/W(001): A non-contact atomic force microscopy study at low temperature in UHV*

16.3.2015: J. Wiebe, J. Warmuth, M. Michardi, T. Hänke, M. Bianchi, R. Wiesendanger, P. Hofmann, and A. A. Khajetoorians, 79$^{\text{th}}$ Spring Conference, Deutsche Physikalische Gesellschaft, Berlin (Germany): *Bismuth Intercalated Graphene on Iridium Probed by STM and ARPES*

16.3.2015: M. Vondracek, J. Honolka, C. Piamonteze, J. Warmuth, M. Michiardi, P. Hofmann, A. A. Khajetoorians, J. Wiebe, R. Wiesendanger, T. Wehling, J. Minar, H. Ebert, J.-L. Mi, B. B. Iversen, and M. Dunst, 79$^{\text{th}}$ Spring Conference, Deutsche Physikalische Gesellschaft, Berlin (Germany): *XMCD of 3d adatoms on Bi_2Te_3 and Bi_2Te_2Se: experiment and ab initio theory*

16.3.2015: P.-J. Hsu, A. Finco, L. Schmidt, A. Kubetzka, K. von Bergmann, and R. Wiesendanger, 79$^{\text{th}}$ Spring Conference, Deutsche Physikalische Gesellschaft, Berlin (Germany): *Tailoring a Spin Spiral by Uniaxial Strain*

17.3.2015: M. Krizanac, D. Altwein, E. Vedmedenko, and R. Wiesendanger, 79$^{\text{th}}$ Spring Conference, Deutsche Physikalische Gesellschaft, Berlin (Germany): *Non-harmonic quantum dynamics of single spin systems*

17.3.2015: L. Cornils, J. Honolka, M. Vondráček, M. Schüler, M. Dunst, J. Warmuth, L. Zhou, A. Kamlapure, A. A. Khajetoorians, M. Michiardi, L. Barreto, P. Hofmann, J.-L. Mi, M. Bremholm, B. B. Iversen, C. Piamonteze, H. Ebert, J. Minar, T. Wehling, R. Wiesendanger, and J. Wiebe, 79$^{\text{th}}$ Spring Conference, Deutsche Physikalische Gesellschaft, Berlin (Germany): *The Magnetism of Ni Adatoms adsorbed on the TI Bi_2Te_2Se*

17.3.2015: A. Schwarz, G. Fläschner, K. Ruschmeier, R. Wiesendanger, R. Bakhtiari, and M. Thorwart, 79$^{\text{th}}$ Spring Conference, Deutsche Physikalische Gesellschaft, Berlin (Germany): *The Meaning of Temperature in Interferometric Detection Schemes*

18.3.2015: F. Pielmeier, A. Eich, G. Landolt, B. Slomski, J. Berwanger, A. A. Khajetoorians, J. Wiebe, R. Wiesendanger, J. Osterwalder, F. J. Giessibl, and J. H. Dil, 79$^{\text{th}}$ Spring Conference, Deutsche Physikalische Gesellschaft, Berlin (Germany): *Response of the topological surface state to surface disorder in $TlBiSe_2$*

19.3.2015: D. Altwein, E. Y. Vedmedenko, and R. Wiesendanger, 79$^{\text{th}}$ Spring Conference, Deutsche Physikalische Gesellschaft, Berlin (Germany), Berlin (Germany): *Gilbert damping from nonperturbative partial summation*

19.3.2015: A. Kamlapure, L. Cornils, L. Zhou, A. A. Khajetoorians, J. Wiebe, and R. Wiesendanger, 79$^{\text{th}}$ Spring Conference, Deutsche Physikalische Gesellschaft, Berlin (Germany): *ISTS of Fe adatoms in contact to superconducting Ta*

15.4.2015: R. Wiesendanger, University of Cologne(Colloquium, Cologne (Germany): *Ultradichte magnetische Datenspeicher und energieeffiziente Spin-Logik-Bauelemente auf atomarer Skala: Neueste Beiträge aus der Grundlagenforschung*

15.4.2015: M. Bazarnik, Seminar at Institute of Molecular Physics Polish Academy of Sciences, Poznan (Poland): *Long-range magnetic coupling between nanoscale organic-metal hybrids mediated by a nanoskyrmion lattice*

21.5.2015: K. von Bergmann, Colloquium on Solid State Physics, Hannover (Germany): *From Spin Spirals to Magnetic Skyrmions, studied by spin-polarized STM*

26.5.2015: N. Romming, A. Kubetzka, C. Hanneken, K. von Bergmann, and R. Wiesendanger, Seminar at the Centre for Quantum Computation and Communication Technology, Sydney (Australia): *Investigation and Manipulation of Single Magnetic Skyrmions*

27.5.2015: E. Y. Vedmedenko, MACALONS project, Rome (Italy): *Preliminary calculations on how much entropy change can be expected at the SPM.SFM transition in supercrystals (II)*

22.6.2015: M. Bazarnik, J. Brede, N. Atodiresei, V. Caciuc,A. Al-Zubi, S. Blügel, and R. Wiesendanger, SPS 2015 conference, Poznan (Poland): *Tailoring magnetic coupling between organic-metal hybrids mediated by a nanoskyrmion lattice*

23.6.2015: R. Wiesendanger, Acceptance Speech Docor Honoris Causa, Poznan (Poland): *Nanoscience and Nanotechnology*

24.6.2015: M. Bazarnik, J. Brede, N. Atodiresei, V. Caciuc, A. Al-Zubi, S. Blügel, and R. Wiesendanger, SPS 2015, Poznan (Poland): *Tailoring magnetic coupling between organic-metal hybrids mediated by a nanoskyrmion lattice*

24.6.2015: E. Sierda, M. Bazarnik, B. Bugenhagen, M. H. Prosenc, W. Koczorowski, and R. Wiesendanger, SPS 2015, Poznan (Poland): *On-surface preparation of self-terminating molecular chains*

7.7.2015: N. Romming, A. Kubetzka, C. Hanneken, K. von Bergmann, and R. Wiesendanger, 20$^{\text{th}}$ International Conference on Magnetism, Barcelona (Spain): *Field-Dependent Size and Shape of Single Magnetic Skyrmions*

8.7.2015: J. P. Hermenau, A. Sonntag, A. Schlenhoff, J. Friedlein, S. Krause, and R. Wiesendanger, 20$^{\text{th}}$ International Conference on Magnetism (ICM-20), Barcelona (Spain): *Electric-Field-Induced Magnetic Anisotropy in a Nanomagnet Investigated on the Atomic Scale*

8.7.2015: P.-J. Hsu, A. Finco, L. Schmidt, A. Kubetzka, K. von Bergmann, and R. Wiesendanger, 20$^{\text{th}}$ International Conference on Magnetism, Barcelona (Spain): *Guiding of zigzag spin spiral by local uniaxial strain relief*

10.7.2015: S. Krause, A. Schlenhoff, P. Lindner, J. Friedlein, R. Wiesendanger, M. Weinl, M. Schreck, and M. Albrecht, 20$^{\text{th}}$ International Conference on Magnetism (ICM-20), Barcelona (Spain): *A Magnetic Nano-Skyrmion Lattice Observed in a Si-Wafer Based Multilayer System*

10.7.2015: M. Steinbrecher, A. A. Khajetoorians, M. Bouhassoune, M. dos Santos Dias, S. Lounis, M. Ternes, J. Wiebe and R. Wiesendanger, 20$^{\text{th}}$ International Conference on Magnetism, Barcelona (Spain): *Conduction-electron mediated Dzyaloshinskii-Moriya interaction in pairs of adatoms revealed by ISTS*

9.9.2015: J. Grenz, A. Schwarz, and R. Wiesendanger, 18$^{\text{th}}$ International Conference on non-contact Atomic Force Microscopy, Cassis (France): *Adsorption of a magnetic molecule on a magnetic substrate: An nc-AFM study of Fe-PC on Fe/W(001)*

9.9.2015: A. Schwarz, J. Grenz, and R. Wiesendanger, 18$^{\text{th}}$ International Conference on non-contact Atomic Force Microscopy, Cassis (France): *Detecting Antiferromagnetic Domain Walls on the Fe Monolayer on W(001) with Magnetic Exchange Force Microscopy*

18.9.2015: J. Wiebe, Neueröffnung der Ausstellung "Nanotechnologie - Aufbruch in neue Welten", Hamburg (Germany): *Informationstechnologie von Morgen: Logische Gatter aus elf Atomen*

18.9.2015: N. Romming, Neueröffnung der Ausstellung "Nanotechnologie - Aufbruch in neue Welten", Hamburg (Germany): *Magnetische Knoten als Datenspeicher der Zukunft*

18.9.2015: N. Romming, Neueröffnung der Ausstellung "Nanotechnologie - Aufbruch in neue Welten", Hamburg (Germany): *Magnetische Knoten als Datenspeicher der Zukunft*

18.9.2015: N. Romming, Neueröffnung der Ausstellung "Nanotechnologie - Aufbruch in neue Welten", Hamburg (Germany): *Magnetische Knoten als Datenspeicher der Zukunft*

18.9.2015: R. Wiesendanger, Neueröffnung der Ausstellung "Nanotechnologie - Aufbruch in neue Welten", Hamburg (Germany): *Informations- und Kommunikationstechnik als Basis unserer Wissensgesellschaft: Was bringt die Zukunft?*

18.9.2015: S. Krause, Neueröffnung der Ausstellung "Nanotechnologie - Aufbruch in neue Welten", Hamburg (Germany): *Telegramme aus der Nanowelt: Magnetisierungsdynamik auf atomarer Skala*

18.9.2015: A. Schwarz, Neueröffnung der Ausstellung "Nanotechnologie - Aufbruch in neue Welten", Hamburg (Germany): *]KräfteMessen[*

18.9.2015: E. Y. Vedmedenko , Neueröffnung der Ausstellung "Nanotechnologie - Aufbruch in neue Welten", Hamburg (Germany): *Nanofiction und Nanoreality*

19.9.2015: M. Steinbrecher, Neueröffnung der Ausstellung "Nanotechnologie - Aufbruch in neue Welten", Hamburg (Germany): *Informationstechnologie von Morgen: Logische Gatter aus elf Atomen*

19.9.2015: R. Wiesendanger, Neueröffnung der Ausstellung "Nanotechnologie - Aufbruch in neue Welten", Hamburg (Germany): *Informations- und Kommunikationstechnik als Basis unserer Wissensgesellschaft: Was bringt die Zukunft?*

19.9.2015: S. Krause, Neueröffnung der Ausstellung "Nanotechnologie - Aufbruch in neue Welten", Hamburg (Germany): *Telegramme aus der Nanowelt: Magnetisierungsdynamik auf atomarer Skala*

19.9.2015: A. Schwarz, Neueröffnung der Ausstellung "Nanotechnologie - Aufbruch in neue Welten", Hamburg (Germany): *]KräfteMessen[*

19.9.2015: E. Y. Vedmedenko, Neueröffnung der Ausstellung "Nanotechnologie - Aufbruch in neue Welten", Hamburg (Germany): *Nanofiction und Nanoreality*

2.10.2015: M. Steinbrecher, Abschlusskolloquium des Graduiertenkolleg 1286, Hamburg (Germany): *Spinauflösende lokale Spektroskopie von Atom für Atom gebauten magnetischen Nanostrukturen*

2.10.2015: P. Löptien, Abschlusskolloquium des Graduiertenkolleg 1286, Hamburg (Germany): *Passive Bauelemente von Vishay Beyschlag*

3.10.2015: S. Manna, Physics of Interfaces and Layered Structures, Nordita, Stockholm (Sweden): *Interfacial electronic and magnetic properties in Fe-chalcogenide thin films studied by spin-polarized STM*

2.11.2015: J. Warmuth, A. Bruix, M. Michiardi, T. Hänke, M. Bianchi, J. Wiebe, R. Wiesendanger, B. Hammer, P. Hofmann, and A. A. Khajetoorians, 598. Herarus Seminar, Bad Honnef (Germany): *Band gap induced by Bi intercalation of graphene on Ir(111)*

7.11.2015: R. Wiesendanger, 6. Nacht des Wissens, Hamburg (Germany): *Informations- und Kommunikationstechnik als Basis unserer Wissensgesellschaft: Was bringt die Zukunft?".*

7.11.2015: A. Schwarz, 6. Nacht des Wissens, Hamburg (Germany): *]KräfteMessen[*

7.11.2015: S. Krause, 6. Nacht des Wissens, Hamburg (Germany): *Telegramme aus der Nanowelt: Magnetisierungsdynamik auf atomarer Skala*

7.11.2015: R. Wiesendanger, 6. Nacht des Wissens, Hamburg (Germany): *Informations- und Kommunikationstechnik als Basis unserer Wissensgesellschaft: Was bringt die Zukunft?*

7.11.2015: J. Wiebe, 6. Nacht des Wissens, Hamburg (Germany): *Informationstechnologie von Morgen: Logische Gatter aus elf Atomen*

7.11.2015: K. von Bergmann, 6. Nacht des Wissens, Hamburg (Germany): *Magnetische Knoten als Datenspeicher der Zukunft*

7.11.2015: E. Y. Vedmedenko, 6. Nacht des Wissens, Hamburg (Germany): *Nanofiction und Nanoreality*

24.11.2015: H Fuchs, Ringvorlesung "Physik im Alltag", Hamburg (Germany): *Nanotechnologie in Wissenschaft und Alltag*

30.11.2015: R. Wiesendanger, Rotary Club HH -Deichtor, Hamburg (Germany): *Neue bedeutsame Entwicklungen für die Informations- und Kommunikat ionstechnik der Zukunft*

8.12.2015: K. von Bergmann, Junge Wissenschaftler im Gespräch, Universitäts-Gesellschaft Hamburg, Hamburg (Germany): *Magnetische Knoten als Datenspeicher der Zukunft?*

10.12.2015: K. von Bergmann, SFB 1170 Seminar, Würzburg (G): *Topological Magnetic Skyrmions investigated by STM*

14.1.2016: A. Finco, P.-J. Hsu, N. Romming, T. Eelbo, L. Schmidt, A. Kubetzka, K. von Bergmann, and R. Wiesendanger, 2016 IEEE Joint Magnetism and Magnetic Materials - INTERMAG Conference, San Diego (USA): *Temperature and field dependent SP-STM investigation of the non-collinear magnetic structures of several layers of Fe on Ir(111)*

21.1.2016: E. Y. Vedmedenko , European XFEL Theory seminar, Hamburg (Germany): *Description of magnetic phase transitions by Monte-Carlo simulations*

7.3.2016: P.-J. Hsu, A. Kubetzka, A. Finco, N. Romming, K. von Bergmann, and R. Wiesendanger, 80$^{\text{th}}$ Spring Conference, Deutsche Physikalische Gesellschaft, Regensburg (Germany): *Electric field switching of individual magnetic skyrmions*

7.3.2016: J. Hagemeister, E. Vedmedenko, and R. Wiesendanger, 80$^{\text{th}}$ Spring Conference, Deutsche Physikalische Gesellschaft, Regensburg (Germany): *Influence of lattice strain on the formation of magnetic skyrmions*

8.3.2016: A. Schwarz, J. Grenz, and R. Wiesendanger, 80$^{\text{th}}$ Spring Conference, Deutsche Physikalische Gesellschaft, Regensburg (Germany): *Co-Salen on NiO(001): Indication of a superexchange mediated coupling between a magnetic molecule and an antiferromagnetic bulk insulating substrate*

8.3.2016: N. Romming, M. Hoffmann, B. Dupé, A. Kubetzka, K. von Bergmann, S. Heinze, and R. Wiesendanger, 80$^{\text{th}}$ Spring Conference, Deutsche Physikalische Gesellschaft, Regensburg (Germany): *Exchange driven spin spiral in Rh/Fe/Ir(111)*

8.3.2016: M. Bazarnik, J. Brede, and R. Wiesendanger, 80$^{\text{th}}$ Spring Conference, Deutsche Physikalische Gesellschaft, Regensburg (Germany): *Tuning magnetic coupling between organic-metal hybrids mediated by a nanoskyrmion lattice*

8.3.2016: A. Palacio Morales, K. von Bergmann, A. Kubetzka, and R. Wiesendanger, 80$^{\text{th}}$ Spring Conference, Deutsche Physikalische Gesellschaft, Regensburg (Germany): *Competition between complex magnetic states of Fe/Re(0001)*

9.3.2016: L. Cornils, S. Manna, A. Kamlapure, T. Hänke, U. Singh, J. Warmuth, J. Hu, Z. Mao, M. Bremholm, B. B. Iversen, P. Hofmann, J. Wiebe, and R. Wiesendanger, 80$^{\text{th}}$ Spring Conference, Deutsche Physikalische Gesellschaft, Regensburg (Germany): *Investigation of the electronic and magnetic structure of thin layer FeTe on Bi_2Te_3*

9.3.2016: S. Krause, A. Sonntag, J. Hermenau, Johannes Friedlein, and R. Wiesendanger, 80$^{\text{th}}$ Spring Conference, Deutsche Physikalische Gesellschaft, Regensburg (Germany): *High Frequency Magnetization Dynamics of Individual Atomic-Scale Magnets*

9.3.2016: A. Finco, P.-J. Hsu, N. Romming, T. Eelbo, L. Schmidt, A. Kubetzka, K. von Bergmann, and R. Wiesendanger, 80$^{\text{th}}$ Spring Conference, Deutsche Physikalische Gesellschaft, Regensburg (Germany): *Non collinear magnetic order at room temperature*

18.3.2016: J. Wiebe, A. A. Khajetoorians, M. Steinbrecher, M. Ternes, M. Bouhassoune, M. Dos Santos Dias, S. Lounis, and R. Wiesendanger, APS March Meeting, Baltimore, Maryland (USA): *Tailoring the chiral magnetic interaction between two individual atoms*

14.4.2016: R. Wiesendanger, University of Bremen (Colloquium), Bremen (Germany): *Magnetische Knoten auf der Nanometerskala: von der Grundlagenforschung zu neuen Datenspeicherkonzepten*

26.4.2016: L. Cornils, S. Manna, A. Kamlapure, T. Hänke, J. Hu, Z.Q. Mao, J.-L. Mi, B. B. Iversen, Ph. Hofmann, J. Wiebe, and R. Wiesendanger, ICSM2016 Confernce, Fethiye (Turkey): *Magnetic Properties in Fe-Chalcogenide thin films an FeTe bulk crystals studied by spin-polarized STM*

28.4.2016: N. Romming, A. Kubetzka, C. Hanneken, F. Otte, B. Dupé, K. von Bergmann, S. Heinze, and R. Wiesendanger, Seminar Uni Kiel, Kiel (Germany): *Investigation and Manipulation of Single Magnetic Skyrmions*

6.5.2016: R. Wiesendanger, Rotary Club HH-Altona, Hamburg (Germany): *Neue bedeutsame Entwicklungen für die Informations- und Kommunikationstechnik der Zukunft*

9.6.2016: K. von Bergmann, SPIN+X Colloquium, Mainz (Germany): *Magnetic skyrmions: investigation and manipulation by STM*

25.6.2016: E. Sierda, M. Abadia, J. Brede, M. Elsebach, B. Bugenhagen, M. H. Prosenc, M. Bazarnik, and R. Wiesendanger, NanoTech Poland 2016, Poznan (Poland): *Co-Salophene oligomers growth on Ag(111) and Au(111) surfaces – STM and XPS study*

25.7.2016: J. Grenz, A. Schwarz, and R. Wiesendanger, 19$^{\text{th}}$ International Conference on non-contact Atomic Force Microscopy, Nottingham (UK): *Probing the interaction between adsorbed hydrogen and a metallic tip*

25.7.2016: A. Schwarz, J. Grenz, and R. Wiesendanger, 19$^{\text{th}}$ International Conference on non-contact Atomic Force Microscopy, Nottingham (UK): *Indication of a superexchange mediated coupling between Co-Salen and NiO(001)*

2.8.2016: L. Cornils, S. Manna, A. Kamlapure, T. Hänke, U. Singh, J. Warmuth, J. Hu, Z. Mao, M. Bremholm, B. B. Iversen, P. Hofmann, J. Wiebe, and R. Wiesendanger, International Conference on the Physics of Semiconductors, Peking (China): *Evidence for superconductivity in the anti-ferromagnetic phase of monolayer FeTe on Bi_2Te_3*

20.8.2016: J. Hermenau, A. Sonntag, J. Ibanez-Azpiroz, Chr. Hübner, M. Steinbrecher, A. A. Khajetoorians, B. Baxevanis, S. Lounis, J. Wiebe, and R. Wiesendanger, ICN+T 2016, Busan (South Korea): *Magnetic stability of an Fe trimer on Pt(111)*

22.8.2016: N. Romming, K. von Bergmann, A. Kubetzka, and R. Wiesendanger, International Conference on Nanoscience and Technology, Busan (Republic of Korea): *Complex Spin States and Skyrmions in confined geometries*

22.8.2016: M. Bazarnik, B. Bugenhagen, M. Elsebach, E. Sierda, A. Frank, M.H. Prosenc, R. Wiesendanger, 20$^{\text{th}}$ International Vacuum Congress, Busan (Republic of Korea): *Towards tailored all-spin molecular devices*

23.8.2016: E. Y. Vedmedenko, A. Siemens, Y. Zhang, J. Hagemeister, and R. Wiesendanger, JEMS 2016, Glasgow (UK): *Minimal radius of magnetic skyrmions: statics and dynamics*

23.8.2016: A. Schlenhoff, S. Krause, P. Lindner, J. Friedlein, R. Wiesendanger, M. Weinl, M. Schreck, and M. Albrecht, International Conference on Nanoscience and Technology, Busan (Republic of Korea): *A Magnetic Nano-Skyrmion Lattice Observed in a Si-Wafer Based Multilayer System*

23.8.2016: S. Krause, A. Sonntag, J. Hermenau, J. Friedlein, and R. Wiesendanger, International Conference on Nanoscience and Technology, Busan (Republic of Korea): *High Frequency Magnetization Dynamics of Individual Atomic-Scale Magnets*

30.8.2016: M. Bazarnik, E. Sierda, M. Abadia, M. Elsebach, J. Brede, and R. Wiesendanger, SPSTM-2016, Chiba (Japan): *Electronic and magnetic properties of the $GdAu_2$ surface alloy probed by SP-STM*

30.8.2016: J. Hermenau, A. Sonntag, J. Ibanez-Azpiroz, Chr. Hübner, M. Steinbrecher, A. A. Khajetoorians, B. Baxevanis, S. Lounis, J. Wiebe, and R. Wiesendanger, SP-STM 2016, Chiba/Tokyo (Japan): *Magnetic stability of an Fe trimer on Pt(111)*

8.10.2016: R. Wiesendanger, Hamburger Tag der Nanotechnologie, Hamburg (Germany): *Informations- und Kommunikationstechnik als Basis unserer Wissensgesellschaft: Was bringt die Zukunft?*

8.10.2016: S. Krause, Hamburger Tag der Nanotechnologie, Hamburg (Germany): *Telegramme aus der Nanowelt: Magnetisierungsdynamik auf atomarer Skala*

8.10.2016: J. Wiebe, Hamburger Tag der Nanotechnologie, Hamburg (Germany): *Informationstechnologie von Morgen: Logische Gatter aus elf Atomen*

8.10.2016: K. von Bergmann, Hamburger Tag der Nanotechnologie, Hamburg (Germany): *Magnetische Knoten als Datenspeicher der Zukunft*

8.10.2016: J. Hagemeister, Hamburger Tag der Nanotechnologie, Hamburg (Germany): *Nanofiction und Nanoreality*

8.10.2016: A. Schwarz, Hamburger Tag der Nanotechnologie, Hamburg (Germany): *]KräfteMessen[*

3.11.2016: S. Krause, A. Sonntag, J. Hermenau, J. Friedlein and R. Wiesendanger, 61st Annual Conference on Magnetism and Magnetic Materials, New Orleans, LA (USA): *High-Frequency Magnetization Dynamics of Individual Atomic-Scale Magnets*

3.11.2016: A. Palacio Morales, A. Kubetzka, K. von Bergmann, and R. Wiesendanger, MMM16 conference, New Orleans (USA): *Coupling of coexisting non-collinear Spin States in Fe Monolayer on Re(100)*

3.11.2016: E. Y. Vedmedenko, International Conference on Magnetism and Magnetic Materials (MMM2017), New-Orleans (USA): *Stability of interfacial skyrmions, solitons and bound monopoles: how to store energy in topological magnetic quasiparticles*

7.11.2016: H. Zhong, Mini Workshop of the DFG Research Training Group 1991 – quantum mechanical noise in complex systems, Hamburg (Germany): *Interfacing Ultracold Atoms with a Millikelvin Nanomechanical Resonator*

14.11.2016: E. Y. Vedmedenko, Theory-Colloquium, Martin-Luther University of Halle-Wittenberg, Halle (Germany): *Stability of interfacial skyrmions, solitons and bound monopoles: how to store energy in topological magnetic quasiparticles*

22.11.2016: H. Fuchs, Ringvorlesung "Physik im Alltag", Hamburg (Germany): *Nanotechnologie in Wissenschaft und Alltag*

29.11.2016: S. Krause, Kolloquium of SFB 1242, University of Duisburg-Essen, Duisburg (Germany): *High Frequency Magnetization Dynamics of Individual Atomic-Scale Magnets*

1.12.2016: E. Sierda, VIII Seminar on Research Conducted Using Scanning Probe Techniques, Zakopane (Poland): *Engineering of organic nano-wires with magnetic atoms embedded in them*

7.2.2 Posters

3.3.2014: P. Löptien, L. Zhou, J. Wiebe, A. A. Khajetoorians, J.-L. Mi, B. B. Iversen, Ph. Hofmann, and R. Wiesendanger, APS March Meeting 2014, Denver (USA): *Screening and atomic-scale engineering of the potential at a topological insulator surface*

17.3.2014: H. Zhong, G. Fläschner, M. Nitschke, A. Schwarz, and R. Wiesendanger, 78$^{\text{th}}$ Spring Conference, Deutsche Physikalische Gesellschaft, Berlin (Germany): *Set-up of a hybrid quantum optomechanical system at 30 mK*

17.3.2014: C. Staarmann, A. Bick, P. Christoph, O. Hellmig, C. Becker, K. Sengstock, H. Zhong, G. Fläschner, A. Schwarz, and R. Wiesendanger, 78$^{\text{th}}$ Spring Conference, Deutsche Physikalische Gesellschaft, Berlin (Germany): *A Hybrid System in the Quantum Regime*

1.4.2014: J. Warmuth, M. Vondráček, M. Michiardi, L. Barreto, C. Piamonteze, A. Eich, A. A. Khajetoorians, J.-L. Mi, B. B. Iversen, Ph. Hofmann, J. Wiebe, J. Honolka, and R. Wiesendanger, 78$^{\text{th}}$ Spring Conference, Deutsche Physikalische Gesellschaft, Dresden (Germany): *Combined XMCD and STS study of transition metal adatoms adsorbed on the surface of prototypical 3D topological insulators*

1.4.2014: J. Grenz, A. Schwarz, and R. Wiesendanger, 78$^{\text{th}}$ Spring Conference, Deutsche Physikalische Gesellschaft, Dresden (Germany): *CO on NiO(001)*

2.4.2014: J. Wiebe, A. A. Khajetoorians, T. Schlenk, M. Steinbrecher, M. Valentyuk, B. Schweflinghaus, M. dos Santos Dias, M. Bouhassoune, S. Lounis, A. Lichtenstein, and R. Wiesendanger, 78$^{\text{th}}$ Spring Conference, Deutsche Physikalische Gesellschaft, Dresden (Germany): *Manipulating the magnetic properties of a single atom by controlled hydrogenation*

2.4.2014: J. Friedlein, A. Sonntag, J. Harm, S. Krause, and R. Wiesendanger, 78$^{\text{th}}$ Spring Conference, Deutsche Physikalische Gesellschaft, Dresden (Germany): *Toward a multiprobe-high-frequency-spin-polarized scanning tunneling microscope*

2.4.2014: J. Harm, J. Friedlein, A. Sonntag, S. Krause, and R. Wiesendanger, 78$^{\text{th}}$ Spring Conference, Deutsche Physikalische Gesellschaft, Dresden (Germany): *Capacitively guided tip-to-tip positioning for multiprobe spin-polarized scanning tunneling microscopy*

9.4.2014: N. Romming, K. von Bergmann, A. Kubetzka, and R. Wiesendanger, Skymag 2014, Paris (France): *Magnetic field dependent study of the skyrmion size*

9.4.2014: J. Hagemeister, E. Vedmedenko, R. Wiesendanger, Skymag 2014, Paris (France): *Tailoring skyrmion lattices*

10.4.2014: K. von Bergmann, S. Heinze, M. Menzel, J. Brede, G. Bihlmayer, S. Blügel, A. Kubetzka, and R. Wiesendanger, Skymag 2014, Paris (France): *Nanoskyrmion lattices in zero magnetic field: spin-polarized STM on Fe/Ir(111)*

10.4.2014: S. Ouazi, A. Kubetzka, K. von Bergmann, and R. Wiesendanger, Skymag 2014, Paris (France): *Magnetic atom manipulation over a skyrmion lattice*

10.4.2014: C. Hanneken, N. Romming, K. von Bergmann, A. Kubetzka, and R. Wiesendanger, SKYMAG 2014, Paris (France): *Spatial variation of a skyrmion's electronic band structure observed with scanning tunneling spectroscopy*

7.7.2014: L. Cornils, M. Vondráček, M. Michiardi, L. Barreto, C. Piamonteze, A. Eich, A. A. Khajetoorians, J.-L. Mi, B. B. Iversen, Ph. Hofmann, J. Wiebe, J. Honolka, and R. Wiesendanger, New Trends in Topological Insulators, Berlin (Germany): *Combined XMCD and STS study of transition metal adatoms adsorbed on the surface of prototypical 3D topological insulators*

9.7.2014: J. Wiebe, P. Löptien, L. Zhou, A. A. Khajetoorians, J. L. Mi, B. B. Iversen, Ph. Hofmann, and R. Wiesendanger, New Trends in Topological Insulators (NTTI) 2014, Berlin (Germany): *Screening and Atomic-Scale Engineering of the Potential at a Topological Insulator Surface*

10.7.2014: S. Ouazi, A. Kubetzka, K. von Bergamnn, and R. Wiesendanger, International Symposium on Spin-Polarized Electron Physics and Nanomagnetism, Halle (Germany): *Enhanced atomic-scale spin contrast due to spin friction*

12.7.2014: S. Ouazi, A. Kubetzka, K. von Bergmann, and R. Wiesendanger, Max-Planck-Institute Symposium, Halle (Saale) (Germany): *Enhanced atomic-scale spin contrast due to spin friction*

16.7.2014: C. Hanneken, N. Romming, K. von Bergmann, A. Kubetzka, and R. Wiesendanger, SP-STM 2014, Huron (OH), (USA): *Spatial variation of a skyrmion's electronic band structure observed with scanning tunneling spectroscopy*

23.7.2014: C. Hanneken, N. Romming, K. von Bergmann, A. Kubetzka, and R. Wiesendanger, International Conference on Nanoscience and Technology, Vail, Colorado (USA): *Spatial variation of a skyrmion's electronic band structure observed with scanning tunneling spectroscopy*

23.7.2014: S. Krause, A. Sonntag, J. Hermenau and R. Wiesendanger, International Conference on Nanoscience and Technology, Vail, Colorado (USA): *Temperature-Driven Phase Transition of Fe/Ir(111) Nanoskyrmions*

18.9.2014: J. Grenz, A. Schwarz, and R. Wiesendanger, SFB668 Summer School: Magnetism on a Molecular Scale: Experiment and Theory, Hamburg (Germany): *Single molecules Iron-Phthalocyanine on Fe/W(001)*

2.2.2015: C. Friesen and S. Krause, SpinCaT Workshop, Bad Honnef (Germany), 2015-2-2: *Magneto-Seebeck tunneling across a vacuum barrier*

23.2.2015: J. Grenz, A. Schwarz, and R. Wiesendanger, Workshop on high-resolution AFM/STM images using functionalized tips, Prag (Czech Republic): *Single Iron-Phthalocyanine molecules on Fe/W(001): A non-contact atomic force microscopy study at low temperature in UHV*

16.3.2015: L. Schmidt, P.-J. Hsu, C. Hanneken, A. Kubetzka, K. von Bergmann, and R. Wiesendanger, 79$^{\text{th}}$ Spring Conference, Deutsche Physikalische Gesellschaft, Berlin (Germany): *Spin Spirals and Skyrmions in ultrathin Films an in-plane magnetic Fields investigated by SP-STM*

17.3.2015: A. Finco, P.-J. Hsu, L. Schmidt, A. Kubetzka, K. von Bergmann, and R.Wiesendanger, 79$^{\text{th}}$ Spring Conference, Deutsche Physikalische Gesellschaft, Berlin (Germany): *Investigation of the chiral spin structure of the double layer Fe on Ir(111) using SP-STM in a 3D vector magnetic field system*

17.3.2015: T. Eelbo, V. Zdravkov, and R. Wiesendanger, 79$^{\text{th}}$ Spring Conference, Deutsche Physikalische Gesellschaft, Berlin (Germany): *STM study of the preparation of superconducting Ta(110) surfaces*

17.3.2015: J. Hagemeister, N. Romming, K. von Bergmann, E. Y. Vedmedenko, and R. Wiesendanger, 79$^{\text{th}}$ Spring Conference, Deutsche Physikalische Gesellschaft, Berlin (Germany): *Stability of Single Skyrmionic Bits*

17.3.2015: A. Kubetzka, C. Hanneken, N. Romming, K. von Bergmann, R. Wiesendanger, F. Otte, B. Dupé, and S. Heinze, 79$^{\text{th}}$ Spring Conference, Deutsche Physikalische Gesellschaft, Berlin (Germany): *Spin-curvature and local density of states in PdFe/Ir(111)*

18.3.2015: M. Vondracek, M. Schüler, M. Dunst, C. Piamonteze, J. Warmuth, M. Michiardi, L. Barreto, A. A. Khajetoorians, J.-L. Mi, B. B. Iversen, P. Hofmann, J. Wiebe, T. Wehling, J. Minar, H. Ebert, R. Wiesendanger, and J. Honolka, 79$^{\text{th}}$ Spring Conference, Deutsche Physikalische Gesellschaft, Berlin (Germany): *XMCD of 3d adatoms on Bi_2Te_3 and Bi_2Te_2Se: experiment and ab initio theory*

18.3.2015: M. Elsebach, M. Bazarnik, B. Bugenhagen, A. Frank, M. H. Prosenc, and R. Wiesendanger, 79$^{\text{th}}$ Spring Conference, Deutsche Physikalische Gesellschaft, Berlin (Germany): *Development of a Soft-Landing for Electrospray Deposition*

20.3.2015: J. P. Hermenau, A. Sonntag and A. Khajetoorians, 79$^{\text{th}}$ Spring Conference, Deutsche Physikalische Gesellschaft, Berlin (Germany): *Construction of a dilution fridge based UHV spin-polarized STM operational in a vector magnetic field*

26.3.2015: P. Christoph, A. Bick, C. Staarmann, H. Zhong, A. Schwarz, R. Wiesendanger, O. Hellmig, J. Heinze, C. Becker, and K. Sengstock, Asymmetric fiber cavities for quantum opto-mechanics with SiN-membranes, Heidelberg (Germany): *Asymmetric fiber cavities for quantum opto-mechanics with SiN-membranes*

26.3.2015: H. Zhong, P. Christoph, A. Bick, C. Staarmann, J. Heinze, O. Hellmig, C. Becker, A. Schwarz, K. Sengstock, and R. Wiesendanger, DPG-Frühjahrstagung (AMOP), Heidelberg (Germany): *Realizing a sub-kelvin membrane-in-the-middle fiber cavity*

6.7.2015: L. Cornils, J. Honolka, M. Vondráček, L. Zhou, A. Kamlapure, J. Warmuth, J. Wiebe, A. A. Khajetoorians, L. Barreto, M. Michiardi, P. Hofmann, B. B. Iversen, C. Piamonteze, J. L. Mi, T. Wehling, M. Schüler, H. Ebert, J. Minar, and R. Wiesendanger, New Trends in Topological Insulators, San Sebastian (Spain): *A combined XMCD, ARPES and STM study of 3d adatoms on the topological insulator Bi_2Te_2Se*

9.7.2015: J. Hagemeister, A. Kubetzka, E. Vedmedenko, and R. Wiesendanger, 20$^{\text{th}}$ International Conference on Magnetism, Barcelona (Spain): *Confinement effects in lattices of nanoskyrmions*

15.7.2015: S. Krause, A. Sonntag, J. Hermenau, and R. Wiesendanger, International Conference on Magnetism (ICM-20), Barcelona (Spain): *Thermal stability of an interface-stabilized skyrmion lattice*

4.11.2015: M. Steinbrecher, A. A. Khajetoorians, M. Bouhassoune, M. dos Santos Dias, S. Lounis, M. Ternes, J. Wiebe and R. Wiesendanger, 598. WE-Heraeus-Seminar: Frontiers in Scanning Probe Microscopy, Bad Honnef (Germany): *Conduction-electron mediated Dzialoshinsky-Moriya interaction in pairs of adatoms revealed by ISTS*

4.11.2015: J. Grenz, A. Schwarz, and R.Wiesendanger, 598. WE-Heraeus-Seminar: Frontiers in Scanning Probe Microscopy, Bad Honnef (Germany): *Adsorption of a magnetic molecule on a magnetic substrate: An nc-AFM study of Fe-PC on Fe/W(001)*

4.11.2015: N. Romming, A. Kubetzka, C. Hanneken, K. von Bergmann, and R. Wiesendanger, 598. WE-Heraeus-Seminar, Bad Honnef (Germany): *Investigation and Manipulation of Single Magnetic Skyrmions*

4.11.2015: M. Bazarnik, B. Bugenhagen, M. Elsebach, E. Sierda, A. Frank, M.H. Prosenc, and R. Wiesendanger, 598. WE-Heraeus-Seminar on Frontiers in Scanning Probe Microscopy, Bad Honnef (Germany): *Towards tailored all-spin molecular devices*

4.11.2015: J. Hermenau, A. Sonntag, Chr. Hübner, J. Ibanez-Azpiroz, M. Steinbrecher, A. A. Khajetoorians, B. Baxevanis, S. Lounis, J. Wiebe, R. Wiesendanger, 598. WE-Heraeus-Seminar on Frontiers in Scanning Probe Microscopy, Bad Honnef (Germany): *Investivation of the magnetization dynamics of Fe-clusters on Pt(111)*

2.3.2016: T. Wagner, C. Staarmann, P. Christoph, O. Hellmig, A. Bick, K. Sengstock, H. Zhong, A. Schwarz, and R. Wiesendanger, DPG-Frühjahrstagung (SAMOP), Hannover (Germany): *Coupling cold atoms to a cryogenically cooled optomechanical device*

2.3.2016: S. Krause and C. Friesen, SpinCaT Workshop, Bad Honnef (Germany): *Magneto-Seebeck Tunneling across a vacuum barrier*

8.3.2016: M. Steinbrecher, A. A. Khajetoorians, J. Wiebe, and R. Wiesendanger, 80$^{\text{th}}$ Spring Conference, Deutsche Physikalische Gesellschaft, Regensburg (Germany): *Non-collinear spin-states in dilute 1D chains induced by Dzyaloshinskii-Moriya interaction*

8.3.2016: J. Warmuth, A. Bruix, M. Michiardi, T. Hänke, M. Bianchi, J. Wiebe, R. Wiesendanger, B. Hammer, P. Hofmann, and A. A. Khajetoorians, 80$^{\text{th}}$ Spring Conference, Deutsche Physikalische Gesellschaft, Regensburg (Germany): *Band gap engineering by Bi intercalationj of graphene on Ir(111)*

9.3.2016: J. Sassmannshausen, A. Kubetzka, N. Romming, K. von Bergmann, and R. Wiesendanger, 80$^{\text{th}}$ Spring Conference, Deutsche Physikalische Gesellschaft, Regensburg (Germany): *Growth of Pb on ultrathin Fe layers on Ir(111)*

9.3.2016: D. Schwickert, M. Elsebach, M. Bazarnik, B. Bugenhagen, M. H. Prosenc, and R. Wiesendanger, 80$^{\text{th}}$ Spring Conference, Deutsche Physikalische Gesellschaft , Regensburg (Germany): *Tuning the Interaction of Magnetic Molecules with a Metallic Substrate via an Insulating Film*

9.3.2016: L. Schmidt, P.-J. Hsu, A. Kubetzka, K. von Bergmann, and R. Wiesendanger, 80$^{\text{th}}$ Spring Conference, Deutsche Physikalische Gesellschaft, Regensburg (Germany): *Skyrmions and spin spirals in canted and in-plane magnetic fields investigating by STM*

25.4.2016: L. Cornils, A. Kamlapure, S. Manna, T. H/"anke, J. Hu, Z. Q. Mao, J.-L. Mi, B. B. Iversen, Ph. Hofmann, J. Wiebe, and R. Wiesendanger, International Conference on Superconductivity and Magnetism, Fethiye (Turkey): *Magnetic Properties in Fe-Chalcogenide Thin Films and FeTe Bulk Crystals Studied by Spin-Polarized Scanning Tunneling Microscopy*

23.8.2016: L. Schmidt, J. Hagemeister, P.-J. Hsu, A. Kubetzka, K. von Bergmann, and R. Wiesendanger, 8$^{\text{th}}$ Joint European Magnetic Symposia (JEMS 2016), Glasgow (UK): *Skyrmions and spin spirals in canted and in-plane magnetic fields investigating by STM*

6.9.2016: M. Bazarnik, B. Bugenhagen, A. Frank, M.H. Prosenc, and R. Wiesendanger, The 15$^{\text{th}}$ International Conference on Molecule-Based Magnets, Sendai (Japan): *Spin resolved tunneling to salene based magnetic molecules adsorbed on ferromagnetic graphene based substrates*

Chapter 8

Lectures and Courses at the University of Hamburg

- Nanostrukturphysik II
- Magnetismus und Oberflächenphysik
- Einführung in die Rastersondenmikroskopie und -spektroskopie
- Ringvorlesung Physik im Alltag
- Seminar über Nahfeldgrenzflächenphysik und Nanotechnologie
- Seminar über aktuelle Probleme der Rastersensorphysik
- Proseminar über Visionen der Festkörperforschung
- Proseminar über Theorie und Praxis der Rastersensormethoden
- Proseminar über Magnetismus und Oberflächenphysik
- Übungen zur Nanostrukturphysik II
- Übungen zu Magnetismus und Oberflächenphysik
- Übungen zur Einführung in die Rastersondenmikroskopie und -spektroskopie
- Physikalisches Praktikum für Fortgeschrittene
- Nanoscience-Praktikum
- TU-Praktikum
- Studienarbeiten zur Rastersondenmikroskopie
- Bachelorarbeiten zur Grenzflächen- und Tieftemperaturphysik
- Schwerpunktpraktikum Grenzflächen- und Tieftemperaturphysik
- Masterarbeiten zur Grenzflächen- und Tieftemperaturphysik

Chapter 9

Public relations

- Nanotechnology-Exhibition and presentations for schools 2014-2016
  Size of audience: 2700
- Lab tours for schools and interested public 2014-2016
  Size of audience: 1900
- Internships for 5 students from schools in Hamburg
- Summer School "Research" for students from schools
  Size of audience: 140
- 30 press releases
- 35 public talks
- 2 TV broadcasts
- 4 radio broadcasts
- New websites:
  - www.nanoscience.de/astonish
  - www.nanotechnologie-ausstellung.de
- Public event: Neueröffnung der Dauerausstellung: "Nanotechnologie - Aufbruch in neue Welten"
  Date: 18.09.2015 and 18.09.2015
- Public event: Nacht des Wissens in Hamburg: "Nanowissenschaften - Im Reich der Atome und Moleküle"
  Date: 02.11.2015
- Public event: Hamburger Tag der Nanotechnologie
  Date: 08.10.2016

Chapter 10

Contributions to International Organizations

- Member of the International Program Committee of the "41st Conference on the Physics and Chemistry of Surfaces and Interfaces PCSI-41" (USA 2014)
- Member of the International Advisory Committee of the "4th International Conference on Superconductivity and Magnetism ICSM2014" (Antalya, Turkey 2014)
- Member of the International Scientific Committee of the "International Conference on Nanostructures and Self-Assembly NANOSEA 2014" (Marseille, France 2014)
- Member of the International Advisory Committee of the "5th International Conference on Spin-Polarized Scanning Tunneling Microscopy SPSTM-5" (Huron, Ohio 2014)
- Member of the International Steering Committee of the "International Conference on Nanoscience and Technology ICN+T 2014" (Vail / Colorado, USA 2014)
- Member of the International Advisory and Program Committee of the "Eighth International Conference on the Physics and Applications of Spin Phenomena in Solids PASPS VIII" (Washington D.C., USA 2014)
- Member of the International Program Advisory Boards of the "7th International Symposium on Surface Science ISSS-7" (Matsue, Japan 2014)
- Co-Organizer of the "International Workshop on Correlated Electronic Structure and Spin Dynamics CESSD-2015" (Hamburg 2015)
- Co-Chairman of the "7th International Conference on Scanning Probe Spectroscopy SPS '15" (Poznan, Poland 2015)
- Member of the International Advisory Committee of the International "NANO 2015" - Conference (Tamil, Nadu, India 2015)
- Member of the International Advisory Committee of the "5th International Conference on Superconductivity and Magnetism ICSM2016" (Fethiye, Turkey 2016)

- Member of the International Advisory Board of the "NanoTech Poland International Conference" (Poznan, Poland 2016)
- Member of the International Steering Committee of the "International Conference on Nanoscience and Technology ICN+T 2016" (Busan, South-Korea 2016)
- Member of the International Advisory Committee of the "6$^{\text{th}}$ International Conference on Spin-Polarized Scanning Tunneling Microscopy SPSTM-6" (Tokyo, Japan 2016)

Chapter 11

How to reach us

... by mail	write to University of Hamburg, Department of Physics, Jungiusstraße 11, D-20355 Hamburg, Germany.
... by phone	call (++49) 40 42838 5244.
... by fax	send to (++49) 40 42838 6188.
... by e-mail	send to `wiesendanger@physnet.uni-hamburg.de`
... within the WWW	`www.nanoscience.de`
... personally